The life cycle of anvil cirrus clouds from a combination of passive and active satellite remote sensing

Johan Strandgren

München 2018

The life cycle of anvil cirrus clouds from a combination of passive and active satellite remote sensing

Johan Strandgren

Dissertation
an der Fakultät für Physik
der Ludwig–Maximilians–Universität
München

vorgelegt von
Johan Strandgren
aus Tranås

München, den 30. Mai 2018

Erstgutachter: Prof. Dr. André Butz

Zweitgutachter: Prof. Dr. Bernhard Mayer

Tag der mündlichen Prüfung: 18. Juli 2018

Zusammenfassung

Konvektiv erzeugte Zirruswoken bilden sich in der oberen Troposphäre durch das Ausfließen von Eiskristallen aus hochreichenden konvektiven Cumulonimbus-Wolken. Da diese Zirren einfallende Sonnenstrahlung reflektieren sowie terrestrische Wärmestrahlung absorbieren und mit deutlich niedriger Temperatur re-emittieren, spielen sie eine wichtige Rolle im System Erde-Atmosphäre. Wenig verstanden sind jedoch die Prozesse, die den Lebenszyklus dieser Zirren bestimmen. Sie stellen eine der größten Unsicherheiten in der atmosphärischen Fernerkundung sowie in der Klima- und Wettermodellierung dar.

Diese Arbeit untersucht die zeitliche Entwicklung der Eigenschaften von konvektiv erzeugten Zirren während des gesamten Lebenszyklus, sowie die Zusammenhänge mit den meteorologischen Bedingungen. Eine umfassende Beschreibung der Eigenschaften dieses Wolkentyps wurde durch die Anwendung eines neu entwickelten Fernerkundungsalgorithmus namens CiPS (Cirrus Properties from SEVIRI) erreicht. Mithilfe eines Satzes künstlicher neuronaler Netze kombiniert CiPS die großräumige Abdeckung und die hohe zeitliche Auflösung des abbildendes Radiometer SEVIRI auf dem geostationären Satelliten Meteosat Second Generation mit der hohen vertikalen Auflösung und Sensitivität bezüglich dünner Zirruswolken des Lidars CALIOP auf dem polarumlaufenden Satelliten CALIPSO. Im Vergleich zu CALIOP erkennt CiPS 71 % bzw. 95 % aller Zirruswolken mit einer optischen Dicke (IOT) von 0.1 und 1.0. CiPS ist zudem in der Lage gleichzeitig die Wolkenhöhe, die IOT, den Eiswasserpfad (IWP) und, durch eine entsprechende Parametrisierung, den Effektivradius der Eispartikel zu bestimmen. Dies ermöglicht die Kombination von makroskopischen, mikrophysikalischen und optischen Eigenschaften und somit die Interpretation der zeitlichen Entwicklung der Zirruswolken.

Zusammen mit einer Methode zur Beobachtung der konvektiven Aktivität und einem neuen Verfolgungsalgorithmus wird CiPS zur Analyse des Lebenszyklus von 132 konvektiv erzeugten Zirruswolken, welche im Juli 2015 über Südeuropa und Nordafrika beobachtet wurden, verwendet. Während die optische Dicke der Zirruswolken in der gesamten Konvektionsphase ansteigt, nimmt sie schnell wieder ab, sobald die Konvektion endet. Zwei Stunden danach erreichen 92 ± 7 % einer Zirrusfläche die Werte IOT< 1 und IWP$< 30\,\mathrm{g\,m^{-2}}$ mit wahrscheinlichsten Werten bei 0.1–0.2 bzw. 1.5–3 $\mathrm{g\,m^{-2}}$. Im gleichen Zeitraum nimmt auch die Wolkenhöhe ab. Da dies sowohl für langlebige als auch für kurzlebige Zirren gilt, liegt die Schlussfolgerung nahe, dass die Eismenge in dieser Lebensphase hauptsächlich durch Sedimentation gesteuert wird. Eine entsprechende Abnahme des abgeleiteten Effektivradius unterstützt diese These. Während die Konvektionsstärke keinen sichtbaren Einfluss auf IOT und IWP hat, korreliert sie eindeutig mit der Wolkenhöhe und dem Effektivradius. Nach 2–3 Stunden sind Unterschiede im Effektivradius nicht mehr erkennbar, was darauf hindeutet, dass die Konvektionsstärke keinen Einfluss auf die Eiskristallgrößen bei den alternden Zirren hat. Wie ERA5 Reanalysedaten der relativen Feuchte zeigen, ist in dieser Lebensphase insbesondere die relative Feuchte in der oberen Troposphäre wirksam. Bei höhere relativen Feuchte entstehen mehr größere und vor allem langlebigere konvektiv erzeugte Zirren.

Abstract

Anvil cirrus clouds form in the upper troposphere from the outflow of ice crystals from deep convective cumulonimbus clouds. By reflecting incoming solar radiation as well as absorbing terrestrial thermal radiation, and re-emitting it at significantly lower temperatures, they play an important role for the Earth's radiation budget. Nevertheless the processes that govern their life cycle are not well understood and, hence, they remain one of the largest uncertainties in atmospheric remote sensing and climate and weather modelling.

In this thesis the temporal evolution of the anvil cirrus properties throughout their life cycle is investigated, as is their relationship with the meteorological conditions. For a comprehensive retrieval of the anvil cirrus properties, a new algorithm for the remote sensing of cirrus clouds called CiPS (Cirrus Properties from SEVIRI) is developed. Utilising a set of artificial neural networks, CiPS combines the large spatial coverage and high temporal resolution of the imaging radiometer SEVIRI aboard the geostationary satellites Meteosat Second Generation, with the high vertical resolution and sensitivity to thin cirrus clouds of the lidar CALIOP aboard the polar orbiting satellite CALIPSO. In comparison to CALIOP, CiPS detects 71 % and 95 % of all cirrus clouds with an ice optical thickness (IOT) of 0.1 and 1.0 respectively. Furthermore, CiPS retrieves the corresponding cloud top height, IOT, ice water path (IWP) and, by parameterisation, effective ice crystal radius. This way, macrophysical, microphysical and optical properties can be combined to interpret the temporal evolution of the anvil cirrus clouds.

Together with a tool for identifying convective activity and a new cirrus tracking algorithm, CiPS is used to analyse the life cycle of 132 anvil cirrus clouds observed over southern Europe and northern Africa in July 2015. Although the anvil cirrus clouds grow optically thick during the convective phase, they become thinner at a rapid pace as convection ceases. Two hours after the last observed convective activity, 92 ± 7 % of the anvil cirrus area has $\text{IOT}_{\text{CiPS}} < 1$ and $\text{IWP}_{\text{CiPS}} < 30\,\text{g}\,\text{m}^{-2}$ on average, with highest probability density around 0.1–0.2 and 1.5–3 $\text{g}\,\text{m}^{-2}$ respectively. During the same time period, the cloud top height is observed to decrease. Since this is observed for both long-lived and short-lived anvil cirrus, it is deduced that in this life phase the amount of ice in the anvil is mainly controlled by sedimentation. This is in line with a corresponding decrease in the estimated effective radius. While the convective strength has no evident effect on the IOT and IWP, stronger vertical updraught is clearly correlated with higher cloud top height and larger effective radius. Larger ice crystals are, however, observed to be removed effectively within 2-3 h after convection has ceased, suggesting that the convective strength has no impact on the ice crystal sizes in ageing anvils. In this life stage, upper tropospheric relative humidity, as derived from ERA5 reanalysis data, is shown to have a larger impact on the anvil cirrus life cycle, where higher relative humidity govern larger and especially more long-lived anvil cirrus clouds.

Publications

Parts of the results and text presented in this thesis have been published in the following papers:

Strandgren, J., Bugliaro, L., Sehnke, F., and Schröder, L.: Cirrus cloud retrieval with MSG/SEVIRI using artificial neural networks, *Atmos. Meas. Tech.*, 10, 35473573, doi: 10.5194/amt-10-3547-2017, 2017a.

J. Strandgren collocated all data spatially and temporally, developed and validated the new algorithm, compared the performance with COCS (Cirrus Optical Properties from CALIOP and SEVIRI), performed the cirrus life cycle analysis, interpreted the results and wrote the paper. L. Bugliaro supervised the development of the new algorithm and assisted in interpreting the results and writing the paper. F. Sehnke and Leon Schröder shared their knowledge about artificial neural networks and determined the optimal learning rate, momentum and batch size used to train the new algorithm.

Strandgren, J., Fricker, J., and Bugliaro, L.: Characterisation of the artificial neural network CiPS for cirrus cloud remote sensing with MSG/SEVIRI, *Atmos. Meas. Tech.*, 10, 43174339, doi:10.5194/amt-10-4317-2017, 2017b.

J. Strandgren performed the characterisation of CiPS (Cirrus Properties from SEVIRI), analysed and interpreted the results, wrote the paper and supervised J. Fricker. J. Fricker derived the vertical cloud-aerosol structures from CALIOP lidar data. L. Bugliaro reprojected the MODIS surface type data to the SEVIRI grid, supervised the study and assisted in interpreting the results and writing the paper.

Contents

4   CiPS - Cirrus Properties from SEVIRI   33

5   The life cycle of anvil cirrus clouds   81

Chapter 1

Introduction

Cirrus clouds are optically thin clouds in the upper troposphere made up of ice crystals. The name *cirrus*, which is Latin for *lock of hair*, refers to their common wispy visual appearance. *Anvil cirrus* is a type of cirrus cloud that forms from the convective outflow of ice crystals from deep convective cumulonimbus (thunderstorm) clouds. Cumulonimbus clouds form when sufficiently moist air is convected through an unstable troposphere, leading to condensation of water vapour and formation of cloud droplets and, when sufficiently cold, ice crystals. The altitude at which a rising air parcel has the same temperature as its environment is known as the equilibrium level of the atmosphere and marks the end of convective transport. When the rising air approaches this level it spreads horizontally due to temperature inversion. The horizontal spread of ice crystals from the convective core in all directions together with horizontal winds that blow the ice crystals downwind, leads to the characteristic flat anvil formed cirrus clouds. If the upward motion is strong enough, the rising air might penetrate the equilibrium level leading to a so-called overshooting top. The anvil shaped cirrus clouds can also form due to strong vertical wind shear that

Figure 1.1: Anvil cirrus cloud (greyish) together with parent cumulonimbus cloud and overshooting top (white) observed over the U.S. on 29 May 2012. Photo: R. Welser (DLR).

spreads the ice crystals horizontally. Figure 1.1 shows an anvil cirrus and its source cumulonimbus cloud over the U.S., photographed from the DLR (German Aerospace Center) research aircraft Falcon. The brighter white colours represent the cumulonimbus cloud and the overshooting top, whereas the dimmer greyish colours constitute the out-flowing ice crystals forming the anvil cirrus. Furthermore, Fig. 1.2 shows an illustrative drawing of the formation of anvil cirrus clouds, where moist air is entrained at lower levels, convected through the troposphere and later spread horizontally around the height of the tropopause and transported with the wind.
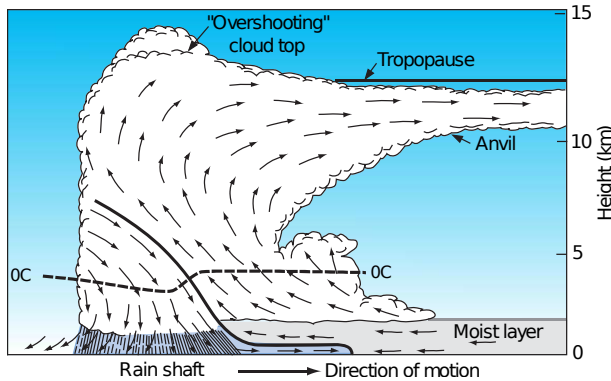

Figure 1.2: Illustration of an anvil cirrus cloud forming from the outflow of ice crystals from a deep convective cumulonimbus cloud near the tropopause. Figure adapted from Wallace and Hobbs (2006).

Several conditions are necessary for anvil cirrus clouds to form. Substantial moisture that can be entrained at lower levels and brought through the troposphere is a prerequisite for deep convection to occur. Whether the state of the atmosphere aids or impedes vertical motion of the moist air, is referred to as atmospheric instability. In a stable atmosphere a lifted air parcel will return to its initial position, whereas in a conditionally unstable atmosphere a lifted air parcel may start to rise without any external forcing if the *level of free convection* is reached, i.e. the point where a lifted air parcel becomes warmer and less dense than the surrounding air. To initiate the vertical motion, an external force is required that can lift the moist air to the level of free convection. Such forces can be e.g. low-level air convergence, cold fronts, surface heating and orographic lifting. The spatial extension of the anvil cirrus in the initial phase is partly related to the size of the convective system, which in turn depends on the low-level moisture and the strength of the vertical updraught. The vertical updraught of moisture from lower levels offers a continuous supply of new ice crystals at the anvil level, typically with larger ice crystals and wider size distributions closer to the convective updraught (Yuan et al., 2011). The spatial extension and persistence of the anvil cirrus and the temporal evolution of the microphysical properties, especially after the convective source has disappeared, further depends on the meteorological conditions in the upper troposphere where the convective outflow and anvil cirrus cloud formation takes place. Lower temperatures and more moisture associated with higher supersaturation aid the persistence of anvil cirrus. Ice supersaturation, i.e. a relative humidity with respect to ice above $100\,\%$, is required for ice crystal persistence through growth by water vapour deposition. In a dry upper atmosphere the anvil cirrus is likely to quickly dissipate due to the absence of deposition growth together with sedimentation and sublimation of the anvil cirrus ice crystals. Substantial moisture in the upper troposphere could, however, have a negative feedback on the anvil cirrus persistence, due to sedimentation of large, rapidly growing, ice crystals. Figure 1.3 shows a simple, but yet
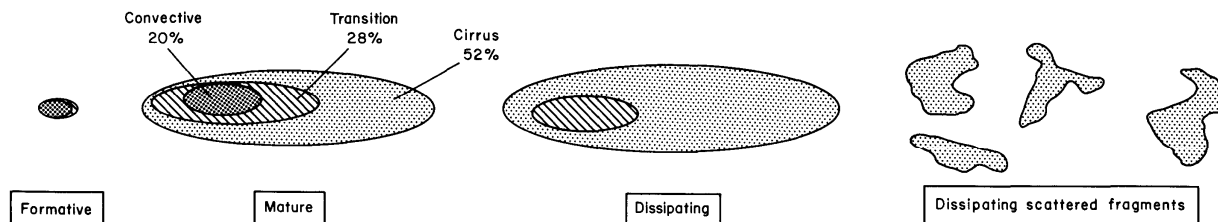
Figure 1.3: Illustration of the life cycle of a convective system and following anvil cirrus. Convective, transition and cirrus refer the parts of the cloud with an albedo > 0.7, 0.5–0.7, ≤ 0.5 respectively. Figure adapted from Machado and Rossow (1993).

representative, schematic of the different stages/types of convective systems and following anvil cirrus as illustrated by Machado and Rossow (1993); from a compact convective core, to a growing anvil and increasing fraction of thin anvil cirrus, to the dissipation and breaking into scattered fragments.

Anvil cirrus typically reach sizes of hundreds of km across (e.g. Machado et al., 1998) and are predominantly found in the tropics where low-level temperatures and moisture are commonly sufficiently high to generate wide spread areas of deep convection and hence anvil cirrus (e.g. Liu et al., 2007; Sassen et al., 2009). Although not as frequently, anvil cirrus clouds are commonly observed during summertime in the mid-latitudes as well. In Europe, they usually form along mountain ridges like e.g. the Alps, Pyrenees, Apennines and Dinaric Alps (e.g. Morel and Senesi, 2002), where the orographic lifting can trigger deep convection and hence anvil cirrus formation.

Anvil cirrus clouds, like all cirrus clouds, play an important role for the Earth's energy budget as they reflect incoming solar radiation and absorb outgoing terrestrial thermal radiation. In general, the net radiative forcing by cirrus clouds strongly depends on the height, thickness and microphysical properties (e.g. ice crystal shape, size distribution and ice water content) of the cloud (e.g. Fu and Liou, 1993; Zhang et al., 1999; Meerkötter et al., 1999; Liou, 2002; Wendisch et al., 2007). While the cooling effect through reflection of solar radiation is likely to be the dominant process for thick anvil cirrus clouds, it can be outweighed by the absorption and trapping of thermal radiation in ageing thinning anvil cirrus, leading to a positive net radiative forcing and warming of the Earth–atmosphere system, as is the case for thin cirrus clouds (e.g. Jensen et al., 1994; Chen et al., 2000). This is especially true for anvil cirrus that remain into the night, where the net radiative forcing is bound to be positive, independent of the optical and physical properties of the cloud. Deep convection and anvil cirrus further affects the Earth's climate by moistening the upper troposphere through the vertical transport of water vapour and, to some degree, the sublimation of cloud ice crystals (e.g. Luo and Rossow, 2004; Soden, 2004; Horváth and Soden, 2008; Wright et al., 2009, and references therein).

Potential anvil cirrus feedback mechanisms on a warming climate further demonstrate the importance of understanding the physical processes of anvil cirrus clouds. The "thermostat hypothesis" (Ramanathan and Collins, 1991) describes an increase in anvil cirrus amount with increasing sea surface temperature, leading to increased albedo and hence a

negative feedback on a warming climate. On the contrary, the "iris hypothesis" (Lindzen et al., 2001) suggests that higher sea surface temperatures lead to enhanced precipitation and rainout of cloud condensate, leading to reduced anvil cirrus cloud amount. The feedback is nevertheless assumed to be negative as a result of the reduced absorption of longwave radiation. According to the "fixed anvil temperature (FAT) hypothesis" (Hartmann and Larson, 2002) anvil cirrus top temperatures remain constant in a warming climate, leading to increased anvil cirrus top height and hence a positive feedback on the climate. Furthermore the "stability iris" hypothesis (Bony et al., 2016) suggests that as anvil cirrus clouds rise in a warming climate, the convective outflow and hence the anvil cirrus amount is reduced due to increased stability at the detrainment level.

Despite decades of research, cirrus clouds continue to introduce large uncertainties in climate and weather models (Waliser et al., 2009; Eliasson et al., 2011). Understanding the interaction between deep convection and upper-level cloudiness (cirrus) through anvil cirrus formation, and the related feedbacks on a warming climate is recognised as one of the grand challenges in atmospheric research by the World Climate Research Programme (WCRP; Bony et al., 2015). As part of WCRP, the GEWEX (Global Energy and Water Cycle Experiment) process evaluation study on upper tropospheric clouds and convection aims to better understand and quantify the relationship between deep convection and anvil cirrus (Stubenrauch et al., 2017). Anvil cirrus and stratiform convective outflow is also one of the scientific topics within the German-wide research initiative HD(CP)^2 (High Definition Clouds and Precipitation for advancing Climate Prediction), aiming towards an improved representation of anvil cirrus clouds in weather and climate models using enhanced observational data on cloud physical processes.

The ambition with this thesis is to increase the understanding of the temporal evolution of thin anvil cirrus clouds and their optical, macrophysical and microphysical properties throughout their life cycle, using satellite remote sensing data. Over the years, numerous remote sensing studies have been performed on the temporal evolution of deep convective systems and anvil cirrus clouds. A well-established positive correlation between the size of convective systems and anvil cirrus and their observed lifetime has been shown in several studies (e.g. Chen and Houze, 1997; Machado et al., 1998; Mathon and Laurent, 2001; Inoue et al., 2009; Feng et al., 2012; Imaoka and Nakamura, 2012). During the convective phase, the production of anvil cirrus generally outweighs the growth of the convective core itself, leading to a continuously increasing fraction of cirrus (e.g. Machado et al., 1998; Inoue et al., 2009; Imaoka and Nakamura, 2012; Fiolleau and Roca, 2013; Protopapadaki et al., 2017). The anvil coverage and ice water path (IWP) has been observed to peak approx. 1–5 h after the convective intensity peaks (e.g. Soden, 2004; Horváth and Soden, 2008; Sohn et al., 2008; Schröder et al., 2009), but can grow for longer time scales (≈ 15 h) as well (Luo and Rossow, 2004). The peak anvil coverage is followed by a gradual thinning during the dissipating phase with decreasing anvil cirrus coverage, optical thickness and IWP (e.g. Luo and Rossow, 2004; Mace et al., 2006; Horváth and Soden, 2008). Luo and Rossow (2004) and Bouniol et al. (2016) also observe reduced cloud top height for ageing anvil cirrus clouds. Although the number of convective systems decreases almost exponentially with their observed lifetime with most systems having observed lifetimes below ≈ 5 h (Chen

and Houze, 1997; Mathon and Laurent, 2001; Feng et al., 2012; Imaoka and Nakamura, 2012), lifetimes of several days are also possible. E.g. Luo and Rossow (2004) observe anvil cirrus lifetimes of 19–30±16 h, which suggests additional meteorological conditions and processes, in addition to the initial convection that maintains the anvil. Feng et al. (2012) show that lifetimes longer than 6 h are characterised by higher mid-upper tropospheric relative humidity and wind shear. It has also been widely shown that stronger convective updraught associated with colder cloud top temperatures govern larger more long-lived anvil cirrus clouds (e.g. Machado and Rossow, 1993; Machado et al., 1998; Chou and Neelin, 1999; Horváth and Soden, 2008; Schröder et al., 2009; Feng et al., 2012; Protopapadaki et al., 2017), higher optical thickness (Machado and Rossow, 1993) and higher IWP (for IWP$\gtrsim 20\,\mathrm{g\,m^{-2}}$; Horváth and Soden, 2008). Stronger convection can also increase the anvil spreading time i.e. the time lag between peak convective intensity and peak anvil coverage (Horváth and Soden, 2008).

To study the temporal evolution of convective systems and anvil cirrus clouds, most of the previous studies listed above use observations from geostationary imaging radiometers like the Japanese GMS (Geostationary Meteorological Satellites) and MTSAT (Multifunctional Transport Satellites), US GOES (Geostationary Operational Environmental Satellites) and European MFG/MSG (Meteosat First/Second generation) that possess a large spatial coverage and high temporal resolution, required to study the temporal evolution of individual cloud systems. An object or pattern tracking technique is usually combined with brightness temperature thresholds to identify convective systems and subdivide them into classes like convective core and anvil cirrus respectively. Doing so, they are somewhat limited to the thicker anvil cirrus though, since thin cirrus are not well defined by such thresholds and already difficult to detect due to the limited sensitivity to thin cirrus by geostationary imagers. Using data from infrared sounders like AIRS (Atmospheric Infrared Sounder), the sensitivity to thin cirrus can be increased (as in Protopapadaki et al., 2017, with a reliable detection down to visible optical thickness 0.2). The polar orbit of AIRS is, however, insufficient for studying the temporal evolution and life cycle of individual anvil cirrus clouds.

Luo and Rossow (2004) and Horváth and Soden (2008) use data from polar orbiting and geostationary imagers together with split-window techniques to determine the cloud optical and physical properties in order to analyse the temporal evolution of the anvil cirrus optical thickness and IWP. Still with a limited accuracy to thin cirrus clouds though, with observed optical thickness and IWP down to approx. 1.0 and $20\,\mathrm{g\,m^{-2}}$ respectively.

While passive sensors view an area large enough to study the horizontal structure of anvil cirrus clouds, active radar and lidar instruments (TRMM-PR (Tropical Rainfall Measuring Mission - Precipitation Radar), CPR (Cloud Profiling Radar), CALIOP (Cloud-Aerosol Lidar with Orthogonal Polarization)) can be used to study their microphysical properties and vertical structure (e.g. Mace et al., 2006; Futyan and Del Genio, 2007; Yuan et al., 2011; Bouniol et al., 2016). Decreasing radar reflectivities and narrower distributions have been observed with increasing distance to the convective core, representing different ages of the anvil (Yuan et al., 2011; Bouniol et al., 2016). This is in line with the idea that close to the convective core, many ice crystals are present with a wide size distribution,

while with increasing distance from the core, more and more of the larger ice crystals sediment, leading to lower radar reflectivities. The small spatial scale, also together with the poor temporal resolution of space-borne active sensors, is, however, insufficient for life cycle analysis of individual anvil cirrus clouds, even if geostationary imaging data can be used to relate the observed properties to a given anvil cirrus age and/or life cycle stage by tracking the observed cloud backwards in time (Mace et al., 2006; Futyan and Del Genio, 2007; Bouniol et al., 2016).

Although some of the studies have included mid-latitude anvil cirrus clouds (e.g. Machado et al., 1998; Feng et al., 2012), the large majority of the previous work has been limited to tropical convective systems and anvil cirrus.

Scientific objectives of this thesis

The main limiting factors for studying the temporal evolution of anvil cirrus clouds throughout their life cycle have been the low sensitivity to thin cirrus by passive sensors (especially in geostationary orbits), the small spatial scale of profiling lidar and radar as well as the low temporal resolution of polar orbiting satellite instruments. The goal with this thesis is to combine the large spatial scale and high temporal resolution of geostationary imagers (required to study the anvil cirrus life cycle) and the high sensitivity to thin cirrus clouds by space-borne lidars (required to discern thin cirrus and their properties) with a new cirrus retrial algorithm and while doing so, allow for a comprehensive and quantitative analysis of the anvil cirrus life cycle, focusing on the thin part of the anvil cirrus (visible optical thickness < 2).

While much of the previous work on the life cycle and temporal evolution of anvil cirrus clouds has focused on the morphology and horizontal structure of anvil cirrus clouds using brightness temperature or emissivity thresholds, the strength and novelty of this study is the combination of the large spatial coverage and high temporal resolution (from the geostationary imager) together with the high sensitivity to thin cirrus clouds by the new cirrus retrieval algorithm, that allows for detection of thin anvil cirrus clouds and the retrieval of the corresponding cloud top height (CTH), ice optical thickness (IOT), IWP and, by parameterisation, effective radius (REF) every 5 min. This allows for a quantitative analysis of the anvil cirrus optical, mircophysical and macrophysical properties throughout the entire life cycle and makes it possible to address scientific questions related to the physical processes of anvil cirrus clouds. Thus, the following scientific question (SQ) is addressed

SQ-1 *How do the anvil cirrus properties, including spatial extension, cloud top height, ice optical thickness, ice water path and effective radius evolve with time throughout the anvil cirrus life cycle?*

The global mean surface temperature increase is likely to exceed $1.5\,\mathrm{K}$ by the end of the 21th century relative to 1850 to 1900 (with higher temperature increments over land) unless greenhouse gas emissions peak and rapidly start to decrease before 2020. If the greenhouse

gas emissions continue to increase until around 2040, it is more likely than unlikely that the global temperature increase exceeds $2\,K$ (Collins et al., 2013; van Vuuren et al., 2011). With increasing surface temperatures, not only more, but also stronger convection can be expected. While the relationship between the strength of the convective updraught and the anvil cirrus size and lifetime has been presented in the literature, this thesis aims towards an increased understanding of the relationship between the convective strength and the anvil cirrus optical and physical properties as well as their temporal evolution. Hence, the following scientific question is addressed

SQ-2 *How does the convective strength affect the anvil cirrus properties and their temporal evolution?*

To further investigate the observed variability of the anvil cirrus life cycle, the following scientific question is finally addressed

SQ-3 *How do the meteorological conditions influence the life cycle of anvil cirrus clouds?*

To approach and answer the scientific questions, this thesis is divided into five subsequent chapters. Chapter 2 describes the theoretical background of this study including the theory of electromagnetic radiation, atmospheric radiative transfer and satellite remote sensing of cirrus clouds. The satellite instruments, methods and data used in this study are introduced and described in Chap. 3. Chapter 4 presents the new algorithm for the geostationary remote sensing of thin cirrus clouds: CiPS - Cirrus Properties from SEVIRI. Sects. 4.1–4.7 describe the technical development of CiPS, while a detailed validation and characterisation of CiPS as well as a comparison with independent data is presented in Sects. 4.9, 4.10 and 4.11 respectively. Chapter 5 present the life cycle analysis of anvil cirrus clouds. First, the cirrus tracking algorithm is described in Sect. 5.1. Second, the temporal evolution of the anvil cirrus properties throughout the life cycle is analysed in Sect. 5.3 (case study) and Sect. 5.4.1 (statistical approach) respectively, using CiPS as the main tool (**SQ-1**). Third, the relationship between the convective strength and the cirrus properties and their temporal evolution is investigated in Sect. 5.4.2 (**SQ-2**). Fourth, the relationship between modelled meteorological conditions (convective available potential energy, humidity, temperature, horizontal wind speeds) and the anvil cirrus lifetime and maximum spatial extension is investigated in Sect. 5.4.3 (**SQ-3**). Finally, the conclusions drawn from this study together with an outlook is presented in Chap. 6. A list of abbreviations is available in Appendix A.

Chapter 2

Theoretical background and satellite remote sensing of cirrus clouds

Parts of the text in Sect. 2.2 in this chapter have been published in Strandgren et al. (2017a) and Strandgren et al. (2017b).

2.1   Fundamentals of atmospheric radiative transfer

Electromagnetic radiation propagating through the atmosphere and interacting with its matter is described by the theory of *atmospheric radiative transfer*. Electromagnetic radiation refers to oscillating electric and magnetic fields that carry electromagnetic energy as they propagate through a medium. Understanding atmospheric radiative transfer is essential in order to understand and interpret satellite remote sensing in any form.

2.1.1   Radiative quantities

Electromagnetic radiation consists of a stream of photons and is characterised by its *frequency* ν, i.e. by the rate at which it oscillates and its *wavelength* λ, i.e. the distance between two repetitive patterns

$$\lambda = \frac{c}{\nu} \qquad [\mathrm{m}] \, , \tag{2.1a}$$

where c is the speed of light in vacuum. The energy of a photon is described by the *Planck-Einstein*[1] *relation*

$$E = h\,\nu = \frac{h\,c}{\lambda} \qquad [\mathrm{J}] \, , \tag{2.2}$$

where $h = 6.626 \cdot 10^{-34}\,\mathrm{J\,s}$ is the *Planck constant*. Since c and h are constants, the energy of the photons and the electromagnetic radiation itself is directly related to the wavelength/frequency.

---

[1]after the German physicists Max Planck (1858–1947) and Albert Einstein (1879–1955)

The *radiant flux* (or radiant power) Φ describes the radiant energy per unit time

$$\Phi = \frac{dE}{dt} \qquad [\text{W}] \,, \tag{2.3}$$

and the *irradiance I* describes the radiant flux received by a surface element dA per unit area

$$I = \frac{d\Phi}{dA} \qquad [\text{W}\,\text{m}^{-2}] \,. \tag{2.4}$$

The *radiance L* describes the radiant flux received by or leaving a surface element dA per unit *projected* area in a specified direction $\hat{\Omega}$, within a solid angle $d\Omega$, oriented at an angle ϑ to the normal direction $\hat{n}$ of the surface element

$$L = \frac{d^2\,\Phi}{\cos(\vartheta)\,dA\,d\Omega} \qquad [\text{W}\,\text{m}^{-2}\,\text{sr}^{-1}] \,. \tag{2.5}$$

Figure 2.1 shows a graphical interpretation of the radiance as measured by a satellite sensor. The field of view of the sensor covers an area element dA of the observed surface. The satellite sensor does not measure all radiant flux leaving the surface element, but the radiant flux propagating in the direction of the satellite sensor ($\hat{\Omega}$) within the solid angle $d\Omega$. Due to the slant view of the sensor, the projected area is calculated as $\cos(\vartheta)\,dA$, where ϑ is the angle between $\hat{\Omega}$ and the normal $\hat{n}$ to the surface element dA. The solid angle is expressed in units of steradians (sr) and remains constant with increasing/decreasing distance between the observed object and the sensor.
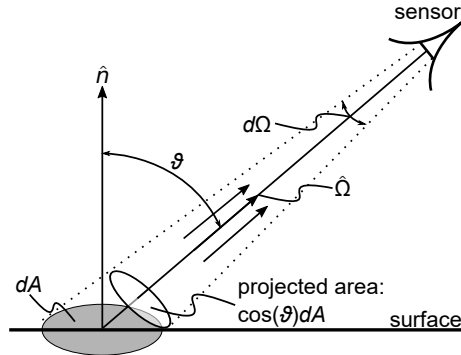
Figure 2.1: Graphical interpretation of the radiance of a surface element dA measured by a satellite sensor with solid angle $d\Omega$, oriented at an angle ϑ to the normal direction $\hat{n}$ of the surface element.

Finally, the *spectral radiance* describes the radiance at a given wavelength/frequency and is defined as

$$L_\lambda = \frac{d^3\,\Phi}{\cos(\vartheta)\,dA\,d\Omega\,d\lambda} \qquad [\text{W}\,\text{m}^{-2}\,\text{sr}^{-1}\,\text{nm}^{-1}] \,. \tag{2.6}$$

2.1.2 Black body radiation

All bodies emit electromagnetic radiation according to their temperature T that can be characterised by Eqs. (2.3)–(2.6). A *black body* is an idealised body that absorbs all incident electromagnetic radiation. According to *Kirchhoff's[2] law*, any body in thermal equilibrium must re-emit all absorbed radiation at a given wavelength. The electromagnetic radiation emitted (in all directions and at all wavelengths) by a black body in thermal equilibrium is described by Planck's law

$$B_\lambda(T) = \frac{2\,h\,c^2}{\lambda^5} \frac{1}{\exp\left(\frac{h\,c}{\lambda\,k_B\,T}\right) - 1} \qquad [\mathrm{W\,m^{-2}\,sr^{-1}\,nm^{-1}}]\,, \tag{2.7}$$

where $k_B = 1.381 \cdot 10^{-23}\,\mathrm{J\,K^{-1}}$ is the *Boltzmann[3] constant*. The spectral black body radiance B_λ is accordingly a function of the black body's temperature alone and independent of any other property of the black body. Black bodies only exist in theory and a grey body[4] at temperature T emits only a fraction of the electromagnetic radiation that a black body at the same temperature would emit. This fraction is known as the *spectral directional emissivity* ϵ_λ

$$\epsilon_\lambda = \frac{L_\lambda}{B_\lambda(T)}\,. \tag{2.8}$$

2.1.3 Interactions with atmospheric matter

As electromagnetic radiation propagates through the atmosphere, gas molecules, aerosols, cloud droplets and ice crystals interact with the radiation through *absorption*, *emission* and *scattering*.

Absorption describes the process when an atom or molecule extracts energy from the incident beam of radiation according to Eq. (2.2) and transitions to a higher energy level. Processes requiring energy and hence leading to photon absorption include: (1) atomic/molecular electronic transitions to a higher-energy electron shell, (2) changes in molecular vibrational motion and (3) changes in molecular rotational motion. The energy required to reach a higher energy level is discrete, leading to the characteristic spectral lines and bands of given atoms and molecules.

Emission describes the process when an atom or molecule transitions to a lower energy level and emits a photon with corresponding energy (and wavelength) according to Eq. (2.2). The processes causing emission are similar to those of absorption.

---

[2]after the German physicist Gustav Kirchhoff (1824–1887)
[3]after the Austrian physicist Ludwig Boltzmann (1844–1906)
[4]a body that does not absorb all incident electromagnetic radiation is usually referred to as a grey body
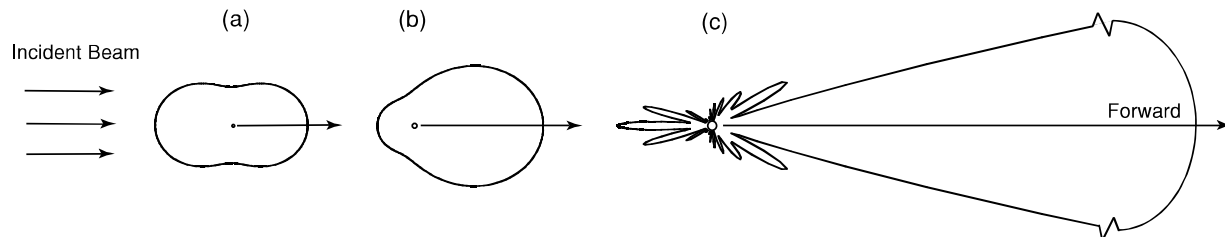
Figure 2.2: The angular distribution of visible radiation at $0.5\,\mu\text{m}$ by spherical particles of three sizes: **(a)** $10^{-4}\,\mu\text{m}$, **(b)** $0.1\,\mu\text{m}$ and **(c)** $1\,\mu\text{m}$. The forward scattering pattern for the $1\,\mu\text{m}$ particle is extremely large and is scaled for presentation purposes. Figure adapted from Liou (2002).

Scattering describes the redirection of electromagnetic radiation from the direction of propagation. How the incident radiation is scattered depends on the wavelength and the properties of the scattering molecule or particle (size, shape, refractive index). The *size parameter* x describes the relationship between the wavelength of the incoming electromagnetic radiation λ and the radius of a scattering particle r

$$x = \frac{2\pi r}{\lambda}\,. \tag{2.9}$$

Figure 2.2 shows the scattering pattern of electromagnetic radiation with $\lambda = 0.5\,\mu\text{m}$ scattered by spherical particles with three different sizes: (a) $10^{-4}\,\mu\text{m}$, (b) $0.1\,\mu\text{m}$ and (c) $1\,\mu\text{m}$. It is clear that larger particles concentrate the scattered radiation in the forward direction, with increasingly complex scattering patterns. The angular re-distribution of scattered radiation from the incident direction Ω' to any direction Ω is described by the *scattering phase function* $P(\Omega', \Omega)$.

   The scattering by particles much smaller than the wavelength ($x << 1$), as in Fig. 2.2a, is usually referred to as *Rayleigh*[5] *scattering*. Under Rayleigh scattering conditions, the scattering efficiency is proportional to λ^{-4}, meaning that shorter wavelengths are scattered more effectively. This explains, for example, the characteristic blue colour of the sky, since the shorter blue wavelengths are scattered most effectively by the air molecules that are significantly smaller ($\approx 10^{-4}\,\mu\text{m}$) than the visible spectrum of the solar radiation (0.39–$0.7\,\mu\text{m}$). Scattering by spherical particles with sizes comparable to, or larger than, the wavelength ($x \gtrsim 1$) can be derived from Maxwell's[6] equations. This is usually referred to as the *Mie*[7] *solution*. In contrast to Rayleigh scattering, scattering efficiency is not (as) wavelength dependent for Mie scattering. This explains, for example, the characteristic white colour of clouds, since the scattering cloud droplets, that have sizes ($\approx 10\,\mu\text{m}$) approx. ten times the wavelength of visible solar radiation, scatter all visible wavelengths as effectively. In contrast to cloud liquid water droplets, that can be approximated as

---

[5]after the British physicist Lord Rayleigh (John William Strutt, 1842-1919)
[6]after the Scottish mathematician and physicist James Clerk Maxwell (1831–1879)
[7]after the German physicist Gustav Mie (1868–1957)

spherical, cloud ice crystals have a variety of more complex shapes. Consequently, an exact solution for the scattering by ice crystals covering all shapes and sizes present in the atmosphere does not exist. Instead the scattering properties can be derived for a set of idealised crystal shapes, e.g. hexagonal plates, (hollow) columns, (hollow) bullet rosettes and droxtals, for a range of sizes using various methods (e.g. conventional/improved geometric-optics, T-matrix, finite difference time domain). The total scattering effect by an ensemble of ice crystals can then be estimated by averaging the scattering properties over multiple size distributions with prescribed crystal shapes (see e.g. Yang et al. (2015) and references therein for details).

2.1.4   The equation of radiative transfer

A beam of electromagnetic radiation propagating through an atmospheric volume V with area A, infinitesimal thickness ds containing N particles will lose energy due to absorption and scattering. The combined loss in energy/radiance due to absorption and scattering is known as *extinction* and given by

$$
\begin{aligned}
\frac{dL_{\text{ext},\lambda}}{ds} &= -\frac{N\,\sigma_{\text{ext},\lambda}}{A\,ds}L_\lambda \\
&= -\frac{N}{V}\sigma_{\text{ext},\lambda}\,L_\lambda \\
&= -n\,\sigma_{\text{ext},\lambda}\,L_\lambda \\
&= -\beta_{\text{ext},\lambda}\,L_\lambda \ ,
\end{aligned}
\tag{2.10}
$$

where $\sigma_{\text{ext},\lambda}$ is the *extinction cross section*[8] (in m^2) at wavelength λ, V is the *volume* (in m^3), n is the *particle number density* (in m^{-3}) and $\beta_{\text{ext},\lambda}$ is the *extinction coefficient* (in m^{-1}). As mentioned above, the extinction constitutes the attenuation due to absorption *and* scattering and $\beta_{\text{ext},\lambda}$ is defined as the sum of the *absorption coefficient* $\beta_{\text{abs},\lambda}$ and the *scattering coefficient* $\beta_{\text{sca},\lambda}$

$$
\beta_{\text{ext},\lambda} = \beta_{\text{abs},\lambda} + \beta_{\text{sca},\lambda} \ .
\tag{2.11}
$$

The absorption and scattering coefficients describe the radiant attenuation per unit length in the direction of propagation due to absorption and scattering inside the volume.

Solving Eq. (2.10) for a path through the atmosphere ranging from e.g. the Earth's surface ($s = 0$) to the top of atmosphere ($s = \text{TOA}$) yields the *Beer-Lambert-Bouguer*[9] *law*

$$
L_\lambda(\text{TOA}) = L_\lambda(0)\,\exp\!\left(-\int_0^{\text{TOA}}\beta_{\text{ext},\lambda}(s)\,ds\right) = L_\lambda(0)\,\exp(-\tau(\text{TOA})) \ ,
\tag{2.12}
$$

---

[8]The extinction cross section is a measure for the probability that the electromagnetic radiation will interact with a particle, either by scattering or absorption. It is defined as the ratio between the scattered or absorbed radiant flux (Eq. 2.3) and the irradiance (Eq. 2.4)

[9]after the German physicist August Beer (1825–1863) and the French mathematicians Johann Heinrich Lambert (1728–1777) and Pierre Bouguer (1698–1758)

where

$$\tau = \int_0^{\text{TOA}} \beta_{\text{ext},\lambda}(s)\, ds \tag{2.13}$$

is known as the *optical thickness* of the atmospheric path length. The Beer-Lambert-Bouguer law quantifies the radiative attenuation due to absorption and scattering along the path length and thus the spectral radiance of up-welling electromagnetic radiation at TOA.

The beam will also gain radiant energy along the direction of propagation due to emission by the medium. Any body with a temperature T will emit radiation in all directions according to Planck's law (Eq. 2.7). Hence, the gain in spectral radiance due to emission along the path length is given by

$$dL_{\text{emi},\lambda} = \beta_{\text{emi},\lambda}\, ds\, B_\lambda(T)\ , \tag{2.14}$$

where $\beta_{\text{emi},\lambda}$ is the emission coefficient of the medium. Assuming local thermodynamic equilibrium (LTE) and invoking Kirchhoff's law, Eq. (2.14) can be written as

$$\frac{dL_{\text{emi},\lambda}}{ds} = \beta_{\text{abs},\lambda}\, B_\lambda(T)\ . \tag{2.15}$$

Finally, the beam can gain energy if radiation from the outside is scattered into the direction of propagation. The gain in spectral radiance due to scattering from an arbitrary direction Ω' into the direction of propagation Ω is given by

$$dL_{\text{sca},\lambda}(\Omega',\Omega) = \beta_{\text{sca},\lambda}\, ds\, P(\Omega',\Omega)\, L_\lambda(\Omega')\ . \tag{2.16}$$

Integrating over all incident angles Ω' yields

$$\frac{dL_{\text{sca},\lambda}(\Omega)}{ds} = \frac{\beta_{\text{sca},\lambda}}{4\pi} \int_{4\pi} P(\Omega',\Omega)\, L_\lambda(\Omega')\, d\Omega'\ . \tag{2.17}$$

Combining Eqs. (2.10), (2.15) and (2.17), the *equation of radiative transfer* can be formulated

$$\begin{aligned}
\frac{dL_\lambda}{ds} &= \frac{dL_{\text{ext},\lambda}}{ds} + \frac{dL_{\text{emi},\lambda}}{ds} + \frac{dL_{\text{sca},\lambda}(\Omega)}{ds} \\
&= -\beta_{\text{ext},\lambda}\, L_\lambda + \beta_{\text{abs},\lambda}\, B_\lambda(T) + \frac{\beta_{\text{sca},\lambda}}{4\pi} \int_{4\pi} P(\Omega',\Omega)\, L_\lambda(\Omega')\, d\Omega'\ .
\end{aligned} \tag{2.18}$$

The equation of radiative transfer describes the change in spectral radiance for a beam of electromagnetic radiation propagating through an atmospheric volume with thickness ds due to interaction (scattering, absorption, emission) with matter inside the volume.

2.2 Satellite remote sensing of cirrus clouds

An analytical solution to Eq. (2.18) does not exist, and even if it would, it relies on several assumptions (e.g. LTE, *spectral* radiation (at one wavelength/frequency), *elastic* scattering (no change in wavelength/frequency), homogeneous layer) and the inversion from radiances measured from space to e.g. cirrus cloud properties would be an ill-posed problem with too many unknowns compared to the number of satellite measurements. Nevertheless, cirrus clouds and clouds in general can be identified and their properties estimated from satellite platforms using two approaches: *passive* and *active remote sensing*. The following subsections focus on the satellite remote sensing of cirrus clouds, but describe general methods used for liquid water clouds (and thick ice clouds) as well.

2.2.1 Cirrus cloud properties

To study cirrus clouds from space it is central to distinguish the cirrus clouds from the surrounding cirrus-free areas i.e. to derive a cirrus cloud flag (CCF), that classifies each observed scene as cirrus-free or cirrus-covered. The cloud top height (CTH) describes the distance between the Earth's surface and the top of the cirrus cloud. The CTH is an important variable as it is closely related to the cloud top temperature and hence determines the outgoing thermal radiation. The ice optical thickness (IOT) stems from Eq. (2.13) and is defined as the *vertically* integrated attenuation of electromagnetic radiation due to scattering and absorption by cloud ice crystals within an atmospheric column ranging from the surface ($z = 0$) to the top of atmosphere ($z = \mathrm{TOA}$). Similarly, the ice water path (IWP) is defined as the vertically integrated mass of ice within the same atmospheric column

$$\mathrm{IWP} = \int_0^{\mathrm{TOA}} \mathrm{IWC}(z)\,dz \qquad [\mathrm{g\,m^{-2}}]\,, \tag{2.19}$$

where the ice water content (IWC) measures the mass of ice per unit volume of air

$$\mathrm{IWC} = \int \rho_{\mathrm{ice}} V(r) n(r) dr \qquad [\mathrm{g\,m^{-3}}]\,, \tag{2.20}$$

where $\rho_{\mathrm{ice}} = 917\,000\,\mathrm{g\,m^{-3}}$ is the mass density of ice and $V(r)$ and $n(r)$ are the mean volume and number of cloud ice crystals in the size interval r to $r + dr$ *per unit volume of air*. Hence,

$$V_{\mathrm{ice}} = \int V(r) n(r) dr \qquad [\mathrm{m^3\,m^{-3}}]\,, \tag{2.21}$$

is the *total* volume of ice per unit volume of air. IWP and IWC are, in contrast to IOT, physical quantities, that can be directly used for comparisons with climate and weather models. The effective radius (REF; Hansen and Travis, 1974) describes the area weighted mean radius for an ensemble of cloud particles. For spherical cloud particles it is defined as the ratio between the third and second moment of the cloud particle size distribution

$$\mathrm{REF} = \frac{\int r \pi r^2 n(r) dr}{\int \pi r^2 n(r) dr} \qquad [\mathrm{m}]\,. \tag{2.22}$$

Several definitions of the effective radius for an ensemble of non-spherical ice crystals have been presented in the literature (see e.g. McFarquhar and Heymsfield (1998) for an inter-comparison). In this study the following definition is used

$$\mathrm{REF} = \frac{3V_{\mathrm{ice}}}{4A_{\mathrm{ice}}} \qquad [\mathrm{m}] , \tag{2.23}$$

where A_{ice} is the total projected area of ice per unit volume of air. The fraction 3/4 is introduced in order to solve Eq. (2.22) for spherical particles. Following Eqs. (2.20) and (2.21) the total volume of ice per unit volume of air can be expressed in terms of IWC

$$V_{\mathrm{ice}} = \mathrm{IWC}/\rho_{\mathrm{ice}} \qquad [\mathrm{m}^3\,\mathrm{m}^{-3}] . \tag{2.24}$$

Similarly, the total projected area of ice per unit volume of air can be expressed in terms of the (volume) extinction coefficient β_{ext}

$$A_{\mathrm{ice}} = \int A(r)n(r)dr = \int \frac{\sigma_{\mathrm{ext}}(r)}{Q_{\mathrm{ext}}}n(r)dr = \frac{\beta_{\mathrm{ext}}}{Q_{\mathrm{ext}}} \qquad [\mathrm{m}^2\,\mathrm{m}^{-3}] , \tag{2.25}$$

where $A(r)$ is the mean projected area of cloud ice crystals in the size interval r to $r + dr$ per unit volume of air and Q_{ext} is the (constant) *extinction efficiency*. Using Eqs. (2.24) and (2.25), Eq. (2.23) can be rewritten as

$$\mathrm{REF} = \frac{3\,Q_{\mathrm{ext}}\,\mathrm{IWC}}{4\rho_{\mathrm{ice}}\beta_{\mathrm{ext}}} \approx \frac{3\,\mathrm{IWC}}{2\rho_{\mathrm{ice}}\beta_{\mathrm{ext}}} \qquad [\mathrm{m}] , \tag{2.26}$$

for larger ice crystals (REF $\gtrsim 10\,\mu\mathrm{m}$), for which $Q_{\mathrm{ext}} \approx 2$ (e.g. Schumann et al., 2011). Eq. (2.26) is used to estimate the effective radius of cloud ice crystals by e.g. Jensen et al. (2009) and Hong and Liu (2015).

2.2.2   Passive satellite remote sensing

Passive satellite sensors like the imaging radiometers SEVIRI (Spinning Enhanced Visible Infrared Imager; Schmetz et al., 2002), ABI (Advanced Baseline Imager; Schmit et al., 2015), MODIS (Moderate Resolution Imaging Spectroradiometer; King et al., 1992) and AVHRR (Advanced Very High Resolution Radiometer; Hastings and Emery, 1992) measure radiances of thermal radiation emitted by the Earth and reflected solar radiation leaving the Earth–atmosphere system at TOA. A passive imaging radiometer cannot resolve vertical cloud features and has a limited sensitivity to thin and sub-visual (visible optical thickness < 0.03) cirrus clouds, but typically it views an area large enough (by scanning or otherwise) to observe complete cloud systems.

   Imaging radiometers measure the TOA radiances within given wavelength ranges, referred to as channels or spectral bands. Hence, the measured radiances in the thermal range cannot be described directly with Eq. (2.7), but are instead given by

$$L = \frac{\int \varphi_\lambda L_\lambda d\lambda}{\int \varphi_\lambda d\lambda} = \frac{\int \varphi_\lambda B_\lambda(T_b)d\lambda}{\int \varphi_\lambda d\lambda} , \tag{2.27}$$

where φ_λ is the *spectral response function*[10] of a given channel/band and the (equivalent black body) brightness temperature (T_b) represent the temperature a black body would have in order to emit according to the spectral radiance L_λ of the observed grey body. For channels in the solar spectrum, the reflectance R can be calculated, describing the incident solar radiation reflected by the observed object

$$R = \frac{\pi \int \varphi_\lambda L_\lambda d\lambda}{\cos(\vartheta_\odot) \int \varphi_\lambda I_\lambda d\lambda} = \frac{\pi L}{\cos(\vartheta_\odot) I} \, , \tag{2.28}$$

where I_λ is the spectral solar irradiance, I is the solar irradiance received by a given channel and $\vartheta_\odot$ is the solar zenith angle.

The atmosphere itself is largely transparent to incoming shortwave radiation and the amount of reflected solar radiation reaching TOA in clear sky conditions (no clouds or aerosols) is directly related to the Earth's surface albedo. Ice crystals and liquid water droplets are generally effective scatterers of solar radiation, leading to increasing reflected solar radiation and radiances at TOA in the presence of clouds, distinguishing them from surrounding cloud free scenes.

The solar radiation that is not reflected back to space by the Earth's surface and atmosphere is absorbed by the Earth-atmosphere system. The absorbed radiation is later re-emitted according to the Earth's and atmosphere's temperature (Eq. 2.7) and emissivity (Eq. 2.8). Most of the emitted radiation is at longer wavelengths, referred to as (longwave) thermal radiation. Cloud ice crystals and water droplets may absorb thermal radiation and emit it in all directions. The radiant energy emitted by a cloud out to space depends mainly on its top temperature. Hence, cirrus clouds located higher up in the atmosphere, at colder temperatures, emit less thermal radiation out to space, leading to lower radiances in the thermal spectra at TOA. The loss in thermal radiation at TOA is further enhanced with increasing absorption by the cloud. Less thermal radiation reaches TOA if the absorbing cloud is optically thicker, since a larger fraction of the thermal radiation is emitted back towards the Earth's surface, resulting in a stronger radiative contrast to (cirrus) cloud free scenes. On the contrary, an optically thin (e.g. sub-visual) cirrus, transmits most of the up-welling thermal radiation and absorbs (and emits) a comparably small fraction, leaving a weak mark on the TOA radiances and thus a small radiative contrast to (cirrus) cloud free scenes. This makes it difficult to discern optically thin cirrus clouds from the surrounding cirrus-free regions using imaging radiometers. Atmospheric gases also absorb and emit parts of the thermal radiation, with water vapour (H_2O), carbon dioxide (CO_2), methane (CH_4) and ozone (O_3) being some of the most important absorbers of thermal radiation in the atmosphere. The absorption by the single molecules strongly depends on the wavelength of the thermal radiation and there are spectral regions where the atmosphere is mostly transparent to thermal radiation (atmospheric windows). Similarly, there are spectral regions where thermal radiation is strongly absorbed by atmospheric gases, for example by water vapour around 5–7 µm, reducing or even obscuring the radiative signals from the Earth's surface and clouds in the lower troposphere. The thermal radiation at

---

[10]the relative efficiency of a sensor to detect photons as a function of wavelength.

TOA, reaching a passive imaging radiometer, thus consists of the radiation directly transmitted from the Earth's surface and the radiation absorbed and emitted out to space by clouds, aerosols and atmospheric gases. Hence, different cirrus clouds leave their unique mark on the TOA radiances observed by an imaging radiometer, depending primarily on the cirrus cloud temperature (height) and optical properties, but also on the presence and properties of underlying liquid water clouds, aerosols, atmospheric gas concentrations and the Earth's surface properties (temperature, emissivity), which regulate the thermal radiation emitted by the Earth.

To study cirrus clouds, their life cycle and climate impact, large-scale satellite observations with imaging radiometers are crucial. Cirrus clouds can be detected from space-borne imaging radiometers (e.g. Saunders and Kriebel, 1988; Derrien et al., 1993; Ackerman et al., 1998; Kriebel et al., 2003; Derrien and LeGléau, 2005; Krebs et al., 2007) by applying spectral tests on brightness temperatures and temperature differences (e.g. Inoue, 1985; Ackerman et al., 1990). Krebs et al. (2007) extend the multispectral threshold test approach by introducing morphological tests that take into account the shape of high-level clouds in thermal channels characterised by strong water vapour absorption. Near-infrared water vapour absorption channels can also be used to detect cirrus clouds (Gao et al., 2002). Due to the limited sensitivity to thin cirrus clouds, algorithms utilising spectral and morphological threshold tests tend to miss a large fraction of those thin cirrus (e.g. Ackerman et al., 2008; Stubenrauch et al., 2010) and thus introduce a bias into the climate impact of cirrus clouds. Another well-known problem related to cirrus cloud detection from passive imagers is the difficulty to distinguish between cirrus clouds and cold surfaces in the polar regions (e.g. Holz et al., 2008).

The CTH is an important variable as it regulates the outgoing longwave radiation. It can be retrieved from passive satellite imagers during both day and night using e.g. radiance ratioing (also referred to as CO_2 absorption, CO_2 slicing and split window technique) (Smith et al., 1970; Smith and Platt, 1978; Menzel et al., 1983; Eyre and Menzel, 1989; Zhang and Menzel, 2002; Menzel et al., 2008), radiance fitting (e.g. Szejwach, 1982; Nieman et al., 1993; Schmetz et al., 1993) and optimal estimation (e.g. Heidinger and Pavolonis, 2009; Sayer et al., 2011; Watts et al., 2011). An intercomparison of different techniques currently used for SEVIRI is presented in Hamann et al. (2014).

Nakajima and King (1990) introduced a commonly applied approach for the retrieval of optical thickness and effective radius of clouds from reflected solar radiation in two spectral channels (e.g. Platnick et al., 2003; Bugliaro et al., 2011; Stengel et al., 2014) for both ice clouds and liquid water clouds. From the optical thickness and effective radius the liquid water path (LWP) and IWP can be estimated for liquid and icy pixels respectively. The solar dependence does, however, limit this approach to daytime and the retrieval becomes ambiguous for optically thin clouds (Nakajima and King, 1990). The same properties can be retrieved for optically thinner cirrus clouds during night as well using only thermal observations (e.g. Prabhakara et al., 1988; Ackerman et al., 1990; Yue and Liou, 2009; Minnis et al., 2011; Heidinger et al., 2015; Wang et al., 2016), but with a limited accuracy due to the low sensitivity to large ice crystal sizes and large optical thicknesses.

2.2.3 Active satellite remote sensing

Active satellite sensors like CALIOP (Cloud-Aerosol Lidar with Orthogonal Polarization; Winker et al., 2003, 2009) and CPR (Cloud Profiling Radar; Stephens et al., 2002) emit visible (CALIOP) and microwave (CPR) radiation and measure the radiation backscattered by clouds and aerosols. Lidar and radar are short for Light/Radio Detection and Ranging. The main principle is to emit radiation and identify objects like airplanes, rain drops, cloud droplets, ice crystals or aerosol particles due to their stronger backscatter compared to the background molecular backscatter (detection). When an object has been identified, the distance between the transmitter and the object can be derived (ranging) from the time it took for the transmitted, backscattered radiation to return to the receiver and the speed of light. By measuring the power of the backscattered radiation for a small path length ds (given by the vertical resolution), the level of attenuation of the layer can be estimated. This is expressed as the extinction (lidar) and reflectivity (radar). Repeating this down to the Earth's surface results in vertical profiles of extinction coefficients (lidar). By integrating the extinction coefficients for a given cloud or aerosol layer detected in the altitude range $s_1 - s_2$ (see Eq. (2.13)) the optical thickness of that cloud or aerosol layer can be estimated (e.g. Young and Vaughan, 2009). With information about the position of the spacecraft, the height of the cloud or aerosol layer with respect to the Earth's surface (e.g. the CTH) can be determined.

The active satellite remote sensing using radar/lidar allows for vertical profiling of clouds and aerosols along the satellite track with a high sensitivity to thin cirrus clouds (using the lidar). However, those sensors have a small footprint and observe only at nadir, which leads to a poor spatial coverage and low temporal resolution.

2.2.4 Synergistic satellite retrievals

Observations from different satellite orbits generate additional advantages and limitations. Sensors observing the Earth from polar orbits (e.g. MODIS, AVHRR, CALIOP and CPR) have a near-global coverage and high spatial resolution, but a low to poor temporal resolution, depending on the swath width/spatial coverage. In contrast, a geostationary imager like SEVIRI lacks a global coverage, but has a constant large field of view, which allows for a high temporal resolution of 15 min (Schmetz et al., 2002) required to study the temporal evolution, life cycle and physical processes of clouds. The advantages of individual instruments can be combined to enhance cloud retrievals if two or more complementary satellite sensors operate aboard the same satellite platform (e.g. the synergistic retrievals for the IIR (Imaging Infrared Radiometer) thermal camera and CALIOP by Garnier et al., 2012, 2013, 2015) or fly in a satellite constellation like the A-Train (e.g. the synergistic retrievals for lidar and radar or lidar, radar and imager by Donovan and van Lammeren, 2001; Delanoë and Hogan, 2008, 2010; Deng et al., 2010; Ceccaldi et al., 2013). Combining the advantages of satellite sensors operating in different orbits is more challenging, as they observe given scenes at different times from possibly different perspectives. Nevertheless, the information from available sensor collocations can be used to learn relationships

between different sets of observations, e.g. through machine learning.

Artificial neural networks (ANNs; Sect. 3.3) are a powerful tool for combining the advantages of different satellite sensors operating in different orbits. With ANNs, the relationship between observations of one set of sensors and the retrieval outcome of another set of sensors can be approximated by learning from available sensor collocations. This has been done by learning and approximating the relationship between collocated passive and active satellite observations in order to indirectly increase the sensitivity and accuracy of the passive satellite retrievals (e.g. Kox et al., 2014; Holl et al., 2014; Minnis et al., 2016). The ultimate goal with such an approach is to retrieve active-like (cirrus) cloud properties from passive satellite observations alone.

Chapter 3

Instrumentation, methods and data

The text in Sects. 3.3, 3.4.3, 3.5 and parts of the text in Sect. 3.2 in this chapter have been published in Strandgren et al. (2017a).

In this chapter the remote sensing instruments, data and methods used to develop CiPS (Cirrus Properties from SEVIRI; Chap. 4) and analyse the life cycle of anvil cirrus clouds are introduced. This includes instruments, methods and data developed by others than the PhD candidate. The two main tools used to analyse the anvil cirrus life cycle have been developed by the PhD candidate and are described in full detail in Chaps. 4 and 5. This includes the CiPS algorithm and the cirrus cloud tracking algorithm respectively.

3.1 SEVIRI aboard the Meteosat Second Generation

SEVIRI is a passive imaging radiometer operating aboard the geostationary Meteosat Second Generation (MSG) satellites since 2004. SEVIRI is the main instrument used for the analysis presented in Chap. 5 as well as the main source of input data for CiPS.

SEVIRI measures the up-welling radiation within 12 channels in the visible to thermal infrared spectrum, in which the radiances (Eq. 2.27) are measured and the corresponding brightness temperatures (Eq. 2.27) and reflectances (Eq. 2.28) retrieved. The operational MSG satellite is positioned ca. $35\,800\,\mathrm{km}$ above the Earth's Equator at $0°\,\mathrm{E}$ giving SEVIRI an excellent view of the Earth from its remote location, with a spatial coverage from approx. $80°\,\mathrm{W}$ to $80°\,\mathrm{E}$ and $80°\,\mathrm{S}$ to $80°\,\mathrm{N}$ (from now on referred to as the *SEVIRI disc*). The broadband high resolution visible (HRV) channel has a limited coverage and includes the European and most of the African continent. The spatial sampling of SEVIRI is $3{\times}3\,\mathrm{km}^2$ at nadir ($1{\times}1\,\mathrm{km}^2$ for the HRV channel) which increases to approx. $3.5{\times}5\,\mathrm{km}^2$ on average over Europe. The SEVIRI channel characteristics are summarised in Table 3.1. Furthermore, Fig. 3.1 shows the spectral response functions of the SEVIRI narrowband channels (1–11 in ascending order from left to right) together with simulated spectra of reflected solar radiation and outgoing longwave radiation. Channels 1–3 and 12 measure reflected solar

Table 3.1: Characteristics of the SEVIRI spectral bands. Table adapted from Schmetz et al. (2002).

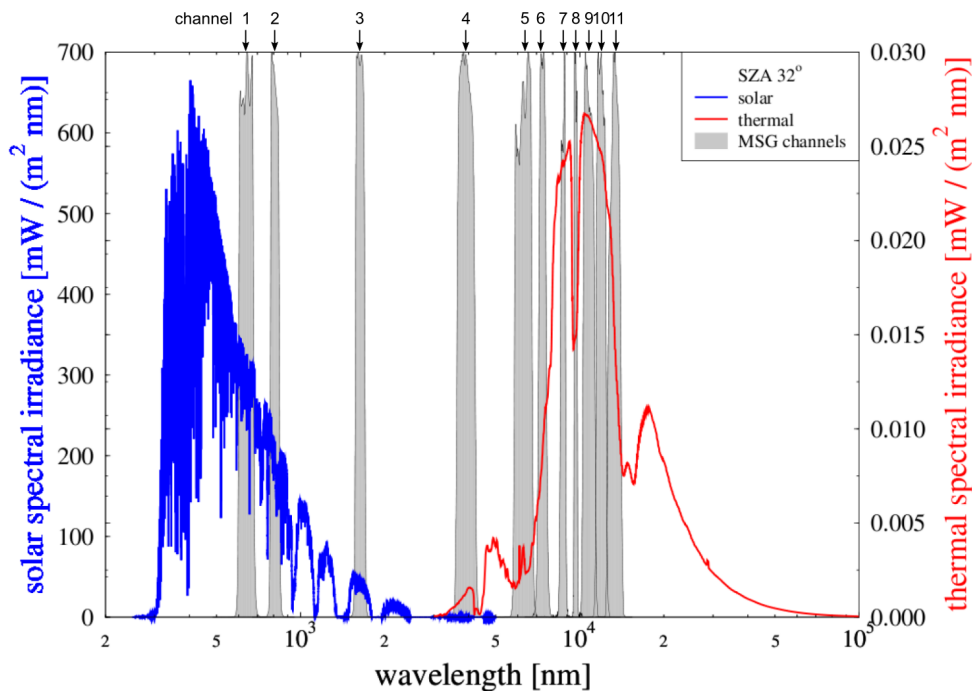|	Channel	Spectral band / µm	Central wavelength λ_c / µm	Spatial sampling at nadir / km^2
1	VIS 0.6	$0.56 - 0.71$	0.635	3×3
2	VIS 0.8	$0.74 - 0.88$	0.81	3×3
3	NIR 1.6	$1.50 - 1.78$	1.64	3×3
4	IR 3.9	$3.48 - 4.36$	3.90	3×3
5	WV 6.2	$5.35 - 7.15$	6.25	3×3
6	WV 7.3	$6.85 - 7.85$	7.35	3×3
7	IR 8.7	$8.30 - 9.10$	8.70	3×3
8	IR 9.7	$9.38 - 9.94$	9.66	3×3
9	IR 10.8	$9.80 - 11.80$	10.80	3×3
10	IR 12.0	$11.00 - 13.00$	12.00	3×3
11	IR 13.4	$12.40 - 14.40$	13.40	3×3
12	HRV	$0.4 - 1.1$	-	1×1

Figure 3.1: The spectral response functions of the SEVIRI narrowband channels 1–11 together with simulated spectra of reflected solar radiation and outgoing longwave radiation. Figure adapted from Vázquez-Navarro et al. (2013).

radiation, whereas channels 5–11 measure the terrestrial thermal radiation. Channel 4 is a mixed channel measuring both reflected solar and terrestrial thermal radiation. Channels 5–11 have a weak solar contribution which allows for observations during both day and night. Due to the stationary position above a fixed point on the Earth ($0°\,\text{E}/0°\,\text{N}$ in operational mode) SEVIRI has a high temporal resolution of 15 min. Limiting the spatial coverage to the upper part of the SEVIRI disc (north of approx. $15°\,\text{N}$), the temporal resolution can be increased to 5 min using the rapid scanning service.

For a graphical interpretation of the SEVIRI channel observations, Fig. 3.2 shows the reflectances R retrieved from the three narrowband solar channels (1–3) and the brightness temperatures (from now on also denoted as BT) retrieved from the mixed solar/thermal channel (4) and the seven thermal channels (5–11). This gives a good overview of (1) the type of data that SEVIRI retrieves every 15 minutes and (2) the spatial coverage of the SEVIRI narrowband channels. The channel number and name is included in the lower left corner of the respective figures and the data range represented by the colour scale is included in the respective lower right corners. The black stripe along the south-east border only present in the solar channels indicates night time conditions and hence the absence of reflected solar radiation. The lower-right figure is a false colour RGB composite using the three SEVIRI channels centred at 0.6, 0.8 and $10.8\,\mu\text{m}$ (channels 1, 2, 9). With this channel combination, thick and thin cirrus clouds are identified as white and bluish, whereas the warmer liquid water clouds are recognised as yellow. A band of cirrus clouds is observed along the intertropical convergence zone (ITCZ). Furthermore several frontal (cirrus) clouds are observed over Europe and the southern and northern Atlantic Ocean. In the tropics, large areas of shallow cumulus clouds can be seen over the Atlantic Ocean.

In channels 1, 2, 3 (and 12, not shown here), bright desert areas and especially clouds have a strong signal as they reflect a large fraction of the incoming solar radiation. Ice crystals do, however, absorb and transmit solar radiation comparably effectively in the range $1.50 - 1.78\,\mu\text{m}$ (channel 3) leading to lower reflectances by high cirrus clouds for this channel compared to channels 1 and 2. Similarly, areas with lower albedo, like forests and especially the ocean, have low reflectances in the solar channels.

In the thermal spectrum the atmospheric gas absorption of longwave thermal radiation plays an important role at certain wavelengths. The two water vapour channels (6 and 7) are characterised by strong absorption by water vapour, consequently those channels give information about the large-scale water vapour structures in the troposphere. Upper level cirrus clouds located above the altitudes where the contribution to the water vapour channels peak further absorb the emit thermal radiation leading to lower radiances and brightness temperatures (Sect. 2.2.2). Channel 5 is located more in the centre of the water vapour absorption band, leading to less transmission/contribution from the lower troposphere and hence generally lower brightness temperatures and weaker radiative contrast between (thin) cirrus and cirrus-free areas. It is clear that the surface and low-level clouds, e.g. the shallow cumulus over the tropical Atlantic Ocean, cannot be identified in the two water vapour channels.

The three window channels (7, 9 and 10) are characterised by little atmospheric gas absorption of thermal radiation (Sect. 2.2.2). In these channels, most of the thermal
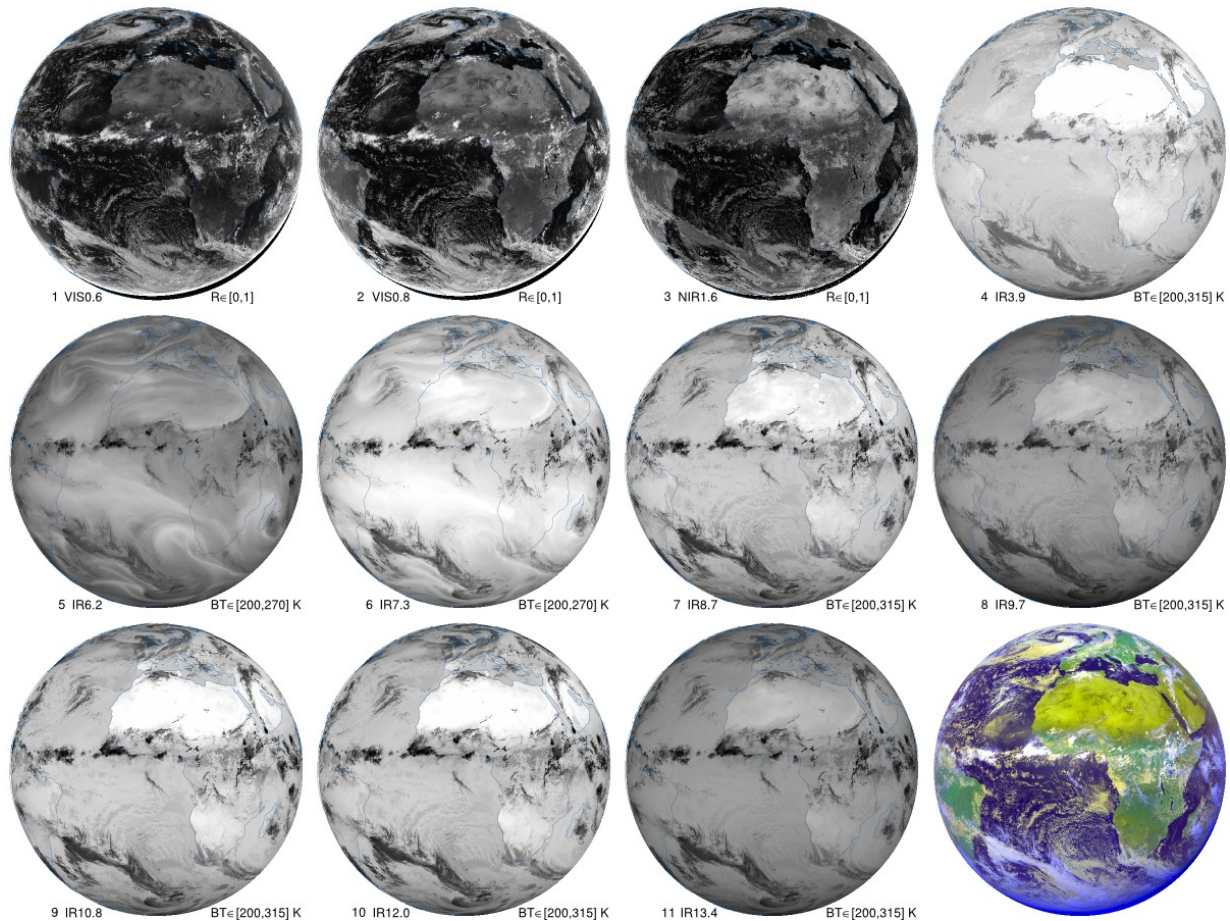
Figure 3.2: The reflectances (R) and brightness temperatures (BT) retrieved from the three solar narrowband (1–3) and eight thermal (4–11) SEVIRI channels respectively. The images were retrieved on 1 June 2015 at 12:30 UTC from MSG-3/SEVIRI. The channel number and name together with the data range represented by the colour scale is included below the respective figures. Higher reflectances and brightness temperatures are represented by brighter colours. The lower-right figure is a false colour RGB composite using the three SEVIRI channels 1, 2 and 9 (inverted) centred at 0.6, 0.8 and 10.8 µm respectively. Please note that the broadband HRV channel is not depicted here.

radiation emitted by the Earth reaches the satellite if no absorbing/scattering atmospheric particulates are present. Consequently the Earth's surface can be recognised and especially warm surfaces like deserts lead to high radiances and brightness temperatures observed by the satellite. The low liquid water clouds scatter, absorb and emit parts of the up-welling thermal radiation and due to the colder temperatures at the cloud level, this results in reduced radiances and brightness temperatures. This can be seen for the shallow marine cumulus over the tropical Atlantic Ocean, recognised as yellow in the RGB. The high cirrus clouds emit an even smaller fraction of the absorbed up-welling thermal radiation due to the considerably lower temperatures at the cirrus altitudes. Consequently, high cirrus

clouds can easily be identified in those channels due to the large difference in brightness temperatures compared to cirrus free areas. From 8.7 to 12.0 µm the absorption of thermal radiation by ice increases with the wavelength, making thin cirrus clouds more pronounced in channel 9 and especially channel 10. This is difficult to recognise by eye in Fig. 3.2, but by looking at brightness temperature differences between the window channels, as in Figs. 4.4 and 4.5, thin cirrus clouds can be identified more effectively. Channel 4 is also a window channel (centred at 3.9 µm), but adjacent to the CO_2 absorption band at 4–5 µm. Higher radiances and brightness temperatures are observed with channel 4 compared to channels 7, 9 and 10, both for cloudy and cloud-free areas. This is mainly an effect of the reflected solar radiation that is not considered in the brightness temperature definition, but nevertheless contributes to the observed radiances and indirectly increases the brightness temperatures.

Channels 8 and 11 are characterised by moderate absorption of thermal radiation by ozone and CO_2 respectively. Consequently lower brightness temperatures are observed for those channels compared to the window channels.

3.2   CALIOP aboard CALIPSO

CALIOP was launched as the main instrument aboard the CALIPSO (Cloud-Aerosol Lidar and Infrared Pathfinder Satellite Observations) satellite in 2006. CALIPSO is flying in a sun-synchronous orbit as part of the A-Train (Stephens et al., 2002). Cirrus cloud properties derived from CALIOP retrievals are used as training reference data for CiPS as well as for the validation and characterisation in Chap. 4.

CALIOP is an elastic backscatter lidar operating at two wavelengths: 532 and 1064 nm. By emitting approx. 20 laser pulses per second, a ∼70 m footprint is produced every 335 m on the Earth's surface, resulting in curtains of attenuated backscatter profiles along the CALIPSO track (Winker et al., 2009). The left panel in Fig. 3.3 shows a vertical profile of the CALIOP attenuated backscatter coefficients at 532 nm, averaged over 5 km in the horizontal. The right panel shows a 20 min orbit segment of CALIOP attenuated backscatter coefficients. The red arrow at the top shows the location where the vertical profile in the left panel was retrieved. Such vertical profiles are continuously retrieved at both 532 nm and 1064 nm as CALIPSO orbits the Earth. Due to the enhanced backscatter by clouds, aerosols and the surface of the Earth, those can be discerned from the background molecular backscatter intensity. If a layer of atmospheric particulates is too optically thick, the laser beam will get saturated, meaning that the backscatter return is too weak to be discerned form the background molecular backscatter. This is evident around 3–17° N and 39–45° N, where no signal is received from low altitudes. Due to the narrow swath width, CALIOP has a poor temporal resolution of around 16 days.

A long set of algorithms are applied to the backscatter profiles in order to detect cloud and aerosol layers (Vaughan et al., 2009), differentiate between the two (Liu et al., 2009), determine the cloud phase (Hu et al., 2009) and finally derive profiles of volume extinction coefficients (Young and Vaughan, 2009). For the cloudy regions where the cloud phase
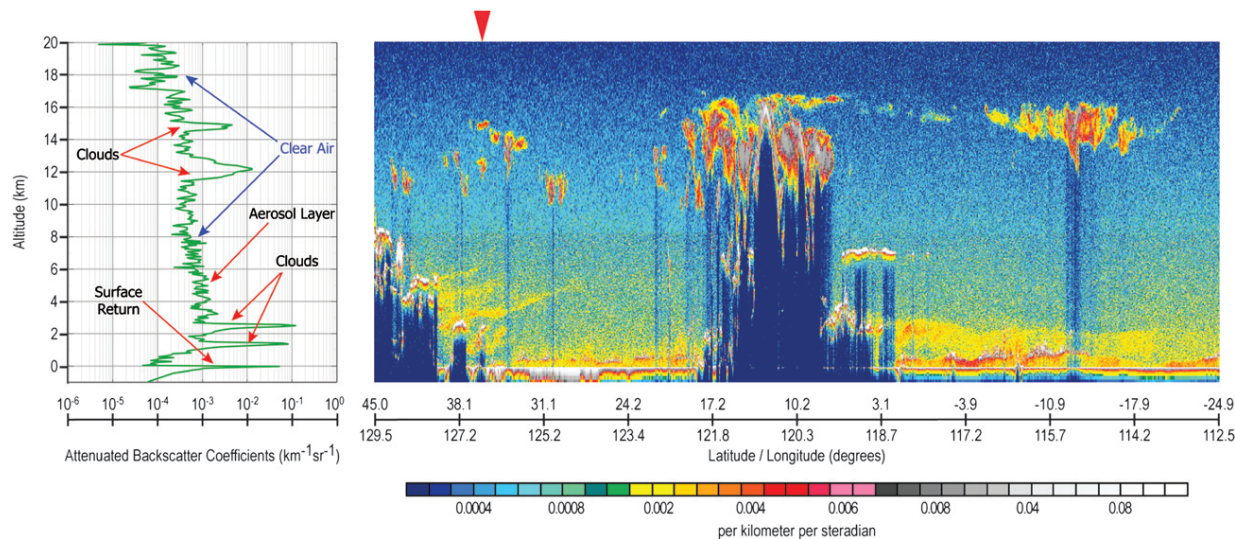
Figure 3.3: **Left:** 5 km horizontal average of the attenuated backscatter coefficients acquired by CALIOP at 532 nm on 13 August 2006. **Right:** A 20 min orbit segment of attenuated backscatter coefficients illustrating the type of data CALIOP retrieves. The red arrow on top of the right panel shows the location where the vertical profile in the left panel was retrieved. Figure reproduced from Vaughan et al. (2009).

is determined to be ice, the IWC is calculated from the retrieved extinction coefficients using a parameterisation derived by Heymsfield et al. (2005) based on extensive in situ measurements. The layer IOT and IWP are obtained by integrating the vertical profiles of extinction coefficients and IWC.

3.3 Artificial neural networks

An artificial neural network (ANN) consists of a number of neurons that exchange information with each other, in a similar manner as biological nerve cells transmit information via synapses in the human brain. By assigning each neuron-neuron connection a numeric tunable weight, the ANN has the ability to learn patterns and approximate functions. The goal of an ANN is to derive a vector of unknown output variables given a vector of known input data. This tool is applied in Sect. 3.4.3 and Chap. 4 to the remote sensing of cirrus clouds and is thus introduced in the following.

3.3.1 Multilayer perceptron

In this study a multilayer perceptron (MLP), a feed-forward ANN, is used. An MLP consists of three major units; (1) the input layer, (2) the output layer and (3) the hidden layer(s). The input layer holds as many neurons as input variables and the output layer as many neurons as desired output variables. The hidden layer(s) hold an arbitrary number of
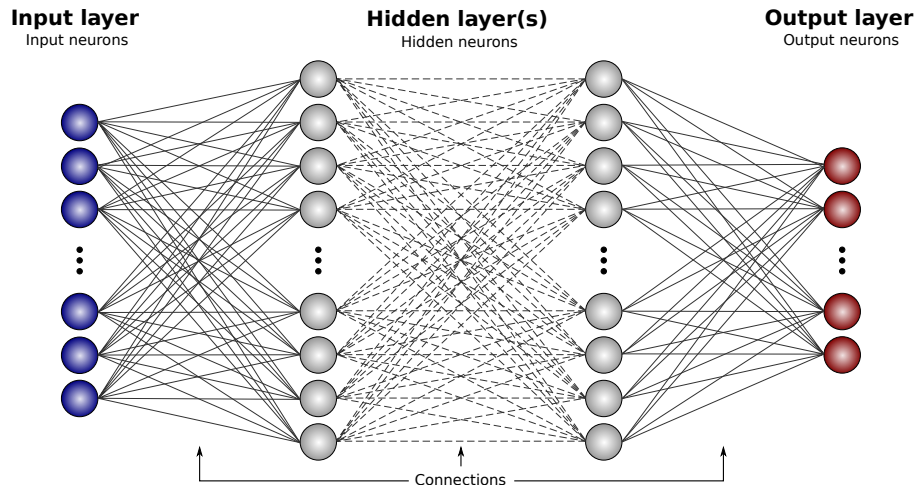
Figure 3.4: Generic structure of a multilayer perceptron (MLP), a form of a feed-forward ANN used in this study. Figure reproduced from Strandgren et al. (2017a).

additional neurons distributed over an arbitrary number of hidden layers (Haykin, 1999). All connections between the neurons within the MLP are in the forward direction (input layer → hidden layer(s) → output layer). Connections backward or within a layer are forbidden (Rumelhart et al., 1986). The value of a neuron is calculated by processing the output from the preceding neurons connected to that neuron and the corresponding weights through an activation function. These non-linear functions allow the ANN to solve complex problems with a limited number of neurons (Haykin, 1999). A generic structure of an MLP is illustrated in Fig. 3.4. In addition to the input and hidden neurons, a constant bias neuron is commonly added to the input and hidden layers in order to give the MLP more flexibility during the training.

When the MLP is given a vector of input data it uses the connection weights, possible bias neurons and the activation function to estimate the vector of output data. Thus, it is crucial that the weights and bias neurons are assigned correct values.

3.3.2 Learning through back-propagation

The weights are tuned by training the MLP, which is done with a teacher–trainer approach, more known as supervised training. A commonly used training algorithm is the back-propagation algorithm. The most essential steps in the back-propagation algorithm are explained below, but for the curious reader the algorithm as a whole is well explained in Rumelhart et al. (1986).

Using back-propagation the network is fed with a set of training examples where the vector of input variables as well as the vector of expected output variables is known. From the training input data the MLP estimates its own output data using the current weights. From the vector of *estimated* output and the corresponding vector of *expected* output the total error E (squared difference) is calculated. The error is then propagated backwards

through the MLP and used to update each weight using gradient descent in such a way that the total error is minimised. Each weight is updated using the following equation:

$$w_{ij}^* = w_{ij} - \eta \frac{\delta E}{\delta w_{ij}} = w_{ij} - \Delta w_{ij}\,, \tag{3.1}$$

where w_{ij} and w_{ij}^* are the old and new values for a weight connecting the two neurons i and j. $\frac{\delta E}{\delta w_{ij}}$ describes how much a change in w_{ij} affects the total error E. To adjust how aggressive the weight updates should be, a *learning rate* η is multiplied with $\frac{\delta E}{\delta w_{ij}}$ before the weight update. A larger learning rate means larger changes in the weights and thus a faster training. This can, however, lead to an oscillation of the total error around a minimum solution. With a small learning rate the total error will not oscillate around a minimum solution, but the training is slower and the risk of getting stuck in local minima is higher. By introducing a *momentum* term α, possible oscillations in the iterative search for the minimum error are attenuated, which allows for a larger learning rate. The momentum makes use of the previous update of the corresponding weight in order to get a weighted sum of the current and previous error gradients. The momentum term is added to the second term on the right-hand side of Eq. (3.1) such that

$$\Delta w_{ij}^k = \eta \frac{\delta E}{\delta w_{ij}} + \alpha \Delta w_{ij}^{k-1}\,, \tag{3.2}$$

where k represents the kth update of the weight w_{ij}, meaning that Δw_{ij}^{k-1} is the previous update of weight w_{ij} (Rumelhart et al., 1986).

To find the minimum total error between the estimated and expected output vectors for a complex problem and tune the weights accordingly, a large training dataset is required. Training an MLP is an iterative process, where each training example is presented to the ANN multiple times until a satisfying result has been achieved. With common ANN terminology the training completes one *iteration* every time the weights are updated and one *epoch* when all training examples contained in the training dataset have been presented to the ANN. The amount of iterations required for one epoch does therefore depend on the amount of training examples the ANN is given for every update of the weights, i.e. the batch size. With stochastic gradient descent (sometimes referred to as momentum stochastic gradient descent, when the momentum term is used) the weights are updated for each training example (batch size = 1), whereas for full batch gradient descent the weights are updated using all training examples at once (batch size = N, where N is the total number of training examples). Stochastic gradient descent leads to a noisy error gradient whereas the full batch gradient descent requires more computational power to converge. With mini-batch gradient descent an intermediate number of training examples is used for each weight update ($1 <$ batch size $< N$).

While in recent years very potent new learning methods that are based on back-propagation were developed, stochastic gradient descent is still the most used method due to its simplicity and robustness (Schmidhuber, 2015).

3.4 Supporting data

3.4.1 Cb-TRAM

Cb-TRAM (Cumulonimbus Tacking and Monitoring; Zinner et al., 2008, 2013; Merk and Zinner, 2013) was initially developed to identify, track, monitor and nowcast deep convection and early stages of it from SEVIRI. Parts of Cb-TRAM are used to identify deep convective cumulonimbus clouds and monitor their convective activity in Chap. 5, and Cb-TRAM thus shortly introduced here.

Cb-TRAM identifies three stages of thunderstorm development/activity (Zinner et al., 2013):

Stage 1 early development

Stage 2 rapid development/convective initiation,

Stage 3 mature stage.

Stage 2, which represents rapid cooling in the upper troposphere, is defined as regions with a brightness temperature cooling of more than $1\,\mathrm{K}\,(15\,\mathrm{min})^{-1}$ in the water vapour channel centred at $6.2\,\mathrm{\mu m}$. Stage 3 targets mature convective cell patterns, including the active cell centres within a developed anvil cirrus cloud. To this end, the brightness temperature difference between the two channels centred at 6.2 and $10.8\,\mathrm{\mu m}$ ($\mathrm{BT}_{6.2\,\mathrm{\mu m}} - \mathrm{BT}_{10.8\,\mathrm{\mu m}}$) is used together with texture/smoothness information from the HRV channel (WV 6.2 during night time). Furthermore, the brightness temperature difference $\mathrm{BT}_{10.8\,\mathrm{\mu m}} - \mathrm{BT}_{12.0\,\mathrm{\mu m}}$ is used to identify and exclude cirrus clouds that match these two criteria (Zinner et al., 2013). Stage 1 is not used in this study and therefore not further described here. Using Cb-TRAM Stage 2 and 3, 85 to 95 % of all thunderstorms (> 10 flashes $\mathrm{pixel}^{-1}\,(15\,\mathrm{min})^{-1}$) are detected on average during daytime (Zinner et al., 2013).

3.4.2 ECMWF ERA5

The European Centre for Medium-Range Weather Forecasts (ECMWF) recently released the first segment of the fifth major global reanalysis dataset *ERA5*. For ERA5, ECMWF uses a wealth of past and present satellite and in situ measurements in order to model a long time series of climate data. ERA5 provides estimates of more than 240 atmospheric, land and oceanic climate variables, both at the surface and at 137 pressure levels (down to $0.01\,\mathrm{hPa}$). Two major improvements over its predecessor, ERA-Interim, are the increased spatial resolution from $79\,\mathrm{km}$ to $31\,\mathrm{km}$ globally and the increased temporal resolution from $6\,\mathrm{h}$ to $1\,\mathrm{h}$ for analysis data (Hersbach and Dee, 2016).

ERA5 air temperature, relative humidity (RH), convective available potential energy (CAPE) and horizontal wind analysis data are used in Chap. 5 to characterise the meteorological conditions in which deep convective cumulonimbus clouds and anvil cirrus form.

3.4.3 COCS

The COCS (Cirrus Optical properties from CALIOP and SEVIRI; Kox et al., 2014) algorithm retrieves CTH and IOT of cirrus clouds from SEVIRI. It combines Version 2 (V2) CALIOP level 2 (L2) cloud layer data, SEVIRI thermal observations and auxiliary data using an ANN in order to retrieve CALIOP-like cirrus properties for the full SEVIRI field of view every 15 min and 24 h per day. The cirrus properties retrieved with COCS are used for comparison with CiPS in Sect. 4.9 and COCS is thus shortly introduced here.

COCS is an MLP with 10 input neurons (7 BTs and BT differences, viewing zenith angle (VZA), land–sea mask and latitude), 2 output neurons (IOT and CTH) and 600 neurons in one single hidden layer. COCS was trained with 3 years of data including SEVIRI observations from both MSG-1 and MSG-2. The detection of cirrus clouds takes place indirectly in COCS: a pixel is cirrus-covered if its IOT (IOT_{COCS}) ≥ 0.1, meaning that pixels with $IOT_{COCS} < 0.1$ are considered too uncertain and regarded as cirrus-free. The value of 0.1 was chosen as a trade-off between high probability of detection (Eq. 3.3) and low false alarm rate (Eq. 3.4).

The V2 CALIOP L2 cloud layer products contain no information on data quality and the feature classification flag and feature optical thickness among other variables were released as beta products (early release). V2 CALIOP layer data used in Kox et al. (2014) therefore had to fulfil three filtering conditions to be classified as a cirrus cloud: (1) to exclude inaccurate retrievals due to diverging extinction retrievals in opaque cloud layers, the maximum IOT was limited to 2.5. (2) To ensure that the cirrus clouds were not falsely classified layers of aerosols or liquid water clouds, the mid-layer temperature had to be 243 K or colder. (3) The layer top height had to exceed 9.5 km in the tropics and 4.5 km in polar regions, with a linear decrease between these two values in mid-latitudes.

3.5 Validation metrics

This section introduces the validation metrics used for the validation and characterisation of CiPS in Chap. 4. The probability of detection (POD) is used to measure how efficiently CiPS detects cirrus clouds and is given by

$$\mathrm{POD} = \frac{N_{\mathrm{TP}}}{N_{\mathrm{TP}} + N_{\mathrm{FN}}}, \tag{3.3}$$

where the number of true positives, N_{TP}, is all points correctly classified as cirrus and the number of false negatives, N_{FN}, all cirrus clouds that remain undetected. The denominator, $N_{\mathrm{TP}} + N_{\mathrm{FN}}$, is thus the total number of points with a reference cirrus cloud. The false alarm rate (FAR) measures the fraction of cirrus-free points that are falsely classified as being cirrus clouds:

$$\mathrm{FAR} = \frac{N_{\mathrm{FP}}}{N_{\mathrm{FP}} + N_{\mathrm{TN}}}. \tag{3.4}$$

Table 3.2: Contingency table for the cirrus detection from CALIOP and CiPS. Table reproduced from Strandgren et al. (2017a).

		CALIOP	
		Cirrus	No cirrus
CiPS	Cirrus	N_{TP}	N_{FP}
	No cirrus	N_{FN}	N_{TN}

The number of false positives, N_{FP}, is all points falsely classified as cirrus (false alarms) and the number of true negatives, N_{TN}, all points correctly identified as cirrus-free. The denominator, $N_{\mathrm{FP}} + N_{\mathrm{TN}}$, is thus the total number of points with no reference cirrus cloud. The corresponding CALIOP data are used as a reference when calculating the POD and FAR in Chap. 4. Table 3.2 clarifies the quantities used to calculate the two metrics. The POD and FAR are also used to measure how effectively CiPS can determine the opacity/transparency of detected cirrus clouds.

The mean percentage error (MPE) and mean absolute percentage error (MAPE) are used to measure the accuracy of the retrieved cirrus properties with respect to CALIOP. The MPE is given by

$$\mathrm{MPE} = \frac{100\,\%}{N} \sum_{i=1}^{N} \frac{E_i - O_i}{O_i}, \tag{3.5}$$

where O is the observed reference value by CALIOP and E the estimated value by CiPS. The sum spans over all samples $i = 1, \ldots, N$ used for the evaluation. The MPE gives information about the direction of the deviations, i.e. whether CiPS tends to overestimate (positive MPE) or underestimate (negative MPE) the values with respect to CALIOP. When calculating the MPE, over- and underestimations can cancel out each other, potentially leading to zero MPE (bias) even if the magnitude of the errors is large. Therefore the MAPE has been considered as well. The MAPE is given by

$$\mathrm{MAPE} = \frac{100\,\%}{N} \sum_{i=1}^{N} \left| \frac{E_i - O_i}{O_i} \right| \tag{3.6}$$

and gives information about the average magnitude of the errors relative to the expected reference values observed by CALIOP. A vanishing MAPE means no deviation from the observed values and a perfect correlation.

Chapter 4

CiPS - Cirrus Properties from SEVIRI

The results and text in this chapter (except Sects. 4.11 and 4.12) have been published in Strandgren et al. (2017a) and Strandgren et al. (2017b).

CiPS is a new algorithm for cirrus cloud remote sensing with SEVIRI that exploits the basic idea of COCS: retrieving cirrus properties using ANNs trained with CALIOP and SEVIRI data. However, CiPS clearly differs from COCS in the implementation of this idea and the achieved performance. For a more accurate cirrus detection and determination of CTH and IOT, CiPS utilises a different set of input parameters including numerical weather model data and information from nearby pixels. In addition, CiPS classifies each pixel as either cirrus-free, transparent cirrus or opaque cirrus by means of dedicated classification ANNs. As CALIOP gets saturated for thicker clouds, the opacity information is an important additional piece of information in order to better characterise the cirrus and the reliability of the ANN results that was absent in COCS. Furthermore, CiPS is trained to retrieve the IWP, resulting in a total of three climate relevant cirrus cloud properties that can be estimated during both day and night for the full SEVIRI field of view every 15 min. CiPS targets thin cirrus clouds, as those clouds are most difficult to retrieve using thermal satellite observations from geostationary orbits. Although the approach of training a set of ANNs with lidar data does not directly increase SEVIRI's sensitivity to thin cirrus clouds, it is expected to allow for a more effective exploitation of the SEVIRI spectral information, compared to present spectral threshold tests and physically based retrievals, indirectly increasing the sensitivity to thin cirrus clouds.

4.1   Multiple artificial neural networks

In contrast to COCS, which uses one single ANN to retrieve IOT and CTH, CiPS utilises four ANNs, making it possible to customise the input variables, training data and ANN structures individually for each task to be solved.

1. The first ANN is a classification network trained to detect cirrus clouds using a binary cirrus cloud flag (CCF). Due to the continuous activation function used by the ANN (Sect. 3.3.1), the retrieved value of the CCF neuron is a real number in the interval (0,1) represented by a 32 bit floating point number. This value can be interpreted as a cirrus probability, where high and low values indicate a high and low probability of cirrus presence respectively. This provides at least three major advantages over an IOT threshold-based detection. (1) The CCF detection threshold (0–1) can be determined depending on the application. A higher threshold means a lower FAR (Eq. 3.4), whereas a lower threshold means a higher POD (Eq. 3.3). (2) The cirrus detection is independent of the IOT and not limited to cirrus clouds with an estimated optical thickness greater than 0.1, as is the case for COCS. (3) Since no additional information is needed for the pixels classified as cirrus-free by the cirrus detection ANN, the ANNs for CTH, IOT, IWP and opacity information retrieval can be trained only with cases where cirrus clouds are present. This excludes a large number of largely different input data combinations representing the same "cirrus" properties, i.e. the situations where $IOT = IWP = 0$.

2. The second ANN is used for the CTH retrieval.

3. The third ANN is used for the IOT/IWP retrieval. These two variables are provided by the same network since they are physically closely related (Heymsfield et al., 2005).

4. CALIOP cannot provide accurate IOT/IWP retrievals for thicker cirrus clouds where the laser beam is completely attenuated. Hence the estimated IOT and IWP by CiPS for such situations should not be trusted. Therefore a second classification network is introduced with CiPS, trained to identify the cirrus clouds where CALIOP gets saturated. Similarly to the cirrus detection ANN, the opacity classification ANN retrieves real numbers in the interval (0,1), which can be regarded as an opacity probability information. From here a binary opacity flag (OPF) is obtained using a suitable opacity classification threshold (Sect. 4.6).

4.2   Input data

The CiPS input data selection is based on physical considerations. The following subsections introduce all input data used to train and apply CiPS. An overview is provided in Table 4.1.

4.2.1   Brightness temperatures from SEVIRI

CiPS works pixel by pixel and uses the single brightness temperatures from the SEVIRI channels centred at 6.2, 7.3, 8.7, 10.8, 12.0 and 13.4 μm. Water vapour channels (centred at 6.2 and 7.3 μm) should help detecting ice clouds (see e.g. Krebs et al., 2007), identifying opaque pixels as well as determining its height, together with the CO_2 channel centred

at $13.4\,\mu m$ (e.g. Menzel et al., 1983, 2008). Window channels (8.7, 10.8, $12.0\,\mu m$) and especially their brightness temperature differences are both useful for detection (e.g. Inoue, 1985) and for the optical thickness determination (e.g. Ackerman et al., 1990). The ozone channel centred at $9.7\,\mu m$ is excluded because its sensitivity peaks in the stratosphere, where no cirrus clouds are present, and because of its strong annual cycle due to the ozone variability (Ewald et al., 2013). Channels with significant solar contribution are excluded in order to have the same conditions and similar performance during both day and night. Furthermore, CiPS exploits the information from nearby SEVIRI pixels by utilising the regional maximum brightness temperature from the window channels (for all ANNs, as a proxy for cirrus-free conditions) and the regional average brightness temperature from the water vapour channels (only for cirrus detection and opacity classification, as a proxy for the smoothness of the surroundings). The regional maximum brightness temperature is defined as the maximum brightness temperature within a 19×19 pixels large box (corresponding to an area of $\approx 57 \times 57\,km^2$ at nadir) centred at the pixel under consideration. Similarly the regional average brightness temperature is defined as the boxcar average temperature within the same box (inspired by Krebs et al., 2007). The box size of 19×19 pixels is chosen such that the region is small enough to reduce the risk of unrepresentative maximum temperatures over inhomogeneous surfaces (e.g. coast lines) but large enough to increase the chance of capturing a representative cirrus-free pixel.

4.2.2 Surface temperature from ECMWF

With CiPS, modelled data from the ECMWF ERA-Interim reanalysis dataset (Dee et al., 2011) are introduced to the list of input variables. The modelled surface temperature, T_{surf}, from ECMWF provides a cirrus-free characterisation of the surface and should be useful in all ANNs. It also helps the ANNs to distinguish between cirrus clouds and cold surfaces like Greenland and Antarctica. The temporal resolution of $6\,h$ and spatial grid of $0.125°$ is used.

4.2.3 Auxiliary data

Along with the SEVIRI and ECMWF data, CiPS uses information about the latitude, the viewing zenith angle (VZA) of SEVIRI, two surface type flags (seawater and permanent ice and snow) and the day of year (DOY, 1–365; to avoid a hard transition from 31 December to 1 January, two input neurons are used for the DOY: $\sin(2\pi\,DOY/365)$ and $\cos(2\pi\,DOY/365)$). Latitude and DOY are selected since the appearance of cirrus and their top height strongly depends on general circulation and convective strength, with higher clouds in the tropics and generally lower clouds towards the polar regions and with stronger convection in summer with respect to spring/autumn and, of course, winter in mid-latitudes. VZA shall account for the path length of radiation through the atmosphere, while the two selected surface types identify on one side (sea) thermally quite homogeneous surfaces and on the other side (ice/snow) cold surfaces with similar absorption properties as the ice clouds. In total, 18 input variables are used for the cirrus detection and opacity

Table 4.1: Input data used to train the four ANNs contained in CiPS. regavg is regional average, regmax is regional maximum, $DOY_{SIN} = \sin(2\pi\,DOY/365)$ and $DOY_{COS} = \cos(2\pi\,DOY/365)$. Table adapted from Strandgren et al. (2017a).

	CCF	OPF	CTH	IOT/IWP
$BT_{6.2\,\mu m}$	✓	✓	✓	✓
$BT_{7.3\,\mu m}$	✓	✓	✓	✓
$BT_{8.7\,\mu m}$	✓	✓	✓	✓
$BT_{10.8\,\mu m}$	✓	✓	✓	✓
$BT_{12.0\,\mu m}$	✓	✓	✓	✓
$BT_{13.4\,\mu m}$	✓	✓	✓	✓
$BT_{6.2\,\mu m,\,regavg}$	✓	✓		
$BT_{7.3\,\mu m,\,regavg}$	✓	✓		
$BT_{8.7\,\mu m,\,regmax}$	✓	✓	✓	✓
$BT_{10.8\,\mu m,\,regmax}$	✓	✓	✓	✓
$BT_{12.0\,\mu m,\,regmax}$	✓	✓	✓	✓
T_{surf}	✓	✓	✓	✓
Latitude	✓	✓	✓	✓
VZA	✓	✓	✓	✓
Water flag	✓	✓	✓	✓
Snow/ice flag	✓	✓	✓	✓
DOY_{SIN}	✓	✓	✓	✓
DOY_{COS}	✓	✓	✓	✓

classification and 16 input variables for the CTH, IOT and IWP retrievals (see Table 4.1). Although the selection of input quantities is inspired by physical principles, the task of combining input variables is left to the ANNs.

4.3   Output data: cirrus properties from CALIOP

The training reference data, including a CCF and an OPF as well as the CTH, IOT and IWP, are derived from the Version 3 (V3) CALIOP L2 5 km cloud and aerosol layer products (CAL_LID_L2_05kmC|ALay-Prov-V3-0X CALIPSO Science Team, 2015a,b,c,d). Major improvements with respect to V2 data include enhanced cloud–aerosol discrimination, improved cloud thermodynamic phase determination, more accurate estimates of layer spatial and optical properties as well as an improved estimate of the low cloud fraction. Furthermore, new products like the IWP and retrieval uncertainties are included. Most importantly, the maturity level of all products used to develop CiPS has been upgraded from beta status to provisional or higher, meaning that the data have at least been

compared to independent sources in order to correct obvious artefacts (NASA Atmospheric Science Data Center, 2010).

Even though the cloud and aerosol layer products are reported with a spatial resolution of 5 km, two additional coarser resolutions of 20 and 80 km are used to detect the cloud and aerosol layers reported in the 5 km products (Vaughan et al., 2009). At a spatial resolution of 5 km, the signal-to-noise ratio (SNR) of a faint cirrus or aerosol layer is usually too weak to be distinguished from the clear-sky atmospheric signal. By averaging 4 or 16 consecutive 5 km profiles the SNR is increased, which allows for detection of very thin cirrus and aerosol layers. For example if a thin cirrus cloud with an optical thickness of 0.1 and a top altitude of 10 km is identified only when 16 consecutive 5 km profiles are averaged (80 km spatial resolution), 16 consecutive bins in the L2 5 km cloud layer data will report an optical thickness of 0.1 and a top altitude of 10 km. This can result in a vertical overlap between layers detected at different spatial resolutions. This is accounted for by identifying the part of an icy layer vertically overlapped by another layer (water cloud or aerosol) detected at a higher spatial resolution and correcting the corresponding extinction coefficients, IWC and CTH accordingly. The column IOT and IWP are then derived by combining the properties of all icy layers in each profile. Finally, the OPF is extracted from the "Opacity_Flag" product. The Opacity_Flag gives the information whether the CALIOP backscatter signal was completely attenuated within a detected layer. During the CALIOP retrieval, a cirrus cloud layer is classified as opaque if it is the lowermost layer and not identified as a surface return (Vaughan et al., 2005). A digital elevation model is partly used to identify surface returns, meaning that high cirrus clouds should not be falsely classified with respect to transparency. Cirrus cloud layers detected at the coarser 20 or 80 km resolutions are classified as transparent if the corresponding base altitude is higher than the lowermost detected feature in at least 50 % of the 4 or 16 consecutive 5 km profiles that constitute the 20 and 80 km averages.

The minimum detectable backscatter of CALIOP depends on the scattering target (the cirrus cloud in this case), the altitude as well as the vertical and horizontal averaging of the data (McGill et al., 2007). Davis et al. (2010) show that CALIOP can detect approx. one-third of the sub-visual cirrus clouds with an optical thickness below 0.01.

With the improved quality of the V3 CALIOP products, the filtering processes applied to the V2 data used for COCS can be omitted (see Sect. 3.4.3). To assure a high-quality dataset, the extinction quality control flag, retrieval uncertainties and the feature classification flag including the quality assessments have been considered though. All columns containing at least one layer with unknown feature type, unknown cloud phase or a feature/phase quality assessment flag less than 3 (high confidence) are excluded. Additionally, only those columns with solely constrained or unconstrained cirrus/ice cloud retrievals where the initial lidar ratio remained unchanged during the solution process are included. Furthermore, the columns containing stratospheric features are excluded due to lack of information about whether the features are stratospheric clouds or aerosol layers.

The CALIOP products are chosen as training reference data for CiPS as they should provide the most accurate estimates of especially CTH but also IOT for thin cirrus clouds from space. It is important to note that an ANN can never be better than its training

reference and all deficiencies and/or biases in the training reference data will be inherited by the ANN. Since possibly inherited artefacts of the ANN will not show when validated against independent CALIOP retrievals, one must be aware of the accuracy and limitations of the training data.

Yorks et al. (2011) and Hlavka et al. (2012) validate the spatial and optical properties of cirrus clouds from the V3 CALIOP products using the airborne Cloud Physics Lidar (CPL; McGill et al., 2002) during the CALIPSO-CloudSat Validation Experiment (CC-VEX). CPL has a higher SNR, higher vertical and horizontal resolution and lower multiple scattering compared to CALIOP, making it the most comprehensive tool for validating the CALIOP retrieved cirrus properties. Ten underpass flights with CALIOP were performed and over 9500 bins of collocated extinction coefficients were obtained. During the 10 flights, extinction coefficients ranging from approx. 0.001 to $10\,km^{-1}$ and column optical thickness up to approx. 3 were retrieved. CALIOP and CPL agree on 90 % of the scene classifications (cirrus or no cirrus) on average. For all bins classified as cirrus by CPL, CALIOP agrees on 82 % and for the bins classified as cirrus-free by CPL, CALIOP agrees on 91 %. For cases where both CALIOP and CPR detect cirrus, the agreement in cirrus top height is excellent (Yorks et al., 2011).

For transparent cirrus layers the agreement in IOT between CALIOP and CPL is good with on average 15 % higher extinction for CALIOP (0.65 in correlation between CALIOP and CPL). For the unconstrained retrievals where the initial lidar ratio remains unchanged the average difference in extinction is only 7 % (0.80 in correlation between CALIOP and CPL; Hlavka et al., 2012). The latter are the ones used to train CiPS (see above), along with the constrained retrievals. At the time of the CC-VEX campaign (between 26 July and 14 August 2006) the laser of CALIOP was pointing just 0.3° from nadir leading to a strong specular reflection by layers of horizontally orientated ice (HOI) (Winker et al., 2009). This led to disagreements in the extinction retrieval with CPL, whose laser pointed 2° from nadir and therefore only received a very small fraction of specular reflections from the HOI (Hlavka et al., 2012). Since November 2007 the CALIOP lidar points 3° from nadir in order to overcome this issue for layers with HOI. When the column optical thickness is derived for all cirrus-covered bins, the relative difference between CALIOP and CPL is only 2.2 % due to cancellation of opposing CALIOP effects. Holz et al. (2016) recently showed that the single-layer IOT derived from unconstrained CALIOP retrievals is low-biased with respect to a single-channel thermal/infrared IOT retrieval combining CALIOP/MODIS observations and forward radiative transfer modelling. The bias is shown to increase with increasing IOT.

The accuracy of the CALIOP IWC/IWP is directly related to the accuracy of the extinction retrievals as well as the IWC parameterisation from Heymsfield et al. (2005). A proper independent validation of the CALIOP IWC/IWP is a difficult task due to the lack of reference data at a comparable spatial and temporal resolution. Protat et al. (2010) evaluate the IWC parameterisation used for CALIOP for tropical cirrus using ground-based radar–lidar retrievals. The results suggest that the parameterisation is quite robust and is shown to work well at most altitudes. Above $\approx 12\,km$ the IWC is clearly underestimated with respect to the ground-based radar–lidar retrieval. Avery et al. (2012) evaluate

the CALIOP IWC using coincident data from CloudSat and in situ measurements inside a tropical convective cloud. At the lower altitudes (8–12 km), the CALIOP IWC is underestimated with respect to the in situ measurements, which could be attributed to a lower penetration depth of CALIOP and the removal of CALIOP layers containing HOI. Between 12 and 14 km the agreement between the CALIOP IWC and the in situ measurements is good. At all altitudes CALIOP seems to underestimate the IWC with respect to CloudSat. Wu et al. (2014) show that the V3 CALIOP IWC agrees well with airborne in situ measurements up to approx. $20\,\mathrm{mg\,m^{-3}}$ at an altitude of 12 km. The CALIOP IWC agrees well with the CloudSat IWC within the regions where their sensitivities overlap. This occurs between 5 and $20\,\mathrm{mg\,m^{-3}}$ at an altitude of 12 km and between 30 and $200\,\mathrm{mg\,m^{-3}}$ at 15 km.

In the following, all quantities referring to CALIOP will be denoted as $\mathrm{IOT_{CALIOP}}$, $\mathrm{IWP_{CALIOP}}$ and $\mathrm{CTH_{CALIOP}}$.

4.4   Data preparation

To learn the relationship between the SEVIRI, ECMWF, auxiliary data and the cirrus properties from CALIOP, an extensive dataset is created containing spatial and temporal collocations of all variables. The training dataset covers the time period from April 2007 to January 2013, which is the time when MSG-2 was the operational satellite at 0.0° E. CiPS is restricted to MSG-2 alone, to avoid mixing data from multiple SEVIRI instruments since their characteristics are slightly different.

4.4.1   Data collocation

For this time period all quality-controlled CALIOP data within the SEVIRI field of view are identified and collocated with single SEVIRI pixels in time and space. Due to the different viewing geometries of SEVIRI and CALIOP, the same cloud seen by SEVIRI and CALIOP at the same time appears to be located at two different positions. The magnitude of this displacement depends on the VZA and the altitude of the cloud layer. This effect has been corrected for using the latitude, longitude and CTH from CALIOP (parallax correction) to project ice clouds onto the SEVIRI grid. The cirrus properties from CALIOP are spatially collocated with SEVIRI observations from the pixel having the largest overlap with the 5 km CALIOP orbit segment. The data are temporally collocated by identifying the SEVIRI observation that has the smallest difference in acquisition time compared to CALIOP. With a temporal resolution of 15 min for SEVIRI, the maximum difference in acquisition time between SEVIRI and CALIOP is 7.5 min.

When collocating SEVIRI and CALIOP observations with the purpose of training an ANN one must consider two aspects. (1) Even though the 5 km average of CALIOP point measurements fits the spatial resolution of SEVIRI ($3 \times 3\,\mathrm{km}^2$ at nadir and approx. $3.5 \times 5\,\mathrm{km}^2$ in mid-latitudes) quite well in the along-track direction, the two observations differ largely in scale in the across-track direction as the footprint of CALIOP is approx. 70 m wide at the Earth's surface. Consequently the 5 km CALIOP orbit segment is representative

only for a relatively small fraction of a SEVIRI pixel. This will induce inevitable errors and lead to imperfect information used to train the ANN. This is especially relevant for partial cloud cover, where CALIOP may observe a cloud-free area in an otherwise cloud-covered SEVIRI pixel. If the error from imperfect collocations is random, this will have a limited effect on the ANN. Only if there is a recurrent systematic difference as a result of the different spatial scales this will lead to biased retrievals (Holl et al., 2014). (2) Although cirrus clouds leave their mark on both SEVIRI and CALIOP measurements in a similar way, SEVIRI does not share CALIOP's possibility of discerning vertically separated ice clouds, liquid water clouds and aerosols. Consequently SEVIRI should not be expected to discern the signal from liquid water clouds and aerosols when retrieving the IOT as effectively as CALIOP.

The ECMWF surface temperatures are spatially collocated with the satellite observations using nearest neighbour. For the temporal collocation, the ECMWF reanalysis data are linearly interpolated between the ECMWF 6 h time steps and the satellite acquisition time.

4.4.2   Training and validation data

The full collocated dataset, covering the entire SEVIRI disc and a time period of almost 6 years, contains close to 50 million collocations. Of those collocations, 80 % are used to create the four datasets required for the training of the four ANNs contained in CiPS. For the CCF ANN, both cirrus-free collocations and collocations with transparent and opaque cirrus clouds are included in the training dataset. Collocations with no cirrus cloud present are excluded from the training datasets used to train the OPF ANN as well as the CTH and IOT/IWP retrieval ANNs, since those networks will be applied only on pixels identified as cirrus-covered by the CCF ANN. Furthermore, the IOT/IWP ANN is trained only with collocations containing transparent cirrus clouds, where the CALIOP signal was not saturated such that the true, rather than the apparent, IOT and IWP could be retrieved. Figure 4.1 shows the relative number distributions of the IOT, IWP and CTH retrieved by CALIOP. It is clear that the collocation dataset is unbalanced in several aspects. The IOT and IWP have exponential distributions with very few thicker cirrus clouds. Similarly there are comparably few low and high cirrus clouds available and the CTH distribution has two peaks, corresponding to mid-latitudes and tropics. To improve the end performance for those rare points the unbalance of the training datasets is reduced "by hand". For the cirrus detection and IOT/IWP ANNs, four duplicates of all cirrus clouds with $\text{IOT}_{\text{CALIOP}} \geq 1.0$ have been added to the training datasets. Similarly four duplicates of all cirrus clouds with $\text{CTH}_{\text{CALIOP}} > 17 \, \text{km}$ or $\text{CTH}_{\text{CALIOP}} < 5 \, \text{km}$ have been added to the CTH training dataset. For the opacity classification ANN, four duplicates of all opaque cirrus clouds have been added to the training dataset. This approach does not introduce any new information that the ANNs can learn from but does increase the weight of the added points during the training. Adding too few duplicates has a negligible effect whereas too many duplicates give the added points too strong an impact during the training. By testing different numbers, four duplicates are seen to yield the best results for all ANNs. Furthermore,
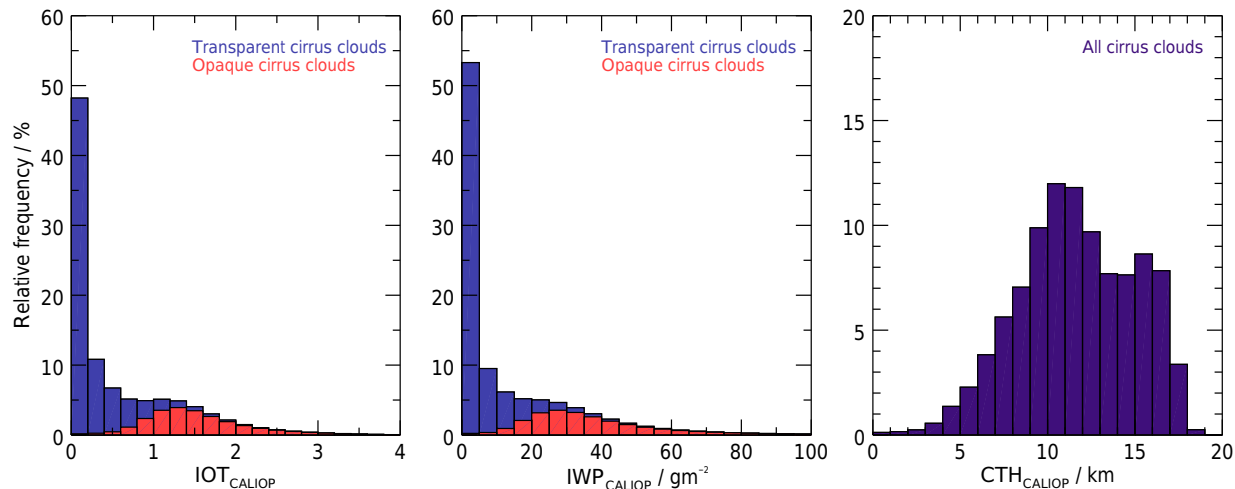
Figure 4.1: The relative number distribution of the cirrus IOT (bin size = 0.2), IWP (bin size = $5\,\mathrm{g\,m^{-2}}$) and CTH (bin size = $1\,\mathrm{km}$), from almost 6 years of V3 CALIOP L2 layer data over the SEVIRI disc. Figure reproduced from Strandgren et al. (2017a).

the IOT and IWP are transformed to their logarithmic counterparts before the training ($\mathrm{IOT}^* = \log_{10}(\mathrm{IOT}), \mathrm{IWP}^* = \log_{10}(\mathrm{IWP}/1\,\mathrm{g\,m^{-2}})$). Finally, the single input variables are normalised to have zero mean and unit variance (LeCun et al., 1998) and the output data are scaled to fit the ranges of the activation functions (Sect. 4.5) used by the ANNs.

The remaining 20 % of the collocation dataset is used for validation. Half of these data are used to create internal validation datasets that are used to monitor the error against independent data during the training in order to avoid overfitting (see Sect. 4.5) and to determine training meta-parameters, ANN structures (see Sect. 4.7) and classification thresholds (see Sect. 4.6). The internal validation datasets have been filtered in the same manner as the training datasets but have not been balanced by adding duplicates of selected points. The second half of the validation data are used for final validating and characterising CiPS (and COCS) presented in Sects. 4.9 and 4.10 respectively. These final validation data are not used for any purpose during the development and training of CiPS. With common ANN terminology the internal and final validation data are usually referred to as validation and test data respectively.

4.5 Training

To train and apply CiPS the Fast Artificial Neural Network library (FANN; Nissen, 2003) is used. The four ANNs contained in CiPS are trained using the standard back-propagation algorithm and mini-batch gradient descent described in Sect. 3.3.2.

Three hidden layers are used for the cirrus cloud detection, two for the CTH and IOT/IWP retrievals and a single hidden layer for the opacity classification. All ANNs use 16 hidden neurons per hidden layer (see Sect. 4.7 for details on the MLP structures).

For the classification ANNs (CCF, OPF) the sigmoid activation function is used for both hidden and output layers, whereas the tanh activation function is used for hidden and output layers for the regression ANNs (CTH and IOT/IWP). A batch size of 1024 is used, meaning that the ANNs look at 1024 input and output data combinations before each weight update. The value of 1024 was chosen as a trade-off between the noise in the error gradient that increases with smaller batch sizes and the required computational power that increases with larger batch sizes. The learning rate and momentum are sensitive to the problem that should be solved, the corresponding training data as well as the number of input and output variables (Schaul et al., 2013). To find the optimal values an extensive iterative test approach is performed. For this test a large GPU cluster (120 teraFLOPS – 20 NVIDIA GTX Titan GPUs) is used to train numerous ANNs with different numbers of hidden layers and hidden neurons and a wide range of learning rates and momentum values. To find the optimal values for each meta-parameter, a random search according to Bergstra and Bengio (2012) is performed within intervals chosen based on expert knowledge. Sets of meta-parameters are randomly drawn from the pre-defined intervals and used to train corresponding sets of ANNs. Assuming an infinite number of samples, this procedure can be regarded as a global optimisation technique. The optimal set of meta-parameters is defined as the one that minimises the mean square error (MSE) between the ANN and the internal validation data. All resulting optima are well within these chosen intervals, so it is assumed that the choice of the intervals does not introduce any distortion or bias. For both the classification and regression tasks a learning rate around 0.05 and momentum around 0.99 are found to provide ANNs with the lowest MSE against the independent internal validation data.

The ANNs are initially trained using 25 % of the training data. This is done in order to speed up the training. This first phase continues until the accuracy of the ANNs does no longer improve with respect to the internal validation data. During this first phase of the training a rough estimate of the error gradient is sufficient as the general direction towards a minimum solution is searched for. Thus a larger learning rate and smaller mini-batches are preferred. When the ANN approaches the region of an optimal solution, those large step-sizes and small mini-batches are too blunt to find the finer structures needed to solve the problem better. Thus the learning rate and batch size should be adjusted accordingly in order to make smaller and more informed steps in the search space. During this iterative tuning phase, the learning rate is reduced by a factor of 4 and the batch size is increased by a factor of 2. In order to not impede the effect of the finer learning rate and batch size, the momentum is reduced accordingly. Furthermore the size of the training dataset, which started at 25 % during the first phase, is increased by a factor of 2. This is a schedule procedure that is commonly used in the machine learning/ANN community. As the tuning phase continues the meta-parameters are refined according to the schedule above as soon as the total error stops to decrease with respect to the internal validation dataset. The tuning phase and thereby the training stops when the respective ANNs have reached a point where additional epochs do not reduce the error, using 100 % of the respective training datasets.

To avoid overfitting, the error against the independent internal validation datasets (Sect. 4.4.2) is always monitored. Overfitting occurs when an ANN learns the training

dataset itself rather than the relationship between the input and output variables and thus loses its ability to generalise. To make sure that the ANNs are not overfitting, the updated weights are only saved if the error against the internal validation dataset decreases; otherwise the training continues but the set of weights having the current minimum error against the internal validation dataset is kept.

For each task/ANN the training is repeated twice in order to reduce the risk of having a bad end performance as a result of a bad set of initial weights (from Widrow and Nguyen's algorithm; Nguyen and Widrow, 1990). In the end, only the best performing network is used. The differences between the two networks trained for each task/ANN are, however, very small (ca. 3 ‰ relative difference in MSE).

Using a common standard desktop PC (using 1 core @ 3.40 GHz, Intel Core i5-3570), the final set of ANNs, called CiPS, takes approx. 60 s to process a complete SEVIRI image (3712×3712 pixels) including I/O. Approximately 40 s are needed for the cirrus cloud detection and another 20–30 s for the opacity classification as well as the retrieval of CTH, IOT and IWP. The cirrus cloud detection takes longer as this ANN must be applied to all SEVIRI pixels, whereas the other ANNs only have to be applied to those pixels classified as icy by CiPS. This is ca. 10 times faster than the combined CTH and IOT retrieval by COCS (Kox et al., 2014). ANN computations are highly parallelisable, meaning that the computation time can be reduced significantly by distributing the computations across multiple cores.

4.6   Cirrus detection and opacity classification thresholds

As described in Sect. 4.1 the thresholds for the CiPS CCF and OPF ANNs can be selected between 0 and 1 depending on the application. These two thresholds are chosen based on a trade-off between the POD (Eq. 3.3) and FAR (Eq. 3.4) using the internal validation dataset. Figure 4.2 shows the FAR and POD of the CiPS classification ANNs as a function of classification threshold (also known as the receiver operating characteristic curve). It is clear that the two quantities are anti-correlated where a lower threshold yields a higher POD, but this comes at the expense of an increased FAR and vice versa. For the application, validation, characterisation and anvil cirrus life cycle analysis presented in thesis, as well as for the standard usage of CiPS, a CCF threshold of 0.62 is chosen, resulting in a total POD of 71 % and a FAR of 3.9 %. The low POD is a direct effect of the large amount of very thin to sub-visual cirrus (IOT < 0.03) that CiPS does not detect (see Figs. 4.1 and 4.7). For the OPF a threshold of 0.86 is chosen, resulting in a POD of 71 % and a FAR of 4.0 % for the cirrus clouds that CiPS successfully detects. The two thresholds chosen for CiPS are indicated in Fig. 4.2 with red circles.
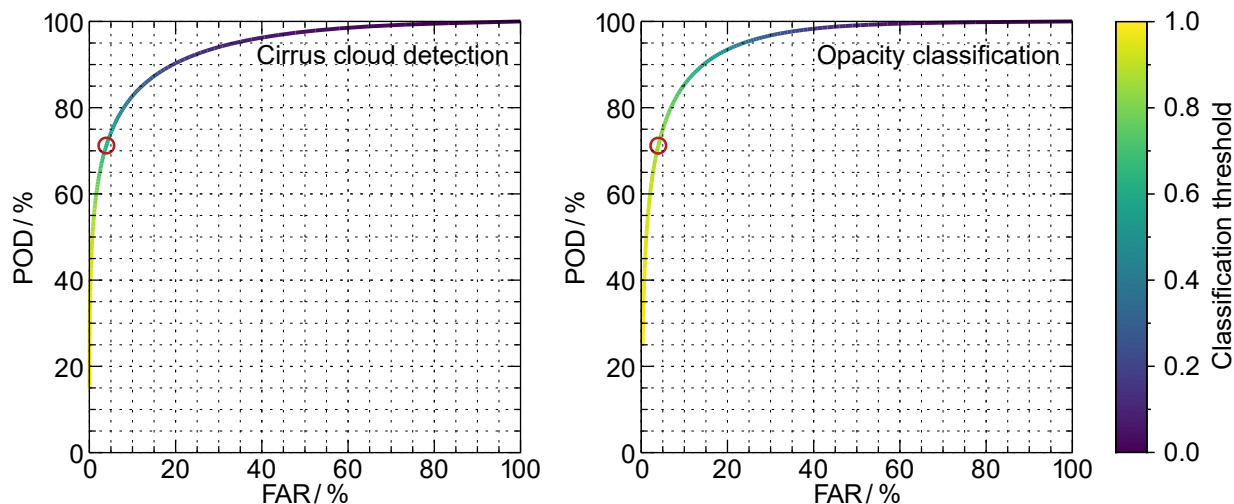
Figure 4.2: The POD and FAR of the CiPS cirrus cloud detection and opacity classification ANNs as a function of classification threshold. The red circles indicate the final thresholds selected for the two ANNs. Figure adapted from Strandgren et al. (2017a).

4.7 Evaluating different MLP structures

When developing CiPS, several ANNs with different MLP structures were trained in order to investigate the effect of the MLP structure on the end performance and to determine the respective structures that offer the best trade-off between accuracy and application time. For each ANN contained in CiPS several networks with different structures were trained using one, two and three hidden layers with either 16 or 64 hidden neurons per hidden layer. For the single hidden layer structures a network with 128 hidden neurons is also trained. Also here the training is repeated twice for each network in order to reduce the risk of having a bad end performance as a result of a bad set of initial weights. Again, only the best performing network among the two is further evaluated after the training. All different structures are trained according to the first phase as explained above (Sect. 4.5), i.e. using 25 % of the respective datasets. After this stage the accuracy of the different MLP structures is evaluated and compared using the internal validation datasets. This investigation was used to determine the MLP structures used for CiPS (see Sect. 4.5).

Figure 4.3a shows the difference in POD (Eq. 3.3) between each structure and the least complex structure, which has one hidden layer and 16 hidden neurons (denoted as 1–16) for the cirrus cloud detection ANN with respect to CALIOP for the seven different structures that were investigated. Similarly, Fig. 4.3b and c show the difference in MAPE (Eq. 3.6) between each structure and the least complex one for the CTH and IOT retrieval ANNs respectively. The MAPE behaviour of the IWP is very similar to the MAPE of the IOT and is therefore not presented here. For the OPF, the structure of the network does not seem to have any significant influence on the performance and is thus not presented here. For the cirrus detection and IOT retrieval, only the transparent cirrus clouds are considered.
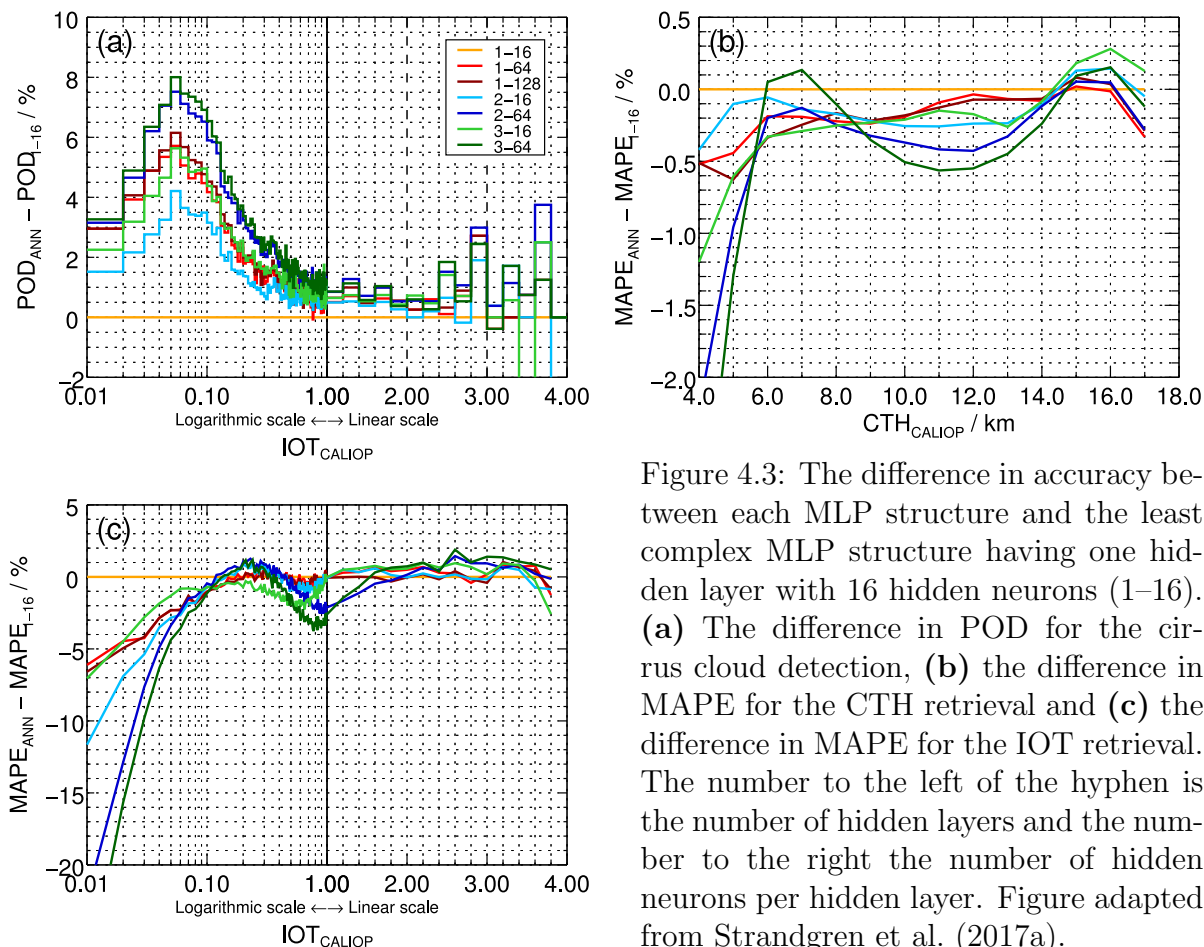
Figure 4.3: The difference in accuracy between each MLP structure and the least complex MLP structure having one hidden layer with 16 hidden neurons (1–16). **(a)** The difference in POD for the cirrus cloud detection, **(b)** the difference in MAPE for the CTH retrieval and **(c)** the difference in MAPE for the IOT retrieval. The number to the left of the hyphen is the number of hidden layers and the number to the right the number of hidden neurons per hidden layer. Figure adapted from Strandgren et al. (2017a).

Please note that for a better visualisation for the lower IOT values, the horizontal axes in Fig. 4.3a and c are divided into one logarithmic range ($IOT_{CALIOP} < 1.0$) and one linear range ($IOT_{CALIOP} \geq 1.0$). Furthermore, Table 4.2 lists the approximate amount of time required to process 1 million data points/pixels (including I/O) with the different structures using the above specified desktop PC.

In all cases, already small networks produce reasonable results. In many cases differences between structures are not very large. Nevertheless, it is also clear that larger ANNs

Table 4.2: Approximate time required to process 1 million data points using the different ANN structures investigated in this study. The number to the left of the hyphen is the number of hidden layers and the number to the right the number of hidden neurons per hidden layer. Table reproduced from Strandgren et al. (2017a).

Structure	1–16	2–16	3–16	1–64	1–128	2–64	3–64
Time / s	2.1	3.1	4.0	5.2	9.5	14.4	23.6

can always solve the problems in a more accurate way and especially for the cirrus cloud detection it is beneficial to either use more hidden neurons or add more hidden layers rather than using a simple structure with one hidden layer and 16 hidden neurons (1–16). Using two or three hidden layers with 64 hidden neurons each (2–64, 3–64) yields a POD that is up to 8 percentage points higher compared to one hidden layer with 16 hidden neurons (1–16). Similarly, a structure with three hidden layers and 16 hidden neurons (3–16) yields a POD that is up to 5.5 percentage points higher compared to the structure with one hidden layer and 16 hidden neurons (1–16). Although three hidden layers with 64 neurons each (3–64) offer the highest accuracy for all cases, such a complex structure processes the data significantly slower by a factor of 8 or 6 compared to the smaller structures with 2 or 3 hidden layers and 16 neurons per layer. For the IOT retrieval, a larger ANN is mostly beneficial for the thinner cirrus and the MAPE with respect to CALIOP seems to be saturated and hardly improvable for $IOT_{CALIOP} > 0.1$ using this approach and training data. For the sub-visual cirrus, the MAPE with respect to the CALIOP reference IOT is up to 13 percentage points lower using two hidden layers instead of one hidden layer with 16 hidden neurons each. For the CTH retrieval, only marginal improvements in the MAPE with respect to CALIOP (≈ 0.1–0.5 percentage points) are observed using the more complex structures in comparison to the least complex one (1–16). Only for the lowermost clouds ($CTH_{CALIOP} < 6.0\,km$) is the advantage of using more hidden layers and neurons more evident.

4.8   Applying CiPS to a real scene

In this section CiPS is applied to the MSG-3 SEVIRI scene acquired on 1 June 2015 12:30 UTC (same scene as in Fig. 3.2). Figure 4.4a shows a false colour RGB composite for the full SEVIRI disc using the three SEVIRI channels centred at 0.6, 0.8 and 10.8 µm. Remember, that with this channel combination the thick and thin cirrus clouds are identified as white and bluish, whereas the warmer liquid water clouds are recognised as yellow. As already described in Sect. 3.1, a band of cirrus clouds can be seen along the ITCZ. Furthermore several frontal (cirrus) clouds can be seen over Europe and the southern and northern Atlantic Ocean. In the tropics, large areas of shallow cumulus clouds can be seen over the Atlantic Ocean. Figure 4.5a shows a subset of the SEVIRI disc consisting of 350×350 pixels comprising western and central Europe. Two large cirrus clouds can be seen ranging from the south-western parts of France towards the Alps and southern parts of Scandinavia. Also over England and Norway, cirrus clouds are present and clearly visible in the RGB. Liquid water clouds are mainly present over the central parts of France, Switzerland and Germany as well as over the North Sea, Mediterranean Sea and southern parts of Scandinavia. For an enhanced view of thin cirrus clouds, Fig. 4.4b and 4.5b show the corresponding brightness temperatures difference between the SEVIRI channels centred at 8.7 µm and 10.8 µm. In those pictures, cirrus clouds are characterised by positive or slightly negative values.

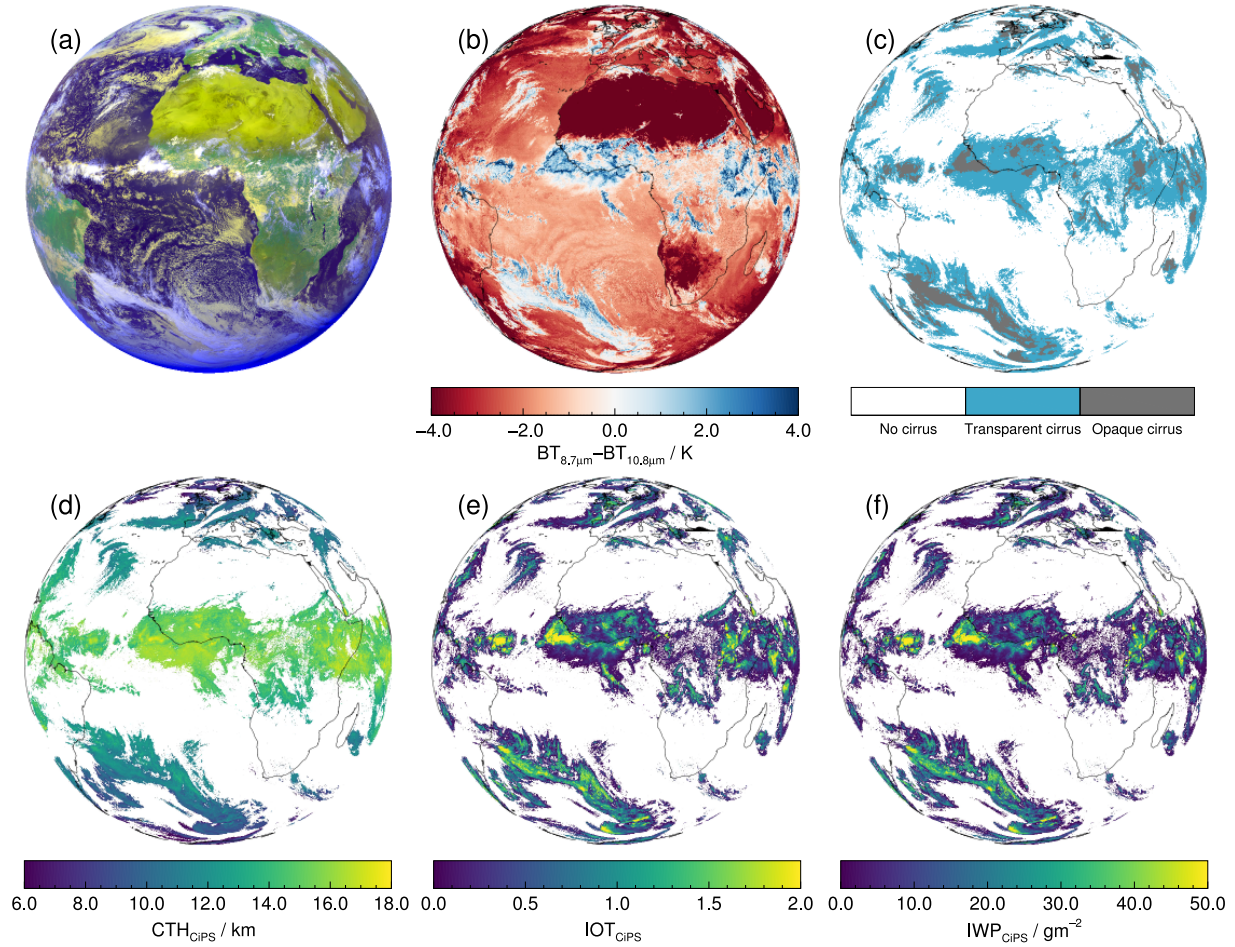Figure 4.4c and 4.5c show the cirrus cloud mask retrieved by CiPS for the same scenes.

Figure 4.4: **(a)** MSG-3/SEVIRI false colour RGB composite for the entire SEVIRI disc on 1 June 2015 at 12:30 UTC, the corresponding **(b)** brightness temperature difference $BT_{8.7\,\mu m} - BT_{10.8\,\mu m}$ and the **(c)** cirrus cloud mask with opacity information, **(d)** CTH, **(e)** IOT and **(f)** IWP retrieved by CiPS.

The blue and grey areas show all pixels that CiPS classifies as cirrus, of which the grey pixels are classified as opaque. This means that for the grey pixels the retrieved IOT and IWP is likely to be underestimated. Figure 4.4d-f and 4.5d-f show the corresponding CTH, IOT and IWP retrieved by CiPS.

CiPS clearly detects all cirrus clouds that can be identified in the false colour RGB composites (Fig. 4.4a and 4.5a) and from the brightness temperature differences (Fig. 4.4b and 4.5b). The OPF correlates well with the cirrus brightness in the RGB. The brightest parts of the cirrus clouds, which represent the thickest parts, are classified as opaque by CiPS. CiPS captures the latitude dependency of the CTH, with generally lower values at higher latitudes. Elevated heights for the thicker cirrus cloud areas are also observed. The cloud edges are generally seen to have lower altitudes, which could indicate ice crystal sedimentation or partial cloud cover inside the SEVIRI pixels. As expected, the IOT
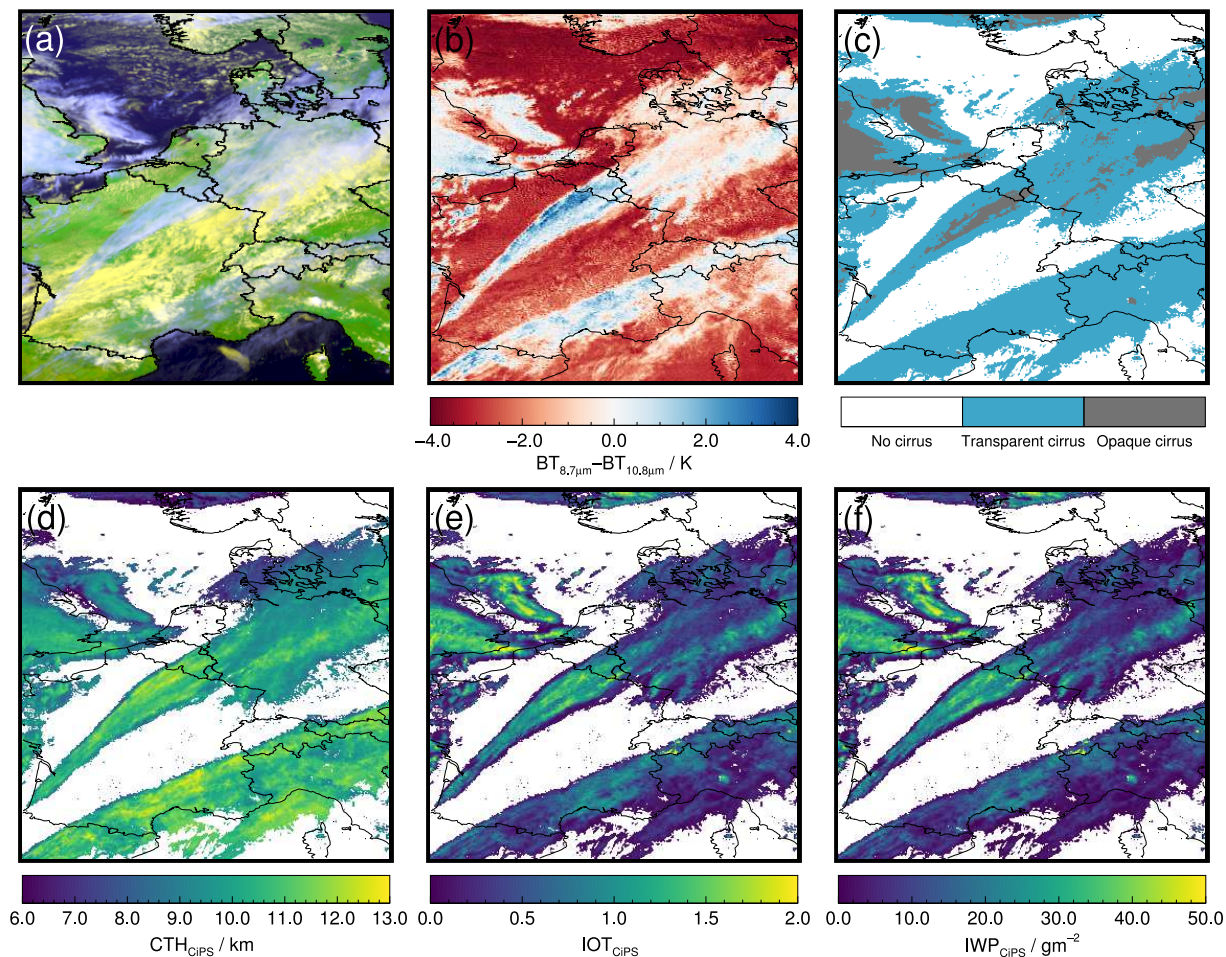
Figure 4.5: **(a)** MSG-3/SEVIRI false colour RGB composite over parts of Europe on 1 June 2015 at 12:30 UTC, the corresponding **(b)** brightness temperature difference $BT_{8.7\,\mu m} - BT_{10.8\,\mu m}$ and the **(c)** cirrus cloud mask with opacity information, **(d)** CTH, **(e)** IOT and **(f)** IWP retrieved by CiPS. Figure reproduced from Strandgren et al. (2017a).

and IWP are well correlated and qualitatively the values correspond well to the level of transparency of the different cirrus clouds seen in Fig. 4.4a and 4.5a. For a quantitative evaluation of the IOT and IWP as well as the other quantities, readers are referred to Sect. 4.9.

4.9 Validating CiPS against CALIOP

In this section the performance of CiPS is validated against V3 CALIOP products using the 10 % subset (≈ 4.9 million collocations) of the full collocation dataset excluded from the training of CiPS (Sect. 4.4.2). The results are presented for the full SEVIRI field of view. Since CiPS and COCS share the concept of using ANNs trained with primarily SEVIRI
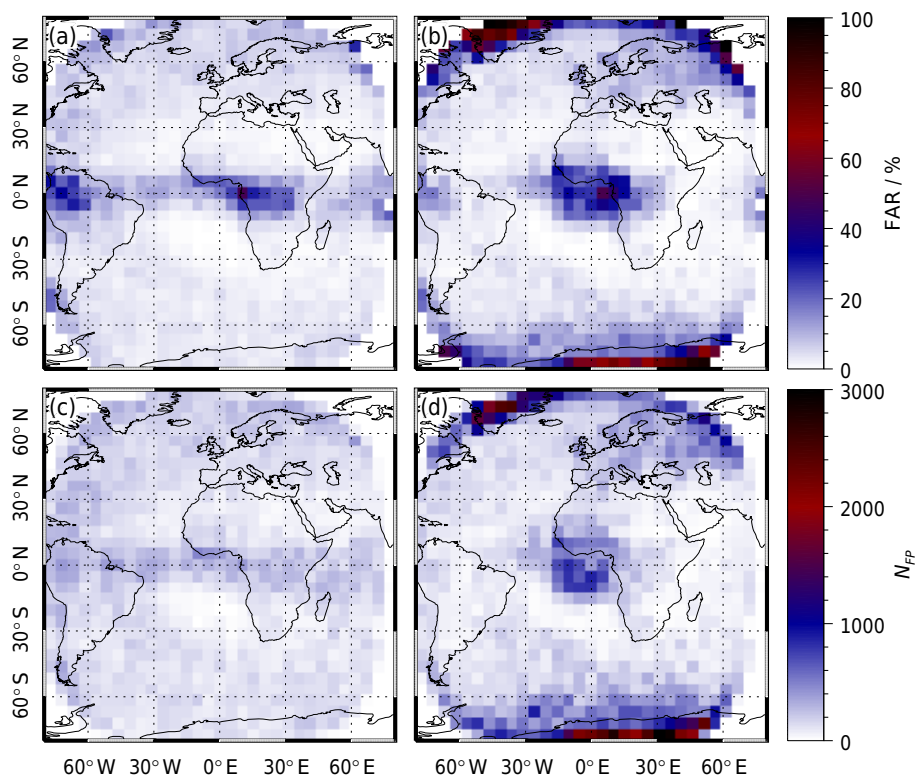
Figure 4.6: Top: the FAR of the CCF retrieved by **(a)** CiPS and **(b)** COCS. Bottom: the absolute number of false alarms by **(c)** CiPS and **(d)** COCS for the approx. 3.3 million cirrus-free points included in the final validation dataset. Figure reproduced from Strandgren et al. (2017a).

and CALIOP data, the corresponding validation results of COCS are also presented.

An in-depth characterisation of CiPS with respect to (1) the relative importance of the different input variables, (2) the effect of the underlying surface type as well as underlying liquid water clouds and aerosol layers on the cirrus cloud retrieval, (3) the retrieval errors as a function of IOT_{CALIOP} and CTH_{CALIOP} combined and (4) the sensitivity to radiometric noise in the SEVIRI input data is presented in Sect. 4.10.

4.9.1 Cirrus cloud classification

The CCF of CiPS and COCS and the OPF of CiPS are evaluated as a function of the geographic position. This aspect is interesting due to the very different meteorological conditions present on the SEVIRI disc. Figure 4.6a and b show the gridded FAR (Eq. 3.4) for the CCF of CiPS and COCS, respectively, over $5° \times 5°$ boxes, using the V3 CALIOP products as reference.

As mentioned in Sect. 4.6 the average FAR for the CiPS cirrus detection is 3.9 %. The FAR is sensitive to the frequency of the events, meaning that over regions where the

natural probability of cirrus presence is high, a single false alarm will have a larger impact on the total FAR than over regions where the natural probability of cirrus presence is low. Although the FAR of CiPS is relatively homogeneous across the SEVIRI disc, this effect can be observed with higher FARs along the ITCZ and lower FARs over the Sahara, for example.
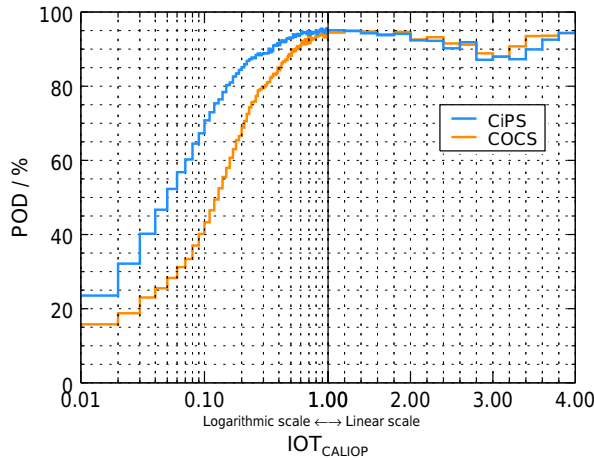

Figure 4.7: The POD of CiPS and COCS as a function of the IOT retrieved by CALIOP. Figure reproduced from Strandgren et al. (2017a).

COCS has an equally low FAR over arid regions but has a clearly higher FAR in general. In particular over icy surfaces like Greenland and Antarctica, COCS overestimates the cirrus presence, with FARs up to approx. 90 %. But for high latitudes in general, the FAR of COCS remains higher than CiPS. In the polar regions (latitude $\geq$ 65° N/S) the average FAR is 33 % for COCS and 5.3 % for CiPS. Also over Europe the FAR of CiPS is clearly lower. Furthermore, COCS strongly overestimates the cirrus presence around the sub-satellite point of SEVIRI. For VZAs smaller than 15°, COCS has an average FAR of 23 %. This deficiency is not shown by CiPS, which has an average FAR of 8.5 % for the same area.

Furthermore, a false alarm of COCS has $IOT_{COCS} \geq 0.1$, whereas a false alarm of CiPS can have an IOT_{CiPS} down to 0.0, i.e. $IOT_{CiPS} > 0.0$.

Due to the high probability of cirrus cloud presence along the ITCZ, the effect of the higher FAR of CiPS over this region is small, since a high cirrus probability prevents false alarms from occurring. Figure 4.6c and d show the total number of false alarms/positives N_{FP} by CiPS and COCS, respectively, i.e. the total number of cirrus-free points in the validation dataset (approx. 3.3 millions) that are falsely classified as cirrus. Again the numbers are calculated over 5° × 5° boxes. Even if the probability of having a false alarm by CiPS is higher than the average FAR along the ITCZ (Fig. 4.6a), the absolute number of false alarms is just as high as for most regions across the SEVIRI disc (Fig. 4.6c). Looking at N_{FP} by COCS (Fig. 4.6d), more false alarms are observed at high latitudes (especially over icy surfaces), over Europe and around the sub-satellite point.

The FAR can easily be optimised by reducing the number of detected cirrus clouds (see Fig. 4.2). Thus it is necessary to simultaneously look at the performance in cirrus detection alongside the false alarm analysis. A reduced POD would be a natural effect if the FAR is reduced, but despite the low FAR of CiPS the POD remains high. Figure 4.7 shows the POD of CiPS, again in comparison to COCS. The POD is a function of IOT_{CALIOP} and within each IOT_{CALIOP} interval the POD given by Eq. (3.3) is calculated, using the V3 CALIOP products as reference. For a better visualisation the POD is presented with a logarithmic scale for $IOT_{CALIOP} < 1.0$ and with a linear scale for $IOT_{CALIOP} \geq 1.0$. For cirrus clouds with $IOT_{CALIOP} > 1.0$, CiPS and COCS perform similarly. A strong difference

is instead seen for the thin cirrus clouds, where CiPS detects more cirrus clouds compared to COCS. For example at $IOT_{CALIOP} = 0.1$, CiPS detects 71 % of the cirrus clouds and COCS 43 %. A higher POD for thin cirrus clouds is an important improvement when studying contrail cirrus or the cirrus life cycle for example. Figure 4.7 only presents the results for the transparent cirrus clouds where the CALIOP laser was not saturated. For the opaque cirrus clouds the average POD is 98 % for both CiPS and COCS. The geographical dependency of POD is clearly anti-correlated with the geographical dependency of the FAR, meaning that CiPS has its highest and lowest POD over regions where the natural probability of cirrus presence is high and low respectively. Apart from that, the POD of CiPS is homogeneous across the SEVIRI disc.

Figure 4.8 shows the FAR of the CiPS OPF, again over $5° \times 5°$ boxes, using the V3 CALIOP products as reference. Since the OPF is a new variable introduced with CiPS, the results cannot be compared to COCS. As mentioned in Sect. 4.6 the average POD and FAR is 71 and 4.0 % respectively. Both quantities are relatively homogeneous across the SEVIRI disc, but the risk of falsely classifying a transparent cirrus cloud as opaque is slightly lower in the tropical regions (latitude < 30° N/S).
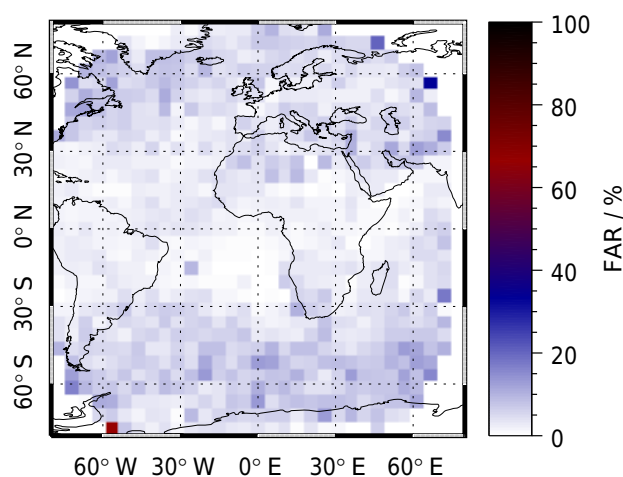
Figure 4.8: FAR of the CiPS OPF (opacity flag). Figure reproduced from Strandgren et al. (2017a).

4.9.2 Cirrus cloud properties

Figure 4.9 shows two density scatter plots, with CTH_{CALIOP} on the horizontal axes and CTH_{CiPS} (Fig. 4.9a) and CTH_{COCS} (Fig. 4.9b) on the vertical axes. The colour shows the normalised relative frequency, which is the relative frequency normalised to the interval 0–1. Along with the scatter plots the MPE and MAPE (Eqs. 3.5 and 3.6) of CiPS and COCS with respect to CALIOP as a function of CTH_{CALIOP} are shown (Fig. 4.9c). CiPS and COCS are validated using their own respective cirrus flags, meaning that CTH_{CiPS} is validated using the cirrus-covered points that CiPS detects, whereas CTH_{COCS} is validated using those cirrus-covered points that COCS detects. Using a common cirrus flag (i.e. those cirrus-covered points that both CiPS and COCS detect) shows marginal differences, with slightly reduced errors for CiPS, as a result of the reduced amount of very thin cirrus that only CiPS detect, for which the CTH is more difficult to accurately estimate.

With CiPS the CTH is retrieved with a higher accuracy compared to COCS, especially for high and low cirrus clouds. The correlation between CALIOP and CiPS is 0.90. For CALIOP and COCS, the correlation is 0.82.

The MPE shows that CiPS overestimates and underestimates the CTH of the lowest and highest cirrus clouds, respectively, even if the errors are smaller than for COCS. From 8 to 15 km the MPE is close to zero, meaning that the CTH retrieval by CiPS is unbiased
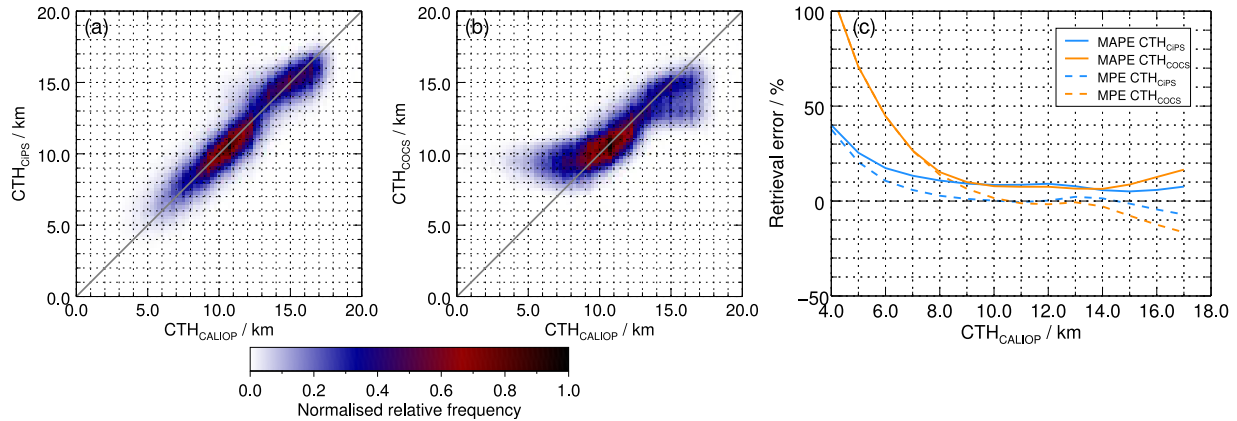
Figure 4.9: Density scatter plots with the CTH retrieved by **(a)** CiPS and **(b)** COCS on the vertical axes and the corresponding V3 CALIOP data on the horizontal axes. The grey lines represent the 1–1 line. **(c)** The MAPE (solid) and MPE (dash) of the CTH retrieved by CiPS and COCS with respect to the CTH measured by CALIOP. Figure reproduced from Strandgren et al. (2017a).

in this CTH_{CALIOP} range. The MAPE shows that the average magnitude of the CiPS error is 10 % or less for cirrus clouds having a CTH above 8 km. Furthermore, the MAPE clearly shows the better accuracy of CiPS. For example, for cirrus clouds with a CTH_{CALIOP} between 4 and 5 km, representing mid-level clouds with icy tops, the MAPE is 38 % for CiPS. For COCS the corresponding number is 107 % with solely overestimated values (MAPE = MPE). This is mainly an effect of the CTH filtering used for COCS (Sect. 3.4.3), which excluded cirrus clouds with a $CTH_{CALIOP} < 4.5$ km from the training dataset, leading to strong overestimations of lower values. Furthermore, this type of low cirrus/icy clouds are found in the polar regions (see Fig. 4.10b), where the retrieval conditions for SEVIRI are more challenging with larger VZAs and pixel sizes.

The CTH has a strong latitude dependency and the CiPS results shown in Fig. 4.9 are not representative for all latitudes. Figure 4.10a shows the MPE of the CTH_{CiPS} retrievals with respect to CALIOP as a function of CTH_{CALIOP} and the latitude. Figure 4.10b shows the corresponding occurrences of the points that make up the statistics shown in Fig. 4.10a. Please remember that the validation dataset is a random subset of CALIOP data collected over a time period of almost 6 years and hence represents the natural latitudinal distribution of CTHs.

The MPE shows a clear latitude dependency and in contrast to Fig. 4.9c, where CiPS is shown to have no bias (MPE ≈ 0) between 8 and 15 km, it can be seen that the CTH_{CALIOP} limit when CiPS starts to over- and underestimate the CTH increases towards the Equator. At higher latitudes (e.g. over Europe), it is clear that CiPS is more likely to underestimate the CTH also for lower CTH_{CALIOP} around 11–14 km, with an increasing bias towards higher latitudes. Similarly the CTH_{CiPS} for cirrus clouds with $CTH_{CALIOP} < 13$ km is more likely to be overestimated along the ITCZ, with increasing errors towards the Equator. From Fig. 4.10b it is clear that the situations with higher errors and stronger biases
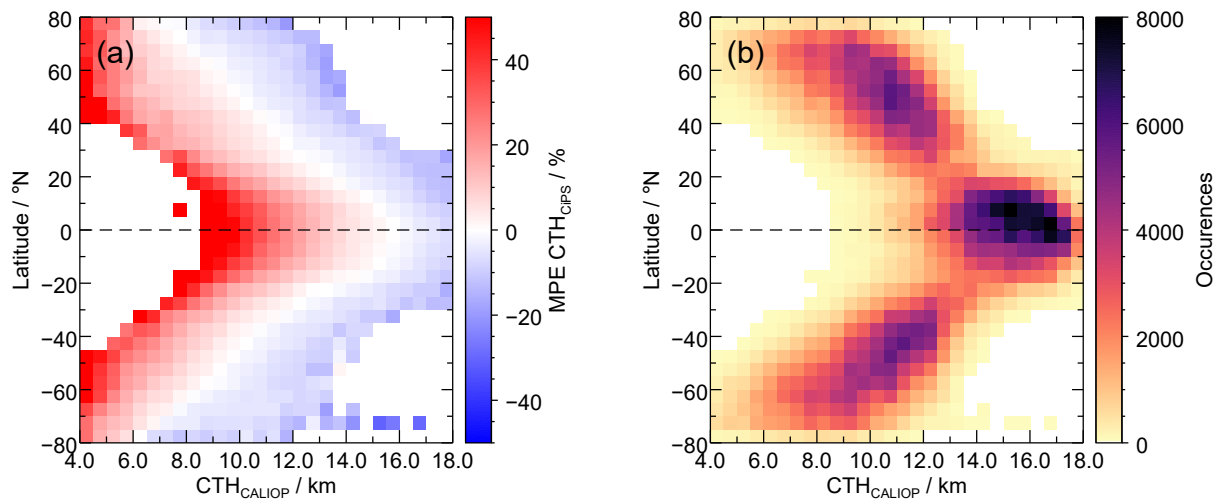
Figure 4.10: **(a)** Two-dimensional histogram showing the MPE of the CTH$_{\text{CiPS}}$ retrieval as a function of the reference CTH retrieval by CALIOP and the latitude. **(b)** The corresponding occurrences of the points that make up the statistics shown in **(a)**. Figure adapted from Strandgren et al. (2017a).

(|MPE| $\gtrsim$ 20 %) are comparably rare and that CTH$_{\text{CiPS}}$ is unbiased for the more frequent combinations of CTH$_{\text{CALIOP}}$ and latitude.

Note the difference between the CiPS CTH retrieval and standard ones (e.g. Menzel et al., 2008), where the determination of CTH requires the knowledge of the appropriate vertical temperature profile from NWP (numerical weather prediction) models, while CiPS only requires the surface skin temperature from a NWP along with the SEVIRI brightness temperatures and auxiliary data.

Figure 4.11 shows again two density scatter plots, now with IOT$_{\text{CALIOP}}$ on the horizontal axes and IOT$_{\text{CiPS}}$ (Fig. 4.11a) and IOT$_{\text{COCS}}$ (Fig. 4.11b) on the vertical axes. As before the colour shows the normalised relative frequency. Only transparent cirrus clouds, where CALIOP was not saturated, are included here. The two algorithms are validated using their respective cirrus cloud flags (as explained above for the CTH). This is not 100 % true for the IOT$_{\text{COCS}}$ scatter plot, however, where all points with a retrieved IOT$_{\text{COCS}}$ > 0.0 are included. Instead the black grid on top of the scatter plot illustrates the area where COCS does not detect any cirrus clouds as a result of the COCS cirrus detection threshold at IOT$_{\text{COCS}}$ = 0.1 (Sect. 3.4.3). A relatively large scatter is observed for both algorithms. CiPS shows a better correlation with the CALIOP retrievals though. The correlation between CiPS and CALIOP is 0.65, whereas the correlation between COCS and CALIOP is 0.61. Furthermore, CiPS shows higher frequencies along the 1–1 line down to IOT$_{\text{CALIOP}} \approx 0.09$, but also below this value the correlation between CALIOP and CiPS is evident. Only below IOT$_{\text{CALIOP}}$ = 0.04 does the correlation get lost.

For a better visualisation of the lower IOT range, where most points are located, the density scatter plots have logarithmic axes. This does, however, visually reduce the errors,
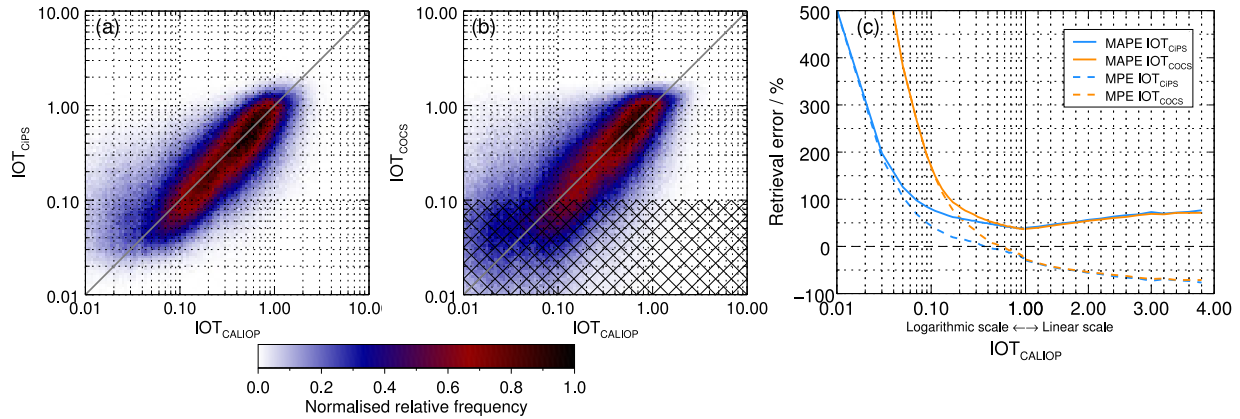
Figure 4.11: Density scatter plots with the IOT retrieved by **(a)** CiPS and **(b)** COCS on the vertical axes and the corresponding V3 CALIOP data on the horizontal axes. The grey lines represent the 1–1 line. **(c)** The MAPE (solid) and MPE (dash) of the IOT retrieved by CiPS and COCS with respect to the IOT retrieved by CALIOP. The black grid on top of the right scatter plot illustrates the area where COCS does not detect any cirrus clouds as a results of the COCS cirrus detection threshold at $IOT_{COCS} = 0.1$ (Sect. 3.4.3). Figure reproduced from Strandgren et al. (2017a).

so for a quantitative evaluation attention should be paid to Fig. 4.11c showing the MPE and MAPE of CiPS and COCS with respect to CALIOP. The MPE and MAPE are functions of IOT_{CALIOP} and again the results are presented using a logarithmic scale for $IOT_{CALIOP} < 1.0$ and a linear scale for $IOT_{CALIOP} \geq 1.0$. From the MAPE the low accuracy of CiPS for sub-visual cirrus clouds becomes evident. For $IOT_{CALIOP} < 0.03$, MAPE = MPE, meaning that CiPS entirely overestimates the IOT in this region. For COCS, the same is observed for $IOT_{CALIOP} < 0.1$ as a direct effect of the inability of COCS to detect cirrus clouds with an $IOT_{COCS} < 0.1$. The opposite is observed for thicker cirrus clouds ($IOT_{CALIOP} \gtrsim 2.0$), where both CiPS and COCS entirely underestimate the IOT (MAPE = $-$MPE). With CiPS the IOT can be retrieved with a MAPE of 50 % or less for cirrus clouds with $0.35 \lesssim IOT_{CALIOP} \lesssim 1.8$. Similarly the MAPE of the retrieved IOT_{CiPS} is 100 % or less for cirrus clouds with $IOT_{CALIOP} > 0.07$ and 230 % or less down to sub-visual cirrus clouds ($IOT_{CALIOP} > 0.03$). The corresponding MAPEs for the IOT retrieved by COCS within the same IOT_{CALIOP} intervals are 59, 290 and 720 %. A MAPE of 100 % might seem high, but one should keep in mind that this translates into small absolute errors for such thin cirrus clouds. For the lower IOT_{CALIOP} range, a similar scatter is observed between IOT_{CALIOP} and modelled IOT from infrared radiances for thin cirrus clouds in Holz et al. (2016).

Figure 4.12 shows a density scatter plot with IWP_{CALIOP} on the horizontal axis and IWP_{CiPS} on the vertical axis (Fig. 4.12a) together with the MPE and MAPE (Eqs. 3.5 and 3.6) of CiPS with respect to CALIOP as a function of IWP_{CALIOP} (Fig. 4.12b). Please note that again the density scatter plot has logarithmic axes and the retrieval errors are presented using logarithmic scale for the thinner cirrus clouds ($IWP_{CALIOP} < 10.0 \, \mathrm{g \, m^{-2}}$)
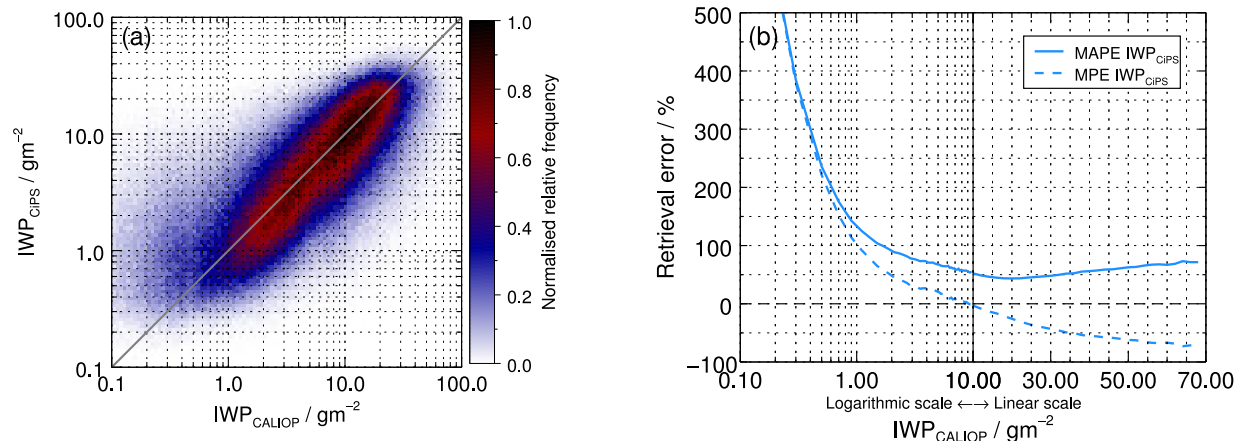
Figure 4.12: **(a)** Density scatter plot with the IWP retrieved by CiPS on the vertical axis and the corresponding V3 CALIOP data on the horizontal axis. The grey line represents the 1–1 line. **(b)** The MAPE (solid) and MPE (dash) of the IWP retrieved by CiPS with respect to the IWP retrieved by CALIOP. Figure reproduced from Strandgren et al. (2017a).

and with linear scale for the thicker ones ($\text{IWP}_{\text{CALIOP}} \geq 10.0\,\text{g}\,\text{m}^{-2}$). Since the IWP is not retrieved by COCS, no additional results are shown here for comparison. Again only transparent cirrus clouds are included.

The scatter between IWP_{CiPS} and $\text{IWP}_{\text{CALIOP}}$ is very similar to that between IOT_{CiPS} and $\text{IOT}_{\text{CALIOP}}$. This is not surprising since the IWC from CALIOP is retrieved from the measured extinction coefficients using a parameterisation. The correlation between CiPS and CALIOP is, however, slightly lower for the IWP retrieval (0.59) compared to the IOT retrieval. This is also expected since possible deficiencies in the CALIOP IWC parameterisation will make it more difficult for the ANN to learn the relationship between the input data and the IWP. Nevertheless, these results show that the ANN is capable of reproducing this relationship in a good way. With CiPS the IWP can be retrieved with a MAPE of $100\,\%$ or less for cirrus clouds with $\text{IWP}_{\text{CALIOP}} > 1.7\,\text{g}\,\text{m}^{-2}$ and $200\,\%$ or less down to $\text{IWP}_{\text{CALIOP}} \approx 0.7\,\text{g}\,\text{m}^{-2}$. Please note that deviations of $100\,\%$ are common even when microwave information is considered (e.g. Holl et al., 2014, even if their error measure is different).

In contrast to the CTH_{CiPS} retrieval, CiPS shows a stable performance for the IOT and IWP retrievals across all latitudes (not shown here). The only anomaly observed is that the CiPS retrieval errors for thin to sub-visual cirrus are lower over convergence zones like the ITCZ, where they are mostly found (Sassen et al., 2009; Martins et al., 2011).

As expected and as seen in Figs. 4.9, 4.11 and 4.12, CiPS is not able to perfectly model the CALIOP cirrus properties using the SEVIRI, ECMWF and auxiliary data. There are several sources of error that add to the final performance of CiPS. Most importantly CALIOP and SEVIRI have different sensitivities to cirrus clouds. This is especially clear for thin to sub-visual cirrus clouds where CALIOP is able to accurately retrieve the top

height and optical properties. Such faint cirrus leave a considerably weaker or no mark on the SEVIRI observations though, making it difficult to inversely determine the cirrus properties. Similarly the CTH is not necessarily defined equally by CALIOP and SEVIRI, as CALIOP is able to discern thinner icy layers at the cloud top that may appear as "invisible" to SEVIRI. Also for thicker cirrus clouds where both CALIOP and SEVIRI (thermal observations) approach the point of saturation, the different sensitivities lead to ambiguous collocations. When an ANN is trained with a set of different output values that correspond to approximately the same input data as a result of the lower sensitivity, the ANN will not be able to model an accurate relationship. The reason for this is that the input vector contains no information on how the difference in sensitivity affects the target values. This can be regarded as an unknown hidden variable. This weakness is not specific to ANNs but applies to all regression models minimising the squared error. When such a set of incomplete input data (in the sense that there is a strong hidden variable) is given to the final ANN, it will output a conservative mean value that can be understood as an average over the distribution of the most likely solutions weighted by their probability. The larger the difference in sensitivity is, the higher the variance within the distribution of the most likely solutions will be, leading to larger retrieval errors. Throughout most of the output data range this error will be random. But, obviously, the distribution of the most likely solutions cannot be centred around the extreme values leading to systematic over- and underestimations of low and high output values when a conservative mean value is calculated. This effect increases towards the extreme values as the desired output value is skewed towards the edge of the distribution of the most likely solutions. This effect is clearly seen in Figs. 4.11c and 4.12c where low and high $IOT_{CALIOP}/IWP_{CALIOP}$ are over- and underestimated respectively. This is to some extent also seen for the CTH_{CiPS} retrieval in Fig. 4.9c, especially for low CTH_{CALIOP}. Due to the randomness of the effects a lower sensitivity introduces, adding information about the magnitude of the sensitivity to the input vector is not likely to improve this situation. The larger CTH_{CiPS} retrieval errors observed for low clouds can also be attributed to the smaller temperature contrast with respect to the surface temperature and thus the weaker radiative signal that those clouds have compared to higher cirrus clouds. Another source of error that amplifies the effect discussed above is the risk that there are additional variables relevant for finding an accurate relationship that are not represented by the vector of input data.

As discussed in Sect. 4.4.1, imperfect collocations as a result of the different spatial scales of CALIOP and SEVIRI together with partial cloud cover or spatially inhomogeneous clouds will further add to the retrieval errors. In a situation where CALIOP observed a small optically thin area of an otherwise optically thick cirrus inside a SEVIRI pixel, CiPS is likely to overestimate IOT_{CALIOP} and IWP_{CALIOP}. Similarly if CALIOP observed a small optically thick area of an otherwise optically thin cirrus inside a SEVIRI pixel, CiPS is likely to underestimate IOT_{CALIOP} and IWP_{CALIOP}.

Improvements with respects to COCS can be attributed to several factors. (1) New input data including the modelled surface skin temperature and the regional maximum and average brightness temperatures. (2) The training meta-parameters and ANN structures have been thoroughly investigated and optimised for CiPS. (3) The training of CiPS was

more rigorous, with mini-batch learning rather than stochastic learning as well as a tuning phase with gradually increasing batch size and gradually decreasing learning rate and momentum. Furthermore an internal validation dataset was used during the training of CiPS in order to monitor the accuracy and avoid overfitting. (4) The use of the more accurate V3 CALIOP data as training reference. (5) The use of multiple ANNs. COCS uses one single ANN trained with cirrus-covered as well as cirrus-free pixels. On the contrary, the CiPS ANNs that retrieve the CTH, IOT, IWP and OPF were trained exclusively with cirrus-covered pixels, resulting in lower retrieval errors of CiPS. The larger retrieval errors of COCS for thin cirrus clouds also affect the IOT dependent cirrus cloud detection of COCS, with both a lower POD and a higher FAR compared to CiPS.

4.10 Characterising CiPS

Although ANNs are a powerful alternative to physically based cloud retrievals (e.g. Platnick et al., 2003; Bugliaro et al., 2011; Minnis et al., 2011; Stengel et al., 2014; Heidinger et al., 2015; Wang et al., 2016; Iwabuchi et al., 2016), they are trained to learn patterns and model relationships, and physical principles are not imposed for the scenes being investigated. Consequently, ANNs will in general perform better for retrieval scenes that occur more frequently in the training dataset as those scenes will have a stronger weight during the training. This, together with the fact that ANNs provide no direct uncertainty estimates, highlights the importance of properly characterising the ANN retrievals. In Sect. 4.9 the CiPS retrieval accuracy for cirrus detection, opacity classification and derivation of the physical and optical properties CTH, IOT and IWP with respect to CALIOP was presented. In this section, a more differentiated investigation is performed that aims at characterising the ANNs according to various aspects. First, despite the fact that CiPS input quantities have been selected according to physical principles (see Sect. 4.2), it is unclear which importance the single input variables have been assigned by the ANNs. This a posteriori examination also gives hints about the ability of the ANNs to model physical relationships among the variables. Second, the combination of cirrus products from visible backscattered vertically resolved "monochromatic" lidar radiation (CALIOP) and thermal "columnar" narrowband brightness temperatures from imager channels (SEVIRI) is supported by the knowledge that cirrus clouds leave their mark on both measurements types in a "similar" way: for instance, both methods are sensitive to visible IOT up to ca. 5 (e.g. DeSlover et al., 1999). Nevertheless, CALIOP's ability of discerning vertical features (ice clouds, liquid water clouds, aerosols) is not shared by SEVIRI, which poses the question whether the proposed CALIOP–SEVIRI synergy is always meaningful. To clarify this aspect, the CiPS performance is investigated for various vertical arrangements of cloud and aerosol layers and for various surface types. Furthermore, cirrus clouds are classified according to their IOT and CTH to provide a better understanding of the CiPS retrieval errors (magnitude and bias). Finally, the sensitivity to radiometric noise in the SEVIRI data is quantified.

4.10.1   Relative importance of the CiPS input data

To understand, improve and extend CiPS and similar ANN-based retrieval algorithms, it is valuable to understand what input data have essential contributions to the solution of a given problem. Important input variables are identified by the ANN and given a strong weight during the training. Similarly, less important input variables are given a weaker weight and thus a smaller role in retrieving the output data.

The importance of an input variable can be estimated as the euclidean length of the vector holding all weights that connect that input neuron with the hidden neurons in the first hidden layer (LeCun et al., 1990). The importance (or total weight) of an input variable i is thus calculated as $W_i = \sqrt{w_{i,1}^2 + w_{i,2}^2 + \cdots + w_{i,N}^2}$, where $w_{i,1}$ to $w_{i,N}$ are the single weights connecting input variable i with the N neurons in the first hidden layer. Figure 4.13 shows the relative importance of the 18 input variables used by CiPS. The relative importance of all input variables is calculated as $W_i^* = 100\,\% \times W_i/(W_1 + W_2 + \ldots + W_{18})$ for the respective ANNs such that the sum of the relative importance across all input variables adds up to $100\,\%$ for each ANN. The four columns represent the four ANNs.

Relative input variable importance / %

	CCF$_{\text{CiPS}}$	OPC$_{\text{CiPS}}$	CTH$_{\text{CiPS}}$	IOT$_{\text{CiPS}}$ / IWP$_{\text{CiPS}}$
BT$_{6.2\mu m}$	3.0	4.4	8.4	5.1
BT$_{7.3\mu m}$	7.5	11.2	11.5	10.7
BT$_{8.7\mu m}$	10.1	18.6	6.0	11.7
BT$_{10.8\mu m}$	13.5	14.7	3.3	12.7
BT$_{12.0\mu m}$	18.0	9.0	9.7	15.0
BT$_{13.4\mu m}$	4.3	7.4	6.8	5.3
BT$_{6.2\mu m}^{regavg}$	3.6	3.4	-	-
BT$_{7.3\mu m}^{regavg}$	7.6	4.6	-	-
BT$_{8.7\mu m}^{regmax}$	4.1	4.2	4.4	6.1
BT$_{10.8\mu m}^{regmax}$	6.3	6.2	4.1	4.4
BT$_{12.0\mu m}^{regmax}$	7.8	5.7	5.5	7.9
T_{surf}	2.0	2.2	5.3	5.4
Latitude	4.4	1.4	18.1	4.9
VZA	2.6	3.0	6.6	4.7
Water flag	0.4	1.7	1.7	1.1
Snow/ice flag	4.0	1.6	2.3	3.5
DOY$_{\text{SIN}}$	0.2	0.5	1.9	0.4
DOY$_{\text{COS}}$	0.6	0.4	4.5	1.0

Figure 4.13: Relative importance of the CiPS input variables (vertical axis) for the four ANNs (horizontal axis). The blue shades further highlight the magnitude of the relative importance with fading colours for decreasing importance. Figure reproduced from Strandgren et al. (2017b).

No relative importance of the regional average brightness temperatures is reported for the CTH$_{\text{CiPS}}$, IOT$_{\text{CiPS}}$ and IWP$_{\text{CiPS}}$ retrievals since those are used exclusively for the cirrus detection and opacity classification (see Sect. 4.2).

It is clear that the window channels of SEVIRI are essential for the detection and opacity classification of cirrus clouds as well as for the determination of IOT$_{\text{CiPS}}$ and IWP$_{\text{CiPS}}$. This reflects the importance of these channels in physically based retrievals (e.g. Ewald et al., 2013; Heidinger et al., 2015; Iwabuchi et al., 2016). For the CTH$_{\text{CiPS}}$ retrieval, the latitude is the dominant input variable, followed by the water vapour channels. Similarly the DOY has a comparably strong importance for the CTH$_{\text{CiPS}}$ retrieval. The relative importance of BT$_{13.4\,\mu m}$ is surprisingly low for the CTH$_{\text{CiPS}}$ retrieval, although observations from around 13.4 μm are commonly used by the CO$_2$-slicing method for CTH retrievals (e.g. Menzel et al., 2008). This is a hint that the ANN may model a statistical, rather than physical,

relationship between the input and output variables, as the CTH has an annual cycle and a clear latitude dependency (Stubenrauch et al., 2013). It might also be that the 13.4 μm brightness temperature only provides redundant information with respect to CTH since also water vapour channels and surface skin temperatures are available to the ANN (see discussion about the physical motivation of the input variables in Sect. 4.2). For the CCF_{CiPS}, OPF_{CiPS}, IOT_{CiPS} and IWP_{CiPS} retrievals, the DOY has a very low importance and consequently a minor contribution to the retrievals. The surface temperature from the model is clearly helpful for determining the CTH_{CiPS}, IOT_{CiPS} and IWP_{CiPS}. The information about whether the Earth's surface is covered by permanent ice or snow is valuable for the cirrus detection as well as the IOT_{CiPS} and IWP_{CiPS} retrievals, whereas the surface water flag has a comparably small contribution to the retrievals. Exploiting the information from nearby SEVIRI pixels using the regional maximum and regional average temperatures is clearly helpful in all aspects; their relative importance is comparable to the relative importance of T_{surf} for the CTH_{CiPS}, IOT_{CiPS} and IWP_{CiPS} retrievals, for example.

4.10.2 The CiPS retrieval accuracy for different surface types

In this section the performance of CiPS is characterised with respect to a set of five land surface type classes extracted from MODIS level 3 (L3) data. For this section as well as for Sects. 4.10.3 and 4.10.4 the performance of CiPS is always evaluated with respect to the cirrus cloud retrievals by CALIOP using the final validation dataset (see Sect. 4.4.2) used to validate CiPS in Sect. 4.9.

4.10.2.1 Surface type classes from MODIS

The International Geosphere-Biosphere Programme (IGBP; Loveland and Belward, 1997) has defined 17 land surface types including 11 natural vegetation classes, 3 developed and mosaicked land classes and 3 non-vegetated land classes. The MODIS L3 product MCD12C1 (Friedl et al., 2010) provides the majority land cover type at a resolution of 0.05° according to the IGBP classification. The MCD12C1 V051 dataset for 2012 has first been reprojected to the SEVIRI grid using the nearest neighbour method. Then, for characterising CiPS with respect to the underlying surface type, the different surface type classes have been grouped into the five following classes: (1) *water* including ocean, lakes, rivers and wetlands; (2) *barren* including surfaces covered by soil, sand and rocks with a maximum vegetation of 10 %; (3) *permanent ice and snow* including surfaces permanently covered by ice and/or snow; (4) *forest* including all surfaces dominated by trees (canopy cover > 60 %); and (5) *vegetation excluding forest* including all surfaces with other types of vegetation i.e. shrublands, savannahs, grasslands and croplands. Detailed information about the IGBP surface types can be found in Loveland and Belward (1997).

These surface types are expected to have different spectral properties and humidity contents that might affect the thermal SEVIRI channels (Sect. 3.1) and therefore the CiPS ANNs. The geographical coverage of the five surface type classes used in this study is visualised in Fig. 4.14. Please note that the barren class is composed mostly of bright

desert surfaces on the SEVIRI disc. Hence the results presented for barren in this section are mostly representative for retrievals over desert and only to a very limited extent for retrievals over other types of barren present in e.g. the Andes and Iceland. Permanent ice and snow is only found in Greenland, Antarctica, and to a limited extent in high mountain ranges.

4.10.2.2 Cirrus cloud detection

The CCF_{CiPS} is evaluated as a function of the underlying surface type using the POD (Eq. 3.3) and the FAR (Eq. 3.4). To avoid the presence of (liquid water cloud/aerosol) layers between cirrus and surface that would shield radiation emitted by the surface, the CALIOP L2 data are used to identify and include only those profiles with clear air (at most a faint aerosol layer with aerosol optical thickness (AOT) ≤ 0.2) below a possible transparent cirrus cloud in the analysis (see class C1 (for POD) and class C7 (for FAR) in Sect. 4.10.3.1 and Fig. 4.17). In total approx. 600 000 such collocations are available in the extended final validation dataset, with the largest number of occurrences over water (360 000) and the smallest number over barren (36 000). The goal of the OPF retrieved by CiPS is to detect cirrus clouds that are opaque, i.e. where the vertical structure below the cirrus is unknown for CiPS/CALIOP. Consequently, the OPF of
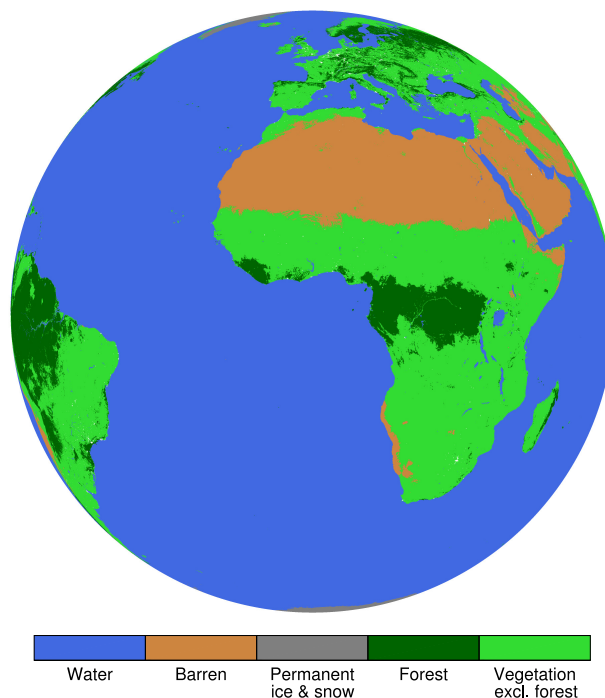

Figure 4.14: Visualisation of the geographical coverage of the five surface type classes across the SEVIRI disc. Figure reproduced from Strandgren et al. (2017b).

CiPS is not characterised for the different surface types as it cannot be ruled out that there are no liquid water clouds or aerosol layers with AOT > 0.2 below an opaque cirrus. Please note that the more accurate OPF of CALIOP is used to identify profiles with opaque cirrus clouds that are excluded from the analysis as explained in Sect. 4.10.3.1. Also remember that the terms "transparent" and "opaque" in this context are solely related to the saturation of the CALIOP laser beam and tell whether it was able to fully penetrate the cirrus cloud (transparent cirrus) or not (opaque cirrus).

Figure 4.15 shows the POD of CiPS for the five surface type classes as a function of IOT_{CALIOP}. For a better visualisation of thin cirrus, the scale is again logarithmic for $IOT_{CALIOP} < 1.0$ and linear for $IOT_{CALIOP} \geq 1.0$. As a reference, the average POD for all surface types is included (black line). A lower limit of 10 samples is required for the statistics, so no POD over barren is available for thicker cirrus clouds ($IOT_{CALIOP} \gtrsim 3.0$).

The same is done for the remainder of this section.

CiPS has a clearly lower POD over barren and permanent ice and snow for cirrus clouds with $IOT_{CALIOP} \lesssim 0.5$: up to 20% less cirrus clouds are detected than on average. Both are known to be difficult (cirrus) cloud retrieval conditions (Frey et al., 2008; Holz et al., 2008). Over ice and snow the radiative contrast between the cirrus and the cold surface is reduced, making the cirrus cloud detection more difficult. Furthermore, mixed-phase clouds or supercooled liquid water layers above ice layers in the polar regions (Mioche et al., 2015; Verlinde et al., 2007; Shupe et al., 2006) may also reduce the POD as CiPS requires the water to be frozen to be classified as a cirrus. Moreover, temperature inversions, frequent in these areas (Wetzel and Brümmer, 2011), can make the cloud top of low ice clouds (Devasthale et al., 2011) appear warmer than the snow/ice-covered surface and thus
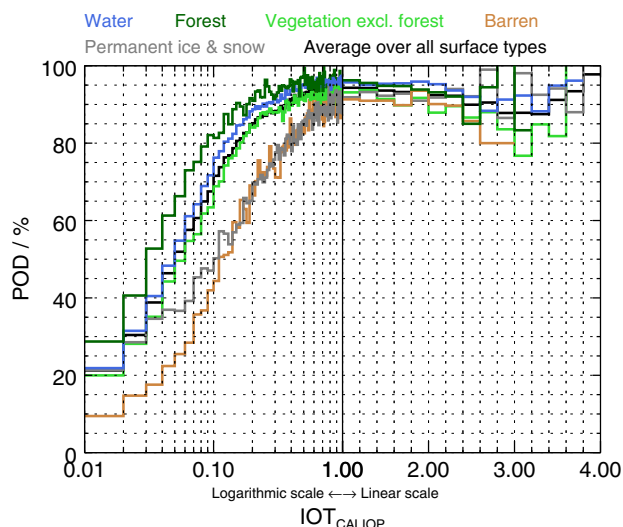

Figure 4.15: The cirrus POD of CiPS as a function of the IOT retrieved by CALIOP for the five surface type classes. Note that the line colours correspond to the colours used in Fig. 4.14. Figure reproduced from Strandgren et al. (2017b).

reduce their detection (Wilson et al., 1993; Gao et al., 1998). Furthermore, the retrieval conditions over Greenland and Antarctica are the least favourable ones for SEVIRI, with the largest VZAs and pixel sizes. The FAR over permanent ice and snow is 4.3%, which is higher than the average FAR of 3.2% over all surface types. Barren is to a large extent made up by deserts, where cirrus clouds rarely form, yet they can be found there when they drift towards mid-latitudes after formation in the ITCZ. The ANN is likely to learn such a pattern of low occurrence frequency and thus miss more thin cirrus in those regions. This is supported by the fact that the FAR is lowest over barren, where only 1.1% of the cirrus-free cases are falsely classified as cirrus. The highest POD is observed over forest: up to 15% more than on average for IOT_{CALIOP} up to 0.5. This is due to the high cirrus cloud occurrence over the tropical rainforests that increases the POD in a similar manner as the POD is reduced over barren. Again this is supported by the highest FAR of 7.1% over forest. Similar trends could be seen in Fig. 4.6, with the minimum FAR over the Sahara and the maximum FAR above the African and South American rainforests. Water and other vegetation (vegetation excluding forest) have similar POD, but the cirrus detection is slightly better over homogeneous water surfaces than over vegetation excluding forest. The corresponding FARs are 3.1% over water and 3.5% over vegetation excluding forest. Notice finally that due to their large number over the SEVIRI disc the water pixels dominate the average curve.
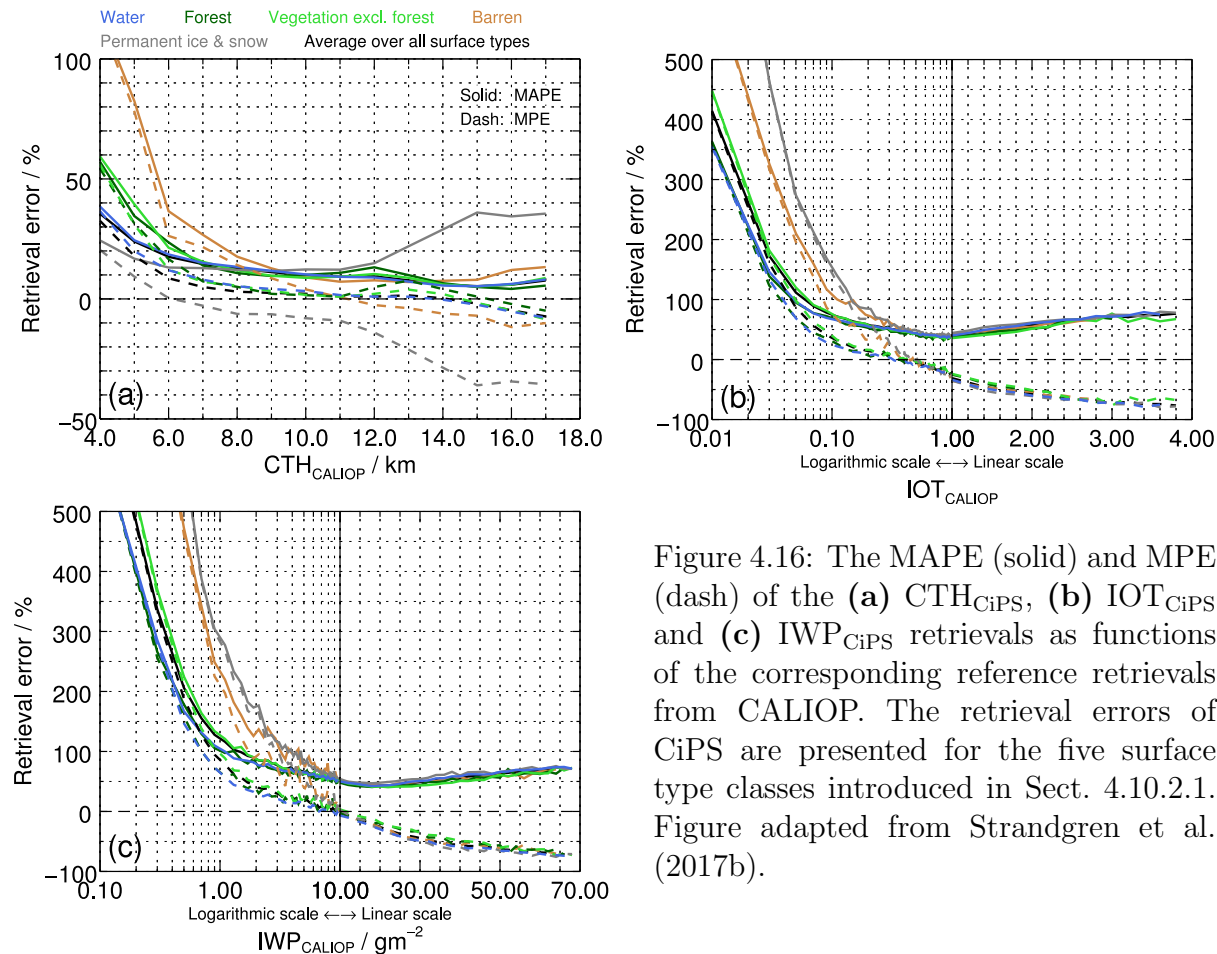
Figure 4.16: The MAPE (solid) and MPE (dash) of the **(a)** CTH_{CiPS}, **(b)** IOT_{CiPS} and **(c)** IWP_{CiPS} retrievals as functions of the corresponding reference retrievals from CALIOP. The retrieval errors of CiPS are presented for the five surface type classes introduced in Sect. 4.10.2.1. Figure adapted from Strandgren et al. (2017b).

4.10.2.3 Cirrus cloud properties

Figure 4.16 shows the MAPE and MPE for the (a) CTH_{CiPS}, (b) IOT_{CiPS} and (c) IWP_{CiPS} retrievals as functions of the corresponding reference retrievals by CALIOP and the five surface type classes. Within each CTH_{CALIOP}, IOT_{CALIOP} and IWP_{CALIOP} interval in Fig. 4.16, the MAPE and MPE given by Eq. (3.6) and (3.5) is calculated. Please note that again the results are presented with a logarithmic scale for $IOT_{CALIOP} < 1.0$ and $IWP_{CALIOP} < 10.0 \, \mathrm{g \, m^{-2}}$ and with a linear scale for $IOT_{CALIOP} \geq 1.0$ and $IWP_{CALIOP} \geq 10.0 \, \mathrm{g \, m^{-2}}$. The average MAPE and MPE (bias) over all surface type classes are included as reference. Again, only those profiles with clear air (no liquid water clouds and AOT ≤ 0.2) below the cirrus cloud are considered.

Mostly the same patterns of the MAPE and MPE are observed as in Sect. 4.9.2, namely that CiPS tends to overestimate the CTH for low cirrus/ice clouds and slightly underestimate the CTH for high cirrus. Similarly the IOT and IWP is predominantly over- and underestimated for the lower and upper extreme values respectively.

Overall, the CTH_{CiPS} retrieval is mostly insensitive to the underlying surface type for

$CTH_{CALIOP} > 8.0$ km. A stronger underestimation of CTH_{CALIOP} (20–40 %) is, however, observed over permanent ice and snow for high cirrus clouds ($CTH_{CALIOP} > 12$ km). Those are cirrus/ice clouds that extend into the stratosphere. A stronger tendency for underestimations is observed also for lower clouds over permanent ice and snow. For the lowermost cirrus clouds, the CTH_{CiPS} retrieval is best over permanent ice and snow. This is most likely due to the fact that the average CTH is lowest in the polar regions, making it easier for the ANN to model and estimate the CTH for low cirrus/ice clouds there. In contrast, barren, forest and vegetation excluding forest do, to a large extent, cover regions where the CTH is typically higher, making it more difficult to model and estimate the CTH for low cirrus. Over desert, where the air is dry, it is plausible that the signal from the water vapour channels (which were shown to have strong relative importance for the CTH_{CiPS} retrieval in Sect. 4.10.1) peak at lower altitudes in the atmosphere compared to more moist regions, resulting in biases for the CTH retrieval over barren. On average the CTH is estimated with the lowest MAPE and bias over homogeneous water surfaces.

The underlying surface type has a similar effect on the IOT_{CiPS} retrieval as on the IWP_{CiPS} retrieval. For $IOT_{CALIOP} > 0.5$ and $IWP_{CALIOP} > 10.0$ g m^{-2}, the underlying surface type has no effect on the IOT_{CiPS}/IWP_{CiPS} retrievals; i.e. already for these low values of IOT_{CALIOP}/IWP_{CALIOP} are the characteristics of surface radiation negligible. For thinner cirrus clouds the retrieval errors increase substantially over permanent ice and snow. This should be related to the effects discussed above, namely the reduced radiative contrast of the cirrus above cold snow and ice and the unfavourable conditions for SEVIRI in the polar regions. IOT_{CiPS}/IWP_{CiPS} retrievals over barren are also less certain for thin cirrus clouds. Deserts are characterised by a lower emissivity at 8.7 µm than at 10.8 or 12.0 µm (e.g. Hulley et al., 2015; De Paepe and Dewitte, 2009; Trigo et al., 2008). It is possible that this induces larger IOT_{CiPS}/IWP_{CiPS} retrieval errors because the ANN cannot localise desert regions unambiguously using only latitude and VZA. The retrieval errors over vegetation excluding forest are close or identical to the average performance for all IOT_{CALIOP} and IWP_{CALIOP}. The lowest IOT_{CiPS} and IWP_{CiPS} retrieval errors are again obtained over homogeneous water surfaces as well as over forest.

4.10.3 The CiPS retrieval accuracy for different vertical cloud–aerosol structures

In this section the performance of CiPS is characterised with respect to a set of seven vertical cloud–aerosol structure classes derived from the V3 CALIOP L2 layer products. This is important in order to understand the accuracy of the retrievals for different scattering and absorbing atmospheres. Although the OPF already yields quality information indicating when the IOT_{CiPS} and IWP_{CiPS} retrievals can be trusted, there is still the chance that the passive instrument SEVIRI is not able to deal with all possible vertical arrangements of clouds and aerosols as the active instrument CALIOP does, since SEVIRI lacks the vertical resolution.

The characterisation is performed for all surface types combined. Although the retrieval

accuracy shows a dependency on the underlying surface type (Sect. 4.10.2), the effect of liquid water clouds and aerosol layers below the cirrus cloud has a similar effect on the cirrus cloud retrieval over all underlying surface types (not shown here). The patterns and results obtained for all surface types combined (presented here) are consequently to a large extent representative for the single surface types as well. Due to the large coverage of oceans on the SEVIRI disc (see Fig. 4.14), the results presented here are, however, more representative for retrievals over water.

Again, only the CiPS quantities CCF_{CiPS}, CTH_{CiPS}, IOT_{CiPS} and IWP_{CiPS} are characterised for the different vertical cloud–aerosol structures. The OPF_{CiPS} is excluded from the analysis since its goal is to detect cirrus clouds where the vertical structure below the cirrus cannot be resolved by CALIOP. Opaque cirrus clouds are identified and excluded using the OPF of CALIOP as described in the following section.

4.10.3.1 Vertical cloud–aerosol structures from CALIOP

The final validation dataset presented in Sect. 4.4.2 is extended to characterise the entire atmospheric column observed by CALIOP (and SEVIRI). The column optical thickness and the corresponding top and base heights for aerosol layers, cirrus clouds and liquid water clouds are derived from the CALIOP cloud and aerosol layer products (see Sect. 4.3). The column AOT is read from the "Column_Optical_Depth_Aerosols_532" product contained in the L2 aerosol layer products. The corresponding top and base heights of the upper and lowermost aerosol layers are read from the "Layer_Base_Altitude" and "Layer_Top_Altitude" products. Finally the opacity information is retrieved from the "Opacity_Flag". For clouds, the column optical thickness is reported for liquid water and ice clouds combined. The cloud properties, including IOT, liquid water optical thickness, the corresponding top and base heights and the opacity information, are instead derived using the same approach used to derive the cirrus cloud properties in Sect. 4.3. Notice that mixed-phase clouds, i.e. layers where ice and supercooled liquid water coexist, are classified as either liquid, ice or unknown phase clouds by CALIOP. The high confidence criteria imposed to the CALIOP cloud phase (see below) shall, however, constrain the selected cloud and cloud profiles to high confidence liquid and high confidence ice clouds. Nevertheless, especially at high latitudes, an uncertainty remains due to the difficult cloud phase determination (Cesana et al., 2016).

Using the vertical position, optical thickness and opacity information of all clouds and aerosol layers, the seven vertical cloud–aerosol structure classes listed below are created. To analyse the effect of thicker aerosol layers on the cirrus cloud retrieval by CiPS, only those aerosol layers with an AOT > 0.2 are acknowledged. These aerosols come mainly from desert dust (Weinzierl et al., 2011; Groß et al., 2015) but also from biomass burning (Rosário et al., 2011; Ten Hoeve et al., 2012) or, sometimes, sea salt (Toth et al., 2013). It is assumed that AOT $\leq$ 0.2 is a good approximation for the AOT of typical aerosol loads. In comparison, the rural aerosol model by Shettle (1989) in the boundary layer for spring–summer conditions and a visibility of 50 km together with background aerosol above 2 km represent an AOT of 0.162.

C1 Profiles where only transparent cirrus clouds (and possible aerosols with AOT $\leq$ 0.2) are observed.

C2 Profiles where cirrus clouds are observed over an aerosol layer with AOT $>$ 0.2.

C3 Profiles where cirrus clouds are observed above a low opaque liquid water cloud. To ensure that the cirrus is well separated from the water cloud, the vertical distance between the two has to be 4.0 km or more. This class aims to capture scenes with cirrus clouds over low-level clouds. The threshold of 4 km was chosen such that it is applicable both in the tropical regions as well as at higher latitudes, where the vertical separation between high-level cirrus clouds and low-level clouds is smaller.

C4 Profiles where cirrus clouds are observed vertically close or adjacent to an opaque liquid water cloud. To ensure that the cirrus is close to the water cloud, the vertical distance between the two has to be 0.5 km or less. This spatial separation value enables to neglect small cloud gaps due to turbulence, evaporation, sedimentation or wind shear inside clouds. This class aims to capture mainly convective clouds with a cirrus shield/anvil.

C5 Profiles where only opaque liquid water clouds are observed. No cirrus clouds are present.

C6 Profiles where only an aerosol layer with AOT $>$ 0.2 is observed. No clouds are present.

C7 Profiles where only clear sky or aerosols with AOT $\leq$ 0.2 are observed. No clouds are present.

Please note that all liquid water clouds were opaque for the CALIOP lidar. Hence there is the possibility of having a thicker aerosol layer below the liquid water clouds. The effect of the aerosol layer is, however, assumed to be negligible due to the use of observations in the infrared spectrum where the liquid cloud is also opaque. This vertical cloud–aerosol structure information is extracted and appended to the corresponding collocations contained in the final validation dataset (Sect. 4.4.2) forming the *extended* final validation dataset. For a graphical interpretation of the vertical cloud–aerosol structure classification, all classes are visualised in Fig. 4.17. The number of samples for each class is also indicated; class C7 with more the 1.7 million samples is the most common situation, while C4 with less than 14 000 samples the most seldom.

Some CALIOP profiles do not fit into one of the seven classes, for example if the cirrus cloud is opaque or if the vertical distance between a cirrus cloud and an underlying liquid water cloud is between 0.5 and 4.0 km. Furthermore, all CALIOP retrievals used for the validation of CiPS in Sect. 4.9 do not necessarily pass the quality screening, since liquid water clouds and aerosols are included as well. In total, 75 % of the CALIOP retrievals contained in the final validation dataset passed the quality screening and could be grouped into one of the seven classes. The remaining 25 % were excluded from the present analysis.
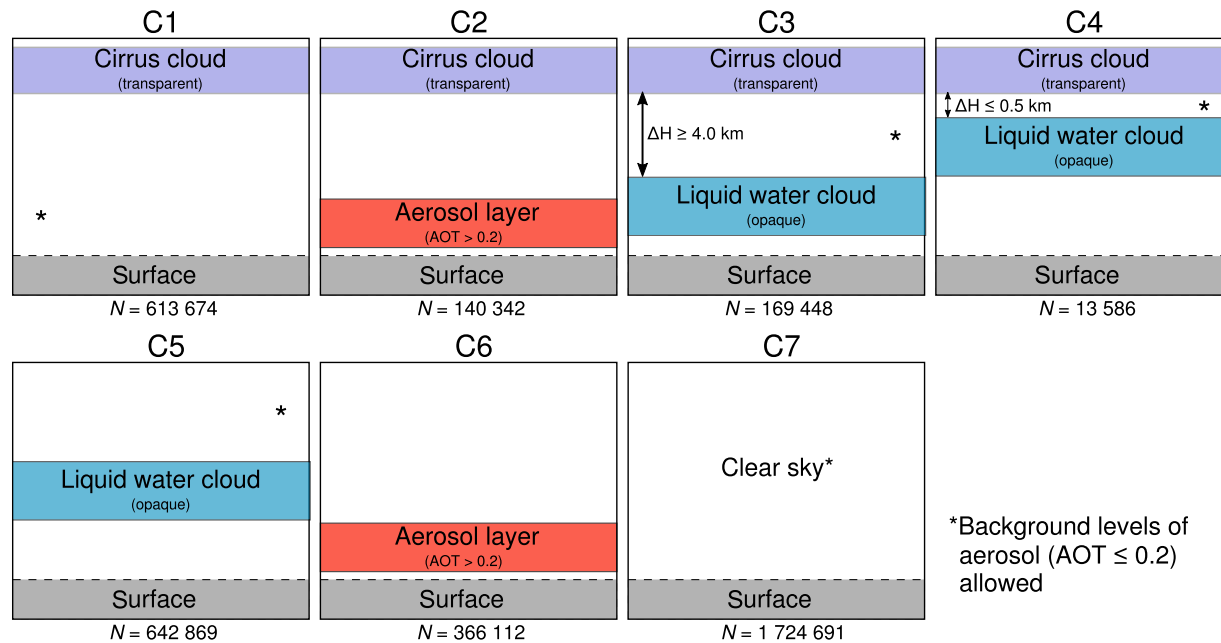
Figure 4.17: Visualisation of the seven vertical cloud–aerosol structure classes. Classes C1–C4 contain transparent cirrus clouds and are used to characterise the CiPS cirrus cloud detection (probability of detection) together with the CTH_{CiPS}, IOT_{CiPS} and IWP_{CiPS} retrievals. Classes C5–C7 contain no cirrus clouds and are used to characterise the false alarm rate of the CiPS cirrus cloud detection. Figure reproduced from Strandgren et al. (2017b).

4.10.3.2 Cirrus cloud detection

Figure 4.18a shows the POD of CiPS as a function of IOT_{CALIOP} for the vertical cloud–aerosol structure classes C1–C4, i.e. those classes defined in Sect. 4.10.3.1 that contain cirrus clouds. For a better visualisation the scale is again logarithmic for $IOT_{CALIOP} < 1.0$ and linear for $IOT_{CALIOP} \geq 1.0$. As a reference, the average POD for all cirrus clouds in the dataset, including those that did not fit any of the four classes C1–C4, is included.

The cirrus cloud detection by CiPS shows little interference with different vertical cloud–aerosol structures. It is, however, considerably easier for CiPS to detect a thin cirrus cloud when a liquid water cloud is present vertically close to the base altitude of the cirrus (C4). Even for sub-visual cirrus the POD is close to 60 % in such situations. If the vertical separation between the cirrus cloud and the liquid water cloud is larger (≥ 4.0 km, C3), only a marginal increase in POD with respect to profiles with no liquid water cloud below the cirrus is observed. For thicker cirrus clouds with $IOT_{CALIOP} > 1.0$, the POD is close to 100 % with a liquid water cloud below the cirrus (C3 and C4), compared to 95 % for scenes with only a transparent cirrus cloud (C1). An aerosol layer has a small effect on the CiPS cirrus detection in general, but for cirrus clouds with $IOT_{CALIOP} < 0.08$ an aerosol layer appears to attenuate the radiative contrast of the cirrus, leading to a slightly lower POD.
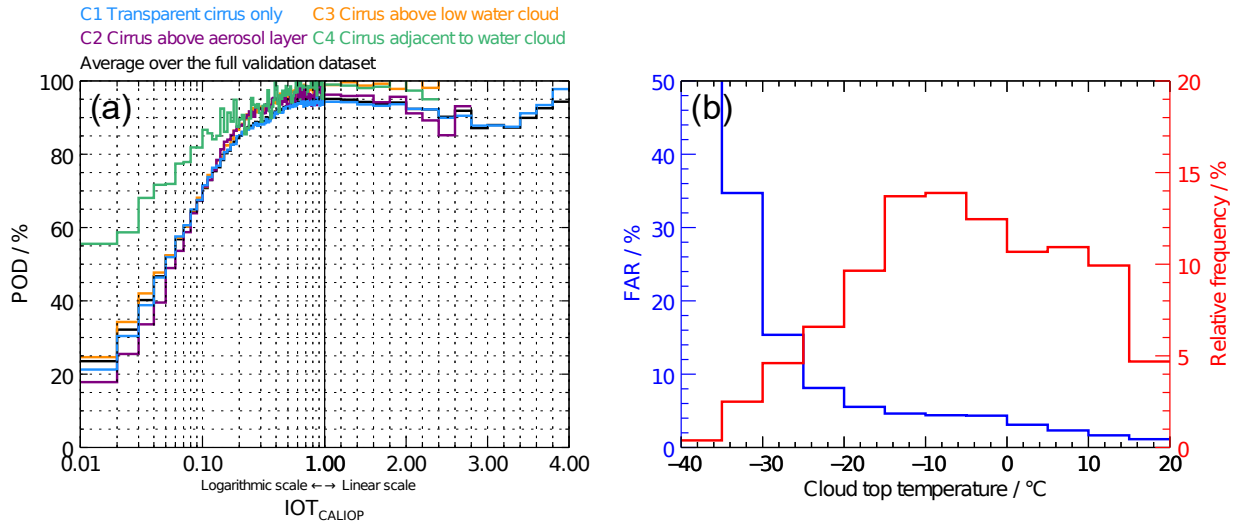
Figure 4.18: **(a)** The cirrus POD of CiPS as a function of the IOT retrieved by CALIOP for the vertical cloud–aerosol structure classes C1–C4 along with the average POD over the full final validation dataset. **(b)** The FAR of CiPS for scenes with liquid water clouds (C5) as a function of the corresponding top temperature of the liquid water clouds. Along with the FAR, the relative frequency of occurrence of the different liquid water cloud top temperatures is shown. Figure adapted from Strandgren et al. (2017b).

For scenes with clear sky (C7) or thicker aerosol layers (C6) CiPS has a FAR of 3.2 %, meaning that it correctly classifies close to 97 % of such scenes as cirrus-free (not further shown here). An increased average FAR of 5.5 % is obtained when a liquid water cloud is present (C5). This is a result of CiPS falsely classifying some high liquid water clouds as cirrus clouds. Figure 4.18b shows the FAR for scenes with liquid water clouds (C5) as a function of the liquid water cloud top temperature along with the relative frequency of occurrence of the different cloud top temperatures. It is clear that the colder (higher up) the liquid water cloud is, the higher is the risk of falsely classifying it as a cirrus cloud. At temperatures below $-30\,°C$, the FAR is approx. 35–65 %. The relative frequency of such supercooled liquid water clouds is, however, low. Most liquid water clouds have a top temperature between -15 and $+15\,°C$ and thus a clearly lower FAR of less than 5.0 %.

4.10.3.3 Cirrus cloud properties

Figure 4.19 shows the MAPE and MPE for the (a) CTH_{CiPS}, (b) IOT_{CiPS} and (c) IWP_{CiPS} retrievals as functions of the corresponding reference retrievals by CALIOP and the vertical cloud–aerosol structure.

Within each CTH_{CALIOP}, IOT_{CALIOP} and IWP_{CALIOP} interval in Fig. 4.19, the MAPE and MPE given by Eq. (3.6) and (3.5) are calculated. Again the results are presented with a logarithmic scale for $IOT_{CALIOP} < 1.0$ and $IWP_{CALIOP} < 10.0\,g\,m^{-2}$ and with a linear scale for $IOT_{CALIOP} \geq 1.0$ and $IWP_{CALIOP} \geq 10.0\,g\,m^{-2}$. The average retrieval errors for
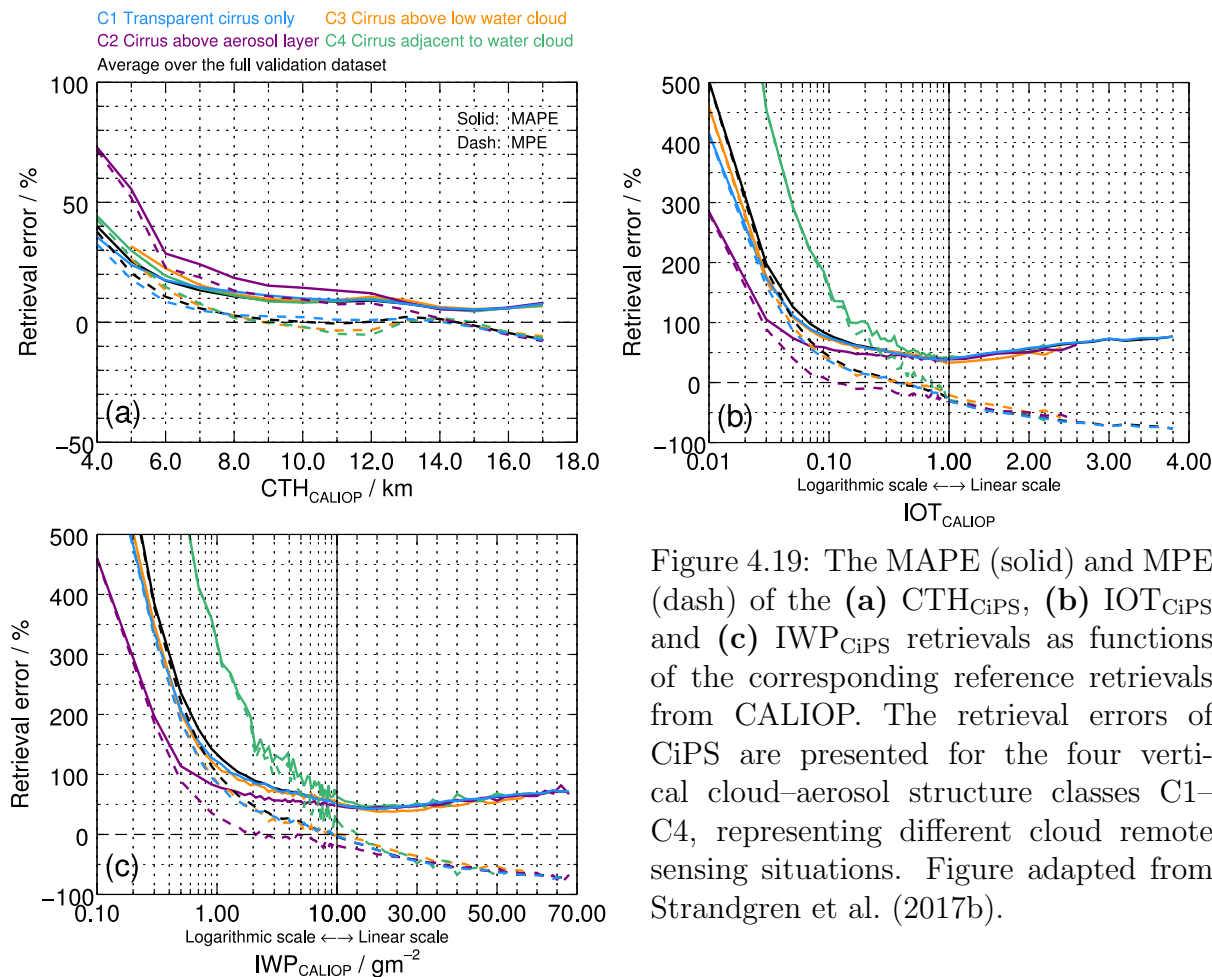
Figure 4.19: The MAPE (solid) and MPE (dash) of the (a) CTH_{CiPS}, (b) IOT_{CiPS} and (c) IWP_{CiPS} retrievals as functions of the corresponding reference retrievals from CALIOP. The retrieval errors of CiPS are presented for the four vertical cloud–aerosol structure classes C1–C4, representing different cloud remote sensing situations. Figure adapted from Strandgren et al. (2017b).

all vertical cloud–aerosol structures are included as a reference.

The presence of liquid water clouds (C3 and C4) has a negligible effect on the CTH_{CiPS} retrieval. An aerosol layer below the cirrus cloud introduces a stronger positive bias (positive MPE), with a MAPE and MPE of up to 70 % for the lowermost cirrus clouds. This is not necessarily an effect of the aerosol layer itself, and it is likely to be related to the fact that most aerosol layers with AOT > 0.2 are found in the tropical regions (not shown here), where CTHs are typically higher leading to a stronger tendency of overestimating comparably low CTHs. This effect is seen to diminish with increasing CTH_{CALIOP}. At $CTH_{CALIOP} = 9.0$ km the MAPE introduced by an underlying aerosol layer is approx. 5 % larger compared to retrievals without an aerosol layer. Above 13 km, the aerosol layer has no effect on the CTH_{CiPS} retrieval error.

The presence of a low liquid water cloud below the cirrus (C3) has a negligible effect on the IOT_{CiPS} and IWP_{CiPS} retrievals, with the same MPE and MAPE as for situations with solely clear sky or background aerosols below the cirrus cloud (C1). If the liquid water cloud is located vertically close or adjacent to the cirrus (C4), the retrieval error clearly increases for thin cirrus clouds. The increase in error for those retrievals is seen

for $IOT_{CALIOP} \lesssim 0.5$ and $IWP_{CALIOP} \lesssim 10.0\,\mathrm{g\,m^{-2}}$ and increases rapidly with decreasing IOT_{CALIOP} and IWP_{CALIOP}. At $IOT_{CALIOP} \approx 0.08$ and $IWP_{CALIOP} \approx 2.0\,\mathrm{g\,m^{-2}}$, the MAPE is $200\,\%$ for class C4, which is about twice the error of the IOT_{CiPS}/IWP_{CiPS} retrievals for situations with solely clear sky or background aerosols below the cirrus cloud (C1). This pattern is to be expected as it is impossible for a radiometer to know where the transition between ice and liquid water occurs when the two clouds are not vertically well separated, especially since the liquid water cloud is thick and thus opaque to infrared radiation. Furthermore, it is more difficult to extract information about the cirrus from the brightness temperature differences, also utilising the regional maximum brightness temperatures, if the vertical separation, and hence the radiative contrast between the cirrus cloud and the underlying liquid water cloud, is small. A corresponding increase is observed for the MPE, meaning that the increased MAPE is a result of larger overestimations of IOT_{CiPS} and IWP_{CiPS}.

Opposite to the CTH_{CiPS} retrieval, an aerosol layer below the cirrus cloud (C2) reduces the IOT_{CiPS} and IWP_{CiPS} retrieval errors for thin cirrus clouds. This does not imply that it is easier to retrieve the IOT_{CiPS} and IWP_{CiPS} of thin cirrus clouds when an aerosol layer is present below the cirrus. It is rather related to the fact that CiPS predominantly overestimate IOT_{CALIOP} and IWP_{CALIOP} for thin cirrus, an effect that is reduced if an aerosol layer is present below the cirrus.

4.10.4 The CiPS retrieval errors as a function of ice optical thickness and cloud top height

In this section the retrieval errors of CiPS are investigated as a function of IOT_{CALIOP} and CTH_{CALIOP}. This gives information about typical errors of CiPS for different types of cirrus clouds (e.g. low and thick or high and thin cirrus). To remove any effects from different vertical cloud–aerosol structures, again only those profiles with transparent cirrus clouds and possible faint aerosols ($AOT \leq 0.2$) as defined by CALIOP L2 data are used (class C1 in Sect. 4.10.3.1). This distribution is depicted in Fig. 4.20c, which represents a 2-D histogram with IOT_{CALIOP} on the horizontal axis and CTH_{CALIOP} on the vertical axis. The colour map shows the number of occurrences for each combination of IOT_{CALIOP} and CTH_{CALIOP} of class C1 in the extended final validation dataset. As mentioned in Sect. 4.4.2, both the final validation dataset and the training datasets used to train CiPS consist of a random subset of CALIOP data collected over a time period of almost 6 years and do to some extent (limited by the sun-synchronous orbit of CALIPSO) represent the natural distribution of IOT and CTH frequencies and their combinations. The occurrences in Fig. 4.20c are thus to a large extent representative for the corresponding occurrences in the dataset used to train CiPS as well. The highest occurrence of cirrus clouds in Fig. 4.20c is between 9 and $17\,\mathrm{km}$, with tropical cirrus covering the high-altitude cirrus fraction and mid- to low-latitude cirrus covering the low-altitude cirrus fraction. Low cirrus clouds are thicker than high cirrus, with an occurrence peak for cirrus with CTH_{CALIOP} between 10.5 and $12.5\,\mathrm{km}$ and IOT_{CALIOP} between 0.3 and 1.0.
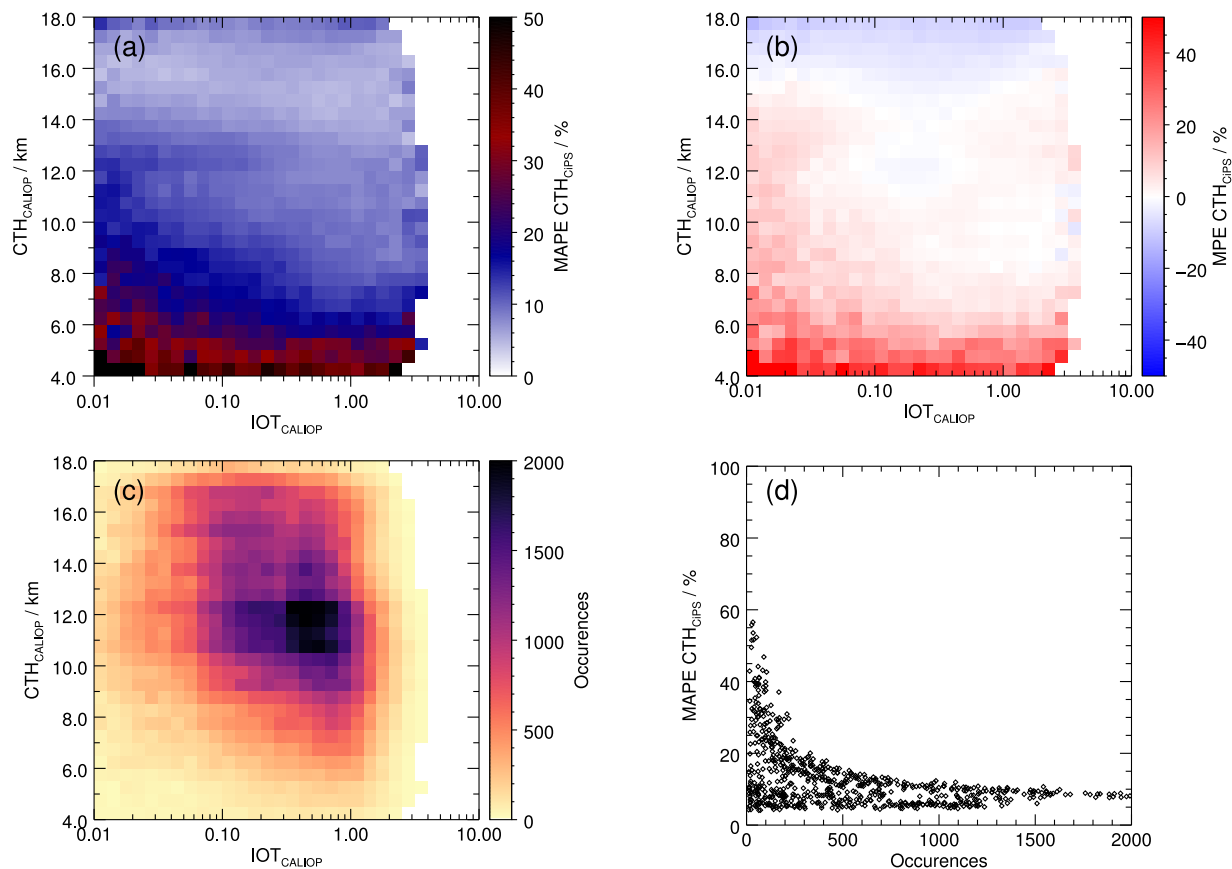
Figure 4.20: **(a)** Two-dimensional histogram showing the MAPE of the CTH_{CiPS} retrievals as a function of the reference retrieval quantities IOT_{CALIOP} and CTH_{CALIOP}. **(b)** Two-dimensional histogram showing the MPE of the CTH_{CiPS} retrievals as a function of IOT_{CALIOP} and CTH_{CALIOP}. **(c)** Two-dimensional histogram showing the number of occurrences for different combinations of IOT_{CALIOP} and CTH_{CALIOP}. **(d)** The MAPE of the CTH_{CiPS} retrievals for the different $IOT_{CALIOP}/CTH_{CALIOP}$ combinations as a function of the number of occurrences (each diamond represents two corresponding grid boxes in **(a)** and **(c)**). Figure reproduced from Strandgren et al. (2017b).

Figure 4.20a and b show two 2-D histograms with the IOT_{CALIOP} and CTH_{CALIOP} on the horizontal and vertical axes respectively. The colour maps show the MAPE and MPE of the CTH_{CiPS} retrievals with respect to the reference CALIOP data.

The CTH_{CiPS} retrieval shows a stable performance with a MAPE between 5 and 15 % for most combinations of top height and optical thickness. For optically thin cirrus clouds, radiation from below has a larger contribution to the observed brightness temperatures, which reduces the radiative contrast between the cirrus cloud and the underlying surface (Sect.2.2.2). Similarly, the radiative contrast decreases if the cirrus cloud is located further down in the atmosphere at warmer temperatures, with more water vapour above the cirrus cloud that makes the interpretation of window channel brightness temperatures and

brightness temperature differences more difficult. These effects can be seen in the retrieval errors, with generally decreasing MAPE for increasing CTH_{CALIOP} and IOT_{CALIOP}. It is clear that the combination of low and optically thin cirrus induce the maximum CTH_{CiPS} retrieval errors (MAPE $\gtrsim 25\,\%$) while high and optically thick cirrus induce the minimum CTH_{CiPS} retrieval errors (MAPE $\approx 5\,\%$). The lowest retrieval errors are observed at high altitudes ($CTH_{CALIOP} \in [15, 17]\,\text{km}$), where the CTH_{CiPS} can be retrieved with a small error also for sub-visual cirrus. Similar features are observed using an optimal estimation method in Iwabuchi et al. (2016). For thin to sub-visual cirrus clouds, CiPS is more likely to overestimate the CTH (positive MPE). With increasing IOT_{CALIOP} the bias weakens, and for $IOT_{CALIOP} > 0.05$ and $CTH_{CALIOP} > 8\,\text{km}$ CiPS is mostly unbiased (MPE ≈ 0). As already discussed in Sect. 4.9.2, the extreme high and low CTH_{CALIOP} are primarily under- and overestimated though, irrespective of IOT_{CALIOP}.

A correlation between higher MAPE and a low number of occurrences is evident. For the region of low optically thin cirrus, where the MAPE of the CTH_{CiPS} retrieval is highest, there are only few points. This is further clarified in Fig. 4.20d, showing the MAPE of the CTH_{CiPS} retrieval as a function of the number of occurrences. Each diamond in Fig. 4.20d represents one pair of grid boxes in Fig. 4.20a and c (708 pairs of boxes with valid data are represented). It is clear that the high MAPEs rarely occur and that most CTH_{CiPS} retrievals have comparably low MAPEs. This provides primarily three pieces of information. (1) The learning of the ANNs is sensitive to the distribution of the training dataset, leading to difficulties to accurately retrieve the cirrus properties for comparably rare situations. An effort was made to balance the training datasets for CiPS by adding duplicates for some rare situations (Sect. 4.4.2) to increase their weight during the training. This approach does not, however, introduce any new information that the ANNs can learn from. Nevertheless, not even a perfectly balanced dataset is likely to result in an ANN that performs equally well for all kinds of cirrus clouds and retrieval conditions, as certain retrieval conditions have physical limitations, as discussed above for low and optically thin cirrus clouds. CiPS can also retrieve the CTH for high sub-visual cirrus clouds with a low MAPE despite few occasions. (2) With comparably few occasions, the high MAPEs of CiPS have a small effect for the average usage of CiPS, as the MAPE for the comparably common situations is low. (3) Due to their few occurrences, the high MAPEs of CiPS have a low statistical value such that these values have to be treated with caution.

On average CiPS can retrieve the CTH with a MAPE around $8\,\%$ and zero bias (MPE) for the most common combinations of CTH_{CALIOP} and IOT_{CALIOP}. Taking the number of occurrences into account, which represents the natural distribution of transparent cirrus clouds over clear air observed by CALIOP, $37\,\%$ of all CTH_{CiPS} retrievals have a MAPE of $5\,\%$ or less. Another 27 and $16\,\%$ of all retrievals have a MAPE between 5 and 10 and between 10 and $15\,\%$ respectively.

Figure 4.21 is similar to Fig. 4.20, but here the IOT_{CiPS} retrieval errors are in focus. Figure 4.21a–c again show 2-D histograms with IOT_{CALIOP} on the horizontal axes and CTH_{CALIOP} on the vertical axes. The colour maps show (a) the MAPE and (b) the MPE of the IOT_{CiPS} retrievals with respect to the CALIOP reference retrievals and (c) the corresponding number of occurrences for the different $IOT_{CALIOP}/CTH_{CALIOP}$ combinations.
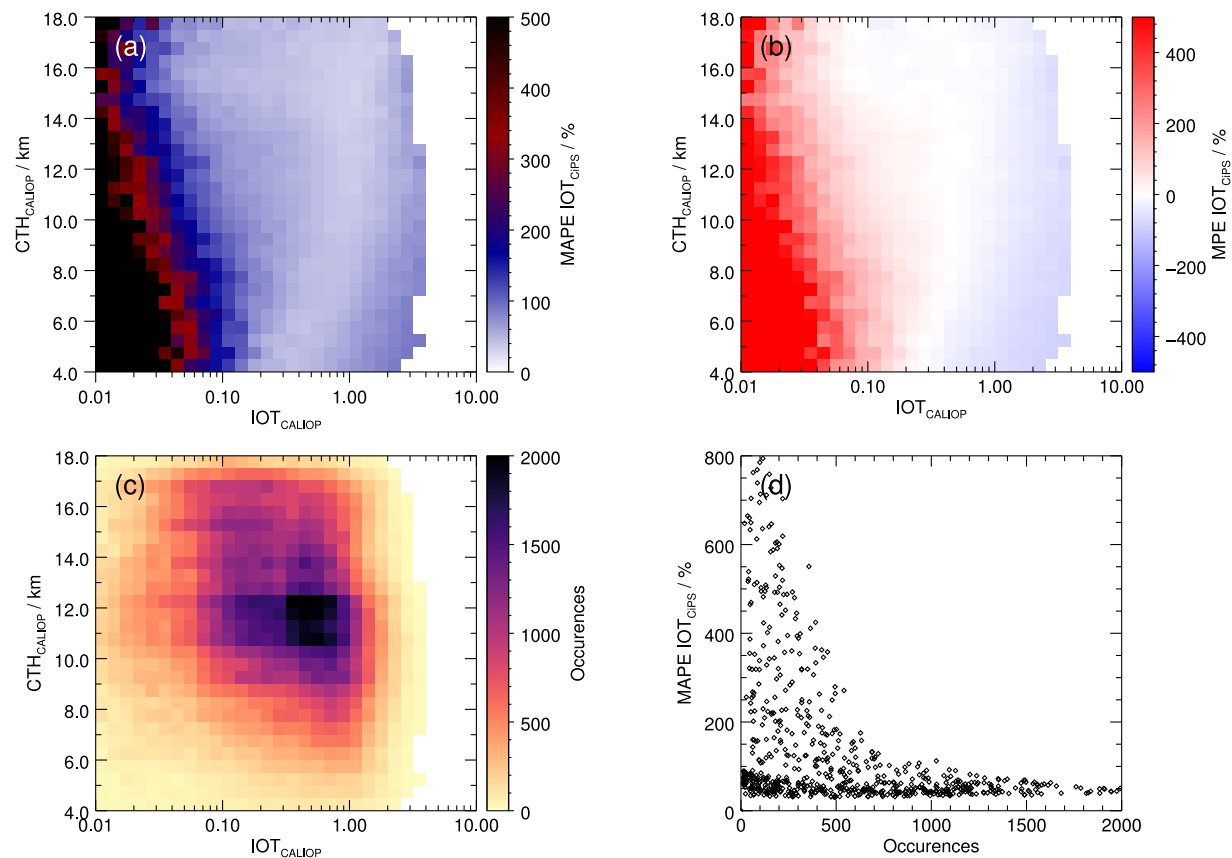
Figure 4.21: **(a)** Two-dimensional histogram showing the MAPE of the IOT_{CiPS} retrievals as a function of the reference retrieval quantities IOT_{CALIOP} and CTH_{CALIOP}. **(b)** Two-dimensional histogram showing the MPE of the IOT_{CiPS} retrievals as a function of IOT_{CALIOP} and CTH_{CALIOP}. **(c)** Two-dimensional histogram showing the number of occurrences for different combinations of IOT_{CALIOP} and CTH_{CALIOP}. **(d)** The MAPE of the IOT_{CiPS} retrievals for the different $IOT_{CALIOP}/CTH_{CALIOP}$ combinations as a function of the number of occurrences (each diamond represents two corresponding grid boxes in **(a)** and **(c)**). Figure reproduced from Strandgren et al. (2017b).

Figure 4.21c is consequently a duplicate of Fig. 4.20c but is included twice for the reader's convenience. Please note that the retrieval errors are significantly larger for IOT_{CiPS} compared to CTH_{CiPS} and the axes for the MAPE and MPE now range from 0 to 500 % and from -500 to 500 % respectively. The MAPE of the IOT_{CiPS} retrievals as a function of the number of occurrences is shown in Fig. 4.21d. Similarly to the CTH_{CiPS} retrievals, the IOT_{CiPS} retrieval errors show clear patterns across the IOT_{CALIOP} and CTH_{CALIOP} domains. The large retrieval errors for thin cirrus clouds already shown in Sect. 4.9.2 are evident but are seen to decrease with increasing CTH_{CALIOP}. Above 14 km CiPS can estimate the IOT with a MAPE (Fig. 4.21a) of 30–120 % down to sub-visual cirrus clouds. Again, the combination of low ($CTH_{CALIOP} < 8$ km) and optically thin ($IOT_{CALIOP} < 0.1$) cirrus induces the

largest IOT_{CiPS} retrieval errors (MAPE $> 150\,\%$), while high ($\text{CTH}_{\text{CALIOP}} > 13\,\text{km}$) and optically thicker ($\text{IOT}_{\text{CALIOP}} > 0.06$) cirrus induce the smallest retrieval errors (MAPE between 30 and $80\,\%$ and MPE close to zero). Furthermore, there is a band with $\text{IOT}_{\text{CALIOP}}$ between 0.2 and 0.5 at $4\,\text{km}$ height that expands with $\text{CTH}_{\text{CALIOP}}$ to reach $\text{IOT}_{\text{CALIOP}}$ between 0.1 and 1.0 at $16\,\text{km}$ where the MAPE is smaller than $50\,\%$. The smallest bias (MPE, Fig. 4.21b) is observed where the MAPE is lowest and increases slightly with decreasing $\text{CTH}_{\text{CALIOP}}$. For $\text{IOT}_{\text{CALIOP}} > 0.3$, the IOT_{CiPS} retrieval has a negative or zero bias on average (MPE between -80 and $0\,\%$), whereas for $\text{IOT}_{\text{CALIOP}} < 0.3$ the IOT_{CiPS} retrieval has no or a positive (up to $400\,\%$ or more) bias.

Again an evident correlation between low MAPEs and a high number of occurrences is observed (Fig. 4.21d). Even though high MAPEs of $800\,\%$ are possible, the large majority of the IOT_{CiPS} retrievals have MAPEs between 50 and $150\,\%$. Please also note that a $800\,\%$ MAPE observed at $\text{IOT}_{\text{CALIOP}} = 0.01$ translates into a small absolute error (0.08). Similar optical thickness retrieval errors are shown for the optimal estimation retrieval by Iwabuchi et al. (2016), demonstrating that the large errors are not an artefact of the ANN but rather due to physical constraints discussed above. There are approx. 250 points/diamonds with less than 200 occurrences and low MAPE ($< 100\,\%$). Those points represent cirrus clouds with a comparably high optical thickness ($\text{IOT}_{\text{CALIOP}} \gtrsim 1.5$). In this region CiPS predominantly underestimates $\text{IOT}_{\text{CALIOP}}$, meaning that the MAPE of the IOT_{CiPS} retrieval is bounded above by $100\,\%$.

On average CiPS can retrieve the IOT with a MAPE around $50\,\%$ and bias around $\pm 10\,\%$ for the most common combinations of $\text{CTH}_{\text{CALIOP}}$ and $\text{IOT}_{\text{CALIOP}}$. Taking the number of occurrences into account, again representing the natural distribution of transparent cirrus clouds over clear air observed by CALIOP, $55\,\%$ of all IOT_{CiPS} retrievals have a MAPE of $50\,\%$ or less. Another $28\,\%$ of the retrievals have a MAPE between 50 and $100\,\%$, meaning that only $17\,\%$ of the retrievals have a MAPE larger than $100\,\%$.

The corresponding results for the IWP_{CiPS} retrieval are similar to the IOT_{CiPS} with 48 and $31\,\%$ of all IWP_{CiPS} retrievals having a MAPE of $50\,\%$ or less and between 50 and $100\,\%$ respectively. Due to the similarities with the IOT_{CiPS} retrieval, the IWP_{CiPS} retrieval errors as a function of $\text{CTH}_{\text{CALIOP}}$ and $\text{IOT}_{\text{CALIOP}}$ are not further presented here.

4.10.5 Noise sensitivity analysis of CiPS

In this section the effect of small noisy perturbations in the input data from SEVIRI propagating through the ANNs is quantified. The noise sensitivity analysis is performed for the CTH_{CiPS}, IOT_{CiPS} and IWP_{CiPS} retrievals. The final validation dataset described in Sect. 4.4.2 is used for this purpose in order to have a large temporal and spatial coverage. CiPS classifies 1.3 million points in the final validation dataset as icy, for which the CTH_{CiPS}, IOT_{CiPS} and IWP_{CiPS} is retrieved. Along with the standard CiPS retrieval using the observed SEVIRI brightness temperatures, another 100 retrievals for every point are performed where the SEVIRI brightness temperatures are randomly perturbed within the respective radiometric noise estimate ranges.

Table 4.3: Radiometric noise estimates of MSG-2/SEVIRI thermal channels (first column, including the channel centre wavelength λ_c) at the reported reference brightness temperatures (second column; EUMETSAT, 2007) and at typical brightness temperatures observed for cirrus cloud retrievals (third column). Table reproduced from Strandgren et al. (2017b).

λ_c / µm	NEΔT / K	
6.2	0.05 @ 250 K	0.11 @ 225 K
7.3	0.05 @ 250 K	0.07 @ 237 K
8.7	0.075 @ 300 K	0.15 @ 252 K
10.8	0.07 @ 300 K	0.12 @ 253 K
12.0	0.10 @ 300 K	0.16 @ 251 K
13.4	0.205 @ 270 K	0.27 @ 239 K

4.10.5.1   Perturbing the SEVIRI brightness temperatures

Estimates of the radiometric noise levels of the SEVIRI thermal channels can be derived from measurements of the internal black body calibration target and are reported as noise-equivalent temperature differences (NEΔT) at given reference temperatures in EUMET-SAT (2007) and summarised in Table 4.3 (second column) for all channels (first column) used by CiPS (see Sect. 4.2). However, these reference temperatures are higher than for typical cirrus cloud retrievals. Therefore, the reported noise levels are scaled to the respective cirrus cloud brightness temperatures observed by SEVIRI. In a first step the NEΔT are converted to NEΔR (noise-equivalent radiance differences) using the derivative of Planck's law (with respect to temperature, T) at the reported reference temperatures and respective wavelengths (the centre channel wavelength in the first column of Table 4.3 is used for this purpose). In a second step the NEΔR are converted back to NEΔT at the brightness temperature of the corresponding cirrus cloud retrievals (P. Schöbel-Pattiselanno, EUMETSAT, personal communication, 2017). This results in an individual noise level estimate for all brightness temperatures observed by SEVIRI and used for the standard CiPS retrieval. So with 1.3 million cirrus cloud retrievals in the final validation dataset and 9 SEVIRI brightness temperatures as input (6 brightness temperatures and 3 regional maximum temperatures, Sect. 4.2), a total of $9 \times 1.3 \times 10^6$ individual radiometric noise level estimates are obtained. Please note that those are not metrologically traceable per-pixel noise estimates; instead all noise estimates are directly related via the observed brightness temperatures to the overall noise estimates of the single channels reported in the second column in Table 4.3. For a statistical analysis, however, those estimates are sufficient.

When the radiometric noise in the respective channels is scaled to the observed brightness temperatures, colder cirrus cloud observations get higher radiometric noise levels compared to warmer observations. The third column in Table 4.3 shows the radiometric noise levels for the six SEVIRI channels used by CiPS at reference brightness temperatures given by typical cirrus cloud observations. Those reference temperatures constitute the average brightness temperatures observed by the respective channels across all CiPS cirrus cloud

retrievals in the final validation dataset. It is clear that the noise level estimates of the cirrus cloud observations are higher compared to the noise levels at the warmer reference brightness temperatures reported by EUMETSAT (2007).

Each of the $9 \times 1.3 \times 10^6$ brightness temperature observations in the final validation dataset is associated with a Gaussian distribution with zero mean and standard deviation provided by the $9 \times 1.3 \times 10^6$ individual radiometric noise level estimates produced above. Each Gaussian distribution is finally sampled randomly 100 times yielding $9 \times 1.3 \times 10^6 \times 100$ uncorrelated noise perturbations across the different SEVIRI input brightness temperatures. Hence, a set of 100 randomly perturbed retrievals is obtained for each cirrus cloud retrieval in the final validation dataset that can be directly compared to the corresponding standard (unperturbed) retrieval of CiPS.

4.10.5.2 Noise sensitivity of CiPS

The noise sensitivity of the CTH_{CiPS}, IOT_{CiPS} and IWP_{CiPS} retrievals is determined by calculating the root-mean-square deviation (RMSD) between the standard retrievals and the corresponding 100 perturbed retrievals for the 1.3 million icy collocations. The RMSD is defined as

$$\text{RMSD} = \sqrt{\frac{1}{100}\sum_{i=1}^{100}(S - P_i)^2}, \tag{4.1}$$

where S is the standard CiPS retrieval and P_i are the perturbed retrievals ($i = 1, \ldots, 100$). The sum spans over all 100 perturbed retrievals.

Figure 4.22 shows the RMSD for (a) CTH_{CiPS}, (b) IOT_{CiPS} and (c) IWP_{CiPS} as functions of the respective quantities. For IOT_{CiPS} and IWP_{CiPS} only retrievals classified as transparent by CiPS ($OPF_{CiPS} = 0$) are included. This reduces the number of samples from 1.3 to approx. 1 million. Please note that again the results are presented with a logarithmic scale for $IOT_{CALIOP} < 1.0$ and $IWP_{CALIOP} < 10.0\,\text{g}\,\text{m}^{-2}$ and with a linear scale for $IOT_{CALIOP} \geq 1.0$ and $IWP_{CALIOP} \geq 10.0\,\text{g}\,\text{m}^{-2}$. The surface type and the vertical cloud–aerosol structures are not taken into account for the noise sensitivity analysis and the reported results represent the average sensitivity to radiometric noise across all retrieval conditions.

The CTH_{CiPS} retrieval is clearly robust with a low sensitivity to noise in the SEVIRI input data. The RMSD is around $100\,\text{m}$ throughout the whole CTH_{CiPS} range.

The IOT_{CiPS} and IWP_{CiPS} retrievals have similar noise sensitivities. The RMSD is less than $10\,\%$ of the corresponding IOT_{CiPS}/IWP_{CiPS} throughout most of the IOT_{CiPS} and IWP_{CiPS} ranges. Only for sub-visual cirrus the RMSD of CiPS is higher. For thicker cirrus, the IOT_{CiPS} and IWP_{CiPS} retrievals become more robust to SEVIRI noise as the respective curves flatten towards a constant sensitivity around 1.5 and $30\,\text{g}\,\text{m}^{-2}$ for IOT_{CiPS} and IWP_{CiPS} respectively. For thin cirrus clouds, a small change in IOT/IWP induces a comparably large change in the cloud radiative properties. Similarly, a small change in the cloud radiative properties has a larger effect on the IOT and IWP for thin cirrus clouds
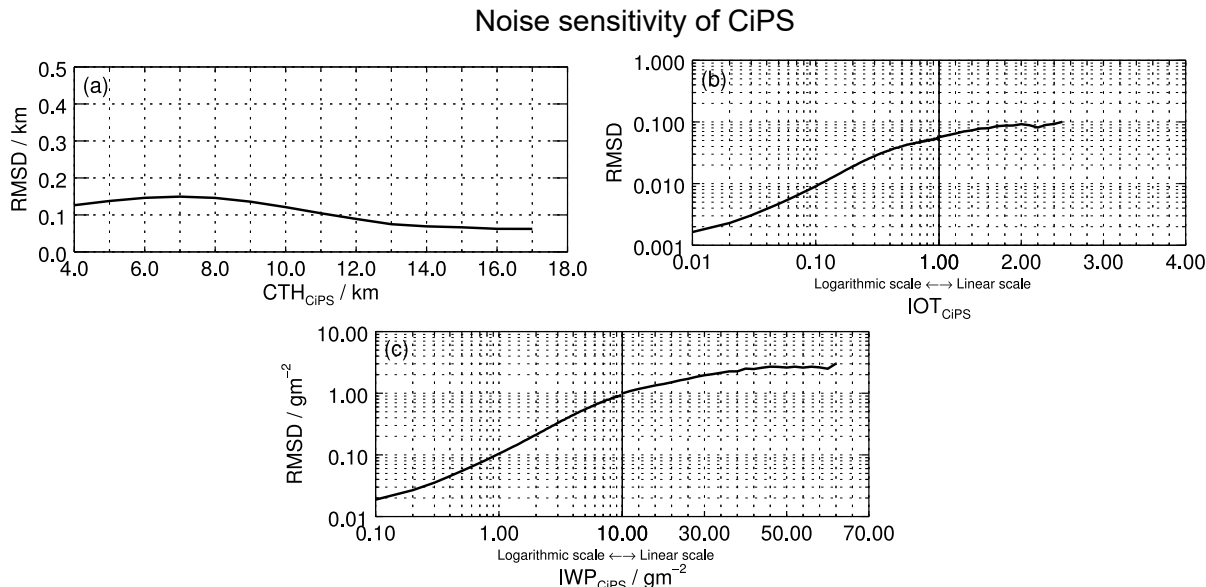
Figure 4.22: The noise sensitivity of the **(a)** CTH_{CiPS}, **(b)** IOT_{CiPS} and **(c)** IWP_{CiPS} retrievals. The noise sensitivity is reported as the RMSD between the CiPS standard retrieval and 100 retrievals where the SEVIRI input data are randomly perturbed within the radiometric noise range of SEVIRI. Figure adapted from Strandgren et al. (2017b).

compared to thicker cirrus where the IOT and IWP is higher. Consequently a small noisy perturbation applied to the SEVIRI input data has a larger impact on the IOT_{CiPS} and IWP_{CiPS} retrievals for thin cirrus clouds, leading to higher relative RMSD for thin cirrus and decreasing relative RMSD for thicker cirrus.

A noise sensitivity of 0.001 at a retrieved optical thickness of 0.01 is low and one may expect noise to have a stronger impact on the retrievals for such faint cirrus. The reported radiometric noise estimates of SEVIRI are, however, very low. Even for cold cirrus cloud retrievals, the radiometric noise level is between 0.07 and 0.27 K on average for the six SEVIRI channels (see third column in Table 4.3), which corresponds to 0.3–1.1 ‰ of the observed average brightness temperatures. Furthermore, the noise is assumed to be Gaussian and peaks at zero across all perturbed retrievals and the individual SEVIRI input variables.

In Sect. 4.10.4 the retrieval error of CiPS is assessed to ≈ 5–15 and ≈ 50–150 % for the CTH_{CiPS} and IOT_{CiPS}/IWP_{CiPS} retrievals respectively. In this section the radiometric noise of SEVIRI is shown to have a minor contribution to the retrieval error. Thus it is clear that the major part of the retrieval error stems from the clearly different characteristics and sensitivities of SEVIRI and CALIOP.

4.11 Intercomparison with independent lidar data

As explained in Sect.4.3, CiPS is bound to inherit all systematic errors of its training reference, CALIOP. As such errors do not show when validated against independent CALIOP data, as in Sects. 4.9–4.10, it is wise to compare the CiPS retrievals with external cirrus cloud retrievals. In this section this is done by comparison with both ground-based and airborne lidar data.

4.11.1 The ground-based lidar RAMSES

RAMSES (Raman Lidar for Atmospheric Moisture Sensing; Reichardt et al., 2012; Reichardt, 2014) is a ground-based Raman lidar with an integrated spectrometer (actually two, but the second is not relevant here) operated at DWD (German Meteorological Service) in Lindenberg, Germany. RAMSES is sensitive to the inelastic Raman backscatter by water molecules in all three phases and measures, in addition to vertical profiles of water vapour mixing ratio and temperature, the optical properties of clouds at 355 nm, and cloud water content. Direct measurement of the latter is available at night only. To obtain estimates of IWC and, by vertical integration, IWP with RAMSES during daytime as well, a temperature dependent relation between IWC and the s-polarized (perpendicular to the plane of incidence) backscatter coefficient has been established.

The cirrus cloud properties retrieved by CiPS have been compared to the counterparts retrieved by RAMSES at 11 occasions (selected by J. Reichardt (DWD)) in 2015/16, when stable cirrus clouds were observed over Lindenberg. CiPS data have been spatially collocated with the RAMSES retrievals using parallax correction and nearest neighbour. Figure 4.23 shows the temporal evolution of the cirrus IOT and IWP retrieved by CiPS and RAMSES at one such occasion (8–9 November 2015). RAMSES IOT has been corrected for multiple scattering effects. Grey areas represent cirrus classified as opaque by CiPS, i.e. where IOT_{CiPS} and IWP_{CiPS} retrievals are considered unreliable. It is clear that CiPS detects all cirrus clouds observed by RAMSES. Also the opacity classification is accurate, and in nearly all situations where CiPS underestimates the high IOT_{RAMSES} and IWP_{RAMSES}, CiPS classifies the cirrus as opaque. There are, however, situations where such opaque cirrus and hence underestimated IOT_{CiPS} and IWP_{CiPS} are not identified. In general the agreement for the IOT and IWP is very good given the different sensitivities and observation techniques, with a linear correlation of 0.93 and 0.88 respectively. CiPS does, however, underestimate the IOT_{CiPS} and IWP_{CiPS} around 16:00, 17:00–17:30 and 18:30 UTC. There are also some differences between the IOT and IWP retrievals. For example around 22:00–22:30 UTC, when CiPS underestimates the IOT, but accurately retrieves the IWP. Similarly, CiPS overestimates the IWP, but accurately retrieves the IOT around 20:15–20:45 UTC. This suggests imperfections in the parameterisation used to estimate the IWC (from the CALIOP extinction coefficients) and by vertical integration the IWP_{CALIOP} used to train CiPS.

Fig. 4.24 shows two scatter plots with the IOT and IWP retrieved by CiPS and RAMSES for all eleven occasions. The RAMSES data, retrieved at a higher temporal resolution,
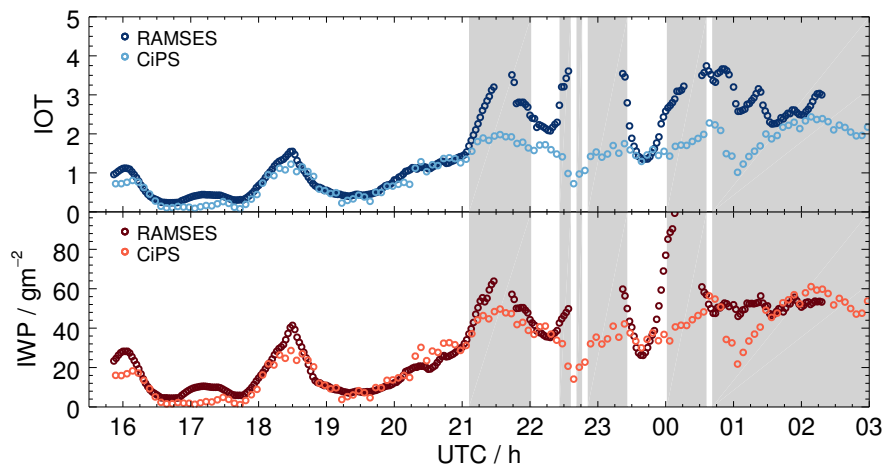
Figure 4.23: The IOT and IWP retrieved by CiPS and the ground-based Raman lidar RAMSES on 8–9 November 2015. Grey areas represent cirrus classified as opaque by CiPS.

have been averaged to the temporal resolution of CiPS. Furthermore, all retrievals classified as opaque by CiPS have been excluded. The agreement is generally good with a linear correlation of 0.81 and 0.70 for IOT and IWP respectively. Despite a good correlation, a slight negative bias for thinner cirrus is observed for CiPS, especially for the IWP_{CiPS} retrieval ($IWP_{RAMSES} \lesssim 5\,g\,m^{-2}$). Many occurrences below the 1-1 line could also be seen with respect to CALIOP in Figs. 4.11a and 4.12a. Moreover, CiPS tends to overestimate the IWP and to some extent the IOT with respect to RAMSES around $IWP_{RAMSES} \approx 12\,g\,m^{-2}$ and $IOT_{RAMSES} \approx 1.0$ respectively
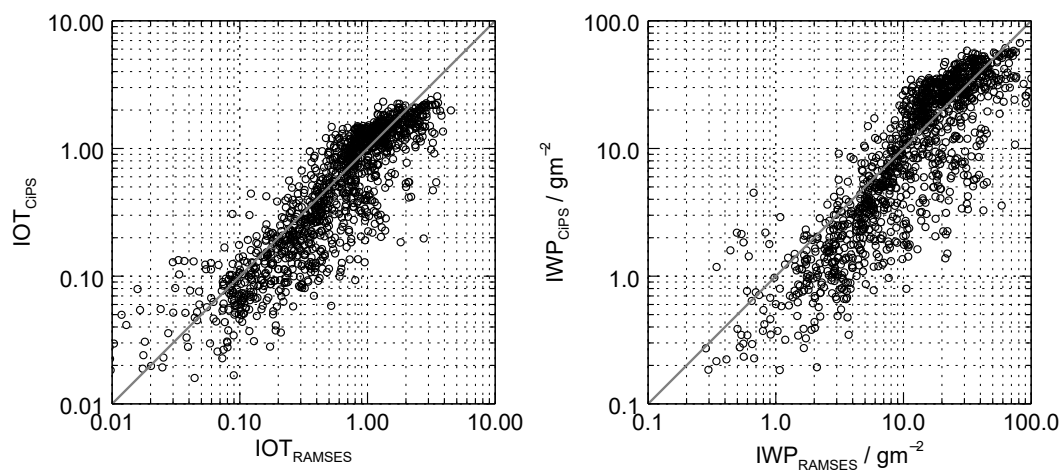
Figure 4.24: Scatter plots with the IOT and IWP retrieved by CiPS on the vertical axes and the corresponding RAMSES data on the horizontal axes. The grey lines represent the 1–1 line.

4.11.2 The airborne lidar WALES

WALES (Water Vapor Lidar Experiment in Space; Wirth et al., 2009; Kiemle et al., 2008) is an airborne differential absorption lidar developed at DLR. In addition to four channels around 932 nm for the retrieval of vertical profiles of water vapour mixing ratio, WALES is equipped with a polarization-sensitive high spectral resolution channel (Esselborn et al., 2008) at 532 nm, which allows for separation between molecular and particulate backscatter and hence measurements of particulate extinction, and by vertical integration, optical thickness. Measured extinction coefficients do, however, not account for multiple scattering effects, that increase with optical thickness.

During the Midlatitude Cirrus experiment (ML-CIRRUS; Voigt et al., 2017) in 2014, the German research aircraft HALO flew over a cluster of optically thin (IOT $\lesssim 0.2$) contrails, for which WALES could measure the extinction by ice and hence the IOT, with little effect from multiple scattering due to the low optical thickness. Figure 4.25 shows the WALES IOT for a time period of ≈ 12 min together with the corresponding IOT retrieved by CiPS. Although there are deviations, CiPS captures the evolution of the IOT very well, given the low optical thickness and the different observation techniques and sensitivities, with remarkable agreement for especially the first part. CiPS data are only shown where CiPS actually detects cirrus, leading to a small data gap around 15.86–15.88 h, where the contrail cluster remains undetected.
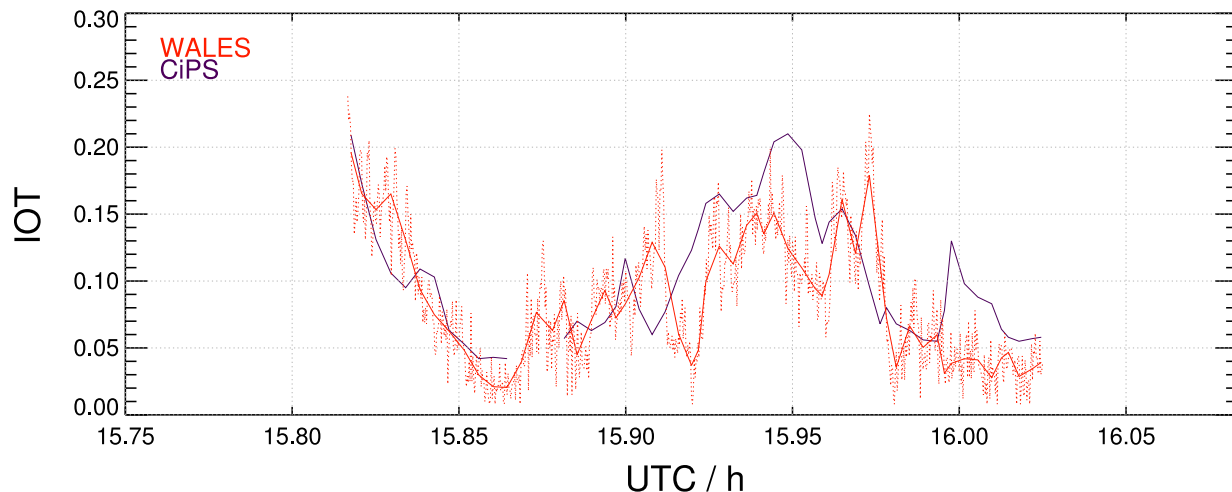
Figure 4.25: IOT retrieved by CiPS and the airborne high spectral resolution lidar WALES for an optically thin contrail cluster. WALES data are shown at full temporal resolution (dotted line) and as averages over the SEVIRI/CiPS pixels (solid line). Figure by L. Bugliaro (DLR).

4.12   Estimating the ice crystal effective radius

The effective radius (Sect. 2.2.1) is an important variable since it is closely related to the physical processes in cirrus clouds. The effective radius cannot be derived from CiPS (nor CALIOP) directly, but following Eq. (2.26) and assuming vertical homogeneity of the effective radius, it can be estimated from the two validated quantities $\mathrm{IOT_{CiPS}}$ and $\mathrm{IWP_{CiPS}}$ using the standard formula

$$\mathrm{REF_{CiPS}} = \frac{3 \cdot 10^6}{2\rho_{\mathrm{ice}}\,[\mathrm{g\,m^{-3}}]} \frac{\mathrm{IWP_{CiPS}}\,[\mathrm{g\,m^{-2}}]}{\mathrm{IOT_{CiPS}}\,[-]} = 1.64 \cdot \frac{\mathrm{IWP_{CiPS}}}{\mathrm{IOT_{CiPS}}} \qquad [\mathrm{\mu m}]. \qquad (4.2)$$

Since $\mathrm{IOT_{CiPS}}$ and $\mathrm{IWP_{CiPS}}$ both refer to the (same) upper part of the cloud, they should be affected similarly by the saturation of CiPS. Hence, the fraction $\mathrm{IWP_{CiPS}}/\mathrm{IOT_{CiPS}}$ allows for $\mathrm{REF_{CiPS}}$ retrievals for the entire cirrus (spatially) and not only for the pixels classified as transparent by CiPS. The accuracy of the $\mathrm{REF_{CiPS}}$ estimates is directly related to the accuracy of $\mathrm{IOT_{CiPS}}$, $\mathrm{IWP_{CiPS}}$ as well as the parameterisation in Eq. (4.2). Assuming vertical homogeneity in the anvil cirrus can introduce further uncertainties, but for the purpose of this thesis, which is to investigate patterns in the temporal evolution of the ice crystal sizes in anvil cirrus clouds, this parametrisation is assumed to be sufficient. The same formula is used by e.g. Bugliaro et al. (2011) and Stengel et al. (2014). Using $\mathrm{IOT_{CiPS}}$ and $\mathrm{IWP_{CiPS}}$ derived for the 1.3 million pixels in the final validation dataset (Sect.4.4.2) classified as cirrus by CiPS, $\mathrm{REF_{CiPS}}$ is sensitive to values ranging from 16 to 50 μm.

Chapter 5

The life cycle of anvil cirrus clouds

In this chapter the life cycle of anvil cirrus clouds and the temporal evolution of their macrophysical, microphysical and optical properties are analysed. CiPS (Chap. 4) is the primary tool for this task, together with a new cirrus tracking algorithm that has been developed in order to track the anvil cirrus clouds from the first detection after convective initiation of the cumulus clouds, until the dissipation of the anvil cirrus. Moreover, Cb-TRAM Stage 3 data (Sect. 3.4.1) are used to identify deep convective clouds and the combination of Cb-TRAM Stage 2 and 3 is used to monitor the convective activity of those clouds. Please note that the tracking and nowcasting of Cb-TRAM are not used for this study. Furthermore, the coldest brightness temperatures observed at $10.8\,\mu m$ in the convective cores (approx. absolute cloud top temperatures) have been used as a proxy for the convective strength to analyse the relationship between convective strength and anvil cirrus properties. Finally, modelled data from the ECMWF reanalysis dataset ERA5 (Sect. 3.4.2) have been used to characterise the meteorological conditions where the anvil cirrus clouds form, in order to investigate what meteorological conditions govern large and long-lived anvil cirrus clouds.

5.1 Cirrus tracking algorithm

To analyse the properties of selected anvil cirrus clouds throughout their life cycle, a cirrus tracking algorithm has been developed. To this end a pattern oriented cross-correlation technique is used. Cross-correlation is a commonly used technique for tracking clouds and deriving cloud motion vectors from geostationary imagers (e.g. Leese et al., 1971; Schmetz et al., 1993; Bolliger et al., 2003). The tracking algorithm works in synergy with CiPS and relies on its cirrus cloud masks.

5.1.1 Selecting a target to track

Figure 5.1 visualises the graphical user interface for the target selection developed for the new tracking algorithm. Figure 5.1a shows a false colour composite over south central
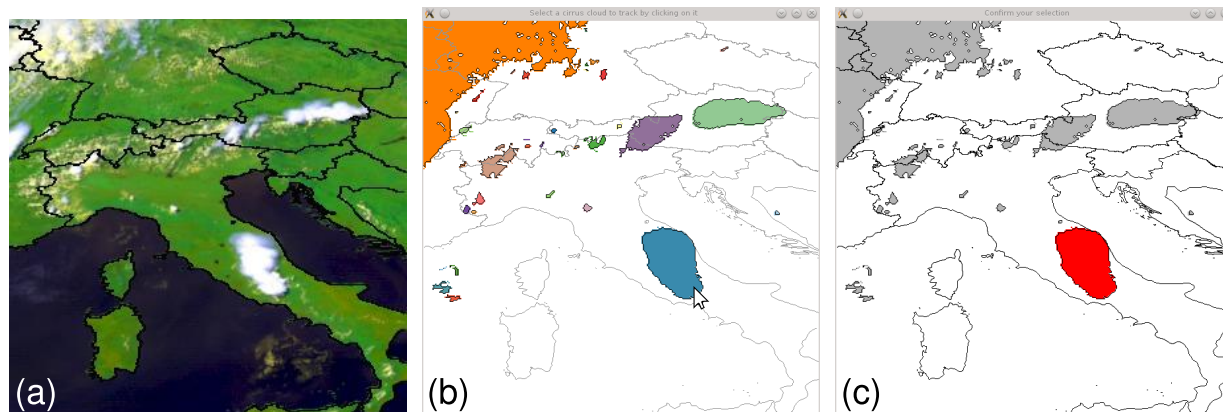
Figure 5.1: **(a)** MSG-2/SEVIRI false colour composite over south central Europe on 7 July 2015 at 14:00 UTC. **(b)** The corresponding CiPS cirrus cloud mask with individual cirrus clouds labelled with different colours. The pointer visualises the cloud selected with point-and-click by the user. **(c)** Same as **(b)**, but with the selected cirrus cloud highlighted in red for confirmation that the correct cloud was selected. All cirrus clouds smaller than 5 SEVIRI pixels are filtered out.

Europe on 7 July 2015 at 14:00 UTC as reference. The first step in the tracking algorithm is to choose a time when the tracking shall start. The algorithm then generates an image with an overview of all cirrus clouds (in the pre-defined geographical area) detected by CiPS (see Fig. 5.1b). To increase the contrast between different cirrus clouds, all clouds are labelled with individual colours. The second step is to select which cirrus cloud to track; this is done by simply clicking at the desired cloud. A new image is generated, highlighting the selected cirrus cloud (see Fig. 5.1c). If this is confirmed to be the desired cloud (with a terminal command by the user), the tracking starts. If not, the previous image with an overview of all cirrus clouds is re-generated (Fig. 5.1b) such that a new cirrus cloud can be selected.

5.1.2   Tracking the target

When a tracking target has been selected, the algorithm starts to track the selected cirrus cloud forward in time (with a similar approach as e.g. Bolliger et al. (2003)). The concept of the cirrus tracking technique is shown in a schematic form in Fig. 5.2. Figure 5.2a shows a cirrus cloud mask at time t, with the tracked cirrus cloud highlighted in red. The minimum bounding box enclosing the selected cirrus cloud at the present time slot t is identified as shown in Fig. 5.2b. Next, a search domain (dashed blue in Fig. 5.2b) is identified, in which the tracked cirrus will be searched for in the next time slot $t + dt$. The search domain is defined as the area covered by the minimum bounding box at t, plus x SEVIRI pixels in each direction. The number x is set by the user and determines the maximum allowed cloud displacement between two time steps. With small x ($x \to 0$), the tracking reminds of an overlapping tracking technique, where the tracked cirrus is expected
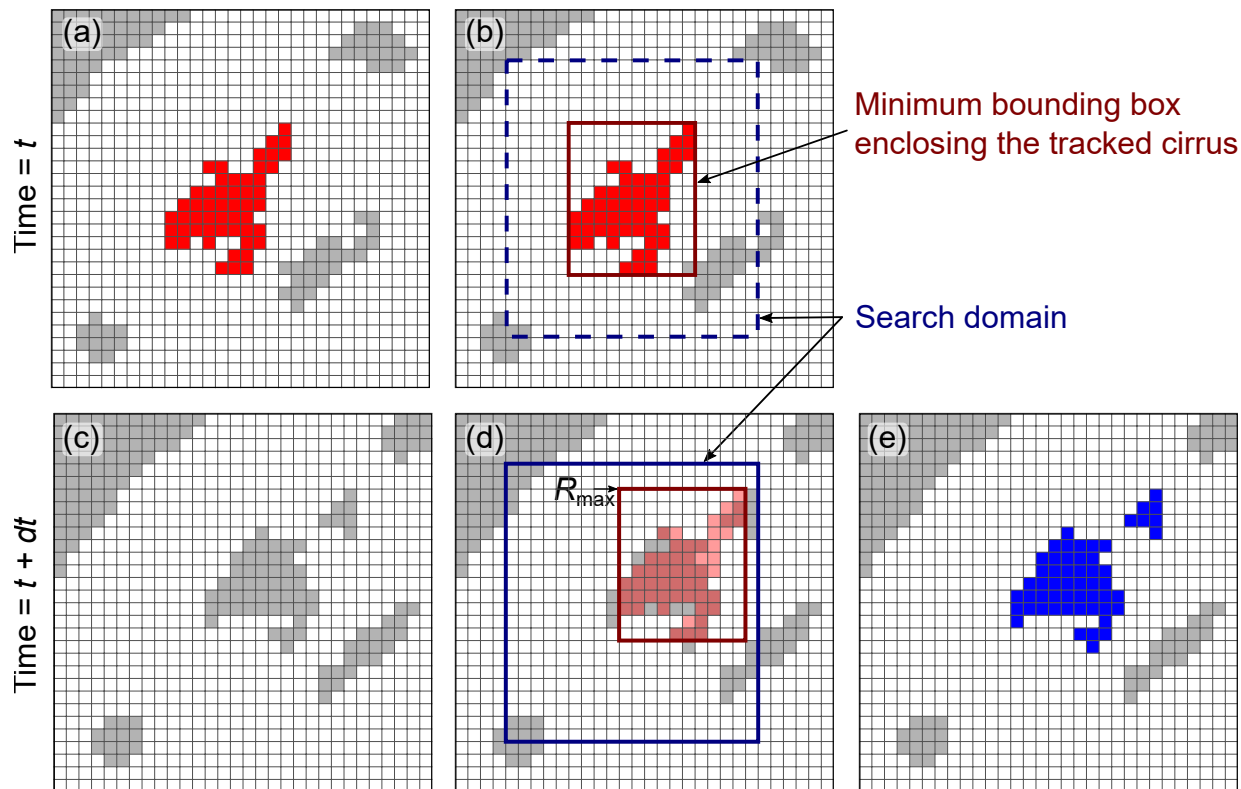
Figure 5.2: **(a)** Schematic cirrus cloud mask with the tracked cirrus cloud highlighted in red. **(b)** Same as **(a)**, but including the minimum bounding box enclosing the tracked cirrus cloud and the outline of the search domain used to identify the tracked cirrus at $t + dt$. **(c)** Schematic cirrus cloud mask at $t + dt$. **(d)** same as **(c)**, but including the search domain (solid blue, from **(b)**) and the point of maximum correlation ($R_{\max}$) between the minimum bounding box (solid red) enclosing the tracked cirrus cloud at t (transparent red) and the sub-domains of the search domain. **(e)** The cirrus cloud mask at $t + dt$ with the cirrus cloud(s) identified as the tracked cirrus highlighted in blue.

to spatially overlap with itself across two time slots (e.g. Williams and Jr., 1987; Arnaud et al., 1992). A larger x gives the tracking more flexibility since such an overlap in space and time is not required, which makes the tracking of small dissipating cloud fragments possible. In this study, the number x is set to equal the temporal resolution of the CiPS data in minutes (similar to Bolliger et al. (2003)). A temporal resolution dt of 5 min results in a search domain 5 pixels larger than the minimum bounding box in all directions. With pixel sizes of approx. $3.5 \times 5\,\mathrm{km}^2$ over Europe, this leads to a search domain that encloses any cloud moving at a speed of up to 58–$83\,\mathrm{m\,s}^{-1}$. For a few selected cases, a smaller x has been used in order to avoid that the wrong anvil cirrus is identified as the tracked cirrus in cases where more cirrus clouds are present close to each other.

Figure 5.2c shows the cirrus cloud mask at the next time slot $t + dt$. The search domain (solid blue in Fig. 5.2d) identified above at t is directly transferred to the cirrus cloud mask

at $t+dt$. Next, the bounding box (solid red in Fig. 5.2d) including the corresponding binary cirrus cloud mask of the tracked cirrus from time slot t (transparent red in Fig. 5.2d) is cross-correlated with the cirrus cloud mask enclosed by the search domain at $t+dt$. During the cross-correlation process the cirrus cloud mask (of the tracked cirrus) at t enclosed by the minimum bounding box is shifted pixel-wise in the horizontal and vertical direction within the search domain of the cirrus cloud mask at $t + dt$. At each position the linear Pearson correlation coefficient is calculated between the cirrus cloud mask of the tracked cirrus at t enclosed by the minimum bounding box and the sub-domain of the cirrus cloud mask at $t + dt$ and the position of maximum correlation R_{max} is identified. A cirrus cloud patch in the cirrus cloud mask at $t + dt$ is considered to be part of the tracked cirrus if it is completely or partly covered by the tracked cirrus enclosed by the bounding box from the previous time slot t at the point of maximum correlation. Such an overlap is represented by the darker red colour in Fig. 5.2d. This allows for a simultaneous tracking of multiple cirrus clouds in the likely event that the tracked cirrus breaks up into multiple smaller cloud patches. The cirrus cloud patches identified as the tracked cirrus at $t + dt$ are highlighted in blue in Fig. 5.2e. With this technique also the smaller patch no longer attached to the larger cirrus at $t + dt$ is identified as the tracked cloud. With a pure overlapping technique, without cross-correlation, that cirrus cloud patch would have been missed. When the tracked cirrus has been identified at $t + dt$, a new minimum bounding box enclosing the tracked cirrus as well as a new search domain for the next time slot $t + 2dt$ is defined. This procedure is repeated until the tracked cirrus cloud can no longer be detected (no valid correlation in the search domain). At that point, the tracking is repeated, but backwards in time starting again from the time slot t, defined above as the tracking starting time.

The output from the tracking algorithm is the information about which pixels at a specific time slot are part of the tracked cirrus cloud. The tracking algorithm itself is, in principle, not limited to cirrus clouds, but can also be used to track low liquid water clouds or other objects. In that case a corresponding cloud/pattern mask, that discriminates the clouds/patterns from the surroundings, must be provided instead of the cirrus clouds mask of CiPS.

5.2   Study region and anvil cirrus dataset

In this thesis, the life cycle of anvil cirrus clouds observed over Europe and the northernmost parts of Africa in July 2015 is analysed. This is the area observed by SEVIRI using the rapid scanning service (Sect. 3.1), which allows for a temporal resolution of 5 min for SEVIRI products (CiPS and Cb-TRAM). In a warming climate, where the amount of deep convection and anvil cirrus clouds can be expected to increase, it is also relevant to focus on the mid-latitudes where convective systems and anvil cirrus clouds can cover large areas during the summer season, making them an important component in the Earth's energy budget as well as the hydrological cycle. Moreover, one should not assume that previous findings on the anvil cirrus life cycle from studies focusing on the tropics (e.g. Machado

and Rossow, 1993; Chen and Houze, 1997; Mathon and Laurent, 2001; Luo and Rossow, 2004; Soden, 2004; Horváth and Soden, 2008; Sohn et al., 2008; Schröder et al., 2009; Inoue et al., 2009; Imaoka and Nakamura, 2012; Fiolleau and Roca, 2013; Protopapadaki et al., 2017) hold true for the mid-latitudes as well. To analyse the temporal evolution of the anvil cirrus properties from convective initiation until the anvil has fully dissipated or can no longer be detected by CiPS, spatially isolated anvil cirrus clouds are favourable. Therefore, anvil cirrus clouds are excluded from the analysis if throughout their life cycle they merge with another cirrus cloud that does not stem from the convective cell(s) from which the tracked anvil cirrus formed.

In total, 132 isolated anvil cirrus clouds were identified (by visual inspection of false colour composites), classified as cirrus clouds (with CiPS), classified as having a convective origin (using Cb-TRAM Stage 3, see Sect. 3.4.1) and tracked, as described above, from the first detection after convective initiation to the point when they are too optically thin for CiPS to detect them. The information from Cb-TRAM Stage 2 and 3 is used to objectively identify convective activity in the cumulonimbus clouds from which the anvil cirrus form.

Figure 5.3 shows the trajectories of all tracked anvil cirrus clouds. Most of the isolated anvil cirrus clouds are found in southern Europe and the northernmost parts of western Africa. Here, the air in sufficiently warm and moist in summer to generate deep convection, and frontal cirrus clouds comparably rare which governs formation of isolated anvil cirrus clouds. Nearly all anvils originate from cumulonimbus clouds that form over land and typically in areas with high orography, which further governs the formation of cumulonimbus clouds and hence anvil cirrus clouds. Although cumulonimbus clouds are commonly observed in the Alps and Pyrenees during the summer season (Morel and Senesi, 2002), it rarely leads to the formation of *isolated* anvil cirrus clouds. The trajectories vary among
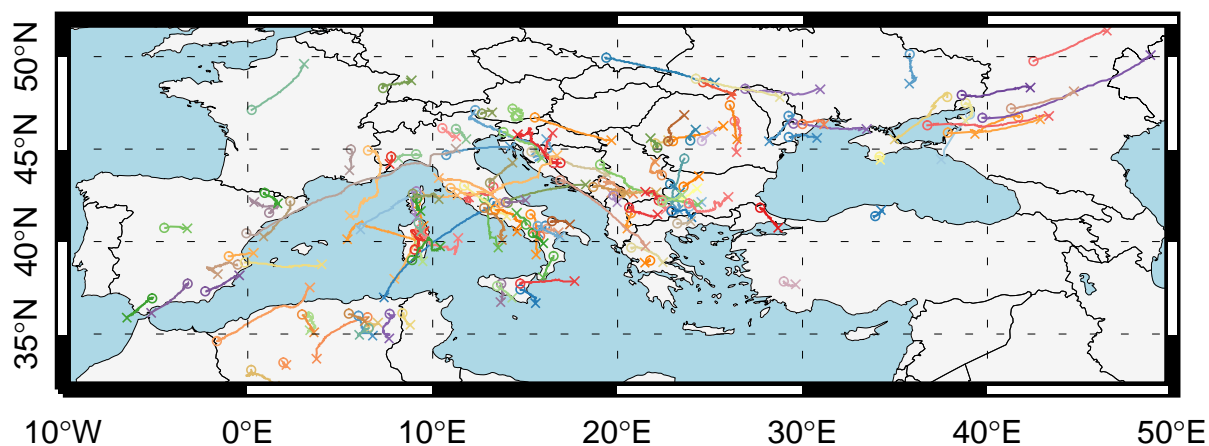

Figure 5.3: Trajectories of the 132 anvil cirrus clouds (w.r.t. the centroid) whose life cycles are analysed in this chapter. The circles (○) indicate the point of formation and crosses (×) the point of the last detection.

the tracked anvil cirrus, but often an eastward direction induced by the westerlies can be observed.

Figure 5.4 shows the distribution of the local time when the convective systems and anvil cirrus clouds are first and last detected. Similar to the climatology of mesoscale convective systems over Europe by Morel and Senesi (2002), most convective systems from which the anvils form are usually first detected at afternoon, between 12:00–17:00, while last detection usually occurs between 18:00–24:00. A substantial part of the anvils remain into late evening, where their radiative forcing on the Earth–atmosphere system is bound to be positive.
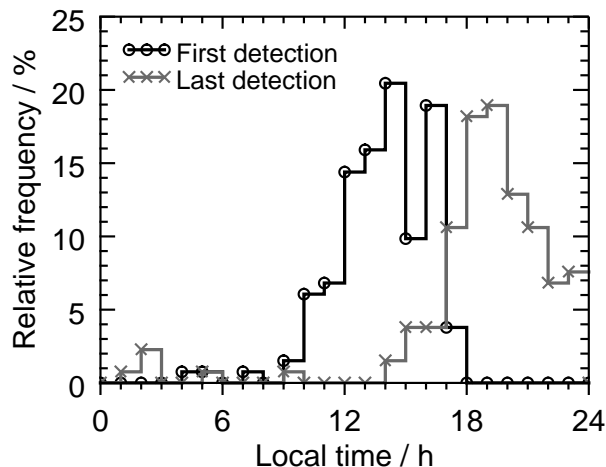
Figure 5.4: Local times of first and last detection (by CiPS) of the 132 isolated convective systems and following anvil cirrus clouds.

5.3   Case study

In this section, the anvil cirrus life cycle is analysed with a case study (a statistical analysis is presented in Sect. 5.4). The purpose of the case study is to illustrate the concept of using CiPS, the tracking algorithm and parts of Cb-TRAM for the analysis of the anvil cirrus life cycle. A case study also allows for a more detailed analysis and is helpful for interpreting the results of the statistical analysis.

The anvil cirrus cloud analysed in this section was observed over Italy on 7–8 July 2015. The cloud was first observed by CiPS at 7 July 11:30 UTC and last observed 14 hours later at 01:25 UTC on 8 July. This anvil cirrus is selected for the case study since it is comparably large and long-lived, but still spatially isolated from other cirrus clouds. Hence, it is more representative for larger mesoscale convective systems. Furthermore, the long lifetime allows for detailed analysis of the different life cycle stages. Please note that in the following the term *lifetime* refers to the anvil cirrus lifetime observed by CiPS (i.e. from first detection after convective initiation to last detection by CiPS), which might deviate from the actual lifetime due to CiPS lower sensitivity to sub-visual cirrus clouds. This anvil cirrus is also interesting since it was observed several hours after sunset, where it has an entirely warming effect on the Earth–atmosphere system. Although this anvil cirrus is larger and more long-lived than most of the other anvil cirrus clouds tracked and analysed in this study, the temporal evolution of its properties is to a large extent representative for the ensemble of anvil cirrus clouds analysed in Sect. 5.4.

Figure 5.5 shows the temporal evolution of the anvil cirrus cloud at a temporal resolution of 30 min using SEVIRI false colour RGB composites. The red contours show the cirrus cloud mask of CiPS and the purple contours show the areas of convective activity as observed with Cb-TRAM. The time is normalized with respect to the point of last convective activity that was observed at 16:50 UTC. Hence 00:00 h represents 16:50 UTC
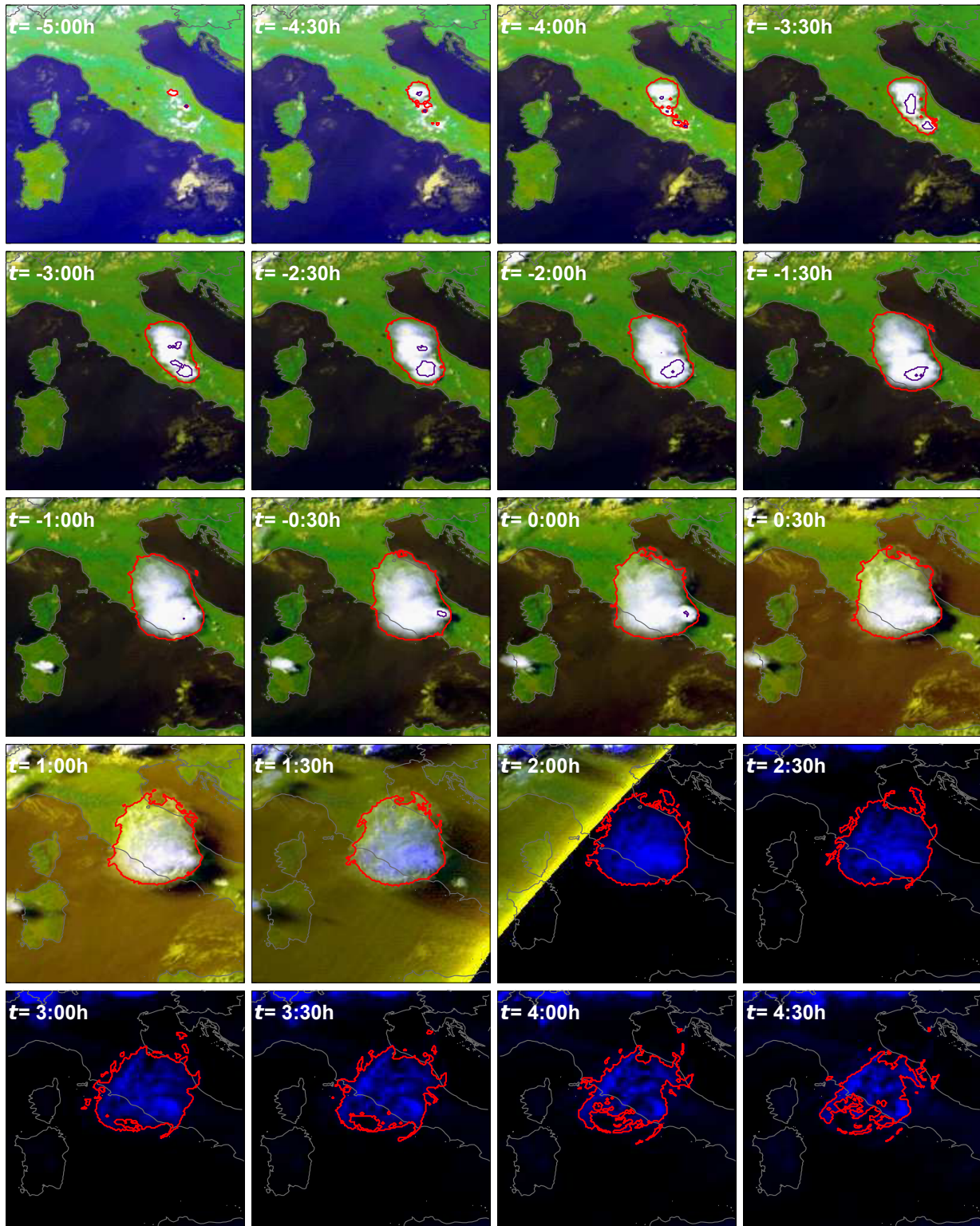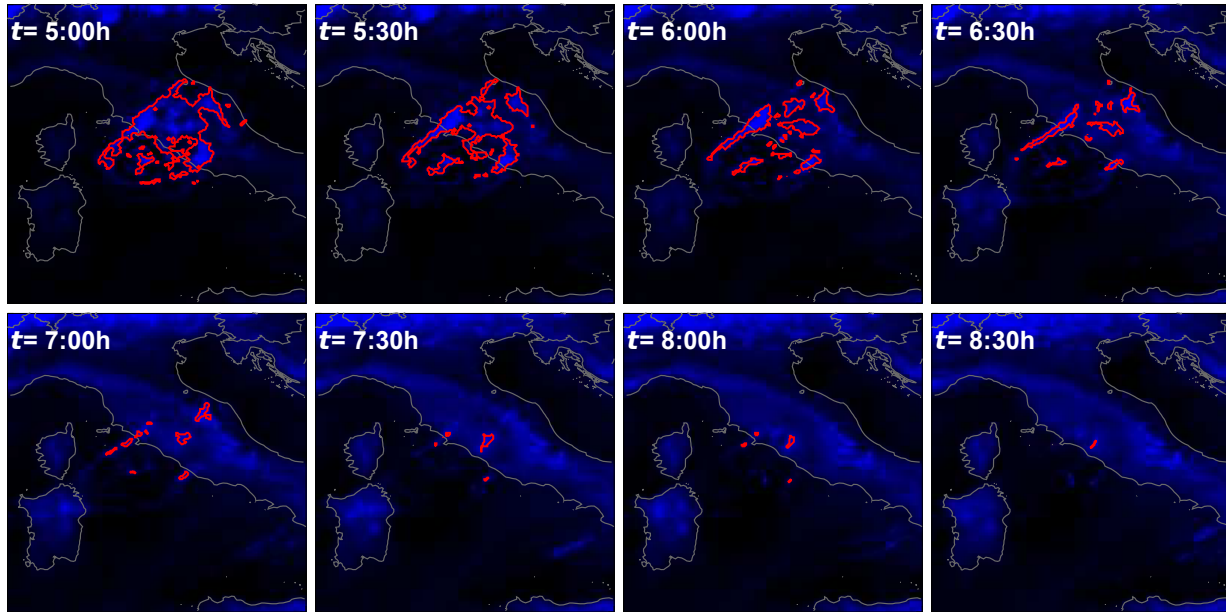
Figure 5.5: SEVIRI false colour RGB composites showing the temporal evolution (at 30 min temporal resolution) of the anvil cirrus cloud over Italy on 7–8 July, 2015. The red and purple contours show the CiPS cirrus cloud mask and the area of convective activity as observed with Cb-TRAM (Stage 2 and 3) respectively. The time has been normalised with respect to the point of last convective activity that was observed by Cb-TRAM at 16:50 UTC, such that a positive t indicates that convection has ceased. In the absence of solar radiation, the RGB composites rely on a single thermal channel leading to a solely blue contribution after sunset.

and e.g. $\pm 04{:}00$ h represents 20:50 UTC and 12:50 UTC respectively. This way a positive time always indicates that convection has ceased. Normalising the lifetime with respect to the point of last observed convective activity (similar to e.g. Luo and Rossow, 2004), rather than a normalisation (e.g. between 0 and 1) of the entire lifetime (e.g. Fiolleau and Roca, 2013) or a normalisation with respect to the observed peak in convective activity (e.g. Soden, 2004; Sohn et al., 2008; Horváth and Soden, 2008; Schröder et al., 2009) allows for a more differentiated analysis of the life cycle phases and a better understanding of the temporal evolution and dissipation of the anvil cirrus from the point when the convective updraught of moisture ceases and the anvil has to "live on its own".

5.3.1   Temporal evolution of the anvil cirrus properties

Figure 5.6 shows the temporal evolution of the spatial extension, i.e. the horizontal area at the cloud top, throughout the life cycle of the anvil cirrus cloud shown in Fig. 5.5 at the full temporal resolution of 5 min. The blue colour represents the cirrus area classified as transparent by CiPS, whereas the grey colour represents the area classified as opaque by CiPS i.e. where IOT_{CiPS} and IWP_{CiPS} should not be trusted (Sect. 4.1). Again the
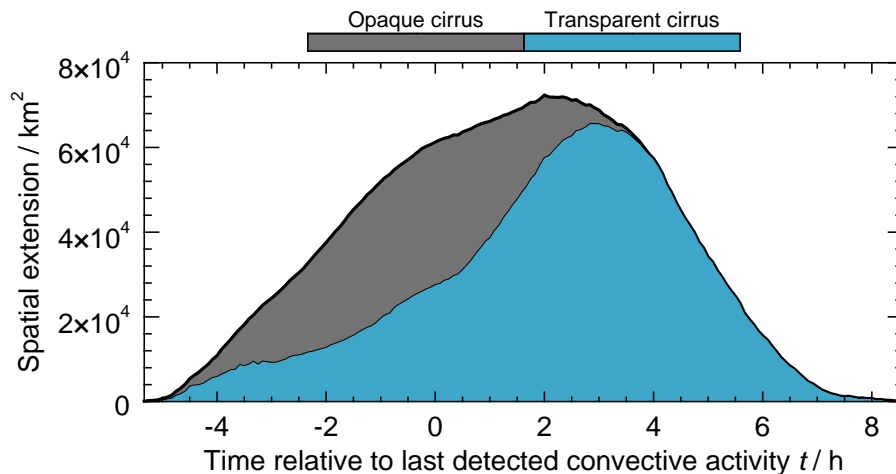
Figure 5.6: Temporal evolution of the anvil cirrus spatial extension together with information about cirrus transparency/opacity as classified by CiPS. $t = 0\,$h denotes the point when the last convective activity was observed with Cb-TRAM.

time has been normalised with respect to the point when the last convective activity was observed with Cb-TRAM.

During the convective phase (negative t) the anvil cirrus grows spatially at a rather constant pace of $10\text{--}15\,000\,\text{km}^2\,\text{h}^{-1}$. When convection ceases the anvil cirrus continues to grow for another two hours, but at a reduced pace of around $5\,000\,\text{km}^2\,\text{h}^{-1}$. As soon as the maximum spatial extension of approx. $70\,000\,\text{km}^2$ is reached, the anvil cirrus starts to become smaller at an increasing pace for $\approx 4\,$h and then at a constant and comparably high pace (w.r.t. the growth) for another $2.5\,$h until the observed anvil covers an area of $10\,000\,\text{km}^2$. During the last $2\,$h the anvil cirrus is continuously becoming smaller at a decreasing pace until it can no longer be detected by CiPS approx. $8.5\,$h after convection ceased. During the convective stage (negative t), the opaque fraction is generally increasing, until $66\,\%$ of the anvil is classified as opaque at $t = -1.5\,$h. At this point the fraction of transparent cirrus starts to increase slowly for $2\,$h and then rapidly ca. $0.5\,$h after convection ceased. $2\,$h after convection has ceased, $80\,\%$ of the cirrus is transparent and after another $2\,$h, there are no opaque pixels left. Thus, the anvil is becoming thinner, although it increases in size after convection has ceased. Please remember that the transparency and opacity indicate whether the observed cirrus is optically thin enough (transparent) or too optically thick (opaque) for CiPS to retrieve reliable IOT_{CiPS} and IWP_{CiPS}.

Figure 5.7 shows the temporal evolution of the (a) CTH_{CiPS}, (b) IOT_{CiPS}, (c) IWP_{CiPS} and (d) REF_{CiPS} throughout the life cycle of the anvil cirrus at a temporal resolution of $5\,$min. Due to the lack of reliable IOT_{CiPS} or IWP_{CiPS} data for opaque pixels, no information is available for the median, 75th and 95th percentiles during large parts of the convective stage.

In the very beginning CTH_{CiPS} increases rapidly as the cumulonimbus cloud develops in the vertical. The updraught of moisture leads to ice crystal formation and growth,
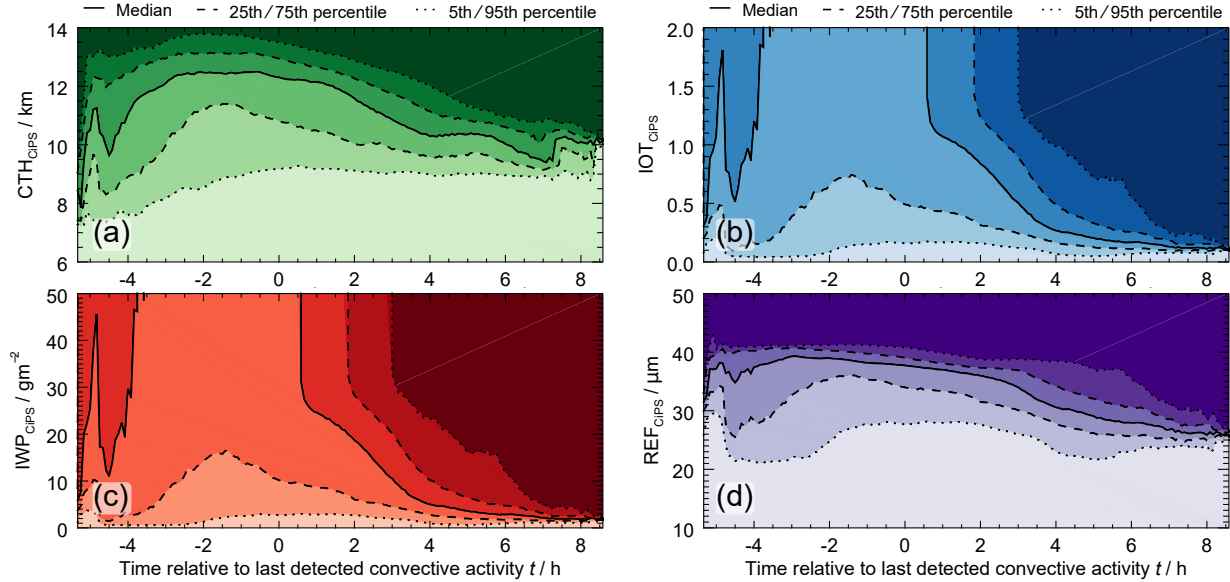
Figure 5.7: Temporal evolution of the anvil cirrus **(a)** CTH_{CiPS}, **(b)** IOT_{CiPS}, **(c)** IWP_{CiPS} and **(d)** REF_{CiPS} throughout the life cycle. $t = 0\,h$ denotes the point when the last convective activity was observed with Cb-TRAM.

which is reflected in the corresponding initial growth of IOT_{CiPS}, IWP_{CiPS} and REF_{CiPS}. Notice that the first part of convection, where liquid droplets are formed, is not observed by CiPS. Due to additional, less developed, convective cores starting shortly after the first detection, there is a sudden drop in the anvil properties at $t = -5\,h$. After approx. two hours ($t = -3\,h$) the convective system is fully developed with a median CTH_{CiPS} of $12.5\,km$ and with $25\,\%$ of the anvil above $13\,km$. During the convective phase, the cirrus is mostly too thick for CiPS to retrieve reliable IOT_{CiPS} and IWP_{CiPS}; up to $65\text{--}70\,\%$ of the anvil is opaque or has $IOT_{CiPS} \geq 2.0$ and $IWP_{CiPS} \geq 50\,g\,m^{-2}$. $25\,\%$ of the anvil is comparably thin though, probably as a result of the convective outflow, with $IOT_{CiPS} < 0.2 - 0.7$ and $IWP_{CiPS} < 4 - 16\,g\,m^{-2}$. REF_{CiPS} is comparably homogeneous. The median, 25th and 5th REF_{CiPS} percentiles increase during the first phase of convection, with values around 28, 35 and $38\,\mu m$ respectively at $t = -1\,h$. The 95th percentile remains constant around $40\,\mu m$ during the convective phase, suggesting a continuous supply of larger ice crystals that compensates for those lost due to sedimentation.

When convection ceases (at $t = 0\,h$) the anvil cirrus starts to lose both height, IOT and IWP. The decrease in IOT_{CiPS} and IWP_{CiPS} is quite rapid and already three hours after convection has ceased, $95\,\%$ of the anvil cirrus has $IOT_{CiPS} \lesssim 1.4$ and $IWP_{CiPS} \lesssim 30\,g\,m^{-2}$. Furthermore, $50\,\%$ of the anvil cirrus has $IOT_{CiPS} \lesssim 0.5$ and $IWP_{CiPS} \lesssim 10\,g\,m^{-2}$. While the median, 75th and 95th CTH_{CiPS} percentiles clearly decreases, from $12.3\text{--}13.5\,km$ at $t = 0\,h$ to $10\text{--}10.6\,km$ at $t = 8\,h$, the 5th CTH_{CiPS} percentile remains constant around $9\,km$. This could be an indication that ice crystals falling below $\approx 9\,km$ either sublime or melt. During the same time period, and starting already before convection ceases, REF_{CiPS}

continuously decreases. This supports the idea that larger ice crystals continuously fall out with a limited production of new large crystals towards the end of, and especially after, the convective updraught.

5.4 Statistical analysis

In this section the life cycle of anvil cirrus clouds is investigated with a statistical approach using all 132 isolated anvil cirrus clouds, whose trajectories are depicted in Fig. 5.3. First, the temporal evolution of CTH_{CiPS}, IOT_{CiPS}, IWP_{CiPS} and REF_{CiPS} probability density functions is investigated. Second, the effect of the convective strength on the anvil cirrus properties and their temporal evolution is analysed. Third, ECMWF ERA-5 data are used to investigate under what meteorological conditions, large and long-lived anvil cirrus clouds form.

5.4.1 Temporal evolution of the anvil cirrus properties

Figure 5.8 shows the temporal evolution of the spatial extension for the 132 isolated anvil cirrus clouds (Sect. 5.2). Again the time has been normalised with respect to the point of last detected convective activity for each individual anvil, such that a positive t means that deep convection is no longer active according to Cb-TRAM. The lifetime and spatial extension is highly variable between the single anvil cirrus as a result of variable meteorological conditions (e.g. temperature, humidity, atmospheric instability). Some anvils are only observed for 1–2 h after convection has ceased and reach a maximum spatial extension of approx. $1000\,\mathrm{km^2}$, while others grow up to 80 times larger and are observed for up to 15 h. The well-established positive correlation between the size of convective systems and anvil cirrus and their observed lifetime (e.g. Chen and Houze, 1997; Machado et al., 1998;
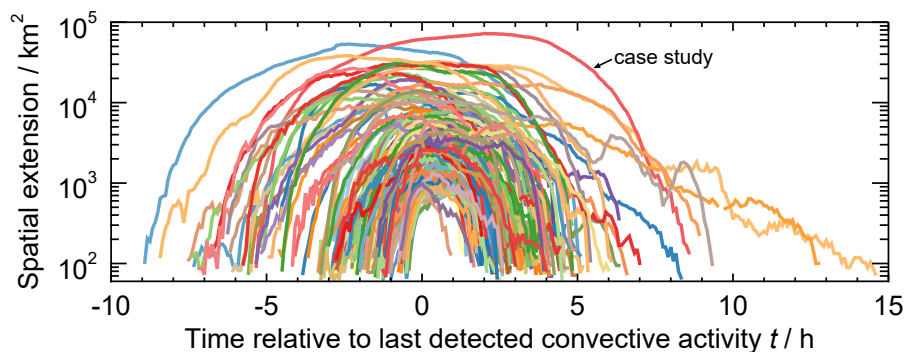

Figure 5.8: Temporal evolution of the spatial extension for the 132 isolated anvil cirrus clouds. The line colours correspond to those used for the trajectories depicted in Fig. 5.3. $t = 0\,\mathrm{h}$ denotes the point when the last convective activity was observed with Cb-TRAM. The anvil cirrus cloud analysed in Sect. 5.3 is indicated with an arrow.

Mathon and Laurent, 2001; Inoue et al., 2009; Feng et al., 2012; Imaoka and Nakamura, 2012) is clearly represented by this dataset as well. For most anvil cirrus clouds, the maximum spatial extension is reached shortly after the point of last observed convective activity ($t = 0.35 \pm 0.9$ h on average), which is shorter than for the case study, where the growth continued for two hours after convection ceased (see Fig. 5.6). This should be in line with the typical anvil spreading time (between peak convective activity and maximum spatial extension) of approx. 1–5 h observed in previous studies (e.g. Soden, 2004; Horváth and Soden, 2008; Sohn et al., 2008; Schröder et al., 2009). While the average time it takes to reach the point of maximum spatial extension is 2.6 ± 1.6 h, it takes slightly longer, 3.2 ± 2.0 h, for the anvil cirrus to dissipate and become invisible to CiPS. There are, however, cases that deviate from this pattern where the dissipation is slower, with especially two anvil cirrus clouds that live for 13–15 h after convection has ceased. Most likely, those anvils formed in and/or were transported to areas with meteorological conditions favourable for the anvil cirrus to persist (as proposed by Luo and Rossow, 2004), such as ice supersaturated regions.

Figures 5.9–5.12 show the temporal evolution of the CTH_{CiPS}, IOT_{CiPS}, IWP_{CiPS} and REF_{CiPS} probability density functions at a temporal resolution of 60 min. The solid lines represent the mean value across the ensemble of 132 anvil cirrus clouds and the shaded areas represent the corresponding standard deviations. Again the time has been normalised with respect to the point of last convective activity and ranges from four hours before convection ceases ($t = -4$ h) up to ten hours after ($t = 10$ h). Please note that the number of anvil cirrus (N) used to calculate the statistics at each time step varies due to the varying lifetimes of the individual anvil cirrus clouds and that only a few isolated anvils cirrus were observed longer than 8 h after convection ceased (Fig. 5.8), making the statistical analysis towards the end of the life cycle less certain for those long-lived anvil cirrus. All pixels classified as opaque by CiPS are contained in the last respective bins for IOT_{CiPS} and IWP_{CiPS}. Please note that the probability density function data are available at 5 min temporal resolution but shown at 1 h resolution here due to limited space.

For CTH_{CiPS}, a comparably large variability in the form of larger standard deviations is observed. This can be attributed to varying tropopause and equilibrium layer heights and different convective strengths (Sect. 5.4.2). Nevertheless, similar patterns in the temporal evolution of CTH_{CiPS} are observed. During the convective stage (negative t), the maximum relative frequency is shifted towards higher CTH_{CiPS} ($\approx 10 - 11$ km on average). But even at $t = 0$ h, $CTH_{CiPS} < 8$ km are observed and minimum CTH_{CiPS} around 6 km indicates that convection has brought up liquid water to this height before freezing. When convection ceases the anvil cirrus sink for a short period of time until most of the anvil top remains quite stable around 8.5–10.5 km on average from approx. 3 h after convection has ceased and onwards. A general decrease with time as seen for the case study and with active satellite remote sensing in Bouniol et al. (e.g. 2016) is not present here. It is also evident that the lower parts of the anvil are removed as convections ceases, possibly due to sublimation at those lower warmer altitudes.

For IOT_{CiPS} and IWP_{CiPS}, the variability across the ensemble of anvil cirrus clouds is comparably small. During the convective phase the anvil cirrus are mostly too thick for CiPS to retrieve reliable IOT_{CiPS} and IWP_{CiPS} and when convection ceases at $t = 0$ h, ap-
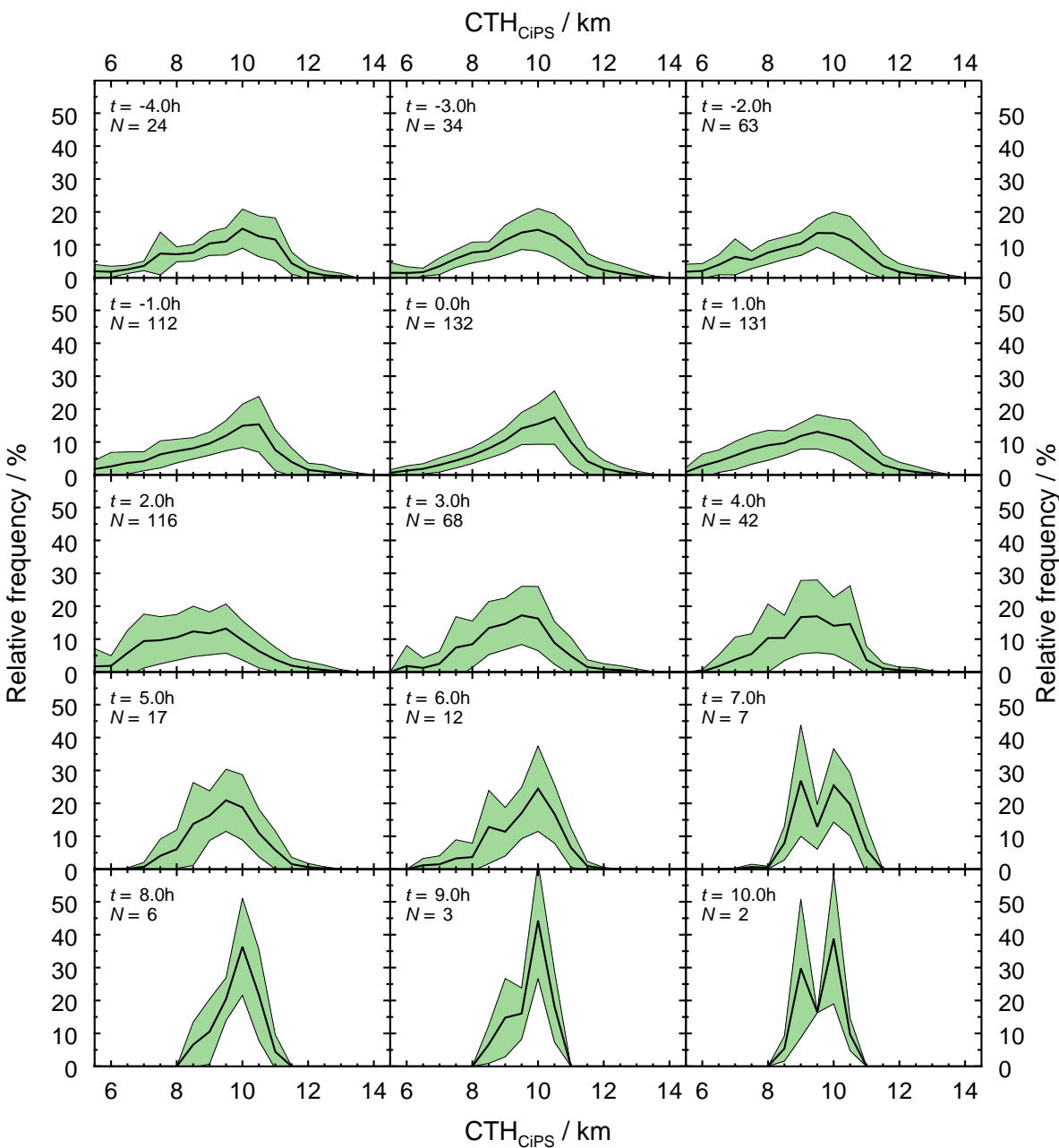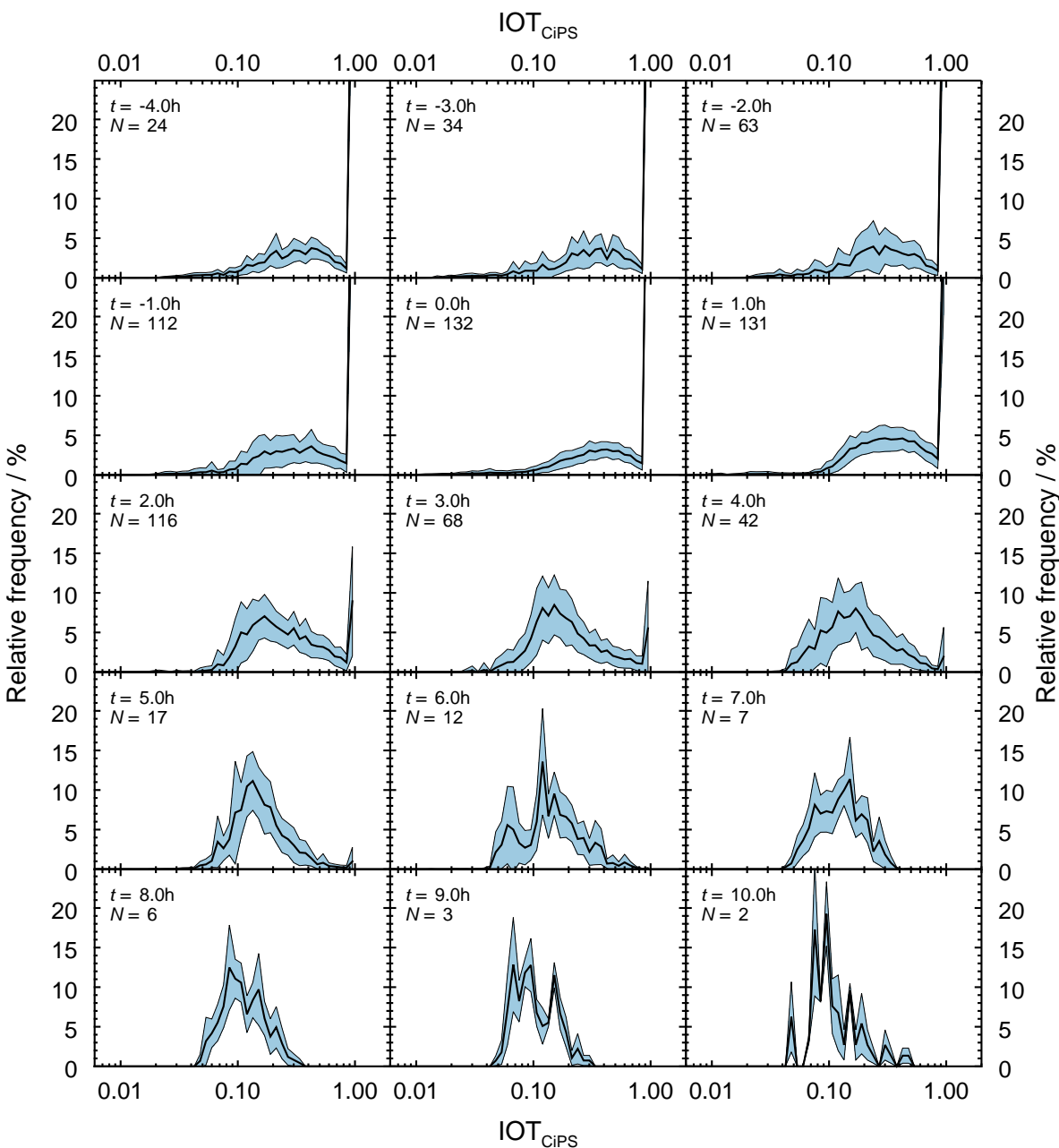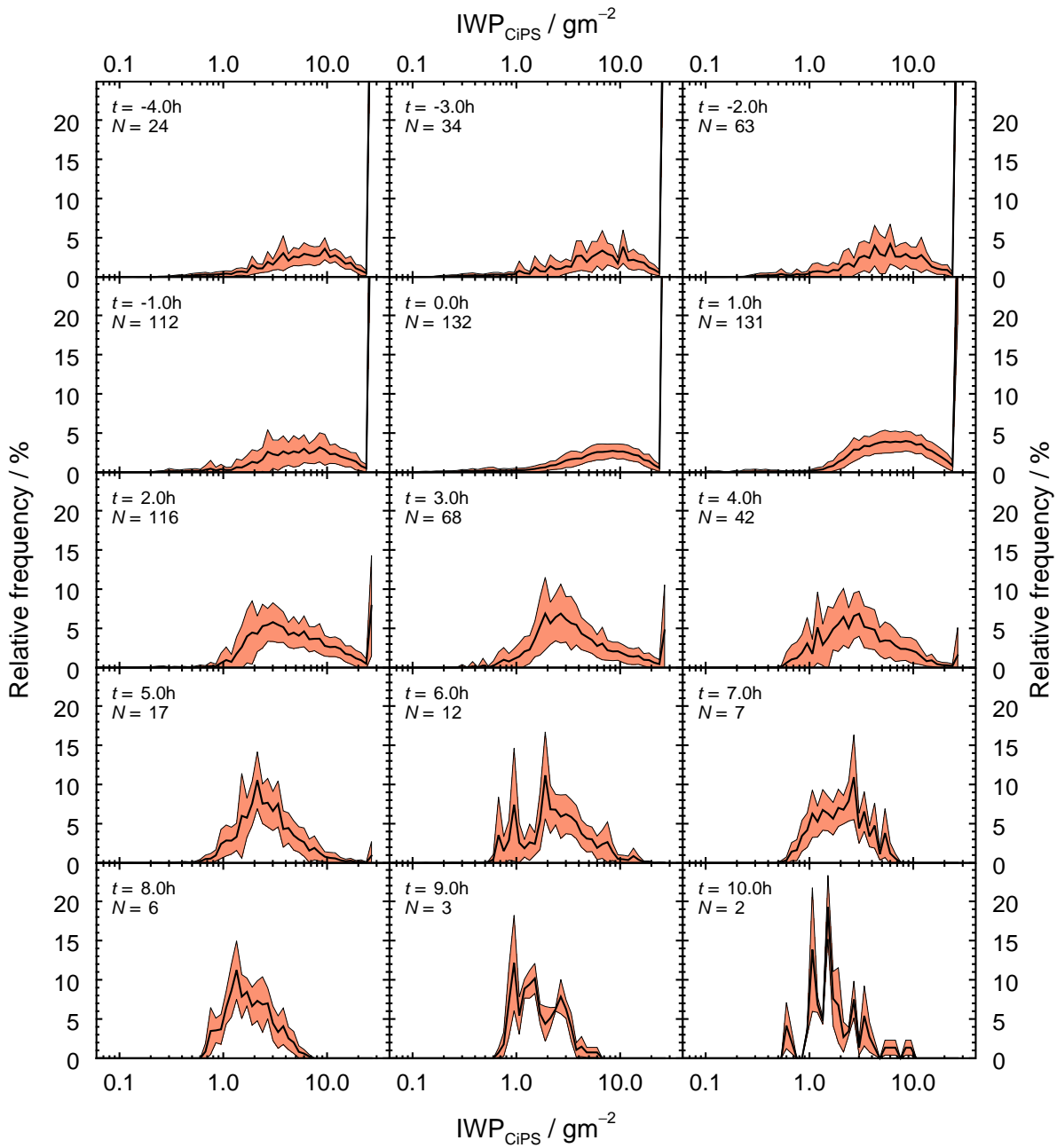
Figure 5.9: Temporal evolution of the anvil cirrus average CTH_{CiPS} probability density function (solid lines) and corresponding standard deviations (shaded areas) at a temporal resolution of 60 min. $t = 0$ h denotes the point when the last convective activity was observed with Cb-TRAM.

prox. 55 % of the anvil is opaque or have $IOT_{CiPS} > 1.0$ or $IWP_{CiPS} > 30$ g m^{-2} on average. For the thinner 45 % of the anvil, IOT_{CiPS} and IWP_{CiPS} are quite evenly distributed be-

Figure 5.10: Temporal evolution of the anvil cirrus average IOT_{CiPS} probability density function (solid lines) and corresponding standard deviations (shaded areas) at a temporal resolution of 60 min. $t = 0\,h$ denotes the point when the last convective activity was observed with Cb-TRAM.

tween 0.15–0.8 and 3–20 $g\,m^{-2}$ respectively at this point. When convection ceases IOT_{CiPS} and IWP_{CiPS} decrease rapidly, even more rapidly than for the case study. Within 2 h after

Figure 5.11: Temporal evolution of the anvil cirrus average IWP_{CiPS} probability density function (solid lines) and corresponding standard deviations (shaded areas) at a temporal resolution of $60\,min$. $t = 0\,h$ denotes the point when the last convective activity was observed with Cb-TRAM.

convection has ceased, the relative frequency of the rightmost bins, containing pixels that are opaque or have $IOT_{CiPS} > 1.0$ and $IWP_{CiPS} > 30\,g\,m^{-2}$ respectively, is reduced from
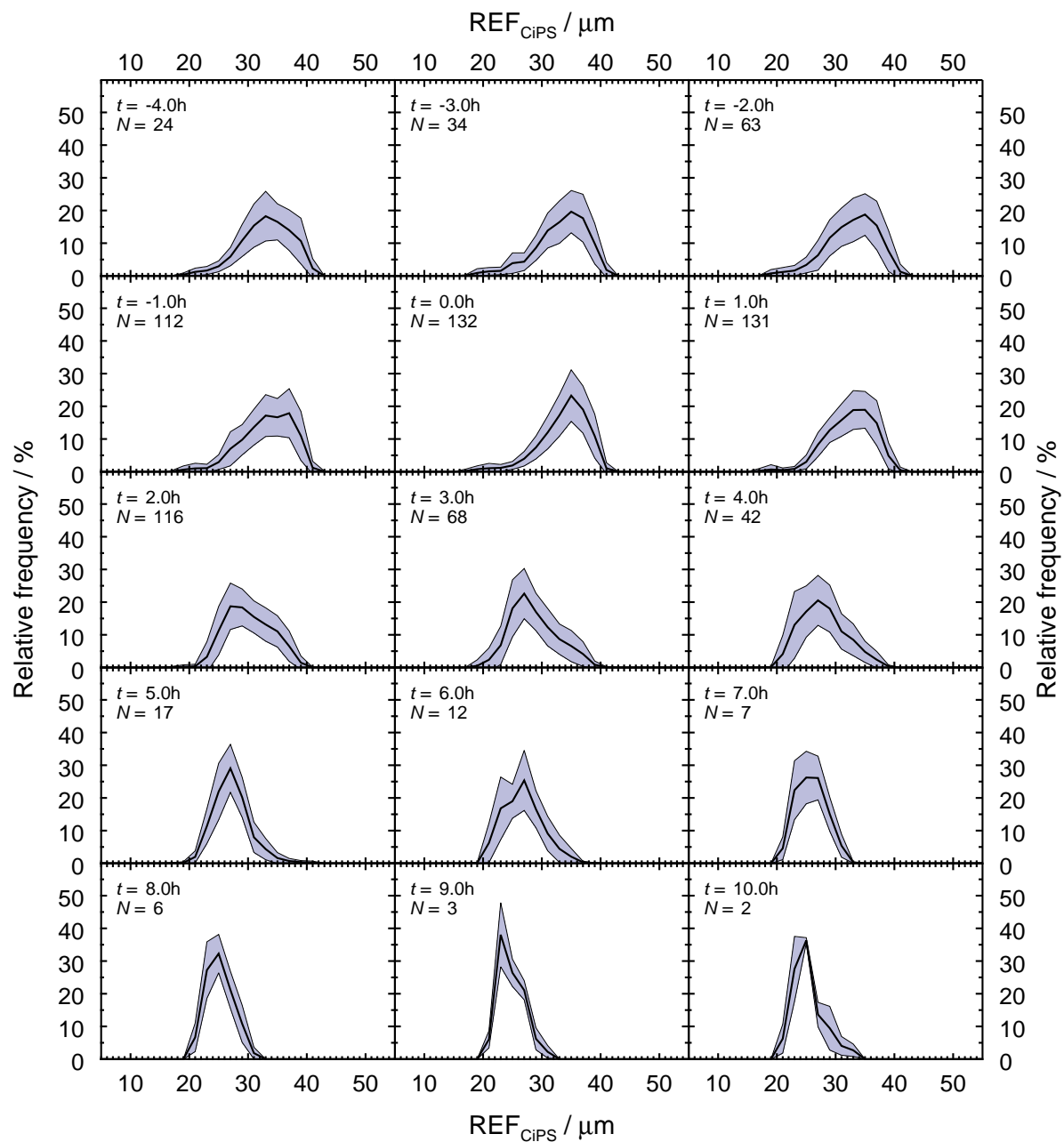
Figure 5.12: Temporal evolution of the anvil cirrus average REF_{CiPS} probability density function (solid lines) and corresponding standard deviations (shaded areas) at a temporal resolution of 60 min. $t = 0$ h denotes the point when the last convective activity was observed with Cb-TRAM.

55 % to 8±6.6 % on average. This is considerably faster than the decrease in IOT and IWP for tropical anvils observed by Luo and Rossow (2004), Horváth and Soden (2008)

and (Mace et al., 2006). The anvils are gradually becoming thinner with time during the non-convective stage, with the maximum relative frequencies being shifted towards lower IOT_{CiPS} and IWP_{CiPS}. Four hours after convection has ceased and onwards, most of the anvil has $IOT_{CiPS} \approx 0.07 - 0.4$ and $IWP_{CiPS} \approx 1.0 - 6.0\,\mathrm{g\,m^{-2}}$ on average.

REF_{CiPS} slightly increases during the convective stage and when the convective activity is observed to cease at $t = 0\,\mathrm{h}$, REF_{CiPS} peaks at $35\,\mu\mathrm{m}$. When convection ceases there is a sudden drop in REF_{CiPS}, possibly due to quick sedimentation of the larger ice crystals, and $2\,\mathrm{h}$ after convection the relative frequency peaks below $30\,\mu\mathrm{m}$. $5\,\mathrm{h}$ after convection has ceased and onwards, most REF_{CiPS} are observed in the range 20–$30\,\mu\mathrm{m}$ on average, with decreasing crystal sizes. This is in line with the decreasing radar reflectivities and narrowing reflectivity distributions observed by Yuan et al. (2011), suggesting smaller ice crystals and less ice crystal size variability further away from the convective event. The numbers are similar to the average REF of $33\,\mu\mathrm{m}$ retrieved in the upper part of a tropical anvil cirrus from in situ measurements (Jensen et al., 2009). Larger average REF (40–$48\,\mu\mathrm{m}$) sampled from the same in situ flight, but 2–$3\,\mathrm{km}$ from the cloud top indicate that REF_{CiPS} is probably more representative for the upper part of the anvil cirrus and not sensitive to larger aggregates located further down in the anvil.

While small standard deviations from the average curve are observed for the temporal evolution of IOT_{CiPS} and IWP_{CiPS}, comparably large standard deviation are observed for REF_{CiPS} and especially CTH_{CiPS}. This is an indication that different meteorological conditions and properties of the convective system might have a comparably small impact on IOT_{CiPS} and IWP_{CiPS} compared to REF_{CiPS} and CTH_{CiPS}, where more variability among the 132 anvil cirrus clouds is observed.

5.4.2 Relationship between convective strength and the anvil cirrus life cycle

In a warming climate, more and stronger convection can be expected. In this section, this is addressed by defining a proxy for convective strength and analysing the anvil cirrus properties and their temporal evolution throughout the life cycle as a function of this proxy. Moreover, variability in the convective strength might explain some of the variability with respect to the life cycle of anvil cirrus clouds and the temporal evolution of their properties observed in Sect. 5.4.1.

For this study the coldest SEVIRI brightness temperature observed at $10.8\,\mu\mathrm{m}$ ($BT_{10.8\mu\mathrm{m}}^{\mathrm{min}}$) throughout the anvil cirrus life cycle is used as a proxy for the convective strength. For deep convective cumulonimbus clouds, opaque ($\epsilon \approx 1$) to up-welling thermal radiation, $BT_{10.8\,\mu\mathrm{m}}$ is a good estimate for the absolute cloud top temperature, since no radiation is transmitted from below and there is little water vapour above the cloud. The estimated cloud top temperature of an opaque cumulonimbus cloud is, in turn, a valid proxy for the convective strength, as it gives a good indication about how deep in the troposphere the convection could reach, which is directly related to the strength of the convective updraught. Similar proxies have been used in the literature (Machado et al., 1998; Pro-
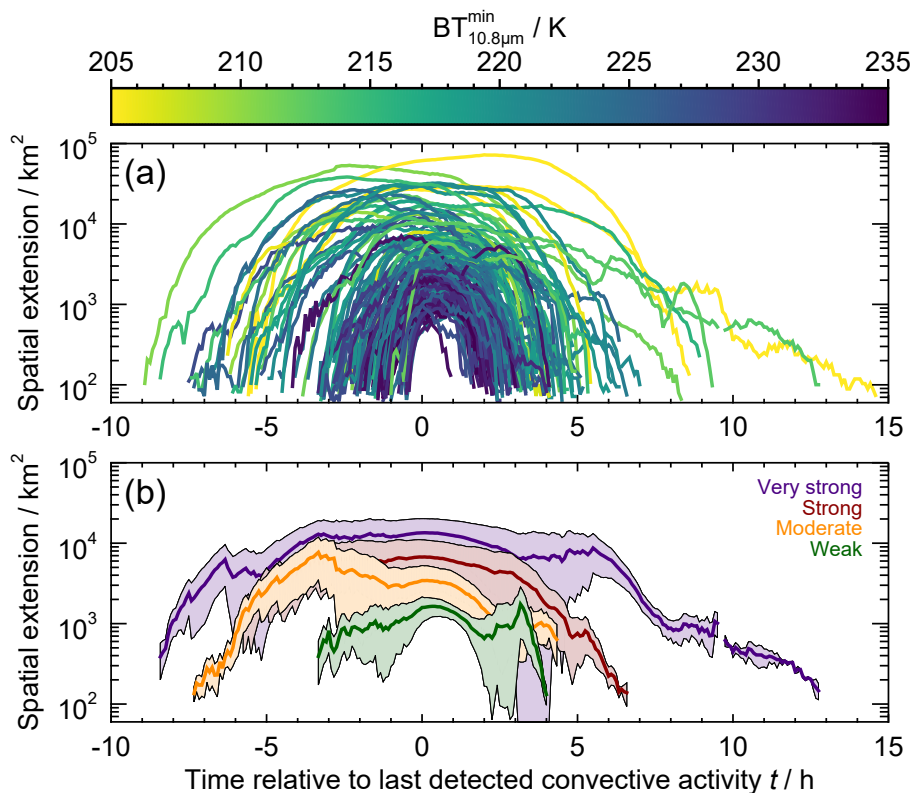
Figure 5.13: **(a)** The temporal evolution of the anvil cirrus spatial extension as a function of convective strength. **(b)** Same as **(a)**, but divided into four classes of increasing convective strength (see text for information about the classification). Solid lines represent the mean values of the respective classes and the shaded areas the corresponding standard deviations. $t = 0\,\mathrm{h}$ denotes the point when the last convective activity was observed with Cb-TRAM.

topapadaki et al., 2017). Other proxies including information about spatial extension and duration of convective activity as observed by Cb-TRAM have been considered, but the present proxy was concluded to be best suited for this study. The brightness temperature at $10.8\,\mu\mathrm{m}$ is a good estimate of the cloud top temperature only for opaque clouds. As the cloud emissivity decreases the observed brightness temperatures have a larger contribution from emitting cloud/land surfaces below (Sect. 2.2.2), leading to higher brightness temperatures and increasing deviations from the absolute cloud top temperatures. Hence, the brightness temperatures alone cannot be used to estimate the top temperature or top height of the anvil cirrus throughout the life cycle.

Figure 5.13a shows the temporal evolution of the anvil cirrus spatial extension (same as Fig. 5.8) as a function of the convective strength proxy (colours). Brighter colours represent colder cloud brightness/top temperatures and hence stronger convection. In Fig. 5.13b, the anvil cirrus clouds have been divided into four equally large convective strength classes using the three $\mathrm{BT}^{\mathrm{min}}_{10.8\mu\mathrm{m}}$ quartiles ($Q_1 = 219\,\mathrm{K}$, $Q_2 = 224\,\mathrm{K}$, $Q_3 = 229\,\mathrm{K}$) representing anvil cirrus clouds originating from convective systems with

Weak $\qquad\qquad\qquad$ $\mathrm{BT}_{10.8\mu m}^{\min} \geq 229\,\mathrm{K}$

Moderate $\quad$ $229\,\mathrm{K} > \mathrm{BT}_{10.8\mu m}^{\min} \geq 224\,\mathrm{K}$

Strong $\qquad$ $224\,\mathrm{K} > \mathrm{BT}_{10.8\mu m}^{\min} \geq 219\,\mathrm{K}$

Very strong $219\,\mathrm{K} > \mathrm{BT}_{10.8\mu m}^{\min}.$

The solid lines represent the mean for the respective classes and the shaded areas the corresponding standard deviations. Hence the purple line represents the strongest 25 % of the anvils and the green line the weakest 25 %. The number of anvils that make up the statistics does again vary with time, as all anvils are observed for unequally long time periods. Please see Figs. 5.9–5.12, for an estimate on how the number of anvils N decreases away from $t = 0\,\mathrm{h}$ and keep in mind that those anvils are further divided into four classes. Furthermore, Fig. 5.14 shows a scatter plot with the lifetime and maximum spatial extension of the anvil cirrus as a function of the convective strength proxy (colours).

In line with the results of previous studies (e.g. Machado et al., 1998; Horváth and Soden, 2008; Schröder et al., 2009; Feng et al., 2012; Protopapadaki et al., 2017), the convective strength is clearly correlated with the lifetime and the maximum spatial extension that the anvils reach. Stronger convection, as defined here, represents colder cloud top temperatures, which favours ice supersaturation and hence anvil persistence. This is especially clear in Fig. 5.13b, where stronger convection is observed to consistently generate larger and more long-lived anvil cirrus. This pattern can also be seen in Fig. 5.14, with generally increasing lifetime and maximum spatial extension with increasing convective strength. There are also deviations from this pattern though and a wide scatter in

Figure 5.14: The anvil cirrus lifetime and maximum spatial extension as a function of convective strength.

general. This is, however, expected, since the proxy of convective strength does not take the number of convective cores into account. Hence a large system that originates from 10 convective cores may have the same convective strength as a smaller single core system if they reach as high up in the atmosphere. This does not invalidate the proxy for convective strength, since it strives to represent the strength in the *vertical*, and not horizontal, development.

Figure 5.15 shows the temporal evolution of $\mathrm{CTH}_{\mathrm{CiPS}}$ for the four convective strength classes defined above at the full 5 min temporal resolution. As expected, higher $\mathrm{CTH}_{\mathrm{CiPS}}$ are observed in case of stronger convection since the convective proxy aims to estimate the
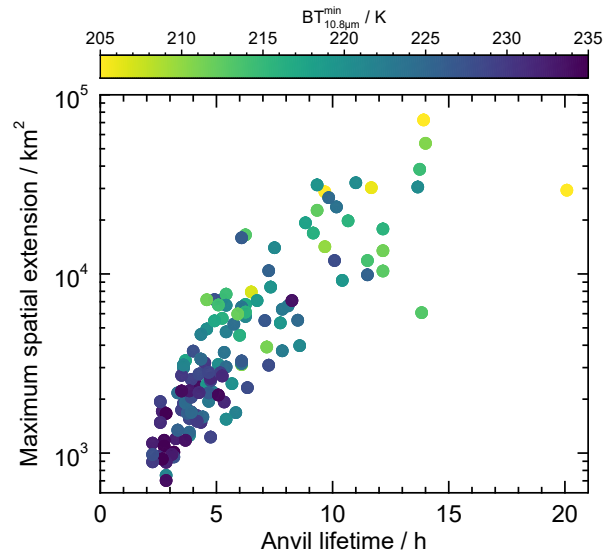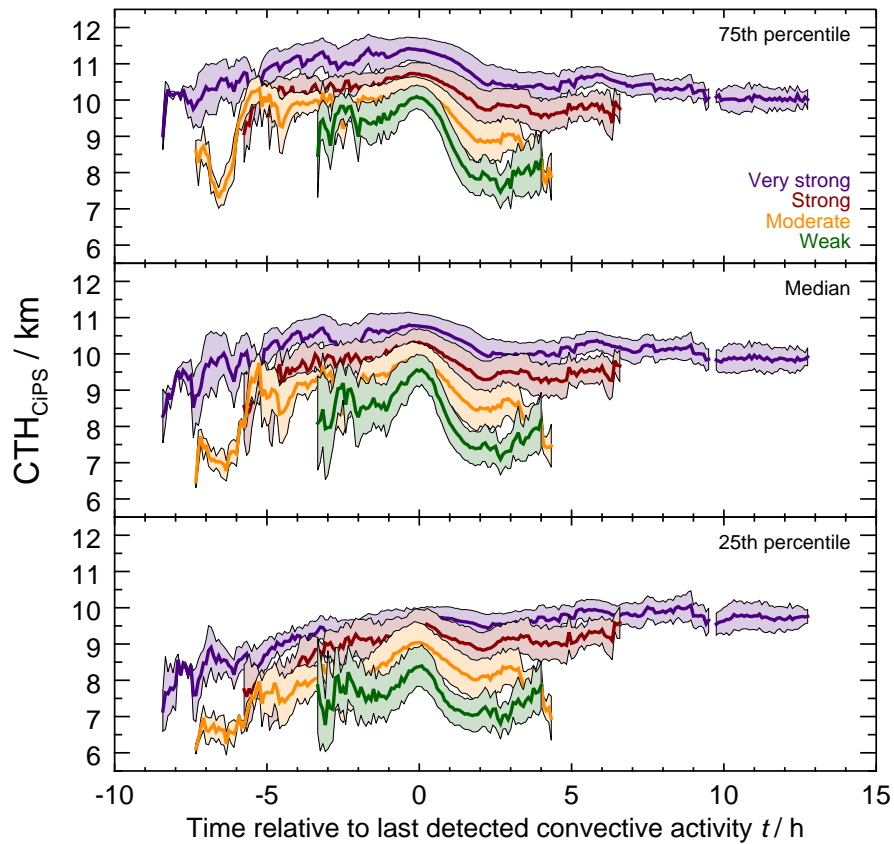
Figure 5.15: The temporal evolution of the anvil cirrus CTH_{CiPS} (median and 25th/75th percentiles) for four classes of increasing convective strength. Solid lines represent the mean values of the respective classes and the shaded areas the corresponding standard deviations. $t = 0\,h$ denotes the point when the last convective activity was observed with Cb-TRAM.

coldest observed cloud temperature, which is closely related to the top height of the anvil. CTH_{CiPS} increases (both median and percentiles) up to the point of last convective activity, then starts to decrease for about 2 h and remains at a comparably constant height on average. The anvils (median and percentiles) are consistently observed at higher altitudes if the convection is stronger, also several hours after convection has ceased. A distinct pattern is that the anvils are observed to sink faster as convection ceases if the convective strength is weaker. For the strongest 25 %, the median CTH_{CiPS} decreases by 0.8 km in 2 h as convection ceases, for the weakest 25 %, the corresponding decrease in height is 2 km. Similar patterns are observed for the 25th/75th percentiles as well. This suggests that sedimentation is an important process as convection stops and $\approx 2\,h$ onwards, especially for anvils that form from weaker convective systems and do not reach sufficiently favourable conditions for ice crystal deposition growth and hence anvil persistence. Anvils originating from stronger convective systems reaching colder temperatures where ice supersaturation
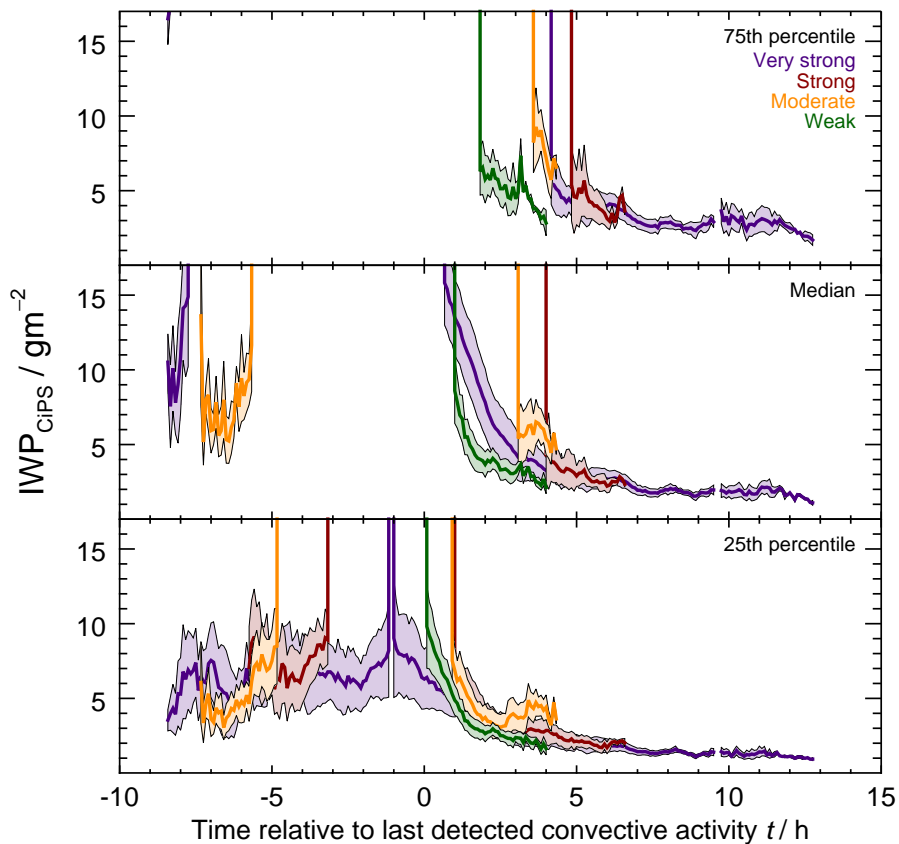
Figure 5.16: The temporal evolution of the anvil cirrus IWP_{CiPS} (median and 25th/75th percentiles) for four classes of increasing convective strength. Solid lines represent the mean values of the respective classes and the shaded areas the corresponding standard deviations. $t = 0\,h$ denotes the point when the last convective activity was observed with Cb-TRAM.

and hence anvil cirrus persistence is more likely, would be more likely to remain for longer time periods and at higher altitudes, despite sedimentation processes. This would be supported by the smaller spatial extension and shorter lifetimes for the anvils originating from weaker convective systems. It is, however, unclear if such a sedimentation process would be directly observed from the retrieved CTH_{CiPS}, as small ice crystals might be expected to remain at higher altitudes.

Figure 5.16 shows the temporal evolution of IWP_{CiPS} for the same four convective strength classes. Again, limited data are available during the convective stage due to the saturation of CiPS at high IWP/IOT. Neither for the median IWP_{CiPS}, nor the percentiles, an evident relationship between the convective strength and the IWP_{CiPS} is observed. Only for the weakest 25 %, IWP_{CiPS} is observed to reach lower values (median $IWP_{CiPS} = 2 - 4\,g\,m^{-2}$) during the first hours after convection has ceased in comparison to anvils forming from stronger convective systems. For the remaining classes, IWP_{CiPS} is
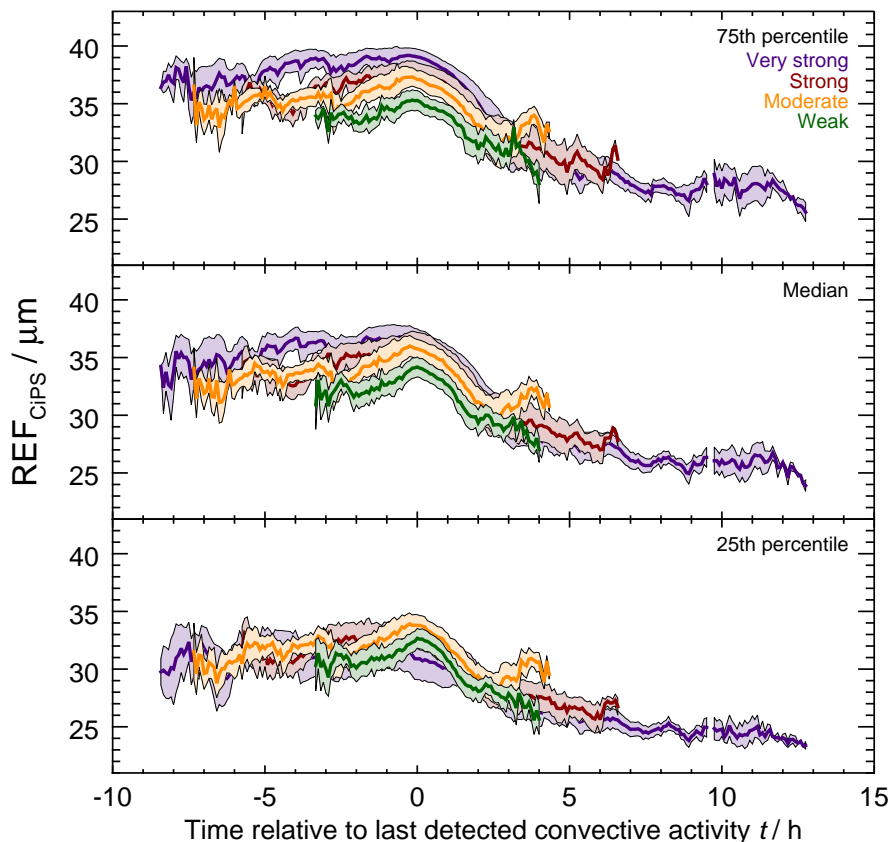
Figure 5.17: The temporal evolution of the anvil cirrus REF_{CiPS} (median and 25th/75th percentiles) for four classes of increasing convective strength. Solid lines represent the mean values of the respective classes and the shaded areas the corresponding standard deviations. $t = 0\,h$ denotes the point when the last convective activity was observed with Cb-TRAM.

rather similar for the different convective strength classes, with no apparent relationship with the convective strength. This suggests that the detrained ice crystals are effectively distributed horizontally, leading to a more widespread (Fig. 5.13), but not necessarily (optically) thicker anvil. This is different from the clear trend of higher average IWP for stronger convective systems observed for tropical convective systems in Horváth and Soden (2008). That pattern is, however, only shown for the thicker part of the anvil ($IWP \gtrsim 20\,g\,m^{-2}$), where IWP_{CiPS} retrievals are usually not possible. In contrast to weaker systems, stronger convection is observed to produce a considerable fraction (25 %) of thin anvil cirrus ($IWP_{CiPS} < 8\,g\,m^{-2}$) already during the convective phase, probably because stronger convection is usually associated with larger convective systems and hence more convective outflow of thin cirrus. In Fig. 5.11, comparably small standard deviations in the IWP_{CiPS} probability density functions were observed, indicating little variability in anvil IWP despite different conditions and properties of the deep convective systems from which

the anvils form. Fig. 5.16 suggests that this is true with respect to the convective strength for at least the thin part of the anvil cirrus. On the contrary, the anvil CTH_{CiPS}, which clearly increases with convective strength (Fig. 5.15), was observed to have significantly higher standard deviations in Fig. 5.9. Similar patterns are observed for the relationship between convective strength and IOT_{CiPS} and are therefore not further shown here.

Figure 5.17 shows the temporal evolution of REF_{CiPS}, again for the same four convective strength classes. An evident drop by $\approx 5\,\mu m$ is observed within $2\,h$ after convection ceases, together with a continuous decrease thereafter. This was observed in Fig. 5.12, but is more evident in Fig. 5.17. This is in line with the idea of sedimentation being an important process within $2\,h$ after convection has ceased, as discussed above. Stronger convection is also observed to generate larger ice crystals initially. For the median and 75th percentile, the classes of stronger convection almost exclusively show higher REF_{CiPS} during the convective stage and up to $2\,h$ after convection has ceased. This could be related to the longer vertical transport into the upper troposphere with stronger convective updraught, meaning that the ice crystals have more time to grow. As convection ceases, REF_{CiPS} for anvils originating from stronger convective systems, having higher REF_{CiPS} at $t = 0\,h$, is observed to decrease faster compared to the REF_{CiPS} for anvils originating from weaker convective systems, possibly due to higher fall speeds and thus, effective removal of larger ice crystals by sedimentation. 2–3 h after convection has ceased (and thereafter), only small differences in REF_{CiPS} are observed across the classes of convective strength, indicating that the convective strength does not affect the ice crystal sizes in ageing anvils. Instead ice supersaturation is likely to control anvil persistence through ice crystal growth by deposition at this life cycle stage.

5.4.3 Relationship between the meteorological conditions and the anvil cirrus life cycle

To further investigate observed variabilities in the anvil cirrus life cycle, the relationship between the meteorological conditions and the observed anvil cirrus life cycle is analysed in this section. To this end, ECMWF ERA5 reanalysis data (Sect. 3.4.2) are used to characterise the meteorological conditions where the deep convective cumulonimbus and anvil cirrus clouds form. Notice that deep convection is parameterised, not resolved, in the ECMWF model. All ERA5 data have been re-projected onto the SEVIRI grid using nearest neighbour. High low-level moisture and atmospheric instability were introduced in Chap. 1 as two key conditions for deep convection and anvil cirrus to form. While relative humidity (RH) is a measure for moisture, convective available potential energy (CAPE) is a good indicator for the instability within the conditionally unstable atmospheric layer between the level of free convection and the equilibrium level. CAPE (measured in $J\,kg^{-1}$) is the energy an air parcel would have if brought from the level of free convection to the equilibrium level and is calculated as the vertical integral of the local buoyancy exerted on the air parcel between these two levels. It is directly related to the maximum potential vertical updraught speed and an increasing CAPE indicates increasing instability. Higher

RH in the lower troposphere is expected to govern larger and possibly more long-lived anvil cirrus clouds, as it indicates that more moisture can be entrained into the deep convective system, transported vertically and detrained at the anvil cirrus level.

For each cumulonimbus cloud, from which the anvils form, average RH (over liquid water) between 850 and 1000 hPa (≈ 100–1500 m) and CAPE are collected from each ERA5 1 h time step over the area of convective activity (using Cb-TRAM). The data are averaged in space for each 1 h time step and later across all ERA5 time steps within the time period of observed convective activity. Hence, no interpolation is performed between the ERA5 time steps and the intermediate 5 min time steps of SEVIRI (as in Sect. 4.4.1). Since especially CAPE weakens as convection is initiated, a temporal offset of approx. -2 h (M. Köhler, DWD, personal communication, 2017) is used in order to allow for temporal differences in convective initiation between model and observation, meaning that the ERA5 data are collected before the convective event was observed from SEVIRI. Furthermore, for each ERA5 time step with observed convective activity (using Cb-TRAM), the area of maximum CAPE is searched for in the vicinity (≈ 50 km; M. Köhler, DWD, personal communication, 2017) of the area of convective activity in order to allow for spatial differences between model and observation. For example if 100 pixels with convective activity are observed by Cb-TRAM at a given time step, CAPE is calculated as the average across the 100 highest CAPE values (after re-projection onto the SEVIRI grid) in the vicinity of the observed convective activity.
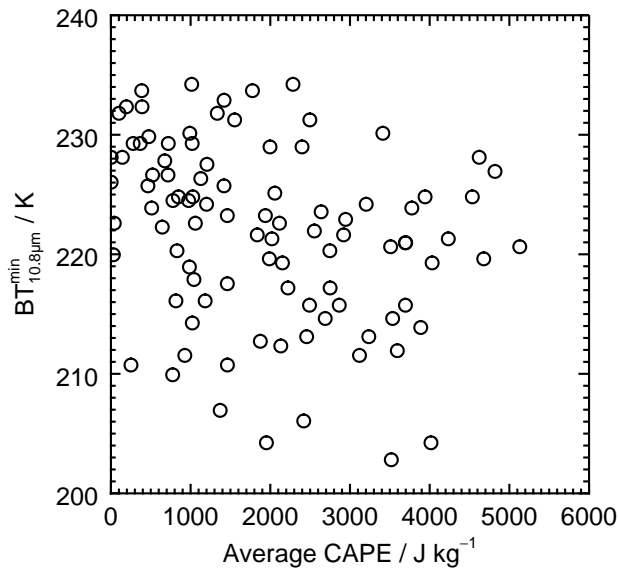

Figure 5.18: The relationship between the modelled CAPE and the proxy for convective strength ($BT^{min}_{10.8\mu m}$).

First, Fig. 5.18 shows the relationship between CAPE and the proxy for convective strength, defined and used in the previous section. Although there is a trend of increasing CAPE for decreasing $BT^{min}_{10.8\mu m}$, the scatter between the two quantities is generally very large. This shows that the two quantities to a large extent provide different information and suggests that an understanding and knowledge of neither CAPE nor $BT^{min}_{10.8\mu m}$ is sufficient for fully understanding anvil cirrus clouds and their temporal evolution. Figure 5.19 shows the anvil cirrus lifetime (symbol colour) and the corresponding maximum spatial extension (symbol size) as a function of CAPE and the average RH between 850 and 1000 hPa. Also here a generally large scatter is observed, further demonstrating the importance of better understanding anvil cirrus clouds and the physical processes that govern their life cycle. Nevertheless, higher CAPE usually leads to more long-lived, and to some extent larger, anvil cirrus. Even though some of the smaller short-lived anvils have CAPE $> 1500 - 2000$ J kg^{-1}, this seems to be

an approximate threshold that the larger more long-lived anvils surpass. The low-level RH has no obvious impact on the anvil spatial extension and lifetime. In contrast to the expectation (see above), there is no positive correlation between the low-level RH and the anvil cirrus spatial extension and lifetime. Instead, generally larger and more long-lived anvils with $CAPE > 3000\,J\,kg^{-1}$ tend to have lower RH between 850–1000 hPa than the generally smaller and more short-lived anvils with $CAPE < 1500\,J\,kg^{-1}$.

While the CAPE and RH from 850 to 1000 hPa target the convective cumulonimbus cloud from which the anvil cirrus eventually form, the relative humidity over ice (RHi), temperature, horizontal wind speeds and vertical wind shear are used to characterise the meteorological conditions in the upper troposphere, where the convective outflow and anvil cirrus formation takes place. As explained in Chap. 1, RHi above 100 % i.e. ice supersaturation is required for ice crystal growth by water vapour deposition and hence essential for anvil cirrus persistence. The horizontal wind speed is directly related to the formation of the anvil as it distributes the ice crystals detrained from the deep convective cloud. Furthermore, strong vertical wind shear in the upper troposphere can have at least two effects on the anvil cirrus. If the anvil is optically
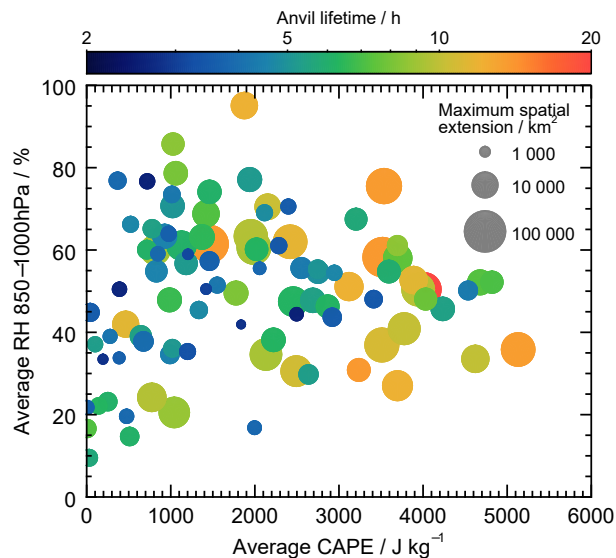

Figure 5.19: The anvil cirrus lifetime (symbol colour) and maximum spatial extension (symbol size) as a function of modelled CAPE and RH between 850 and 1000 hPa.
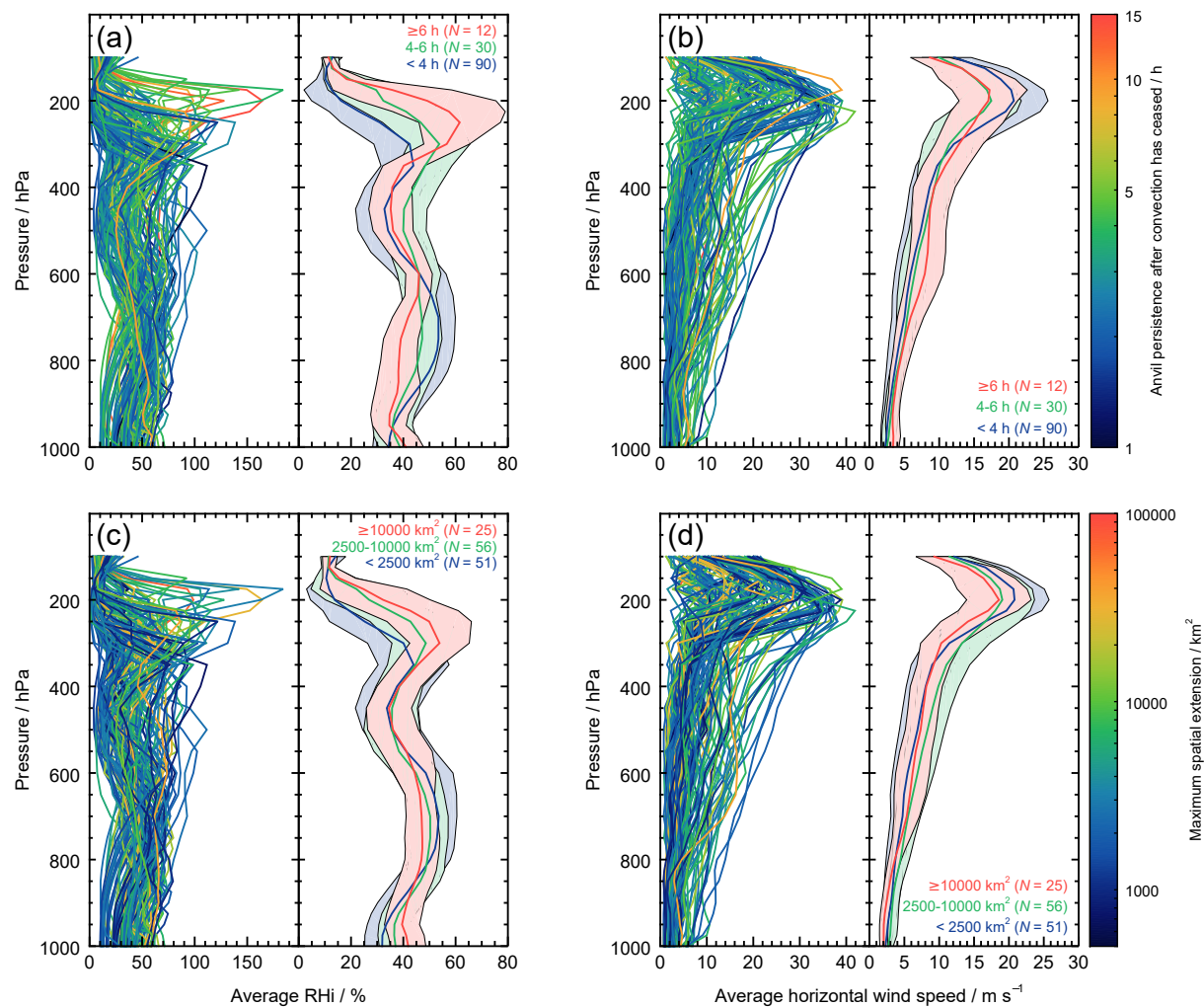
thick, stronger wind shear could distribute the ice more effectively, leading to more widespread anvil cirrus (Feng et al., 2012). On the contrary, if the anvil is optically thin, stronger wind shear might tear the anvil apart, reducing both its spatial extension and lifetime. The RHi, temperature and horizontal wind speeds have been averaged over the entire area covered by the anvil cirrus during its lifetime (without the $\approx 50\,km$ spatial offset used to calculate the average CAPE). However, no temporal averaging has been performed, instead all data have been collected $\approx 2\,h$ before the first detection by CiPS. This way, the upper tropospheric conditions that the anvils form in are obtained, with minimal impact by (modelled) convection itself. The Goff–Gratch formulas (Goff and Gratch, 1946) together with the ERA5 temperatures have been used to convert RH to RHi.

Figure 5.20 shows vertical profiles of RHi (left) and horizontal wind speed (right) as a function of observed anvil cirrus persistence after convection has ceased (top) and the maximum spatial extension (bottom). Vertical profiles are shown for all anvil cirrus individually (left panels), but also for three classes of spatial extension and persistence (right panels) in order to more effectively see general trends. Again the solid lines represent the mean values for the respective classes and the shaded areas the corresponding standard deviations. It is clear that larger and especially more long-lived anvils are associated with

Figure 5.20: Vertical profiles of RHi (**(a)** and **(c)**) and horizontal wind speed (**(b)** and **(d)**) as a function of anvil persistence after convection has ceased (**(a)** and **(b)**) and the maximum spatial extension (**(c)** and **(d)**). The respective left panels show vertical profiles for each individual anvil cirrus, whereas the respective right panels show RHi and horizontal wind speed for three classes of anvil persistence and maximum spatial extension respectively, where the solid lines and shaded areas represent the mean values and corresponding standard deviations respectively. N is the number of anvil cirrus in each class.

higher RHi in the upper troposphere, where e.g. 225 and 300 hPa corresponds to 11.5 and 9.6 km on average across the anvil cirrus dataset respectively, i.e. an altitude range where a large part of the anvil cirrus form (see Figs. 5.9 and 5.15). Although the standard deviations between the different classes overlap, it shows that higher RHi govern larger anvils that persist for longer time periods after convection has ceased. In the lower troposphere,

RHi is generally higher for the small and short-lived anvils, indicating that RHi in the lower troposphere has a comparably small effect on the anvil cirrus life cycle compared to RHi in the upper troposphere, which is in line with the weak/absent positive correlation between the average RH between 850–1000 hPa and the anvil cirrus lifetime and spatial extension in Fig. 5.19. Although the trend is not as strong as for RHi, higher wind speeds in the upper troposphere tend to reduce the anvil cirrus spatial extension and persistence after convection has ceased. Especially smaller ($< 2500\,\mathrm{km}^2$) and short-lived ($< 4\,\mathrm{h}$) anvil cirrus clouds are associated with higher wind speeds in the upper troposphere. Feng et al. (2012) also investigate the vertical profiles of RH and horizontal winds from reanalysis data (North America Regional Reanalysis) for anvil cirrus clouds observed over the U.S. In contrast to what is shown in this study, they show clearly increasing horizontal wind speeds in the upper troposphere for *larger* anvil cirrus clouds, but with little effect on the observed anvil lifetime. Furthermore, they show significantly higher RH between 300–700 hPa for more long-lived anvils, a pattern also not evident in this study. On the other hand, they also show a trend of increasing RH in the upper troposphere for more long-lived anvils, similar to what is seen here. It is possible that the differences between the two studies are related to differences in the reanalysis data, but more likely due to the fact that Feng et al. (2012) collect the reanalysis data during the developing and mature stages of the convective system, whereas in this study the data are collected around 2 h before the convective system was first observed, in order to capture the meteorological conditions of the air mass in which the anvil cirrus form. Hence, it is likely that they already observe the effect of convection in their vertical profiles of horizontal winds and RH.

Figure 5.21 further shows the anvil persistence after convection has ceased (symbol colour) and the corresponding maximum spatial extension (symbol size) for the individual anvil cirrus clouds as a function of the average (a) RHi and temperature and (b) horizontal wind speed and vertical wind shear in the upper tropospheric layer 225–300 hPa. The vertical wind shear in this upper tropospheric layer is calculated as the difference between the average horizontal wind speeds at 225 and 300 hPa respectively. The clear correlation between the temperature and RHi is controlled by the Clausius–Clapeyron relation, describing the decrease in saturation vapour pressure, i.e. the ability of the air to hold moisture, with decreasing temperature. Similar to Fig. 5.20, colder temperatures and higher RHi are associated with longer anvil persistence and to some extent larger spatial extension. Lower RHi ($\lesssim 30\,\%$) generally leads to small and especially short-lived anvils, whereas higher RHi ($\gtrsim 60\,\%$) govern larger and especially more long-lived anvils. There are situations where a low temperature and high RHi still result in small short-lived anvils, this could either be an effect of rapid sedimentation as a result of rapid deposition growth or inaccurate RHi estimates that might not capture small scale variations. For the horizontal wind speed and the vertical wind shear, the correlation with the anvil cirrus spatial extension and persistence after convection has ceased is weaker. Most of the small short-lived anvils do, however, tend to have higher horizontal wind speeds ($\gtrsim 20\,\mathrm{m\,s^{-1}}$) and/or stronger vertical wind shear ($\gtrsim 7\,\mathrm{m\,s^{-1}}$) compared to larger anvil cirrus observed for longer time periods after convection has ceased. Again, there are exceptions from this general pattern though. Two possible effects of strong vertical wind shear on the anvil cir-
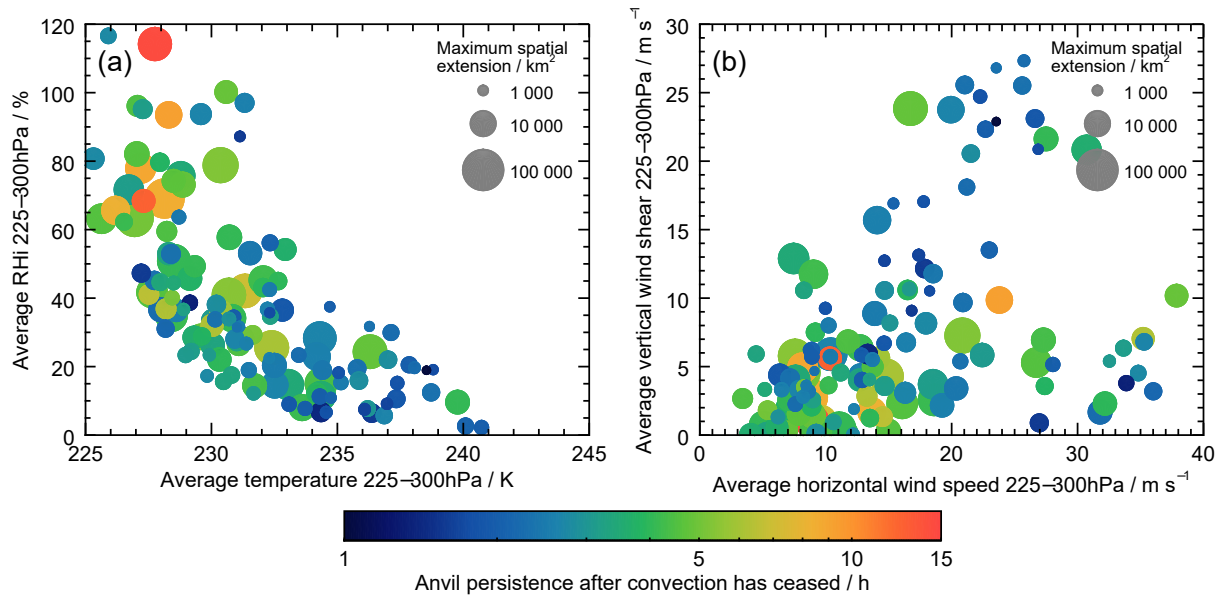
Figure 5.21: The observed anvil cirrus persistence after convection has ceased (symbol colour) and the maximum spatial extension (symbol size) as a function of modelled upper tropospheric **(a)** temperature and RHi and **(b)** horizontal wind speed and vertical wind shear.

rus life cycle were discussed above, where strong vertical wind shear could lead to (1) more efficient horizontal spreading of the ice crystals and thus larger anvils if there is sufficient ice available (2) the anvil being torn apart if there is too little ice available, leading to a reduced anvil cirrus coverage and persistence. It is possible that both, opposing, effects are in play here, leading to ambiguous results.

Chapter 6

Summary, conclusions and outlook

This thesis aims towards new insights in the life cycle of anvil cirrus clouds that form in the upper troposphere from the outflow of ice crystals from deep convective cumulonimbus clouds. This is addressed by means of geostationary satellite remote sensing, which allows for a large spatial coverage and a temporal resolution of up to 5 min, making it possible to track and study individual anvil cirrus clouds continuously throughout their life cycle, from the convective initiation until the dissipation.

In order to study new perspectives of the anvil cirrus life cycle and the temporal evolution of their optical, macrophysical and microphysical properties, the new algorithm CiPS (Cirrus Properties from SEVIRI; Chap. 4) has been developed. CiPS uses a set of four artificial neural networks (ANNs) for the geostationary remote sensing of thin cirrus clouds during day and night from MSG/SEVIRI with unprecedented accuracy for a geostationary passive instrument. In comparison to its training reference data, the space-borne lidar CALIOP, CiPS detects 71 % and 95 % of all cirrus clouds with an IOT of 0.1 and 1.0 respectively, with an average false alarm rate of 4 % across the SEVIRI disc. For pixels classified as icy, CiPS retrieves the corresponding CTH (cloud top height) with relative retrieval errors less than 10 % for 64 % of the scenes with transparent cirrus (over clear air) of varying optical thickness and cloud top height. Similarly, 37 % of the $\mathrm{CTH}_{\mathrm{CiPS}}$ retrievals have errors less than 5 %. CiPS further retrieves the $\mathrm{IOT}_{\mathrm{CiPS}}$ (ice optical thickness) and $\mathrm{IWP}_{\mathrm{CiPS}}$ (ice water path) with relative errors less than 50 % for 55 % and 48 % of the retrievals respectively. The combined retrieval of $\mathrm{IOT}_{\mathrm{CiPS}}$ and $\mathrm{IWP}_{\mathrm{CiPS}}$, further allows for parameterised effective radius ($\mathrm{REF}_{\mathrm{CiPS}}$) estimates. Furthermore, CiPS is able to identify cirrus clouds too optically thick for reliable $\mathrm{IOT}_{\mathrm{CiPS}}$ and $\mathrm{IWP}_{\mathrm{CiPS}}$ retrievals. Intercomparisons with independent airborne and ground-based lidar data further demonstrate the robustness of the CiPS retrievals.

Even though the development of CiPS is based on physical considerations with respect to the selection of training input and output data, the training, and thus the retrieval, is purely mathematical. Nevertheless, the validation and characterisation show that CiPS to a large extent have similar limitations as physically based retrieval algorithms. For example CiPS struggles for optically thin ($\mathrm{IOT}_{\mathrm{CALIOP}} \lesssim 0.08$) cirrus/ice clouds at low altitudes ($\mathrm{CTH}_{\mathrm{CALIOP}} \lesssim 8\,\mathrm{km}$) as well as over barren (dominated by desert) and permanent ice and

snow, conditions that are known to induce difficulties for (cirrus) cloud remote sensing (Frey et al., 2008; Holz et al., 2008). Retrievals over vegetated land surfaces show a similar accuracy as retrievals over homogeneous water surfaces. CiPS can effectively separate the signal contribution from the observed cirrus cloud and underlying liquid water clouds and aerosol layers. While the IOT_{CiPS}/IWP_{CiPS} retrieval errors clearly increase if a liquid water cloud is vertically close ($< 0.5\,km$) to a thin ($IOT \lesssim 0.3$) cirrus cloud, no or small effects on the retrieval accuracy are observed if the vertical separation between the cirrus cloud and the liquid water cloud is large ($> 4\,km$).

To answer the first scientific question raised in Chap. 1

SQ-1 *How do the anvil cirrus properties, including spatial extension, cloud top height, ice optical thickness, ice water path and effective radius evolve with time throughout the anvil cirrus life cycle?*

CiPS has been used in synergy with a new cirrus tracking algorithm and a tool for monitoring convective activity to analyse the temporal evolution of the optical, macrophysical and microphysical properties throughout the life cycle of 132 isolated anvil cirrus clouds, mostly observed in the Mediterranean region in July 2015. The ensemble of tracked anvil cirrus clouds shows large variability with respect to spatial extension and lifetime. Some anvils are only observed for 1-2 h after convection has ceased, with a maximum spatial extension of $\approx 1000\,km^2$, whereas others are observed for 13–15 h and reaching spatial extensions of up to $\approx 70\,000\,km^2$. During the convective stage, the anvil cirrus are mostly too thick for CiPS to retrieve reliable IOT_{CiPS} and IWP_{CiPS}. But as convection ceases, the anvils are rapidly becoming thinner and 2 h after convection has ceased, $92 \pm 7\,\%$ of the anvil area has $IOT_{CiPS} < 1$ and $IWP_{CiPS} < 30\,g\,m^{-2}$ on average with highest probability density around 0.1–0.2 and 1.5–3 $g\,m^{-2}$ respectively. 5 h after convection has ceased, only $13\,\%$ of the anvils could still be observed, having $IOT_{CiPS} \approx 0.07 - 0.4$ and $IWP_{CiPS} \approx 1.0 - 6.0\,g\,m^{-2}$ on average. CTH_{CiPS} and REF_{CiPS} both increase during the convective phase followed by a drop in both height and ice crystal size for approx. 2 h after convection has ceased.

To further investigate observed variabilities in the anvil cirrus life cycle and aiming for an increased understanding of the relationship between convective strength, expected to increase in a warming climate, and the anvil cirrus properties and their temporal evolution, the following scientific question was raised in Chap. 1

SQ-2 *How does the convective strength affect the anvil cirrus properties and their temporal evolution?*

To answer this question, a proxy for the convective strength is defined as the coldest brightness temperature observed by SEVIRI at $10.8\,\mu m$ for the respective anvil cirrus clouds (approx. coldest cloud top temperature). Anvils originating from weaker convective systems, observed at lower altitudes (CTH_{CiPS}), lose height significantly faster within 2 h after convection ceases, compared to anvils forming from stronger convective systems. A corresponding decrease in REF_{CiPS} indicates that sedimentation is an important process controlling the anvil cirrus persistence and life cycle as convection ceases, especially for

weak convective systems, that do not reach as cold temperatures and hence less favourable conditions for ice supersaturation. If colder temperatures and ice supersaturation is reached with stronger convection, this could allow for deposition growth and hence longer anvil persistence at higher altitudes.

Stronger convection is also observed to produce larger ice crystals (REF_{CiPS}) during the convective phase. The larger crystals are observed to be removed rather fast though and 2–3 h after convection has ceased only small differences in REF_{CiPS} are observed for anvils originating from strong and weak convective systems, indicating that even though the convective strength appear to affect REF_{CiPS} during the convective phase and shortly thereafter, it has no or little impact on the ice crystal sizes in ageing anvils. No obvious and consistent relationship is observed between the convective strength and IWP_{CiPS} (and IOT_{CiPS}) and its temporal evolution. This is supported by the comparably low variability in the temporal evolution of IOT_{CiPS} and IWP_{CiPS} discussed above. It is also evident that anvils forming from stronger convective systems grow larger, indicating that the ice crystals are distributed in the horizontal, rather than the vertical, leading to little impact on vertically integrated quantities like IWP_{CiPS} and IOT_{CiPS}.

Differences in the anvil cirrus life cycle cannot be explained solely by the convective strength and there has to be further conditions that control the life cycle of especially ageing anvil cirrus. Hence the following scientific question was raised in Chap. 1 to better understand the impact of the meteorological conditions on the anvil cirrus life cycle

SQ-3 *How do the meteorological conditions influence the life cycle of anvil cirrus clouds?*

ECMWF ERA5 analysis data at 1 h temporal resolution have been used to characterise the meteorological conditions in which the deep convective cumulonimbus clouds and the anvil cirrus form. More convective available potential energy (CAPE) is generally associated with long-lived and to some extent larger convective systems and following anvil cirrus, whereas low-level moisture, defined as the average relative humidity (RH) between 850–1000 hPa, shows no clear relationship with the anvil cirrus lifetime and spatial extension.

RH over ice (RHi) and temperature in the upper troposphere (225-300 hPa) show a clear correlation with the maximum spatial extension and observed persistence after convection has ceased. The smallest anvils observed for $\approx$ 1–2 h after convection has ceased generally form in air with warmer temperatures and lower RHi, whereas colder temperatures ($\lesssim$ 228 K) and higher RHi ($\gtrsim$ 60 %) govern larger and especially more long-lived anvil cirrus. Dividing the 132 anvil cirrus clouds in three classes of increasing maximum spatial extension and observed persistence after convection has ceased respectively, further clarifies the trend of higher RHi in the upper troposphere for larger and more long-lived anvil cirrus clouds and suggests a comparably weak impact by high RH in the lower troposphere. Moreover, high horizontal wind speeds in the upper troposphere tend to reduce the anvil cirrus lifetime and spatial extension.

Outlook

This thesis provides a new cirrus retrieval algorithm and new insights in the life cycle and temporal evolution of anvil cirrus clouds. But it also opens up for further studies in the future. First and foremost, more anvil cirrus clouds could be identified, tracked and analysed in order to have a stronger statistical significance. This can be done by (1) extending the time period from one month to several months or years and (2) also including non-isolated anvil cirrus clouds until the point where they merge with other cirrus. Extending the study time period to several months or years would, however, require a more automatized procedure for detecting and tracking the convective clouds and the anvil cirrus. To further the understanding of the physical properties, one should also extend the analysis of the ERA5 variables and investigate their impact on the anvil cirrus microphysical properties retrieved by CiPS. Moreover, it would be interesting to perform a similar study on tropical anvil cirrus clouds and compare the life cycles and the temporal evolution of the anvil cirrus properties between tropics and mid-latitudes. As aerosols can act as cloud condensation nuclei, it would be interesting to study the temporal evolution of the anvil cirrus properties as a function of e.g. aerosol optical thickness, possibly differentiating between different aerosol types like wildfire smoke, desert dust and sea salt. One could also analyse the temporal evolution of outgoing longwave radiation and reflected solar radiation throughout the life cycle to better understand how they interact with shortwave and longwave radiation and hence contribute to the radiation budget.

A given next step, already in progress within the HD(CP)^2 project, is the evaluation of the representation of anvil cirrus in climate and weather models using CiPS. The temporal evolution of the cirrus coverage and CTH retrieved by CiPS have recently been compared to the corresponding anvil cirrus properties modelled by the ICON large eddy model, NWP and general circulation model, within a closed domain over Germany for several days where deep convection was observed. The high resolution large eddy model data also allow for further investigation of the physical processes that control the anvil cirrus life cycle.

Since neither CiPS, nor the cirrus tracking algorithm, is limited to anvil cirrus clouds, they could be used to study the temporal evolution of other natural or anthropogenic (contrails) cirrus clouds as well. The high temporal resolution of CiPS, also allows for further studies on the diurnal cycles of cirrus coverage and cirrus properties.

To further evaluate the accuracy of CiPS an extended intercomparison with RAMSES (and SPARE-ICE (Holl et al., 2014)), covering a time period of two years, is currently being prepared. Continuous improvements of the CALIOP products also allow for further improvements of CiPS. Based on the analysis in Sect. 4.10.1, one could further optimise the set of input variables for CiPS and possibly introduce new input data, such as temperature and humidity profiles and surface emissivities to further improve the accuracy. Moreover, training CiPS with synergistic lidar/radar retrievals could allow for retrievals of higher IOT and IWP. Extending CiPS to the new generation Japanese and U.S. geostationary imagers (Himawari/AHI, GOES/ABI), with similar channels like SEVIRI, would allow for near global retrievals of cirrus cloud properties and anvil cirrus analysis at a temporal resolution of 15 min.

Appendix A

List of abbreviations

ABI	Advanced Baseline Imager
AHI	Advanced Himawari Imager
AIRS	Atmospheric Infrared Sounder
ANN	Artificial Neural Network
AOT	Aerosol Optical Thickness
AVHRR	Advanced Very High Resolution Radiometer
BT	Brightness Temperature
CALIOP	Cloud Aerosol Lidar with Orthogonal Polarization
CALIPSO	Cloud-Aerosol Lidar and Infrared Pathfinder Satellite Observation
CAPE	Convective Available Potential Energy
Cb-TRAM	Cumulonimbus Tracking and Monitoring
CC-VEX	CALIPSO-CloudSat Validation Experiment
CCF	Cirrus Cloud Flag
CiPS	Cirrus Properties from SEVIRI
COCS	Cirrus Optical Properties from CALIOP and SEVIRI
CPL	Cloud Physics Lidar
CPR	Cloud Profiling Radar
CTH	Cloud Top Height
DAAD	German Academic Exchange Service (Deutscher Akademischer Austauschdienst)
DLR	German Aerospace Center (Deutsches Zentrum für Luft- und Raumfahrt)
DOY	Day of Year
DWD	German Meteorological Service (Deutscher Wetterdienst)
ECMWF	European Centre for Medium-Range Weather Forecasts
ERA	ECMWF Reanalysis
EUMETSAT	European Organisation for the Exploitation of Meteorological Satellites
FANN	Fast Artificial Neural Network Library

FAR	False Alarm Rate
FAT	Fixed Anvil Temperature
GEWEX	Global Energy and Water Cycle Experiment
GMS	Geostationary Meteorological Satellites
GOES	Geostationary Operational Environmental Satellite
HALO	High Altitude and Long range research aircraft
HD(CP)^2	High Definition Clouds and Precipitation for Advancing Climate Prediction
HOI	Horizontally Orientated Ice
HRV	High Resolution Visible
ICON	Icosahedral Nonhydrostatic
IGBP	International Geosphere-Biosphere Programme
IIR	Imaging Infrared Radiometer
IOT	Ice Optical Thickness
IR	Infrared
ITCZ	Intertropical Convergence Zone
IWC	Ice Water Content
IWP	Ice Water Path
L2	Level 2
L3	Level 3
LIDAR	Light Detection and Ranging
MAPE	Mean Absolute Percentage Error
MFG	Meteosat First Generation
MHS	Microwave Humidity Sounder
ML-CIRRUS	Midlatitude Cirrus Experiment
MLP	Multilayer Perceptron
MODIS	Moderate Resolution Imaging Spectroradiometer
MPE	Mean Percentage Error
MSE	Mean Square Error
MSG	Meteosat Second Generation
MTSAT	Multifunctional Transport Satellites
NEΔT	Noise-Equivalent Temperature Difference
NEΔR	Noise-Equivalent Radiance Difference
NIR	Near Infrared
NWP	Numerical Weather Prediction
OPF	Opacity Flag
POD	Probability of Detection
RADAR	Radio Detection and Ranging

RAMSES	Raman Lidar for Atmospheric Moisture Sensing
RH	Relative Humidity
RMSD	Root-Mean-Square Deviation
SEVIRI	Spinning Enhanced Visible and Infrared Imager
SNR	Signal-to-Noise Ratio
SQ	Scientific Question
TOA	Top of Atmosphere
TRMM	Tropical Rainfall Measuring Mission
UTC	Coordinated Universal Time
V2	Version 2
V3	Version 3
VIS	Visible
VZA	Viewing Zenith Angle
WALES	Water Vapor Lidar Experiment in Space
WCRP	World Climate Research programme
WV	Water Vapour

Bibliography

Ackerman, S., Holz, R., Frey, R., Eloranta, E., Maddux, B., and McGill, M.: Cloud detection with MODIS. Part II: validation, *J. Atmos. Oceanic Technol.*, 25, 1073–1086, doi:10.1175/2007JTECHA1053.1, 2008.

Ackerman, S. A., Smith, W. L., Revercomb, H. E., and Spinhirne, J. D.: The 27–28 October 1986 FIRE IFO Cirrus Case Study: Spectral Properties of Cirrus Clouds in the 8–12 μm Window, *Mon. Wea. Rev.*, 118, 2377–2388, doi:10.1175/1520-0493(1990)118<2377:TOFICC>2.0.CO;2, 1990.

Ackerman, S. A., Strabala, K. I., Menzel, W. P., Frey, R. A., Moeller, C. C., and Gumley, L. E.: Discriminating clear sky from clouds with MODIS, *J. Geophys. Res. Atmos.*, 103, 32 141–32 157, doi:10.1029/1998JD200032, 1998.

Arnaud, Y., Desbois, M., and Maizi, J.: Automatic Tracking and Characterization of African Convective Systems on Meteosat Pictures, *J. Appl. Meteor.*, 31, 443–453, doi:10.1175/1520-0450(1992)031<0443:ATACOA>2.0.CO;2, 1992.

Avery, M., Winker, D., Heymsfield, A., Vaughan, M., Young, S., Hu, Y., and Trepte, C.: Cloud ice water content retrieved from the CALIOP space-based lidar, *Geophys. Res. Lett.*, 39, doi:10.1029/2011GL050545, 2012.

Bergstra, J. and Bengio, Y.: Random search for hyper-parameter optimization, *J. Mach. Learn. Res.*, 13, 281–305, 2012.

Bolliger, M., Binder, P., and Rossa, A.: Tracking cloud patterns by METEOSAT rapid scan imagery in complex terrain, *Meteor. Z.*, 12, 73–80, doi:10.1127/0941-2948/2003/0012-0073, 2003.

Bony, S., Stevens, B., Frierson, D. M., Jakob, C., Kageyama, M., Pincus, R., Shepherd, T. G., Sherwood, S. C., Siebesma, A. P., Sobel, A. H., et al.: Clouds, circulation and climate sensitivity, *Nature Geoscience*, 8, 261, doi:10.1038/ngeo2398, 2015.

Bony, S., Stevens, B., Coppin, D., Becker, T., Reed, K. A., Voigt, A., and Medeiros, B.: Thermodynamic control of anvil cloud amount, *Proc. Natl. Acad. Sci. (USA)*, 113, 8927–8932, doi:10.1073/pnas.1601472113, 2016.

Bouniol, D., Roca, R., Fiolleau, T., and Poan, D. E.: Macrophysical, Microphysical, and Radiative Properties of Tropical Mesoscale Convective Systems over Their Life Cycle, *J. Climate*, 29, 3353–3371, doi:10.1175/JCLI-D-15-0551.1, 2016.

Bugliaro, L., Zinner, T., Keil, C., Mayer, B., Hollmann, R., Reuter, M., and Thomas, W.: Validation of cloud property retrievals with simulated satellite radiances: a case study for SEVIRI, *Atmos. Chem. Phys.*, 11, 5603–5624, doi:10.5194/acp-11-5603-2011, 2011.

CALIPSO Science Team: CALIPSO/CALIOP Level 2, Lidar Aerosol Layer Data, version 3.01, Hampton, VA, USA: NASA Atmospheric Science Data Center (ASDC), doi:10.5067/CALIOP/CALIPSO/CAL_LID_L2_05kmALay-Prov-V3-01_L2-003.01, 2015a.

CALIPSO Science Team: CALIPSO/CALIOP Level 2, Lidar Aerosol Layer Data, version 3.02, Hampton, VA, USA: NASA Atmospheric Science Data Center (ASDC), doi:10.5067/CALIOP/CALIPSO/CAL_LID_L2_05kmALay-Prov-V3-02_L2-003.02, 2015b.

CALIPSO Science Team: CALIPSO/CALIOP Level 2, Lidar Cloud Layer Data, version 3.01, Hampton, VA, USA: NASA Atmospheric Science Data Center (ASDC), doi:10.5067/CALIOP/CALIPSO/CAL_LID_L2_05kmCLay-Prov-V3-01_L2-003.01, 2015c.

CALIPSO Science Team: CALIPSO/CALIOP Level 2, Lidar Cloud Layer Data, version 3.02, Hampton, VA, USA: NASA Atmospheric Science Data Center (ASDC), doi:10.5067/CALIOP/CALIPSO/CAL_LID_L2_05kmCLay-Prov-V3-02_L2-003.02, 2015d.

Ceccaldi, M., Delanoë, J., Hogan, R. J., Pounder, N. L., Protat, A., and Pelon, J.: From CloudSat-CALIPSO to EarthCare: Evolution of the DARDAR cloud classification and its comparison to airborne radar-lidar observations, *J. Geophys. Res. Atmos.*, 118, 7962–7981, doi:10.1002/jgrd.50579, 2013.

Cesana, G., Chepfer, H., Winker, D., Getzewich, B., Cai, X., Jourdan, O., Mioche, G., Okamoto, H., Hagihara, Y., Noel, V., and Reverdy, M.: Using in situ airborne measurements to evaluate three cloud phase products derived from CALIPSO, *J. Geophys. Res. Atmos.*, 121, 5788–5808, doi:10.1002/2015JD024334, 2016.

Chen, S. S. and Houze, R. A.: Diurnal variation and life-cycle of deep convective systems over the tropical pacific warm pool, *Quart. J. Roy. Meteor. Soc.*, 123, 357–388, doi:10.1002/qj.49712353806, 1997.

Chen, T., Rossow, W. B., and Zhang, Y.: Radiative effects of cloud-type variations, *J. Climate*, 13, 264–286, 2000.

Chou, C. and Neelin, J. D.: Cirrus detrainment-temperature feedback, *Geophys. Res. Lett.*, 26, 1295–1298, doi:10.1029/1999GL900219, 1999.

Collins, M., Knutti, R., Arblaster, J., Dufresne, J.-L., Fichefet, T., Friedlingstein, P., Gao, X., Gutowski, W., Johns, T., Krinner, G., Shongwe, M., Tebaldi, C., Weaver, A., and Wehner, M.: Long-term Climate Change: Projections, Commitments and Irreversibility, book section 12, pp. 1029–1136, Cambridge University Press, Cambridge, United Kingdom and New York, NY, USA, doi:10.1017/CBO9781107415324.024, 2013.

Davis, S., Hlavka, D., Jensen, E., Rosenlof, K., Yang, Q., Schmidt, S., Borrmann, S., Frey, W., Lawson, P., Voemel, H., and Bui, T. P.: In situ and lidar observations of tropopause subvisible cirrus clouds during TC4, *J. Geophys. Res. Atmos.*, 115, doi:10.1029/2009JD013093, d00J17, 2010.

De Paepe, B. and Dewitte, S.: Dust aerosol optical depth retrieval over a desert surface using the SEVIRI window channels, *J. Atmos. Oceanic Technol.*, 26, 704–718, doi:10.1175/2008JTECHA1109.1, 2009.

Dee, D. P., Uppala, S. M., Simmons, A. J., Berrisford, P., Poli, P., Kobayashi, S., Andrae, U., Balmaseda, M. A., Balsamo, G., Bauer, P., Bechtold, P., Beljaars, A. C. M., van de Berg, L., Bidlot, J., Bormann, N., Delsol, C., Dragani, R., Fuentes, M., Geer, A. J., Haimberger, L., Healy, S. B., Hersbach, H., Holm, E. V., Isaksen, L., Kållberg, P., Köhler, M., Matricardi, M., McNally, A. P., Monge-Sanz, B. M., Morcrette, J.-J., Park, B.-K., Peubey, C., de Rosnay, P., Tavolato, C., Thepaut, J.-N., and Vitart, F.: The ERA-Interim reanalysis: configuration and performance of the data assimilation system, *Quart. J. Roy. Meteor. Soc.*, 137, 553–597, doi:10.1002/qj.828, 2011.

Delanoë, J. and Hogan, R. J.: A variational scheme for retrieving ice cloud properties from combined radar, lidar, and infrared radiometer, *J. Geophys. Res. Atmos.*, 113, doi:10.1029/2007JD009000, 2008.

Delanoë, J. and Hogan, R. J.: Combined CloudSat-CALIPSO-MODIS retrievals of the properties of ice clouds, *J. Geophys. Res. Atmos.*, 115, doi:10.1029/2009JD012346, 2010.

Deng, M., Mace, G. G., Wang, Z., and Okamoto, H.: Tropical Composition, Cloud and Climate Coupling Experiment validation for cirrus cloud profiling retrieval using CloudSat radar and CALIPSO lidar, *J. Geophys. Res. Atmos.*, 115, doi:10.1029/2009JD013104, 2010.

Derrien, M. and LeGléau, H.: MSG/SEVIRI cloud mask and type from SAFNWC, *Int. J. Remote Sens.*, 26, 4707–4732, doi:10.1080/01431160500166128, 2005.

Derrien, M., Farki, B., Harang, L., LeGleau, H., Noyalet, A., Pochic, D., and Sairouni, A.: Automatic cloud detection applied to NOAA-11/AVHRR imagery, *Rem. Sens. Envir.*, 46, 246–267, doi:10.1016/0034-4257(93)90046-Z, 1993.

DeSlover, D., Smith, W., Piironen, P., and Eloranta, E.: A methodology of measuring cirrus cloud visible-to-infrared spectral optical depth ratios, *J. Atmos. Oceanic Technol.*, 16, 251–262, doi:10.1175/1520-0426(1999)016<0251:AMFMCC>2.0.CO;2, 1999.

Devasthale, A., Tjernström, M., Karlsson, K.-G., Thomas, M. A., Jones, C., Sedlar, J., and Omar, A. H.: The vertical distribution of thin features over the Arctic analysed from CALIPSO observations, *Tellus B*, 63, 77–85, doi:10.1111/j.1600-0889.2010.00516.x, 2011.

Donovan, D. and van Lammeren, A.: Cloud effective particle size and water content profile retrievals using combined lidar and radar observations. 1. Theory and examples, *J. Geophys. Res. Atmos.*, 106, 27 425–27 448, doi:10.1029/2001JD900243, 2001.

Eliasson, S., Buehler, S. A., Milz, M., Eriksson, P., and John, V. O.: Assessing observed and modelled spatial distributions of ice water path using satellite data, *Atmos. Chem. Phys.*, 11, 375–391, doi:10.5194/acp-11-375-2011, 2011.

Esselborn, M., Wirth, M., Fix, A., Tesche, M., and Ehret, G.: Airborne high spectral resolution lidar for measuring aerosol extinction and backscatter coefficients, *Appl. Opt.*, 47, 346–358, doi:10.1364/AO.47.000346, 2008.

EUMETSAT: Typical Radiometric Accuracy and Noise for MSG-1/2, URL http://www.eumetsat.int/website/wcm/idc/idcplg?IdcService=GET_FILE&dDocName=PDF_TYP_RADIOMET_ACC_MSG-1-2&RevisionSelectionMethod=LatestReleased&Rendition=Web, EUM/OPS/TEN/07/0314, 2007.

Ewald, F., Bugliaro, L., Mannstein, H., and Mayer, B.: An improved cirrus detection algorithm MeCiDA2 for SEVIRI and its evaluation with MODIS, *Atmos. Meas. Tech.*, 6, 309–322, doi:10.5194/amt-6-309-2013, 2013.

Eyre, J. R. and Menzel, W. P.: Retrieval of Cloud Parameters from Satellite Sounder Data: A Simulation Study, *J. Appl. Meteor.*, 28, 267–275, doi:10.1175/1520-0450(1989)028<0267:ROCPFS>2.0.CO;2, 1989.

Feng, Z., Dong, X., Xi, B., McFarlane, S. A., Kennedy, A., Lin, B., and Minnis, P.: Life cycle of midlatitude deep convective systems in a Lagrangian framework, *J. Geophys. Res. Atmos.*, 117, doi:10.1029/2012JD018362, 2012.

Fiolleau, T. and Roca, R.: Composite life cycle of tropical mesoscale convective systems from geostationary and low Earth orbit satellite observations: method and sampling considerations, *Quart. J. Roy. Meteor. Soc.*, 139, 941–953, doi:10.1002/qj.2174, 2013.

Frey, R. A., Ackerman, S. A., Liu, Y., Strabala, K. I., Zhang, H., Key, J. R., and Wang, X.: Cloud Detection with MODIS. Part I: Improvements in the MODIS Cloud Mask for Collection 5, *J. Atmos. Oceanic Technol.*, 25, 1057–1072, doi:10.1175/2008JTECHA1052.1, 2008.

Friedl, M. A., Sulla-Menashe, D., Tan, B., Schneider, A., Ramankutty, N., Sibley, A., and Huang, X.: MODIS Collection 5 global land cover: Algorithm refinements and characterization of new datasets, *Rem. Sens. Envir.*, 114, 168–182, doi:10.1016/j.rse.2009.08.016, 2010.

Fu, Q. and Liou, K. N.: Parameterization of the radiative properties of cirrus clouds, *J. Atmos. Sci.*, 50, 2008–2025, doi:10.1175/1520-0469(1993)050<2008:POTRPO>2.0.CO;2, 1993.

Futyan, J. M. and Del Genio, A. D.: Deep convective system evolution over Africa and the tropical Atlantic, *J. Climate*, 20, 5041–5060, doi:10.1175/JCLI4297.1, 2007.

Gao, B., Yang, P., Han, W., Li, R., and Wiscombe, W.: An algorithm using visible and 1.38-μm channels to retrieve cirrus cloud reflectances from aircraft and satellite data, *IEEE Trans. Geosci. Remote Sens.*, 40, 1659–1668, doi:10.1109/TGRS.2002.802454, 2002.

Gao, B.-C., Han, W., Tsay, S. C., and Larsen, N. F.: Cloud Detection over the Arctic Region Using Airborne Imaging Spectrometer Data during the Daytime, *J. Appl. Meteor.*, 37, 1421–1429, doi:10.1175/1520-0450(1998)037<1421:CDOTAR>2.0.CO;2, 1998.

Garnier, A., Pelon, J., Dubuisson, P., Faivre, M., Chomette, O., Pascal, N., and Kratz, D. P.: Retrieval of cloud properties using CALIPSO Imaging Infrared Radiometer. Part I: Effective emissivity and optical depth, *J. Appl. Meteor. Climatol.*, 51, 1407–1425, doi:10.1175/JAMC-D-11-0220.1, 2012.

Garnier, A., Pelon, J., Dubuisson, P., Yang, P., Faivre, M., Chomette, O., Pascal, N., Lucker, P., and Murray, T.: Retrieval of cloud properties using CALIPSO Imaging Infrared Radiometer. Part II: effective diameter and ice water path, *J. Appl. Meteor. Climatol.*, 52, 2582–2599, doi:10.1175/JAMC-D-12-0328.1, 2013.

Garnier, A., Pelon, J., Vaughan, M. A., Winker, D. M., Trepte, C. R., and Dubuisson, P.: Lidar multiple scattering factors inferred from CALIPSO lidar and IIR retrievals of semi-transparent cirrus cloud optical depths over oceans, *Atmos. Meas. Tech.*, 8, 2759–2774, doi:10.5194/amt-8-2759-2015, 2015.

Goff, J. A. and Gratch, S.: Low-pressure properties of water-from 160 to 212°F., *Trans. Am. Heat. Vent. Eng.*, 52, 95–122, 1946.

Groß, S., Freudenthaler, V., Schepanski, K., Toledano, C., Schäfler, A., Ansmann, A., and Weinzierl, B.: Optical properties of long-range transported Saharan dust over Barbados as measured by dual-wavelength depolarization Raman lidar measurements, *Atmos. Chem. Phys.*, 15, 11 067–11 080, doi:10.5194/acp-15-11067-2015, 2015.

Hamann, U., Walther, A., Baum, B., Bennartz, R., Bugliaro, L., Derrien, M., Francis, P. N., Heidinger, A., Joro, S., Kniffka, A., Le Gléau, H., Lockhoff, M., Lutz, H.-J.,

Meirink, J. F., Minnis, P., Palikonda, R., Roebeling, R., Thoss, A., Platnick, S., Watts, P., and Wind, G.: Remote sensing of cloud top pressure/height from SEVIRI: analysis of ten current retrieval algorithms, *Atmos. Meas. Tech.*, 7, 2839–2867, doi:10.5194/amt-7-2839-2014, 2014.

Hansen, J. E. and Travis, L. D.: Light scattering in planetary atmospheres, *Space Sci. Rev.*, 16, 527–610, doi:10.1007/BF00168069, 1974.

Hartmann, D. L. and Larson, K.: An important constraint on tropical cloud-climate feedback, *Geophys. Res. Lett.*, 29, 12–1–12–4, doi:10.1029/2002GL015835, 2002.

Hastings, D. A. and Emery, W. J.: The advanced very high resolution radiometer (AVHRR)-A brief reference guide, *Photogramm. Eng. Remote Sens.*, 58, 1183–1188, 1992.

Haykin, S.: Neural Networks: A Comprehensive Foundation, Pearson Prentice Hall, 2 edn., 1999.

Heidinger, A. K. and Pavolonis, M. J.: Gazing at Cirrus Clouds for 25 Years through a Split Window. Part I: Methodology, *J. Appl. Meteor. Climatol.*, 48, 1100–1116, doi:10.1175/2008JAMC1882.1, 2009.

Heidinger, A. K., Li, Y., Baum, B. A., Holz, R. E., Platnick, S., and Yang, P.: Retrieval of cirrus cloud optical depth under day and night conditions from MODIS Collection 6 cloud property data, *Remote Sens.*, 7, 7257–7271, doi:10.3390/rs70607257, 2015.

Hersbach, H. and Dee, D.: ERA5 reanalysis is in production, ECMWF Newsletter No. 147, 2016.

Heymsfield, A. J., Winker, D., and van Zadelhoff, G.-J.: Extinction-ice water content-effective radius algorithms for CALIPSO, *Geophys. Res. Lett.*, 32, doi:10.1029/2005GL022742, 2005.

Hlavka, D. L., Yorks, J. E., Young, S. A., Vaughan, M. A., Kuehn, R. E., McGill, M. J., and Rodier, S. D.: Airborne validation of cirrus cloud properties derived from CALIPSO lidar measurements: Optical properties, *J. Geophys. Res. Atmos.*, 117, doi:10.1029/2011JD017053, 2012.

Holl, G., Eliasson, S., Mendrok, J., and Buehler, S. A.: SPARE-ICE: Synergistic ice water path from passive operational sensors, *J. Geophys. Res. Atmos.*, 119, 1504–1523, doi:10.1002/2013JD020759, 2014.

Holz, R., Ackerman, S., Nagle, F., Frey, R., Dutcher, S., Kuehn, R., Vaughan, M., and Baum, B.: Global Moderate Resolution Imaging Spectroradiometer (MODIS) cloud detection and height evaluation using CALIOP, *J. Geophys. Res. Atmos.*, 113, doi:10.1029/2008JD009837, 2008.

Holz, R. E., Platnick, S., Meyer, K., Vaughan, M., Heidinger, A., Yang, P., Wind, G., Dutcher, S., Ackerman, S., Amarasinghe, N., et al.: Resolving ice cloud optical thickness biases between CALIOP and MODIS using infrared retrievals, *Atmos. Chem. Phys.*, 16, 5075–5090, doi:10.5194/acp-16-5075-2016, 2016.

Hong, Y. and Liu, G.: The Characteristics of Ice Cloud Properties Derived from Cloud-Sat and CALIPSO Measurements, *J. Climate*, 28, 3880–3901, doi:10.1175/JCLI-D-14-00666.1, 2015.

Horváth, A. and Soden, B. J.: Lagrangian Diagnostics of Tropical Deep Convection and Its Effect upon Upper-Tropospheric Humidity, *J. Climate*, 21, 1013–1028, doi:10.1175/2007JCLI1786.1, 2008.

Hu, Y., Winker, D., Vaughan, M., Lin, B., Omar, A., Trepte, C., Flittner, D., Yang, P., Nasiri, S. L., Baum, B., Holz, R., Sun, W., Liu, Z., Wang, Z., Young, S., Stamnes, K., Huang, J., and Kuehn, R.: CALIPSO/CALIOP Cloud Phase Discrimination Algorithm, *J. Atmos. Oceanic Technol.*, 26, 2293–2309, doi:10.1175/2009JTECHA1280.1, 2009.

Hulley, G. C., Hook, S. J., Abbott, E., Malakar, N., Islam, T., and Abrams, M.: The ASTER Global Emissivity Dataset (ASTER GED): Mapping Earth's emissivity at 100 meter spatial scale, *Geophys. Res. Lett.*, 42, 7966–7976, doi:10.1002/2015GL065564, 2015.

Imaoka, K. and Nakamura, K.: Statistical Analysis of the Life Cycle of Isolated Tropical Cold Cloud Systems Using MTSAT-1R and TRMM Data, *Mon. Wea. Rev.*, 140, 3552–3572, doi:10.1175/MWR-D-11-00364.1, 2012.

Inoue, T.: On the temperature and effective emissivity determination of semi-transparent cirrus clouds by bi-spectral measurements in the 10 μm window region, *J. Meteor. Soc. Japan*, 63, 88–99, doi:10.2151/jmsj1965.63.1_88, 1985.

Inoue, T., Vila, D., Rajendran, K., Hamada, A., Wu, X., and Machado, L. A. T.: Life Cycle of Deep Convective Systems over the Eastern Tropical Pacific Observed by TRMM and GOES-W, *J. Meteor. Soc. Japan*, 87A, 381–391, doi:10.2151/jmsj.87A.381, 2009.

Iwabuchi, H., Saito, M., Tokoro, Y., Putri, N. S., and Sekiguchi, M.: Retrieval of radiative and microphysical properties of clouds from multispectral infrared measurements, *Progress in Earth and Planetary Science*, 3, 2016.

Jensen, E., Kinne, S., and Toon, O.: Tropical cirrus cloud radiative forcing: Sensitivity studies, *Geophys. Res. Lett.*, 21, 2023–2026, doi:10.1029/94GL01358, 1994.

Jensen, E. J., Lawson, P., Baker, B., Pilson, B., Mo, Q., Heymsfield, A. J., Bansemer, A., Bui, T. P., McGill, M., Hlavka, D., Heymsfield, G., Platnick, S., Arnold, G. T., and Tanelli, S.: On the importance of small ice crystals in tropical anvil cirrus, *Atmos. Chem. Phys.*, 9, 5519–5537, doi:10.5194/acp-9-5519-2009, 2009.

Kiemle, C., Wirth, M., Fix, A., Ehret, G., Schumann, U., Gardiner, T., Schiller, C., Sitnikov, N., and Stiller, G.: First airborne water vapor lidar measurements in the tropical upper troposphere and mid-latitudes lower stratosphere: accuracy evaluation and intercomparisons with other instruments, *Atmos. Chem. Phys.*, 8, 5245–5261, 2008.

King, M. D., Kaufman, Y. J., Menzel, W. P., , and Tanré, D.: Remote sensing of cloud, aerosol, and water vapor properties from the Moderate Resolution Imaging Spectrometer (MODIS), *IEEE Trans. Geosci. Remote Sens.*, 30, 2–27, doi:10.1109/36.124212, 1992.

Kox, S., Bugliaro, L., and Ostler, A.: Retrieval of cirrus cloud optical thickness and top altitude from geostationary remote sensing, *Atmos. Meas. Tech.*, 7, 3233–3246, doi:10.5194/amt-7-3233-2014, 2014.

Krebs, W., Mannstein, H., Bugliaro, L., and Mayer, B.: Technical note: A new day- and night-time Meteosat Second Generation Cirrus Detection Algorithm MeCiDA, *Atmos. Chem. Phys.*, 7, 6145–6159, doi:10.5194/acp-7-6145-2007, 2007.

Kriebel, K., Gesell, G., Kästner, M., and Mannstein, H.: The cloud analysis tool APOLLO: improvements and validations, *Int. J. Remote Sens.*, 24, 2389–2408, doi:10.1080/01431160210163065, 2003.

LeCun, Y., Denker, J. S., and Solla, S. A.: Optimal Brain Damage, in: Advances in Neural Information Processing Systems 2, edited by Touretzky, D. S., pp. 598–605, Morgan-Kaufmann, 1990.

LeCun, Y., Bottou, L., Orr, G., and Müller, K.: Efficient BackProp, *Neural Networks: Tricks of the Trade*, pp. 546–546, 1998.

Leese, J. A., Novak, C. S., and Clark, B. B.: An Automated Technique for Obtaining Cloud Motion from Geosynchronous Satellite Data Using Cross Correlation, *J. Appl. Meteor.*, 10, 118–132, doi:10.1175/1520-0450(1971)010<0118:AATFOC>2.0.CO;2, 1971.

Lindzen, R. S., Chou, M.-D., and Hou, A. Y.: Does the Earth Have an Adaptive Infrared Iris?, *Bull. Amer. Meteor. Soc.*, 82, 417–432, doi:10.1175/1520-0477(2001)082<0417:DTEHAA>2.3.CO;2, 2001.

Liou, K.: An introduction to atmospheric radiation, vol. 84 of *International geophysics series*, Academic press, 2 edn., 2002.

Liu, C., Zipser, E. J., and Nesbitt, S. W.: Global Distribution of Tropical Deep Convection: Different Perspectives from TRMM Infrared and Radar Data, *J. Climate*, 20, 489–503, doi:10.1175/JCLI4023.1, 2007.

Liu, Z., Vaughan, M., Winker, D., Kittaka, C., Getzewich, B., Kuehn, R., Omar, A., Powell, K., Trepte, C., and Hostetler, C.: The CALIPSO Lidar Cloud and Aerosol Discrimination: Version 2 Algorithm and Initial Assessment of Performance, *J. Atmos. Oceanic Technol.*, 26, 1198–1213, doi:10.1175/2009JTECHA1229.1, 2009.

Loveland, T. R. and Belward, A. S.: The IGBP-DIS global 1km land cover data set, DIS-Cover: First results, *Int. J. Remote Sens.*, 18, 3289–3295, doi:10.1080/014311697217099, 1997.

Luo, Z. and Rossow, W. B.: Characterizing Tropical Cirrus Life Cycle, Evolution, and Interaction with Upper-Tropospheric Water Vapor Using Lagrangian Trajectory Analysis of Satellite Observations, *J. Climate*, 17, 4541–4563, doi:10.1175/3222.1, 2004.

Mace, G. G., Deng, M., Soden, B., and Zipser, E.: Association of Tropical Cirrus in the 10–15 km Layer with Deep Convective Sources: An Observational Study Combining Millimeter Radar Data and Satellite-Derived Trajectories, *J. Atmos. Sci.*, 63, 480–503, doi:10.1175/JAS3627.1, 2006.

Machado, L. A. T. and Rossow, W. B.: Structural Characteristics and Radiative Properties of Tropical Cloud Clusters, *Mon. Wea. Rev.*, 121, 3234–3260, doi:10.1175/1520-0493(1993)121<3234:SCARPO>2.0.CO;2, 1993.

Machado, L. A. T., Rossow, W. B., Guedes, R. L., and Walker, A. W.: Life Cycle Variations of Mesoscale Convective Systems over the Americas, *Mon. Wea. Rev.*, 126, 1630–1654, doi:10.1175/1520-0493(1998)126<1630:LCVOMC>2.0.CO;2, 1998.

Martins, E., Noel, V., and Chepfer, H.: Properties of cirrus and subvisible cirrus from nighttime Cloud-Aerosol Lidar with Orthogonal Polarization (CALIOP), related to atmospheric dynamics and water vapor, *J. Geophys. Res. Atmos.*, 116, doi:10.1029/2010JD014519, 2011.

Mathon, V. and Laurent, H.: Life cycle of Sahelian mesoscale convective cloud systems, *Quart. J. Roy. Meteor. Soc.*, 127, 377–406, doi:10.1002/qj.49712757208, 2001.

McFarquhar, G. M. and Heymsfield, A. J.: The Definition and Significance of an Effective Radius for Ice Clouds, *J. Atmos. Sci.*, 55, 2039–2052, doi:10.1175/1520-0469(1998)055<2039:TDASOA>2.0.CO;2, 1998.

McGill, M., Hlavka, D., Hart, W., Scott, V. S., Spinhirne, J., and Schmid, B.: Cloud physics lidar: Instrument description and initial measurement results, *Appl. Opt.*, 41, 3725–3734, doi:10.1364/AO.41.003725, 2002.

McGill, M. J., Vaughan, M. A., Trepte, C. R., Hart, W. D., Hlavka, D. L., Winker, D. M., and Kuehn, R.: Airborne validation of spatial properties measured by the CALIPSO lidar, *J. Geophys. Res. Atmos.*, 112, doi:10.1029/2007JD008768, 2007.

Meerkötter, R., Schumann, U., Doelling, D., Minnis, P., Nakajima, T., and Tsushima, Y.: Radiative forcing by contrails, *Ann. Geophysicae*, 17, 1080–1094, doi:10.1007/s00585-999-1080-7, 1999.

Menzel, W., Smith, W., and Stewart, T.: Improved cloud motion wind vector and altitude assignment using VAS, *J. Appl. Meteor.*, 22, 377–384, doi:10.1175/1520-0450(1983)022<0377:ICMWVA>2.0.CO;2, 1983.

Menzel, W. P., Frey, R. A., Zhang, H., Wylie, D. P., Moeller, C. C., Holz, R. E., Maddux, B., Baum, B. A., Strabala, K. I., and Gumley, L. E.: MODIS Global Cloud-Top Pressure and Amount Estimation: Algorithm Description and Results, *J. Appl. Meteor. Climatol.*, 47, 1175–1198, doi:10.1175/2007JAMC1705.1, 2008.

Merk, D. and Zinner, T.: Detection of convective initiation using Meteosat SEVIRI: implementation in and verification with the tracking and nowcasting algorithm Cb-TRAM, *Atmos. Meas. Tech.*, 6, 1903–1918, doi:10.5194/amt-6-1903-2013, 2013.

Minnis, P., Sun-Mack, S., Young, D. F., Heck, P. W., Garber, D. P., Chen, Y., Spangenberg, D. A., Arduini, R. F., Trepte, Q. Z., Smith, W. L., Ayers, J. K., Gibson, S. C., Miller, W. F., Hong, G., Chakrapani, V., Takano, Y., Liou, K. N., Xie, Y., and Yang, P.: CERES Edition-2 Cloud Property Retrievals Using TRMM VIRS and Terra and Aqua MODIS Data—Part I: Algorithms, *IEEE Trans. Geosci. Remote Sens.*, 49, 4374–4400, doi:10.1109/TGRS.2011.2144601, 2011.

Minnis, P., Hong, G., Sun-Mack, S., Smith, W. L., Chen, Y., and Miller, S. D.: Estimating nocturnal opaque ice cloud optical depth from MODIS multispectral infrared radiances using a neural network method, *J. Geophys. Res. Atmos.*, 121, 4907–4932, doi:10.1002/2015JD024456, 2016.

Mioche, G., Jourdan, O., Ceccaldi, M., and Delanoë, J.: Variability of mixed-phase clouds in the Arctic with a focus on the Svalbard region: a study based on spaceborne active remote sensing, *Atmos. Chem. Phys.*, 15, 2445–2461, doi:10.5194/acp-15-2445-2015, 2015.

Morel, C. and Senesi, S.: A climatology of mesoscale convective systems over Europe using satellite infrared imagery. II: Characteristics of European mesoscale convective systems, *Quart. J. Roy. Meteor. Soc.*, 128, 1973–1995, doi:10.1256/003590002320603494, 2002.

Nakajima, T. and King, M. D.: Determination of the Optical Thickness and Effective Particle Radius of Clouds from Reflected Solar Radiation Measurements. Part I: Theory, *J. Atmos. Sci.*, 47, 1878–1893, doi:10.1175/1520-0469(1990)047<1878:DOTOTA>2.0.CO;2, 1990.

NASA Atmospheric Science Data Center: CALIPSO Quality Statements Lidar Level 2 Cloud and Aerosol Layer Products Version Releases: 3.01, 3.02, URL https://eosweb.larc.nasa.gov/sites/default/files/project/calipso/quality_summaries/ CALIOP_L2LayerProducts_3.01.pdf, 2010.

Nguyen, D. and Widrow, B.: Improving the learning speed of 2-layer neural networks by choosing initial values of the adaptive weights, in: Proc. International Joint Conference on Neural Networks, vol. 3, pp. 21–26, 1990.

Nieman, S., Schmetz, J., and Menzel, W.: A comparison of several techniques to assign heights to cloud tracers, *J. Appl. Meteor.*, 32, 1559–1568, doi:10.1175/1520-0450(1993)032<1559:ACOSTT>2.0.CO;2, 1993.

Nissen, S.: Implementation of a Fast Artificial Neural Network Library (fann), Tech. rep., Department of Computer Science University of Copenhagen (DIKU), URL http://fann. sf.net, 2003.

Platnick, S., King, M. D., Ackerman, S. A., Menzel, W. P., Baum, B. A., Riedi, J. C., and Frey, R. A.: The MODIS cloud products: algorithms and examples from Terra, *IEEE Trans. Geosci. Remote Sens.*, 41, 459–473, doi:10.1109/TGRS.2002.808301, 2003.

Prabhakara, C., Fraser, R. S., Dalu, G., Wu, M.-L. C., Curran, R. J., and Styles, T.: Thin Cirrus Clouds: Seasonal Distribution over Oceans Deduced from Nimbus-4 IRIS, *J. Appl. Meteor.*, 27, 379–399, doi:10.1175/1520-0450(1988)027<0379:TCCSDO>2.0.CO;2, 1988.

Protat, A., Delanoë, J., O'Connor, E., and L'Ecuyer, T.: The evaluation of CloudSat and CALIPSO ice microphysical products using ground-based cloud radar and lidar observations, *J. Atmos. Oceanic Technol.*, 27, 793–810, doi:10.1175/2009JTECHA1397.1, 2010.

Protopapadaki, S. E., Stubenrauch, C. J., and Feofilov, A. G.: Upper tropospheric cloud systems derived from IR sounders: properties of cirrus anvils in the tropics, *Atmos. Chem. Phys.*, 17, 3845–3859, doi:10.5194/acp-17-3845-2017, 2017.

Ramanathan, V. and Collins, W.: Thermodynamic regulation of ocean warming by cirrus clouds deduced from observations of the 1987 El Nino, *Nature*, 351, 27–32, doi:10.1038/351027a0, 1991.

Reichardt, J.: Cloud and Aerosol Spectroscopy with Raman Lidar, *J. Atmos. Oceanic Technol.*, 31, 1946–1963, doi:10.1175/JTECH-D-13-00188.1, 2014.

Reichardt, J., Wandinger, U., Klein, V., Mattis, I., Hilber, B., and Begbie, R.: RAMSES: German Meteorological Service autonomous Raman lidar for water vapor, temperature, aerosol, and cloud measurements, *Appl. Opt.*, 51, 8111–8131, doi:10.1364/AO.51.008111, 2012.

Rosário, N. E., Yamasoe, M. A., Brindley, H., Eck, T. F., and Schafer, J.: Downwelling solar irradiance in the biomass burning region of the southern Amazon: Dependence on aerosol intensive optical properties and role of water vapor, *J. Geophys. Res. Atmos.*, 116, doi:10.1029/2011JD015956, 2011.

Rumelhart, D. E., Hinton, G. E., and Williams, R. J.: Parallel Distributed Processing: Explorations in the Microstructure of Cognition, Vol. 1, chap. Learning Internal Representations by Error Propagation, pp. 318–362, MIT Press, Cambridge, MA, USA, 1986.

Sassen, K., Wang, Z., and Liu, D.: Cirrus clouds and deep convection in the tropics: Insights from CALIPSO and CloudSat, *J. Geophys. Res. Atmos.*, 114, doi:10.1029/2009JD011916, 2009.

Saunders, R. W. and Kriebel, K. T.: An improved method for detecting clear sky and cloudy radiances from AVHRR data, *Int. J. Remote Sens.*, 9, 123–150, doi:10.1080/01431168808954841, 1988.

Sayer, A. M., Poulsen, C. A., Arnold, C., Campmany, E., Dean, S., Ewen, G. B. L., Grainger, R. G., Lawrence, B. N., Siddans, R., Thomas, G. E., and Watts, P. D.: Global retrieval of ATSR cloud parameters and evaluation (GRAPE): dataset assessment, *Atmos. Chem. Phys.*, 11, 3913–3936, doi:10.5194/acp-11-3913-2011, 2011.

Schaul, T., Zhang, S., and LeCun, Y.: No more pesky learning rates, in: 30th International Conference on Machine Learning, pp. 343–351, 2013.

Schmetz, J., Holmlund, K., Hoffman, J., Strauss, B., Mason, B., Gaertner, V., Koch, A., and Berg, L. V. D.: Operational Cloud-Motion Winds from Meteosat Infrared Images, *J. Appl. Meteor.*, 32, 1206–1225, doi:10.1175/1520-0450(1993)032<1206:OCMWFM>2.0.CO;2, 1993.

Schmetz, J., Pili, P., Tjemkes, S., Just, D., Kerkmann, J., Rota, S., and Ratier, A.: An Introduction to Meteosat Second Generation (MSG), *Bull. Amer. Meteor. Soc.*, 83, 977–992, doi:10.1175/1520-0477(2002)083<0977:AITMSG>2.3.CO;2, 2002.

Schmidhuber, J.: Deep learning in neural networks: An overview, *Neural networks*, 61, 85–117, doi:10.1016/j.neunet.2014.09.003, 2015.

Schmit, T. J., Goodman, S. J., Gunshor, M. M., Sieglaff, J., Heidinger, A. K., Bachmeier, A. S., Lindstrom, S. S., Terborg, A., Feltz, J., Bah, K., et al.: Rapid Refresh information of significant events: Preparing users for the next generation of geostationary operational satellites, *Bull. Amer. Meteor. Soc.*, 96, 561–576, doi:10.1175/BAMS-D-13-00210.1, 2015.

Schröder, M., König, M., and Schmetz, J.: Deep convection observed by the Spinning Enhanced Visible and Infrared Imager on board Meteosat 8: Spatial distribution and temporal evolution over Africa in summer and winter 2006, *J. Geophys. Res. Atmos.*, 114, doi:10.1029/2008JD010653, 2009.

Schumann, U., Mayer, B., Gierens, K., Unterstrasser, S., Jessberger, P., Petzold, A., Voigt, C., and Gayet, J.-F.: Effective Radius of Ice Particles in Cirrus and Contrails, *J. Atmos. Sci.*, 68, 300–321, doi:10.1175/2010JAS3562.1, 2011.

Shettle, E.: Models of aerosols, clouds and precipitation for atmospheric propagation studies, in: Atmospheric propagation in the UV, visible, IR and mm-region and related system aspects, no. 454 in AGARD Conference Proceedings, 1989.

Shupe, M. D., Matrosov, S. Y., and Uttal, T.: Arctic Mixed-Phase Cloud Properties Derived from Surface-Based Sensors at SHEBA, *J. Atmos. Sci.*, 63, 697–711, doi:10.1175/JAS3659.1, 2006.

Smith, W. and Platt, C.: Intercomparison of radiosonde, ground-based laser, and satellite-deduced cloud heights, *J. Appl. Meteor.*, 17, 1796–1802, 1978.

Smith, W., Woolf, H., and Jacob, W.: A regression method for obtaining real-time temperature and geopotential height profiles from satellite spectrometer measurements and its application to Nimbus-3 SIRS observations, *Mon. Wea. Rev.*, 98, 604–611, 1970.

Soden, B. J.: The impact of tropical convection and cirrus on upper tropospheric humidity: A Lagrangian analysis of satellite measurements, *Geophys. Res. Lett.*, 31, doi:10.1029/2004GL020980, l20104, 2004.

Sohn, B.-J., Schmetz, J., and Chung, E.-S.: Moistening processes in the tropical upper troposphere observed from Meteosat measurements, *J. Geophys. Res. Atmos.*, 113, doi:10.1029/2007JD009527, 2008.

Stengel, M., Kniffka, A., Meirink, J. F., Lockhoff, M., Tan, J., and Hollmann, R.: CLAAS: the CM SAF cloud property data set using SEVIRI, *Atmos. Chem. Phys.*, 14, 4297–4311, doi:10.5194/acp-14-4297-2014, 2014.

Stephens, G. L., Vane, D. G., Boain, R. J., Mace, G. G., Sassen, K., Wang, Z., Illingworth, A. J., O'Connor, E. J., Rossow, W. B., Durden, S. L., Miller, S. D., Austin, R. T., Benedetti, A., Mitrescu, C., and Team, T. C. S.: THE CLOUDSAT MISSION AND THE A-TRAIN: A New Dimension of Space-Based Observations of Clouds and Precipitation, *Bull. Amer. Meteor. Soc.*, 83, 1771–1790, doi:10.1175/BAMS-83-12-1771, 2002.

Strandgren, J., Bugliaro, L., Sehnke, F., and Schröder, L.: Cirrus cloud retrieval with MSG/SEVIRI using artificial neural networks, *Atmos. Meas. Tech.*, 10, 3547–3573, doi:10.5194/amt-10-3547-2017, 2017a.

Strandgren, J., Fricker, J., and Bugliaro, L.: Characterisation of the artificial neural network CiPS for cirrus cloud remote sensing with MSG/SEVIRI, *Atmos. Meas. Tech.*, 10, 4317–4339, doi:10.5194/amt-10-4317-2017, 2017b.

Stubenrauch, C., Stephens, G., and Group, G. U. P. W.: Process Evaluation Study on Upper Tropospheric Clouds and Convection, *GEWEX News*, 27, 4–6, 2017.

Stubenrauch, C. J., Cros, S., Guignard, A., and Lamquin, N.: A 6-year global cloud climatology from the Atmospheric InfraRed Sounder AIRS and a statistical analysis in synergy

with CALIPSO and CloudSat, *Atmos. Chem. Phys.*, 10, 7197–7214, doi:10.5194/acp-10-7197-2010, 2010.

Stubenrauch, C. J., Rossow, W. B., Kinne, S., Ackerman, S., Cesana, G., Chepfer, H., Girolamo, L. D., Getzewich, B., Guignard, A., Heidinger, A., Maddux, B. C., Menzel, W. P., Minnis, P., Pearl, C., Platnick, S., Poulsen, C., Riedi, J., Sun-Mack, S., Walther, A., Winker, D., Zeng, S., and Zhao, G.: Assessment of Global Cloud Datasets from Satellites: Project and Database Initiated by the GEWEX Radiation Panel, *Bull. Amer. Meteor. Soc.*, 94, 1031–1049, doi:10.1175/BAMS-D-12-00117.1, 2013.

Szejwach, G.: Determination of semi-transparent cirrus cloud temperatures from infrared radiances: Application to Meteosat, *J. Appl. Meteor.*, 21, 384–393, doi:10.1175/1520-0450(1982)021<0384:DOSTCC>2.0.CO;2, 1982.

Ten Hoeve, J. E., Jacobson, M. Z., and Remer, L. A.: Comparing results from a physical model with satellite and in situ observations to determine whether biomass burning aerosols over the Amazon brighten or burn off clouds, *J. Geophys. Res. Atmos.*, 117, doi:10.1029/2011JD016856, 2012.

Toth, T. D., Zhang, J., Campbell, J. R., Reid, J. S., Shi, Y., Johnson, R. S., Smirnov, A., Vaughan, M. A., and Winker, D. M.: Investigating enhanced Aqua MODIS aerosol optical depth retrievals over the mid-to-high latitude Southern Oceans through inter-comparison with co-located CALIOP, MAN, and AERONET data sets, *J. Geophys. Res. Atmos.*, 118, 4700–4714, doi:10.1002/jgrd.50311, 2013.

Trigo, I. F., Peres, L. F., DaCamara, C. C., and Freitas, S. C.: Thermal Land Surface Emissivity Retrieved From SEVIRI/Meteosat, *IEEE Trans. Geosci. Remote Sens.*, 46, 307–315, doi:10.1109/TGRS.2007.905197, 2008.

van Vuuren, D. P., Edmonds, J., Kainuma, M., Riahi, K., Thomson, A., Hibbard, K., Hurtt, G. C., Kram, T., Krey, V., Lamarque, J.-F., Masui, T., Meinshausen, M., Nakicenovic, N., Smith, S. J., and Rose, S. K.: The representative concentration pathways: an overview, *Climate Change*, 109, 5, doi:10.1007/s10584-011-0148-z, 2011.

Vaughan, M. A., Winker, D. M., and Powell, K. A.: CALIOP Algorithm Theoretical Basis Document Part 2: Feature Detection and Layer Properties Algorithms, PC-SCI-202 Part 2, 2005.

Vaughan, M. A., Powell, K. A., Winker, D. M., Hostetler, C. A., Kuehn, R. E., Hunt, W. H., Getzewich, B. J., Young, S. A., Liu, Z., and McGill, M. J.: Fully Automated Detection of Cloud and Aerosol Layers in the CALIPSO Lidar Measurements, *J. Atmos. Oceanic Technol.*, 26, 2034–2050, doi:10.1175/2009JTECHA1228.1, 2009.

Vázquez-Navarro, M., Mayer, B., and Mannstein, H.: A fast method for the retrieval of integrated longwave and shortwave top-of-atmosphere upwelling irradiances from

MSG/SEVIRI (RRUMS), *Atmos. Meas. Tech.*, 6, 2627–2640, doi:10.5194/amt-6-2627-2013, 2013.

Verlinde, J., Harrington, J. Y., Yannuzzi, V. T., Avramov, A., Greenberg, S., Richardson, S. J., Bahrmann, C. P., McFarquhar, G. M., Zhang, G., Johnson, N., Poellot, M. R., Mather, J. H., Turner, D. D., Eloranta, E. W., Tobin, D. C., Holz, R., Zak, B. D., Ivey, M. D., Prenni, A. J., DeMott, P. J., Daniel, J. S., Kok, G. L., Sassen, K., Spangenberg, D., Minnis, P., Tooman, T. P., Shupe, M., Heymsfield, A. J., and Schofield, R.: The Mixed-Phase Arctic Cloud Experiment, *Bull. Amer. Meteor. Soc.*, 88, 205–221, doi:10.1175/BAMS-88-2-205, 2007.

Voigt, C., Schumann, U., Minikin, A., Abdelmonem, A., Afchine, A., Borrmann, S., Boettcher, M., Buchholz, B., Bugliaro, L., Costa, A., Curtius, J., Dollner, M., Dörnbrack, A., Dreiling, V., Ebert, V., Ehrlich, A., Fix, A., Forster, L., Frank, F., Fütterer, D., Giez, A., Graf, K., Grooß, J.-U., Groß, S., Heimerl, K., Heinold, B., Hüneke, T., Järvinen, E., Jurkat, T., Kaufmann, S., Kenntner, M., Klingebiel, M., Klimach, T., Kohl, R., Krämer, M., Krisna, T. C., Luebke, A., Mayer, B., Mertes, S., Molleker, S., Petzold, A., Pfeilsticker, K., Port, M., Rapp, M., Reutter, P., Rolf, C., Rose, D., Sauer, D., Schäfler, A., Schlage, R., Schnaiter, M., Schneider, J., Spelten, N., Spichtinger, P., Stock, P., Walser, A., Weigel, R., Weinzierl, B., Wendisch, M., Werner, F., Wernli, H., Wirth, M., Zahn, A., Ziereis, H., and Zöger, M.: ML-CIRRUS: The Airborne Experiment on Natural Cirrus and Contrail Cirrus with the High-Altitude Long-Range Research Aircraft HALO, *Bull. Amer. Meteor. Soc.*, 98, 271–288, doi:10.1175/BAMS-D-15-00213.1, 2017.

Waliser, D. E., Li, J.-L. F., Woods, C. P., Austin, R. T., Bacmeister, J., Chern, J., Del Genio, A., Jiang, J. H., Kuang, Z., Meng, H., Minnis, P., Platnick, S., Rossow, W. B., Stephens, G. L., Sun-Mack, S., Tao, W.-K., Tompkins, A. M., Vane, D. G., Walker, C., and Wu, D.: Cloud ice: A climate model challenge with signs and expectations of progress, *J. Geophys. Res. Atmos.*, 114, doi:10.1029/2008JD010015, 2009.

Wallace, J. M. and Hobbs, P. V.: Atmospheric science: an introductory survey, vol. 92, Elsevier, 2006.

Wang, C., Platnick, S., Zhang, Z., Meyer, K., and Yang, P.: Retrieval of ice cloud properties using an optimal estimation algorithm and MODIS infrared observations: 1. Forward model, error analysis, and information content, *J. Geophys. Res. Atmos.*, 121, 5809–5826, doi:10.1002/2015JD024526, 2016.

Watts, P. D., Bennartz, R., and Fell, F.: Retrieval of two-layer cloud properties from multispectral observations using optimal estimation, *J. Geophys. Res. Atmos.*, 116, doi:10.1029/2011JD015883, 2011.

Weinzierl, B., Sauer, D., Esselborn, M., Petzold, A., Veira, A., Rose, M., Mund, S., Wirth, M., Ansmann, A., Tesche, M., Gross, S., and Freudenthaler, V.: Microphysical and optical properties of dust and tropical biomass burning aerosol layers

in the Cape Verde region – an overview of the airborne in situ and lidar measurements during SAMUM-2, *Tellus B: Chemical and Physical Meteorology*, 63, 589–618, doi:10.1111/j.1600-0889.2011.00566.x, 2011.

Wendisch, M., Yang, P., and Pilewskie, P.: Effects of ice crystal habit on thermal infrared radiative properties and forcing of cirrus, *J. Geophys. Res. Atmos.*, 112, doi:10.1029/2006JD007899, 2007.

Wetzel, C. and Brümmer, B.: An Arctic inversion climatology based on the European Centre Reanalysis ERA-40, *Meteor. Z.*, 20, 589–600, doi:10.1127/0941-2948/2011/0295, 2011.

Williams, M. and Jr., R. A. H.: Satellite-Observed Characteristics of Winter Monsoon Cloud Clusters, *Mon. Wea. Rev.*, 115, 505–519, doi:10.1175/1520-0493(1987)115<0505:SOCOWM>2.0.CO;2, 1987.

Wilson, L. D., Curry, J. A., and Ackerman, T. P.: Satellite Retrieval of Lower-Tropospheric Ice Crystal Clouds in the Polar Regions, *J. Climate*, 6, 1467–1472, doi:10.1175/1520-0442(1993)006<1467:SROLTI>2.0.CO;2, 1993.

Winker, D. M., Pelon, J. R., and McCormick, M. P.: The CALIPSO mission: Spaceborne lidar for observation of aerosols and clouds, in: Proc. SPIE, vol. 4893, pp. 1–11, International Society for Optics and Photonics, 2003.

Winker, D. M., Vaughan, M. A., Omar, A., Hu, Y., Powell, K. A., Liu, Z., Hunt, W. H., and Young, S. A.: Overview of the CALIPSO Mission and CALIOP Data Processing Algorithms, *J. Atmos. Oceanic Technol.*, 26, 2310–2323, doi:10.1175/2009JTECHA1281.1, 2009.

Wirth, M., Fix, A., Mahnke, P., Schwarzer, H., Schrandt, F., and Ehret, G.: The airborne multi-wavelength water vapor differential absorption lidar WALES: system design and performance, *Appl. Phys. B*, 96, 201–213, doi:10.1007/s00340-009-3365-7, 2009.

Wright, J. S., Fu, R., and Heymsfield, A. J.: A statistical analysis of the influence of deep convection on water vapor variability in the tropical upper troposphere, *Atmos. Chem. Phys.*, 9, 5847–5864, doi:10.5194/acp-9-5847-2009, 2009.

Wu, D. L., Lambert, A., Read, W. G., Eriksson, P., and Gong, J.: MLS and CALIOP cloud ice measurements in the upper troposphere: A constraint from microwave on cloud microphysics, *J. Appl. Meteor. Climatol.*, 53, 157–165, doi:10.1175/JAMC-D-13-041.1, 2014.

Yang, P., Liou, K.-N., Bi, L., Liu, C., Yi, B., and Baum, B. A.: On the radiative properties of ice clouds: Light scattering, remote sensing, and radiation parameterization, *Adv. Atmos. Sci.*, 32, 32–63, doi:10.1007/s00376-014-0011-z, 2015.

Yorks, J. E., Hlavka, D. L., Vaughan, M. A., McGill, M. J., Hart, W. D., Rodier, S., and Kuehn, R.: Airborne validation of cirrus cloud properties derived from CALIPSO lidar measurements: Spatial properties, *J. Geophys. Res. Atmos.*, 116, doi:10.1029/2011JD015942, 2011.

Young, S. A. and Vaughan, M. A.: The Retrieval of Profiles of Particulate Extinction from Cloud-Aerosol Lidar Infrared Pathfinder Satellite Observations (CALIPSO) Data: Algorithm Description, *J. Atmos. Oceanic Technol.*, 26, 1105–1119, doi:10.1175/2008JTECHA1221.1, 2009.

Yuan, J., Jr., R. A. H., and Heymsfield, A. J.: Vertical Structures of Anvil Clouds of Tropical Mesoscale Convective Systems Observed by CloudSat, *J. Atmos. Sci.*, 68, 1653–1674, doi:10.1175/2011JAS3687.1, 2011.

Yue, Q. and Liou, K.: Cirrus cloud optical and microphysical properties determined from AIRS infrared spectra, *Geophys. Res. Lett.*, 36, doi:10.1029/2008GL036502, 2009.

Zhang, H. and Menzel, W. P.: Improvement in thin cirrus retrievals using an emissivity-adjusted CO2 slicing algorithm, *J. Geophys. Res. Atmos.*, 107, doi:10.1029/2001JD001037, 2002.

Zhang, Y., Macke, A., and Albers, F.: Effect of crystal size spectrum and crystal shape on stratiform cirrus radiative forcing, *Atmos. Res.*, 52, 59–75, doi:10.1016/S0169-8095(99)00026-5, 1999.

Zinner, T., Mannstein, H., and Tafferner, A.: Cb-TRAM: Tracking and monitoring severe convection from onset over rapid development to mature phase using multi-channel Meteosat-8 SEVIRI data, *Meteor. Atmos. Phys.*, 101, 191–210, doi:10.1007/s00703-008-0290-y, 2008.

Zinner, T., Forster, C., de Coning, E., and Betz, H.-D.: Validation of the Meteosat storm detection and nowcasting system Cb-TRAM with lightning network data - Europe and South Africa, *Atmos. Meas. Tech.*, 6, 1567–1583, doi:10.5194/amt-6-1567-2013, 2013.

Acknowledgements